Cranfield University

Chen Liang

TURBULENT FLOW SIMULATIONS AROUND THE FRONT WING OF A RACING CAR

School of Engineering

MSc Thesis

Cranfield University

School of Engineering

MSc THESIS

Academic Year 2008-2009

Chen Liang

Turbulent Flow Simulations Around The Front Wing of A Racing Car

Supervisors: **Dr. Bowen Zhong and Prof. Dimitris Drikakis**

July 2010

This thesis is submitted in partial fulfillment of the requirements for the degree of MSc by research

Abstract

Aerodynamics has played a more and more important role in motorsports for maximising the race car performance. Amongst all the aerodynamic devices of race car, the front wing plays a vital role. In order to evaluate aerodynamic forces and develop new solutions for the race car, Computational Fluid Dynamics (CFD) has become a powerful tool. The most classical numerical simulations are based on solving the Reynolds Averaged Navier-Stokes (RANS) equations.

In this project, the aerodynamics of front wings in ground effect has been studied using computational methods. A serious of simulations has carried out both for a single element wing and a double element wing by using DLR's FLOWer code. Simulations using three numerical schemes and three different turbulence models are carried out and the computational results were compared with the experimental data around the single element wing in ground effect. Further on, numerical studies on the aerodynamics performance have carried out for both single and double element wings in ground effect.

For the investigation of different numerical methods and different turbulence models, the results obtained by using HLLC Riemann solver with 3rd order WENO schemes in conjunction with two-equation SST k-ω turbulence model shows more accurate simulations for the lift, drag coefficients and the pressure distributions at all heights. Furthermore, the numerical study on single element wing shows that the decreased height (to a certain level) and the increased angle of attack (up to the stall angle) will result in larger downforce. For the double element wing, various simulations were carried out under the configurations that the main element is fixed while the flap angle changes. The general tendency for both the downforce and the drag are similar with the single element wing, however the magnitude is much bigger. It is also found that the increased camber which made by the adding flap does not bring a significant vortex shedding after the trailing edge.

Acknowledgements

It has been a big challenge to complete this MSc thesis, and I honestly wish to thank many people who have given me lots of generous help.

Firstly, I would like to thank Dr Bowen Zhong for his supervise throughout the whole research. His patience has encouraged me a lot no matter what problems happened. And also for his considerate help in my life in England. Specially, I would like to express my sincere gratitude to Prof. Xin Zhang of Southampton University, for his generous in providing the geometry of the single element front wing to help me to complete the whole investigation smoothly.

Then, my deepest gratitude goes to my parents who supported me in every field from finance to spirit. Their trust gives me a lot of power to continue pushing myself to step forward.

Last but not least, I am grateful to all of my friends here in Cranfield Univerisity and also in China, for the time they accompany me, especially in the hard times.

Contents

List of Figures

List of Tables

Nomenclature

Symbols

b	Span
c	Chord length
Cl	Lift coefficient
Cd	Drag coefficient
Cp	Pressure coefficient
k	Specific turbulence kinetic energy
Ma	Mach number
p	Static pressure
Pr	Prandtl number
q	Heat flux
R	Gas constant
Re	Reynolds number
S	Reference area
T	Temperature
u	Velocity in x-direction
v	Velocity in y-direction

w	Velocity in z-direction
U_∞	Freestream velocity
u_{min}	Minimum u velocity in wake
x, y, z	Coordinates
y^+	Y plus
α	Angle of attack
α_{flap}	Flap angle of attack
ε	Dissipation rate of the kinetic energy
μ	Molecular dynamic viscosity
μ_t	Turbulent dynamic viscosity
ν	Kinematic viscosity
ρ	Density
τ_{ij}	Stress tensor
ω	Specific turbulent dissipation
δ_{99}	Wake thickness, as measured by 99%displacement thickness
δ_{bottom}	Bottom of wake thickness
δ_{top}	Top of wake thickness

Acronyms

CDS	Central Differencing Scheme
CFD	Computational Fluid Dynamics
CFL	Courant-Friedrichs-Lewy
DLR	Deutsches Institut fur Luft- und Raumfahrt (German Aerospace Center)
HLL	Harten-Lax-van Leer Riemann solver
HLLC	Harten-Lax-van Leer Riemann solver, 'C' denotes contact
ILES	Implicit Large Eddy Simulation
LES	Large Eddy Simulation
MUSCL	Monotonic Upstream Scheme for Conservation Laws
RANS	Reynolds-Averaged Navier-Stokes
S-A	Spalart-Allmaras Turbulence Model
SST	Shear Stress Transport (k-ω turbulence model)
TVD	Total Variation Diminishing
WENO	Weighted Essentially Non-Oscillatory

Chapter 1

Introduction

1.1 Motivation

During the past years, aerodynamics has played a more and more important role in motorsports for maximising the race car performance. In order to get the best race car performance, downforce has become the focus of every race team. The downforce, which at the top speed could be four times of the car weight, can force the racing car closer to the ground. As a result, it improves the acceleration, braking and cornering speed of the car. As the regulation changes every year to reduce the speed of race car, engineers of every race team make their great effort to maximise the downforce in order to win the champion.

Among the aerodynamic devices of race car, the front wing plays a vital role. It is the first part of a racing car to meet the air mass and the airflow which has been disturbed here. The wake which has been generated by the front wing would directly affect the flow field over the body and the rear of the car. For engineers, they expect to gain about 25-30% of the total downforce from the front wing.

In order to get an advantage against the competitors, the most important problem for the aerodynamic designers is to evaluate aerodynamic forces on the race car correctly. In addition to the experimental measurements obtained from wind tunnel tests, the numerical simulations are used for predicting their performance. Hence Computational Fluid Dynamics (CFD) becomes a powerful tool for developing new aerodynamic solutions. It is more economic, also more visualized and efficient. However, the accuracy of the results from CFD simulations is still a huge challenge for the highly complex flow over the front wing. The most classical numerical simulations are based on solving the Reynolds Averaged Navier-Stokes (RANS)

equations. However, the results highly depended on the turbulence models which are not accurate for the complex flows.

1.2 Objective

The aim of the project is to investigate the suitability and the accuracy of some high resolution numerical methods in conjunction with different turbulent flow approaches for simulating the flow around a front wing. In order to achieve this, some numerical studies of a single front wing in ground effect with different heights will be explored by comparing with the experimental results. Furthermore, other set of simulations will be carried out to focus on the aerodynamic performance of the single element with ground effect. Finally, a series simulation around a double element front wing will be performed in order to improve the aerodynamic performance.

Chapter 2

Literature Review

2.1 Aerodynamics and Race Cars

To attain a good performance of race cars, a very good combination among all elements such as engine, tyres, suspension, road and aerodynamics is required. Nowadays, aerodynamics has gained an increased attention in motorsports with regards to the maximization of the race car performance.

2.1.1 The Purpose of Downforce

In the majority of motorsports' series, the aim is to produce the fastest race car with perfect handling. Normally, the effects of aerodynamics on the race car can be represented by lift, drag and stability. The creation of downforce became the main purpose instead of the lift, when designers found out that the stability is related to the downforce. Indeed, the stability means to hold the vehicles onto the racetrack in every driving situation and without a side slipping in corner and breaking processes. For example, Figure 1 shows the forces on a side-slipping situation. The right-hand side shows the vertical force (F_z) and the tangential force (F_y) in a Cartesian coordinate system aligned with the vehicle. The vehicle is moving opposite to the x direction, but slipping with an angle of β. In the linear range, the force is the same as the well-known Coulomb's law:

$$F_y = f \bullet F_z \tag{2.1}$$

Where: f is the static friction coefficient

The simple law shown in Figure 1 demonstrates that: if the driver uses the same velocity (i.e. same F_y, because the velocity in a corner depends on the F_y) to turn in a corner, the larger downforce F_z would cause the tyre to have less slip (point B). Alternatively, the driver can drive much faster (point C) with larger downforce compared to point A in the same slip angle without side slipping.

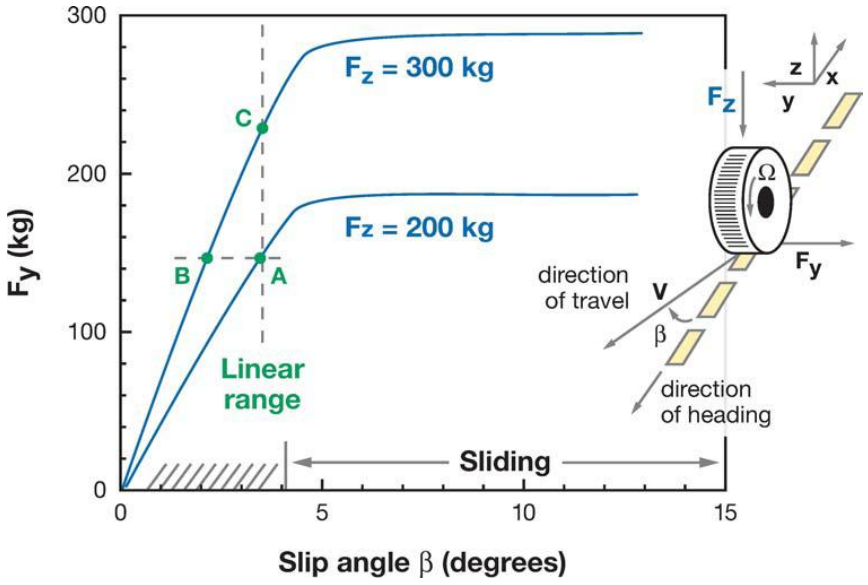

Figure 1: Tyre-generated side force versus slip angle, and the effect of normal force. Inset depicts definition of side slip [Source: Katz 2006]

Figure 2 is another validation of the increase speed in corner due to the benefits of aerodynamic downforce. It shows the trend on the lateral acceleration during the last fifty years. The tremendous increase on lateral acceleration is due to the increased downforce when comparing the two lines in the figure.

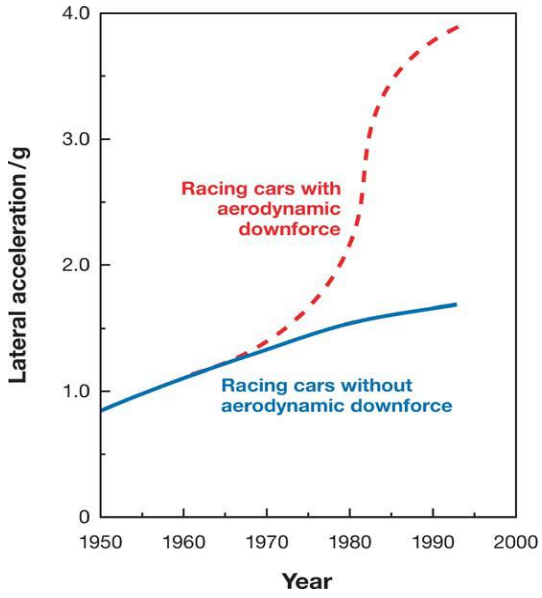

Figure 2: Trends in maximum cornering acceleration, during the past 50 years [Source : Patrick 2006]

2.1.2 Race Car Front Wing

The front wing is not a big part of the race car; however, it is considered as the most crucial aerodynamic component of the race car since it is the first part of a race car to meet the air mass and the airflow which has been disturbed here. The wake that has been generated here would also directly affect the flow field over the body and the rear of the car. The most important contribution of the front wing is to generate a great amount of downforce both for breaking at the end of straight lines and accelerating in corners.

Downforce Generation

The aerodynamic designer has two primary concerns (see in ref). The first one is the creation of the downforce in order to push the car's tyres onto the track and improve the cornering forces. The second one is to minimise the drag caused which acts to slow the car down.

The two main components of the racing car that can be used to create downforce when the car is travelling at racing speed are the shape of the body and the use of the airfoils.

As downforce is referred to as "aerodynamic grip" and is distinguished from the "mechanical grip," which is a function of the car mass repartition, tyres and suspension. The downforce is usually generated by the shape of the body and reversed wings. In the experiments of Zerihan and Zhang (2001), it showed that the front wing generated most of the downforce (25-30% of the total downforce of the race car) while the shape of the body with other components, such as the rear wing and the diffuser, created the rest of it. As it is only an inversion of the aircraft wings, the principle is the same for race car wings. Air flows at different speeds over the two sides of the wing (by having to travel different distances over its contours) and this creates a difference in pressure, a physical rule known as Bernoulli's Principle. As this pressure tries to balance, the wing tries to move in the direction of the low pressure. Aeroplanes use their wings to create lift; race cars use theirs to create downforce. A modern Formula One car is capable of developing 3.5G lateral cornering force (three and a half times its own weight) [Katz (2006)].

Ground Effect

The ground effect was caused by the attention originally from the claims by pilots that in approaching the ground, a cushioning effect was observed. The early test [Zahm and Bear (1921)] using a fixed ground on an RAF6 airfoil demonstrated that the lift increases and the drag reduces for a given angle of attack. Other early tests [Raymond (1921)] also showed that liftslope increases can be expected. After that, it is believed that the pressure on the pressure surface increases due to the image beneath the ground plane inducing a lower velocity in that region [Screbrinsky and Biachuev (1946)]. Therefore, the lift of a wing increases when the wing is approaching to the ground. This effect works well for both airplane wings which generate lift and inverted wings which create downforce. Until very recently, however, studies of

downforce which is produced by wings in ground effect were very much incomplete. Dominy (1992) firstly presented a short description of the aerodynamics of a wing. He pointed out that the ground effect was effectively constraining the flow over the suction surface, hence generating an increase in suction. Dominy hypothesised that in close proximity to the ground, the wing would stall due to the boundary layer separation because of the large suction and the related adverse pressure gradient.

To increase the downforce, the basic idea is to create an area of low pressure underneath the car. Racing car designers have achieved low pressure by designing the underside of the car so that incoming air is accelerated through a narrow slot between the car and the ground to get lowering pressure in light of the Bernoulli's principle. The first car which started the ground effect revolution in Formula One is the Lotus 78 ‘wing car’ used in the 1977 and 1978 seasons [Nye and Doug (1985)]. Wright, one of the designers of this car, set about experimenting with F1 car body shapes using a wind tunnel and a rolling road, when accidently he began to get remarkable results in one of the models. Closer inspection showed that as the rolling road's speed increased, the shaped underbody was being drawn closer to the surface of the road. Wright tested with pieces of cardboard attached to the side of the model car body, and the level of perceived downforce produced was phenomenal.

2.2 The experimental investigations of racing car front wing in ground effect

Although this project is mainly focused on numerical simulations, it is essential for the conduct of this research to investigate the experimental results from the testing of the same devices in wind tunnels. Additionally, the experimental results are necessary for the validation of the CFD results. However, due to the competitive character in the autosports, the published works are rather limited.

As mentioned above, the ground effect becomes noticeable when the wing is approaching the ground. Therefore the ground clearance was found to be a very

influential factor. The data in Figure 3 [Zerihan & Zhang (2000)] shows clearly the relationship between forces and ground clearance. Before the distance of ground clearance is reduced to a certain critical value, the downforce would be increasing. When the distance is further reduced, the downforce will only decrease. This ground critical clearance value is about 0.1c (see Figure 3). It is called the force reduce phenomenon. It is worth noting that the drag always increases when the wing gets closer to the ground (see also Figure 3).

Knowles et al (1994) tested a single element GA (W)-1 wing in a wind tunnel with a moving belt that simulated the moving ground. Forces were measured at a variety of incidences with its suction surface located at a range of heights from 1.0C down to 0.12C from the ground. The test showed that as the ground clearance decreases, the downforce generated increases and the stall angle is reduced. The drag also increases in the same process. However, the effect is smaller than that affected by the height. It is stated that the extra lift is caused by the gap between the wing suction surface and the ground. However, it still lack of understanding thoroughly this phenomenon by the limitation to the region of the aerofoil forming the diffuser.

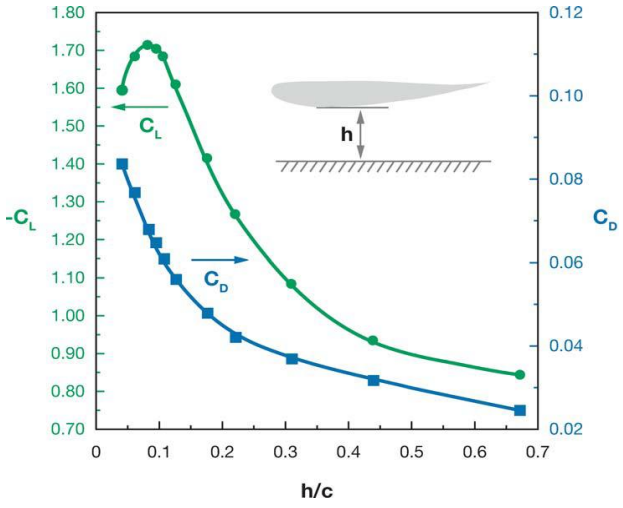

Figure 3: Downforce and drag coefficient versus ground clearance for an inverted LS(1)-0413 airfoil. [Source: Zerihan & Zhang (2000), α =1 deg, Re = 2×10^6, moving ground plane.]

Ranzenbach and Barlow (1994, 1997) presented a series of experiments both on the single element wing and the multi-element wing. Their work begins by using two dimensional experimental work in a fixed ground wing tunnel on a NACA 0015 and NACA 4412 sections for the single element wing. It was found that the force reduced when the suction surface was too close to the ground. This phenomenon happens because the ground plane and airfoil boundary layers merge. They also discovered that the force deduction phenomena happened at a much higher ground clearance for the cambered airfoil such as multi-element wings compared to the symmetric airfoil. They also conducted an additional test in a fixed ground wind tunnel on a NACA 63_2 -215 Mod B section with a 30% slotted flap for a two-dimensional double-element model. The results showed that the force reduction phenomena occurred at the ground clearance less than approximately 22% of front wing chord length.

Jasinski and Selig (1998) performed an experimental study over a UIUC700 two-element airfoil in a Low-Speed wind tunnel. Results showed that the Reynolds number only affects the lift and drag about 3-4% over the range tested. However, by changing the flap deflection of 10 deg, the lift coefficient increased by 0.5, while the drag coefficient was largely unaffected at a constant lift coefficient. Meanwhile, it showed the endplate design is significant in race car front design. When the area is increased, the overall lift coefficient increases while the drag coefficient reduces clearly.

More recent experimental studies on front wing in ground effect have been performed by Zerihan and Zhang (2000) in the University of Southampton using a low-speed wind tunnel (see Figure 4). This single element model was designed as a 80 % scaled model of the main element of the 1998 Tyrrell 026 F1 car front wing. A span of 1100mm was used, to give a wing chord of 223.4mm for the aspect ratio of 4.92. Generic endplates were used throughout the test.

The investigation of the single element wing performed by Zerhan and Zhang (2000)

concluded that the fluid flow around the wing gave rise to different levels of downforce according to ride heights and there was a separation of the boundary layer near the trailing edge of the suction surface. Also, the separation increased when the wing was placed closer to the ground. The force reduction phenomenon occurred due to the combination of both the minimum loss of downforce by flow separation and the maximum of velocity generated in lower surface with small ride height, instead of the merging wing and ground boundary layers.

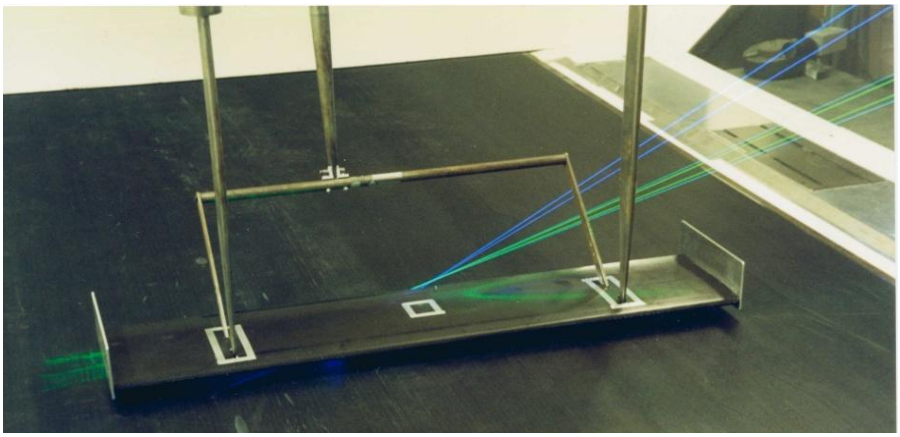

Figure 4: Installation of the Tyrrell 026 wing in the 3.5m x 2.5m wind tunnel [Zerihan and Zhang (2000)]

Furthermore, Zerhan and Zhang (2003) made another investigation on a cambered, double-element wing in ground effect. It was found that most of the downforce was produced by the main element wing. In addition to measure the overall forces and surface pressure, an experiment was also employed using laser Doppler anemometry (LDA) and particle image velocimetry (PIV) methods to capture the wake flow. It showed that the velocity deficit and the thickness of the wake had a close relationship with the flap angles.

The difference between the simplified abstraction of 2-D model and the real 3-D model installed on the racing car is focused on the wing tip and the generated tip vortices. They are the products of flow separation and pressure difference. In turn,

they affect the down-force through strong corner flow and affect the separation on the wing. Zerhan and Zhang (2002) also made a set of investigations on them. They were studied using a range of methods including particle image velocimetry (PIV), laser Doppler anemometry (LDA), surface pressures, force balance measurements, and surface flow visualization. The presence of the tip vortex plays a secondary role in the down-force enhancement process. However it contributes to the down-force enhancement and helps to define the force behaviour in the force enhancement region, in particular near the maximum force height. The rate of change in the down-force curve is linked to the strength of the vortex. When the maximum down-force height is reached the tip vortex breaks down completely. The characters of the tip vortex led to changes in the aerodynamic force behavior in ground effect. The down-force was found affected by the presence of separation on the suction surface and the tip vortices. At larger ground heights, a concentrated tip vortex was produced off the edge of the endplate on the wing through separation, contributing to the down-force enhancement process. The tip vortex induced an up wash on the wing, leading to an effective reduction in the incidence of the wing and hence smaller extents of separation near the wing tip. However, vortex breakdown occurred as the wing was lowered to the ground, leading to a slowdown in the force enhancement.

Although the experiment of single element wing in ground effect has been done almost comprehensively in wind tunnel by Zhang, an optimized car will have no individual element working in its best individual configuration. According to Zerham and Zhang (2001), they also pointed out that to generate best entire car, the downstream devices are therefore tuned for the front wing configuration sometimes. It is possible to generate more downforce from the front wing; however this destroys the flow over the remainder of the car. This may not include the heights extremely close to the ground where the greatest down force is obtained. Meanwhile, as the racing car following closely, the turbulence that a leading car generates reduces the ability of the following car to produce downfroce, particularly the front wing. It needs to improve also in wind tunnel test.

2.3 The CFD investigations of the race car front wing in ground effect

Ranzenbach and Barlow (1996) presented a simulation on a single element wing with the adventage of the ABO scheme in order to allow the quick pre-processing of grids. The solutions used a two-dimensional, multi-block, structured grid RANS solver for the incompressible, viscous flow around arbitrary bodies referred to as Finite Analytic Navier Stokes (FANS). The comparison of the experimental measurements and FANS for the case of NACA 4412 showed that the lift, with the precondition of ground clearance, is qualitatively similar to the experiment test but generates more downforce at all heights. The drag calculation showed similarities to the experimental result although it increased monotonically. Meanwhile, the computed drag was lower for any height except for the minimum ground clearance. Additionally, other RANS computations for an inverted NACA 63_2-215 Mod B airfoil with a single-slotted, 30% chord flap were conducted by Ranzenbach and Barlow (1997). The RANS simulation is excellent for modelling such flow details in the operating region which is steadier with front wing practice.

Another simulation done by Moryoseff and Levy et al (2001) covered steady and unsteady simulation about an oscillating wing in and out of ground effect. The study was carried out using a highly cambered inverted wing with an aspect ratio of 5. The results showed a strong effect of the ground presence on both the lift and drag. The results from the unsteady simulations showed a nonlinear behavior which strengthens with ground effect, and that in ground effect, the range of reduced frequencies for which the unsteady Kutta condition is still applicable, is narrower compared to the range of frequencies out of ground effect.

Kieffer et al (2006) provided some information for teams competing in the minor league Formula Mazda racecar class. A study was carried out using the Star-CD CFD code to perform a turbulent simulation (using a $k-\omega$ model) of the airflow on the

front and rear wings of a Formula Mazda car with different angles of attack and the effect of the ground on the front wing. It was revealed that the ground effect has a remarkable influence on the C_l and that the angle of attack has a significant effect on the lift and drag coefficients. It was also shown that an angle of 12° below the horizontal seems to indicate stalling conditions, suggesting that this information, along with the experimental validation, can be valuable for improving the optimum handling of these Formula Mazda race cars.

A CFD study on a single element wing compared to experimental results was performed by Zerihan and Zhang et al (2001). The method used was solving RANS equations with the Spalart-Allmaras [Spalart and Allmaras (1992)] and $k-\omega$ [Menter (1993)] turbulence models. Using the one-equation model and the surface pressures are compared at different heights. The obtained results showed good qualitative trends for the aerodynamic performance. Overall, the wake thickness is predicted reasonably well in the region near the trailing edge. Furthermore, the wake predicted is thicker than that found in the experiments, with reduced velocities. The ground boundary layer is well predicted using the one-equation model, but it is too thick when using the two-equation model.

Mahon and Zhang (2005) investigated the flow around an inverted double-element airfoil in ground effect numerically, by solving the Reynolds averaged Navier-Stokes equations. The predictive capabilities of six turbulence models with regards to the surface pressures, wake flow field, and sectional forces were quantified. The realisable $k-\omega$ model was found to offer improved forecasts of the surface pressures and wake flow field. Covering various force regions, a number of ride heights were investigated. The surface pressures, sectional forces, and wake flow field were all modelled accurately and offered improvements over previous numerical investigations. The sectional forces showed that the majority of the downforce was generated by the main element, whereas the majority of the drag was generated by the flap. The near field and far field wake development was investigated and suggestions

regarding the reduction of the wake thickness were made. The main element wake contributed greatly to the overall wake thickness, and the thickness increased as the ride height decreased.

Chapter 3

Governing Equations and Turbulence Modelling

The physics of fluid flow can be described by using a set of equations which are the governing equations. These equations are regarded as the Navier-Stokes (N-S) equations. To solve the complex flow phenomenon by using the N-S equations, a mathematical transformation is needed. Starting from the basic continuity, momentum and energy equations will be given in the following sections. Further details about the RANS models and the turbulence treatment, which are used in this project, will also be introduced.

3.1 Navier-Stokes Equations

Depending on the Kundsen number which defines the relative stochastic state of the fluid, the issue the researcher is interested in, the flow over a racing car can be assumed as continuum mechanics. The continuum description of fluid is based on the following Conservation Laws. In any physical system, the following quantities must be conserved: mass, momentum and energy. This set of equations which were mainly derived by Claude Louis Navier and George Gabriel Stokes are called Navier-Stokes equations.

The differential forms of the Navier-Stokes equations are presented in the following equations 3.1 – 3.11.

The continuity equation

$$\frac{\partial \rho}{\partial t} + \nabla \bullet (\rho \vec{U}) = 0 \tag{3.1}$$

The momentum equation

$$\frac{\partial \rho \vec{U}}{\partial t} + \nabla \bullet (\rho \vec{U} \otimes \vec{U}) = \nabla \bullet \tau + \rho \vec{g} \tag{3.2}$$

Where

$$\vec{U} \otimes \vec{U} = \begin{pmatrix} u^2 & uv & uw \\ uv & v^2 & vw \\ uw & vw & w^2 \end{pmatrix} \tag{3.3}$$

The energy equation

$$\frac{\partial \rho E}{\partial t} = -\nabla \bullet (\rho E \vec{U}) + \nabla \bullet (\tau \bullet \vec{U}) - \nabla \bullet q + (\vec{U} \bullet \rho \vec{g}) \tag{3.4}$$

These equations listed above are not in themselves enough to solve the problem. Additional modelling assumptions are required in order to close the variables of stresses, heat flux and energy.

The stress tensor τ_{ij} can be split into pressure and viscous parts; the general form of it in Newtonian fluid is shown in the equations 3.5 and 3.6:

$$\tau_{ij} = -\delta_{ij} + \mu(\frac{du_i}{dx_j} + \frac{du_j}{dx_i} - \frac{2}{3}\delta_{ij}\frac{du_k}{dx_k}) \tag{3.5}$$

Where

$$\delta_{ij} = \begin{pmatrix} 1 & 0 & 0 \\ 0 & 1 & 0 \\ 0 & 0 & 1 \end{pmatrix} \tag{3.6}$$

The heat flux which is due to temperature difference between two points, can be calculated by the well-known Fourier Law shown in equation 3.7.

$$\vec{q} = -k\nabla \bullet T \tag{3.7}$$

The final closure for the whole system is provided by the equations of state. The total energy can be expressed as:

$$E = e + \rho \frac{u_i u_i}{2} \tag{3.8}$$

For a prefect gas,

$$p = \rho RT \text{ And } e = C_v T \tag{3.9}$$

For numerical and computer programming convenience, the N-S equation in differential form is usually expressed by the same generic vector form, given by:

$$\frac{d\vec{U}}{dt} + \frac{d\vec{E}}{dx} + \frac{d\vec{F}}{dy} + \frac{d\vec{G}}{dz} = 0 \tag{3.10}$$

in which,

$$\vec{U} = \begin{pmatrix} \rho \\ \rho u \\ \rho v \\ \rho w \\ \rho E \end{pmatrix} \quad \vec{E} = \begin{pmatrix} \rho u \\ \rho u^2 + p - \tau_{xx} \\ \rho uv - \tau_{xy} \\ \rho uw - \tau_{xz} \\ u(\rho E + p) - u\tau_{xx} - v\tau_{xy} - w\tau_{xz} + q_x \end{pmatrix}$$

$$\vec{F} = \begin{pmatrix} \rho v \\ \rho uv - \tau_{yx} \\ \rho v^2 + p - \tau_{yy} \\ \rho vw - \tau_{yz} \\ v(\rho E + p) - v\tau_{yx} - v\tau_{yy} - w\tau_{yz} + q_y \end{pmatrix} \quad \vec{G} = \begin{pmatrix} \rho w \\ \rho uw - \tau_{zx} \\ \rho vw - \tau_{zy} \\ \rho w^2 + p - \tau_{zz} \\ w(\rho E + p) - u\tau_{zx} - v\tau_{zy} - w\tau_{zz} + q_z \end{pmatrix}$$

(3.11)

As mentioned before, this form is chosen for the finite volume approach for clarity reasons. A detailed derivation and description can be found in Hoffmann et al. (2000).

3.2 Nature of Turbulence

As a very common phenomenon in the natural world, turbulence has become the focus of many observers, from the outer space nebulae to the atmospheric clouds, from the terrible hurricane to the smoke rising from a cigarette. In engineering, engineers concentrate on the influence of turbulent flow which is generated by man-made applications, such as boundary layers over wings and wakes from transportation.

Turbulence is widely believed as a flow which is characterised by apparently random and chaotic three-dimensional vortices. In fact, there are usually three distinct regions for most of the external fluid motions: laminar flow, transitional flow and fully developed turbulent flow. Turbulence occurs when the inertial energy is much greater than the viscous dampening forces in a small or a larger transition region which usually comes after the laminar flow. There are three essential aspects of turbulence: Initial perturbation, vortex stretching and instability. Turbulence is initiated by wave like instabilities in shear layers. Random fluctuations are amplified by inertial forces, they become unstable and interact to become three dimensional. There is then a mutual interaction of many vortices leading to entanglement and deformation.

The turbulent flow comprises the eddies with a wide range of scales. Most of the kinetic energy of turbulence is stored in the large scale. In a so-called cascade process, the kinetic energy cascades from large scale to small scale by some inertial and essential forces. This process continues to create smaller and smaller eddies. It stops when the scales are small enough that the viscous forces are strong enough to dissipate the kinetic energy into internal heat. The scale at which this happens is so-called Kolmogorov (1941) scale. It is assumed that the scales only depend on viscosity and dissipation rate, and can be expressed by the following equations:

Kolmogorov length scale:

$$\eta = (\frac{\nu^3}{\varepsilon})^{\frac{1}{4}} \tag{3.12}$$

Kolmogorov time scale:

$$\tau = (\frac{\nu}{\varepsilon})^{\frac{1}{2}} \tag{3.13}$$

Kolmogorov velocity scale:

$$u = (\nu\varepsilon)^{\frac{1}{4}} \tag{3.14}$$

Where ε is the average rate of energy dissipation per unit mass which has the dimension length^2/time^3, and ν is the kinematic viscosity of the fluid which has the dimension length^2/time.

3.3 Approximate Techniques of Navier-Stokes Equations

As all fluid dynamics is based on the universal law which is the Navier-Stokes Equations, the key issue of CFD is to solve it with the minimum of complexity while describing the information of physical phenomena as much accurate as possible.

To achieve this main aim, Ferziger (1999) classified the flow simulation into five major categories:

1. Correlation Methods

2. Integral Methods

3. Reynolds-Averaged Navier-Stokes Equations

4. Large Eddy simulations

5. Direct Numerical Simulation of Navier-Stokes Equations

In this research project, all of the cases will be investigated by using Reynolds-Averaged Navier-Stokes Equations (RANS) simulations. Therefore, the RANS equations will be described in detail in the following sections, while a brief outline of other simulation methods will also be presented.

3.3.1 Direct Numerical Simulation (DNS)

DNS is a direct approach that solves the N-S equations only by numerical discretisation. This means the results from DNS will be the closest to the real physics flow phenomena, because the whole range of scales of turbulence is resolved directly without any turbulence models. However, this brings a great challenge too. All of the scales including the smallest dissipation, which is well-known as Kolmogorov scale would be resolved in the finest level of mesh. In fact, there is proof that a three-dimensional DNS requires the mesh points of 9/4 power of Reynolds Number. Additionally, the time steps required is also a power of Reynolds Number because the N-S equations must be integrated in time. As a result, the whole computational operation for DNS goes proportionally to the three powers of Reynolds Number.

For these reasons, even at low Reynolds Number cases, the requirements of the computational cost would be beyond the capability of the most powerful computers. This has limited the DNS to very simple geometries such as flat plate at low Reynolds Numbers.

3.3.2 Large Eddy Simulation (LES) and Implicit Large Eddy Simulation (ILES)

As DNS aims to resolve the full range of physical scales in the flow filed, LES only focuses on representing the largest resolved scales, where the grid size is considerably larger than the Kolmogorov scale. For those unresolved small scales, the so-called

subgrid scale (SGS) are often simulated by using a subgrid scale model. Although the computational cost is significantly lower than DNS, LES is still expensive and relies highly on high computer performance.

As an alternative to LES, ILES is referred to as a 'no model' approach, because it does not use any turbulence model for the SGS region while the large eddies are resolved in the same manner as in LES. In ILES, the numerical dissipation infers to generate the eddy dissipation for small scales. So the numerical error caused by discretisation is employed and will be transferred to smaller scales.

Tsubokura et al. (2007) performed one of the world's largest unsteady turbulence simulations around a formula car using LES with the Earth Simulator in Japan. The overall body size of the car is 2.26 metres in length, 0.89 metres in width and 0.48 metres in height. The wheel base is 1.50 metres and the front track and the rear track are 0.75 metres and 0.69 metres, respectively. The car is mounted on the floor of the rectangular computational domain of length/width/height = 34.0m/2.70m/2.47m. The computational grids on the cross section of the car were generated by the commercial software Gridgen. The computational domain was divided into 10 blocks to treat huge amount of grids by unstructured grids. Accordingly total of 117,060,909 elements were employed to fill in the entire computational domain. In conclusion, LES presented an excellent agreement of the lift coefficient that the LES estimates the value only about 1% larger than the wind tunnel data, while the disagreement of the drag coefficient is relatively larger but still the difference is less than 10%. In addition to its accuracy compared with RANS simulation, LES can also capture the transient flow feature.

3.3.3 Detached Eddy Simulation (DES)

To tackle the difficulties of using the standard LES in near boundary region, a modification of RANS model was introduced as SGS model until the grid is fine enough for LES. This hybrid technique is so-called DES and combines the best aspects of both RANS and DES methodologies into a single strategy.

In the DES, according to Spalart et al. (1997), a distance d is defined as:

$$\tilde{d} = \min(d, C_{DES}\Delta) \tag{3.15}$$

Where C_{DES} is a constant and $\Delta = \max(\Delta_x, \Delta_y, \Delta_z)$ is the filter size. In the boundary layer, if $d < C_{DES}\Delta$, the RANS model will be modelled, otherwise in the regions where $d > C_{DES}\Delta$, the RANS model acts as a SGS model of LES.

3.3.4 Reynolds-Averaged Navier-Stokes Equations (RANS)

A very widely used approach for turbulent flow simulation in industry for engineers is a set of time-averaged equations, which is called Reynolds-Averaged Navier-Stokes (RANS) equations. The time-averaged solution for turbulent flow was introduced by Reynolds. This concept is based on replacing all the fluctuant variables such as velocity and pressure with time-averaged part and a fluctuating part. As presented in the following equation:

$$u_i = \overline{u_i} + u_i' \tag{3.16}$$

By applying the time average on the Navier-Stokes equations, the Reynolds-averaged Navier-Stokes equations (RANS) [Ferziger (1997)] can be derived as:

$$\rho\frac{\partial\overline{u_i}}{\partial t} + \rho\frac{\partial\overline{u_i u_j}}{\partial x_j} = -\frac{\partial P}{\partial x_i} + \rho\nu\frac{\partial^2\overline{u_i}}{\partial^2 x_j} - \rho\frac{\partial\tau_{ij}}{\partial x_j} \tag{3.17}$$

In the equation 3.17, the additional stresses $\tau_{i,j}$, which are called the Reynolds Stress Tensor are inducted to get rid of the cancellation of the random fluctuations.

$$\tau_{ij} = -\rho\overline{u_i u_j} = \begin{pmatrix} -\rho\overline{u'^2} & -\rho\overline{u'v'} & -\rho\overline{u'w'} \\ -\rho\overline{v'u'} & -\rho\overline{v'^2} & -\rho\overline{v'w'} \\ -\rho\overline{w'u'} & -\rho\overline{w'v'} & -\rho\overline{w'^2} \end{pmatrix} \tag{3.18}$$

A set of unknown variables are introduced for solving the cancellation of the fluctuations, which is the well known closure problem. In order to collect sufficient equations for the closure problem, some different turbulence models are used as a connection between the time-averaged and the fluctuating part. In this thesis, only the one-equation Spalart-Allmaras model and the two-equation k-ω model are used. They will be further explained in the next section.

The RANS equations are not as powerful as other approaching simulations such as the Large Eddy Simulation (LES) for the large scale turbulent motions or the Direct Numerical Simulation (DNS) which solves the equations directly for all turbulence scales. However, the users can get a fast good solution via the RANS equations.

3.4 Turbulence Models based on RANS

Virtually all the flow around wings is turbulent; hence, turbulence models are required. However, there is not a universal model that could successfully model all the turbulent flow. So choosing an appropriate turbulence model becomes a key issue in most CFD simulations. Depending on the turbulence, the grid size and the computational performance, different turbulence models present diverse results. Some models, which will be used in this thesis, are formulated in the following part.

3.4.1 Spalart-Allmaras (S-A) Turbulence Model

S-A model was introduced by Spalart et al (1992). It is a single equation model, which is widely used due to its computational efficiency.

$$\frac{D\tilde{\nu}}{Dt} = C_{b1}(1-f_{t2})\tilde{S}\tilde{\nu} + \frac{1}{\sigma}\left[\nabla((\nu+\tilde{\nu})\nabla\tilde{\nu}) + C_{b2}|\nabla\tilde{\nu}|^2\right] - \left[C_{w1}f_w - \frac{C_{b1}}{k^2}f_{t2}\right]\left[\frac{\tilde{\nu}}{d}\right] + f_{t1}\Delta U^2 \tag{3.19}$$

Here ν is the Molecular Viscosity. The turbulent viscosity ν_t is obtained from ν as follows

$$\nu_t = \tilde{\nu} f_{v1}$$
$$f_{v1} = \frac{\chi^3}{\chi^3 + C_{v1}^3} \tag{3.20}$$

where $\chi = \frac{\tilde{\nu}}{\nu}$

The production term is given by

$$\tilde{S} = S + \frac{\tilde{\nu}}{k^2 d^2} f_{v2}$$
$$f_{v2} = 1 - \frac{\chi}{1+\chi f_{v1}} \tag{3.21}$$

Here, *S* is the magnitude of vorticity and *d* is the distance from closest wall.

The destruction term is given by

$$f_w = g\left(\frac{1+C_{w3}^6}{g^6 + C_{w3}^6}\right)^{1/6}$$
$$g = r + C_{w2}\left(r^6 - r\right) \tag{3.22}$$
$$r = \frac{\tilde{\nu}}{\tilde{S}k^2 d^2}$$

The trip functions ft_1 and ft_2 are given by

$$f_{t1} = C_{t1} g_t \exp\left(- C_{t2} \frac{w_t^6}{\Delta U^2} \left[d^2 + g_t^2 d_t^2 \right] \right), \quad g_t = \min\left(0.1, \frac{\Delta U}{w_t \Delta x_t} \right) \tag{3.23}$$

$$f_{t2} = C_{t3} \exp\left(- C_{t4} \chi^2 \right) \tag{3.24}$$

The model constants are

$$\sigma = 2/3, \quad k = 0.41$$
$$C_{b1} = 0.1355, \quad C_{b2} = 0.622,$$
$$C_{w1} = C_{b1} / k^2 + (1 + C_{b2}) / \sigma, \quad C_{w2} = 0.3, \quad C_{w3} = 2,$$
$$C_{v1} = 7.1, \quad C_{t1} = 2, \quad C_{t2} = 2, \quad C_{t3} = 1.1 \ \textit{and} \ \ C_{t4} = 2.$$

According to Kroll et al. (2000), the Spalart-Allmaras model is applicable to small separation bubbles rather than large separations. Thus, it is calibrated for the flow around airfoils and wings at high Reynolds numbers.

3.4.2 Wilcox k-ω Model

As a result of the lack of the one-equation model which does not specify the length scale, Wilcox (2006) established a relationship for the kinematic eddy viscosity ν_t by using the turbulence kinetic energy k and a specific turbulent dissipation ω, as written the following in equation:

$$\nu_t = \frac{k}{\omega} \tag{3.25}$$

Two additional equations are necessary to be introduced to resolve the unknown variables *k* and ω.

Turbulence kinetic energy

$$\frac{\partial k}{\partial t}+U_j\frac{\partial k}{\partial x_j}=\tau\frac{\partial U_j}{\partial x_j}-\beta^* k\omega+\frac{\partial}{\partial x_j}\left[(\nu+\sigma^*\nu_T)\frac{\partial k}{\partial x_j}\right] \tag{3.26}$$

Specific dissipation rate

$$\frac{\partial \omega}{\partial t}+U_j\frac{\partial \omega}{\partial x_j}=\alpha\frac{\omega}{k}\tau_{ij}\frac{\partial U_j}{\partial x_j}-\beta\omega^2+\frac{\partial}{\partial x_j}\left[(\nu+\sigma\nu_T)\frac{\partial \omega}{\partial x_j}\right] \tag{3.27}$$

Where the closure coefficients are:

$$\alpha=\frac{5}{9},\beta=\frac{3}{40},\beta^*=\frac{9}{100},\sigma=\sigma^*=\frac{1}{2}$$

According to Kroll et al. (2000), the Wilcox k-ω model can predict moderate flow separation but would fail at strong separation. Due to the lower sensitivity on numerical performance, it highly depends on the quality of the computational grids.

3.4.3 Shear Stress Transport (SST) k-ω Model

By pointing out the importance of turbulent shear stress, Menter (1994) refined the original Wilcox k-ω model. Still two transport equations for the kinetic turbulent energy k and specific dissipation rate ω are introduced in the SST model. However, based on Bradshaw's shear stress transport assumption, the eddy viscosity was redefined as:

Kinematic eddy viscosity

$$\nu_t=\frac{a_1 k}{\max(a_1\omega, SF_2)} \tag{3.28}$$

Turbulence kinetic energy

$$\frac{\partial k}{\partial t}+U_j\frac{\partial k}{\partial x_j}=P_k-\beta^* k\omega+\frac{\partial}{\partial x_j}\left[(\nu+\sigma_k\nu_T)\frac{\partial k}{\partial x_j}\right] \tag{3.29}$$

Specific dissipation rate

$$\frac{\partial \omega}{\partial t}+U_j\frac{\partial \omega}{\partial x_j}=\alpha S^2-\beta\omega^2+\frac{\partial}{\partial x_j}\left[(\nu+\sigma_{\omega_1}\nu_T)\frac{\partial \omega}{\partial x_j}\right]+2(1-F_1)\sigma_{\omega_2}\frac{1}{\omega}\frac{\partial k}{\partial x_i}\frac{\partial \omega}{\partial x_i} \tag{3.30}$$

Where the closure coefficients and auxiliary relations are:

$$F_2=\tanh\left[\left[\max\left(\frac{2\sqrt{k}}{\beta^*\omega y},\frac{500\nu}{y^2\omega}\right)\right]^2\right]$$

$$P_k=\min\left(\tau_{ij}\frac{\partial U_i}{\partial x_j},10\beta^* k\omega\right)$$

$$F_1=\tanh\left\{\left[\min\left[\max\left(\frac{\sqrt{k}}{\beta^*\omega y},\frac{500\nu}{y^2\omega}\right),\frac{4\sigma_{\omega_2}k}{CD_{k\omega}y^2}\right]\right]^4\right\}$$

$$CD_{k\omega}=\max\left(2\rho\sigma_{\omega_2}\frac{1}{\omega}\frac{\partial k}{\partial x_i}\frac{\partial \omega}{\partial x_i},10^{-10}\right)$$

$$\alpha=\frac{5}{9},\beta=\frac{3}{40},\beta^*=\frac{9}{100},\sigma_k=0.85,\sigma_{\omega_1}=0.5,\sigma_{\omega 2}=0.856$$

The use of the *k-ω* formulation in the inner parts of the boundary layer makes the model directly usable all the way down to the wall through the viscous sub-layer; hence the SST *k-ω* model can be used as a Low-Re number turbulence model without any extra damping functions [Karim et al. (2009)].

According to Kroll et al. (2000), all the three turbulence models which are mentioned above have their own applicability when using the FLOWer code. The Spalart-Allmaras model is calibrated for the flow around airfoils and wings at high Reynolds numbers. It is applicable in the case having small separation bubbles, but not in the case of large separated regions. Furthermore, regions of high flow gradients such as

boundary layers and wing tips must be sufficiently resolved. This one equation model is not suitable for the computation of jet-like free shear regions. Since it depends on global minimum wall distances, computations for complex topologies can become very expensive. Moreover, numerical problems are reported for its application to complex flows. The Wilcox k-ω model is recommended for application to rotors and complex configurations at cruise conditions. It is able to predict moderate flow separation, but it is not suitable for strong separation and maximum lift prediction. The model is known to be sensitive to the freestream value of ω and should, therefore, not be applied to free shear layers. This model meanwhile is numerically less robust and highly depends on the quality of the computational grid. Therefore, boundary layers must be sufficiently resolved. The SST k-ω model is closely related to the standard Wilcox k-ω model, but has an improved predictive accuracy for flows with an adverse pressure gradient. It is, thus, suitable for flows with strong separation and has proven to allow maximum lift prediction. However, since the model depends on global minimum wall distances, computations for complex topologies may become very expensive. Due to the big separation which could be foreseen at the trailing edge of front wing in the current project, the SST k-ω model would be expected to perform better than the other two models selected.

3.5 Non-Dimensionalisation

The governing equations are often put into a non-dimensional form. The advantage in doing this is that the dynamic and energetic similarity can be obtained for geometrically similar configuration. Also, by non-dimensionalising the equations, the values of the flow variables will usually fall between the limits such as zero and one, which could avoid possible inaccurate operations during the process of the computations.

For the numerical procedure, it is convenient to use dimensionless quantities when solving the Navier-Stokes equations. Alternatively, this means that a special unit

system of measurement is chosen.

For this reason, the following variables will be used during the calculations:

$$x^* = \frac{x}{c}, \qquad y^* = \frac{y}{c}, \qquad z^* = \frac{z}{c},$$

$$t^* = \frac{t}{t_{ref}}, \qquad \rho^* = \frac{\rho}{\rho_\infty}$$

$$u^* = \frac{u}{u_{ref}}, \qquad v^* = \frac{v}{u_{ref}} \qquad w^* = \frac{w}{u_{ref}},$$

$$T^* = \frac{T}{T_{ref}}, \qquad P^* = \frac{P}{\rho_{ref} u_{ref}^2}, \qquad E^* = \frac{E}{\rho_{ref} u_{ref}^2},$$

$$\mu_l^* = \frac{\mu_l}{\mu_{ref}}, \qquad \mu_t^* = \frac{\mu_t}{\mu_{ref}} \tag{3.31}$$

Where the * represents non-dimensional quantities, the subscript ∞ represents free stream quantities, *c* is the dimensional reference length and *a* is the speed of sound, which is defined by the relations:

$$a = \sqrt{\gamma \frac{p}{\rho}} = \sqrt{\gamma R T} \tag{3.32}$$

The non-dimensional parameters are defined as:

Reynolds number:

$$Re = \frac{\rho_\infty a_\infty L}{\mu_\infty} \tag{3.33}$$

Prandtl number:

$$Pr = \frac{\mu c_p}{k} \tag{3.34}$$

Now, the governing equations can be written in the non-dimensional Navier-Stokes equation form by using the non-dimensional variables in the equation(3.31).

All the variables in the FLOWer code are non-dimensionalised using a reference quantity with the corresponding dimension of the variable. Every reference quantity is a combination of the chord length, the freestream density, pressure and temperature. The variables and the corresponding referenced quantities are given below.

variable	**reference quantity**
length, coordinate	c
density	ρ_∞
pressure	p_∞
temperature	T_∞
time	$c/(p_\infty/\rho_\infty)^{1/2}$
velocity	$(p_\infty/\rho_\infty)^{1/2}$
viscosity μ , modified viscosity $\tilde{\mu}$	$c\ \rho_\infty\ (p_\infty/\rho_\infty)^{1/2}$
heat conductivity k	$c\ p_\infty^{3/2}\ \rho_\infty^{-1/2}\ T_\infty^{-1}$
energy E and enthalpy H	p_∞/ρ_∞
stresses τ	p_∞
turbulent kinetic energy k	p_∞/ρ_∞
dissipation rate ω	$c^{-1}\ (p_\infty/\rho_\infty)^{1/2}$

Chapter 4

Numerical Methods

As mentioned in chapter 3, all the governing equations describing the real physical world are the complicated partial differential equations which are hardly solved analytically. So when it comes to the real industrial world, it is necessary that some applicable numerical methods are used to transfer the governing equations to the computational domain. This process is called discretisation.

Discretisation can be realised by several different solution techniques. Typically, there are three ways which are: the finite difference method, the finite element method and the finite volume method. Since the finite volume method was applied by the FLOWer code, a short introduction will be given in this chapter.

Furthermore, a brief description on space discretisation, higher order schemes and time integration will also be provided in this chapter.

4.1 Finite Volume Method (FV Method)

The finite volume method is a very popular discretisation used in CFD. It is based on integrals in a partial differential equation form of conservation laws. To achieve this discretisation, the first step refers to the division of the domain into a small volume, where each mesh node is located at the centroid. Then, at each volume, these terms of integrals are valued using flux through the end on each time step.

The control volumes are illustrated in Figure 5. In each domain, the conservation law of flow quantities can be expressed as:

$$\frac{\partial U(x,t)}{\partial x}+\frac{\partial F(U(x,t))}{\partial t}=0 \tag{4.1}$$

In integral form:

$$\left(\int_{x_{i-1/2}}^{x_{i+1/2}} U(x,t_{n+1})dx - \int_{x_{i-1/2}}^{x_{i+1/2}} U(x,t_n)dx\right) + \left(\int_{t_n}^{t_{n+1}} F(U(x_{i+1/2},t))dt - \int_{t_n}^{t_{n+1}} F(U(x_{i-1/2},t))dt\right) = 0 \tag{4.2}$$

The discretisation [Toro (2009)] for the conservative form can be expressed as:

$$U_i^{n+1} = U_i^n - \frac{\Delta t}{\Delta x}(F_{i+1/2} - F_{i-1/2}) \tag{4.3}$$

In which,

$$U_i^n = \frac{1}{\Delta x}\int_{x_{i-1/2}}^{x_{i+1/2}} U(x,t^n)dx \tag{4.4}$$

And the flux at the boundary:

$$F_{i+1/2} = \frac{1}{\Delta t}\int_{t^n}^{t^{n+1}} f(U(x_{i+1/2},t))dt \tag{4.5}$$

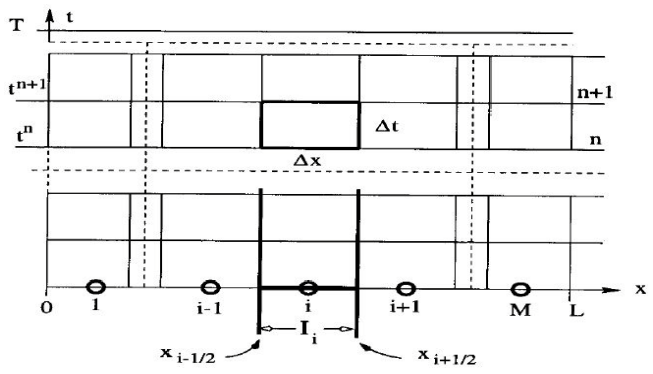

Figure 5: Discretisation of the domain [Source: Toro (2009)]

The wide utilisation of the integral form of the conservation law makes the FV method flexible. It even performs well in discontinuity and variable across the shock waves. Moreover, the FV method is not rigid with grid, accepting both structured grids and unstructured ones. This is the reason for which the FV method is very popular for different types of geometry, especially for the complex ones.

4.2 Jameson's Central Differencing Scheme (CDS)

The Central Differencing Scheme [Jameson (1981)] which leads to an ordinary differential equation for the rate of change of the conservative variables in each grid point is a commonly used conventional scheme for the spatial discretisation. Figure 6 shows a typical control volume where at each grid point, the rate of change of variables is

$$\frac{d}{dt}\vec{W}_{i,j,k} = -\frac{1}{V_{i,j,k}}(\vec{R}^{C}_{i,j,k} - \vec{R}^{V}_{i,j,k}) \tag{4.6}$$

Where $\vec{R}^{C}_{i,j,k}$ and $\vec{R}^{V}_{i,j,k}$ represent the approximation of the inviscid and viscous net flux of mass, momentum and energy for a particular control volume $V_{i,j,k}$ arrangement with volume surrounding the grid node (i, j, k).

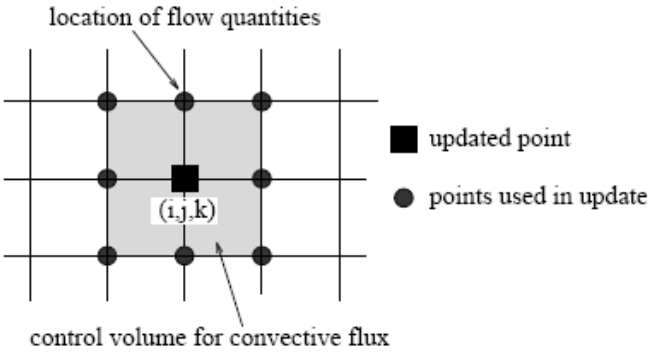

Figure 6: Control volume in a central differencing method [Source: Kroll et al. (2000)]

However, according to Kroll et al. (2000), this finite volume discretisation based on central averaging is not dissipative, which means that high frequency oscillations might occur in the solution. In order to avoid these spurious oscillations, dissipative terms have to be explicitly introduced. In most central schemes the well known scalar dissipation model is implemented. In order to preserve the conservation form of the numerical scheme, artificial dissipative terms are introduced by adding dissipative fluxes to the semi-discrete system

$$\frac{d}{dt}\vec{W}_{i,j,k} = -\frac{1}{V_{i,j,k}}(\vec{R}^{C}_{i,j,k} - \vec{R}^{V}_{i,j,k} - \vec{D}_{i,j,k}) \tag{4.7}$$

In general, the central difference scheme is simpler compared to other discretisation methods. It is easy to implement with either the cell-centred scheme or cell-vertex scheme [J.Blazek (2001)]. The computational cost is relatively lower. Some convergence acceleration methods such as implicit residual smoothing and multigrid can be easily incorporated with the central difference scheme which makes the scheme very fast as large CFL number can be used in the calculation. Because of these advantages, the central difference scheme has been widely utilised in the industry companies as well as in the academic community.

However, for suppressing high frequency oscillations and achieving good convergence properties an artificial viscosity term has to be added explicitly in the present central difference scheme. This makes the scheme very dissipative. The central difference scheme introduced here is only of second order. Compared to the upwind scheme which will be introduced in the following section, the central difference scheme is less accurate in the resolution of discontinuities and boundary layers.

4.3 Riemann Problem with Solver

Riemann problem is a simple hyperbolic equation with initial condition and a single

jump discontinuity. According to Toro (2009), the system of Riemann problem can be written as

$$U_t + AU_x = 0 \quad -\infty < x < \infty, t > 0$$
$$U(x,0) = U_0(x)\begin{cases} U_L & \textbf{if } x < 0 \\ U_R & \textbf{if } x > 0 \end{cases} \tag{4.8}$$

The structure of the solution of the Riemann problem in the *x-t* plane is illustrated in Figure 7. It includes a series of waves and each wave carries a jump discontinuity. Additional details about the Riemann problem can be found in Toro (2009).

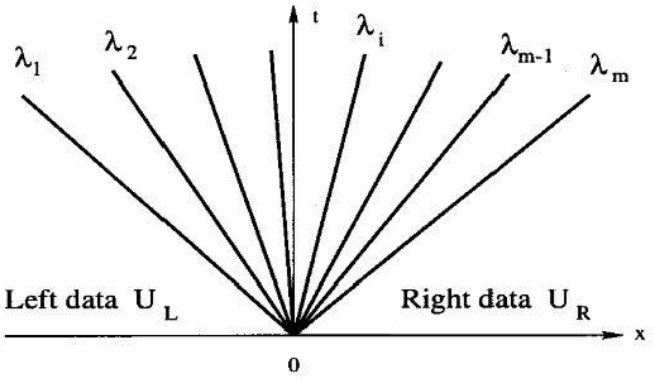

Figure 7: Structure of the solution of the Riemann problem for a general linear hyperbolic system [Source: Toro (2009)]

The exact solution of the Riemann problem is computationally too expensive, because every flux has to be derived at every time step. For this reason, several suitable approximations with numerical methods have been developed to solve the Riemann problem.

The Godunov's scheme provides a strong conservative numerical method to solve the Riemann Problem accurately. As the extensions of Godunov's scheme, some approximate Riemann solvers are used for improving the effectiveness of the scheme.

4.3.1 Godunov's Method

The Godunov's method, suggested by Godunov (1959), is a conservative numerical method. It is based on the already known solution at t^n to obtain the unknown solution at $t^{n+1} = t^n + \Delta t$.

There are three steps to achieve the whole process.

1. Define piecewise constant approximation of the solution at $t^{n+1} = t^n + \Delta t$.
2. Obtain the solution for the local Riemann problem at the cell interfaces.
3. Average the state variables after a time Δt.

To make sure that no wave interaction would take place in the time step Δt, a restriction of time step Δt is imposed by the CFL condition:

$$\Delta t \leq \frac{\frac{1}{2}\Delta x}{S_{\max}^n} \tag{4.9}$$

Where $S_{\max}^n$ is the maximum wave velocity present throughout the domain at time t^n.

4.3.2 The HLL and HLLC Schemes

The waves pertinent to the current project are quite general. Physically in the flow except from the shock waves, all other waves e.g. expansion waves (rarefaction), contact discontinuity may exist. Since we use Riemann solvers (HLL and HLLC) to calculate the flux and solve a complete 3-dimensional problem (instead of 2-d problem), all waves related to the 5 eignevalues (u-a, u, u, u and u+a) of the Euler equations need to be resolved in our current project. In order to resolve all the waves and the related solution, HLL and HLLC Riemann solvers are explained in detail in the following context.

To solve the Riemann problem in the equation 4.8, Figure 8 shows the structure of the exact solution of the Riemann problem for the x – split, three dimensional Euler equations, for which the vectors of conserved variables and fluxes are

$$U = \begin{bmatrix} \rho \\ \rho u \\ \rho v \\ \rho w \\ E \end{bmatrix}, \qquad F = \begin{bmatrix} \rho u \\ \rho u^2 + p \\ \rho uv \\ \rho uw \\ u\left(E + p\right) \end{bmatrix} \tag{4.10}$$

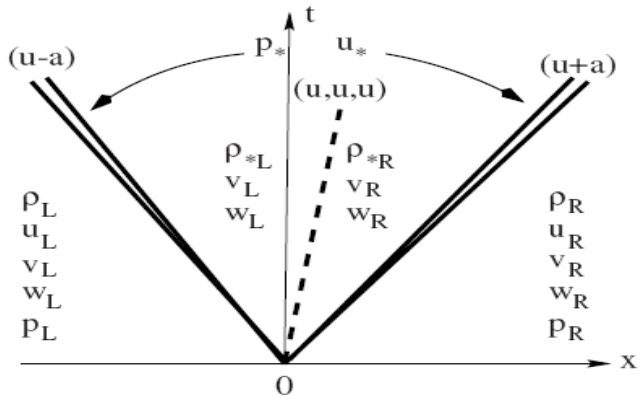

Figure 8: Structure of the exact solution of the Riemann problem for the x – split three dimensional Euler equations. There are five wave families associated with the eigenvalues u − a, u (of multiplicity 3) and u + a [Toro (2009)].

As the solution of the Riemann problem can be approximated, Harten, Lax and van Leer (1983) introduced an approximate Riemann solver, the so-called HLL scheme. According to Toro (2009), the HLL Riemann solver consists of just three constant states separated by two waves (Figure 9, left) which can be expressed as

$$\tilde{U}(x,t)=\begin{cases} \mathrm{U_L} & \text{if} \quad \dfrac{x}{t}\le S_L \\ U^{hll} & \text{if} \quad \mathrm{S_L}\le\dfrac{x}{t}\le S_R \\ U_R & \text{if} \quad \dfrac{x}{t}\ge S_R \end{cases} \tag{4.11}$$

Where U^{hll} is the constant state vector and the speeds S_L and S_R are assumed to be known. By applying the Rankine-Hugoniot conditions across the waves, the flux whereby can be constructed as [Toro (2009)]

$$F^{hll}_{i+\frac{1}{2}}=\begin{cases} F_L & \text{if} \quad 0\le S_L \\ \dfrac{S_R F_L - S_L F_R + S_L S_R (U_R - U_L)}{S_R - S_L} & \text{if} \quad \mathrm{S_L}\le\dfrac{x}{t}\le S_R \\ F_R & \text{if} \quad \dfrac{x}{t}\ge S_R \end{cases} \tag{4.12}$$

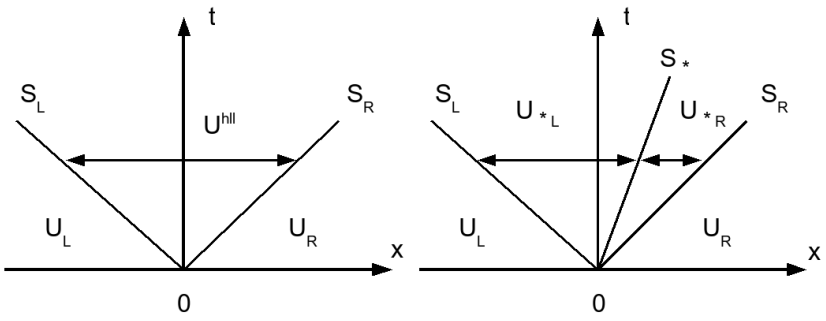

Figure 9: HLL (left) and HLLC (right) approximate Riemann solvers [Source: Toro (2009)]

Another modification of the HLL scheme was carried out by Toro (2009) and lead to the HLLC scheme, which can solve a system that has more than two waves such as contact waves. The HLLC, which is used in FLOWer code, will be introduced with detail information in the following context.

Toro (2009) included a middle wave of speed S* in addition to the slowest and fastest signal speeds S_L and S_R (Figure 9, right), for the Euler equations this corresponds to the multiple eigenvalue $\lambda_2 = \lambda_3 = \lambda_4 = u$. The HLLC solver is called an approximate solver in the fact that it simplifies the problem in three waves, instead of five. This is an evolution of the HLL solver where only the two extreme waves were considered.

The HLLC approximate Riemann solver is given as follows:

$$\tilde{U}(x,t) = \begin{cases} \mathrm{U_L} & \text{if} \quad \dfrac{x}{t} \le S_L \\ \mathrm{U_{*L}} & \text{if} \quad \mathrm{S_L} \le \dfrac{x}{t} \le S_* \\ \mathrm{U_{*R}} & \text{if} \quad \mathrm{S_*} \le \dfrac{x}{t} \le S_R \\ U_R & \text{if} \quad \dfrac{x}{t} \ge S_R \end{cases} \tag{4.13}$$

where we define the integral averages:

$$\begin{cases} \mathrm{U_{*L}} = \dfrac{1}{T(S_* - S_L)} \displaystyle\int_{TS_L}^{TS_*} U(x,T)dx \\ \mathrm{U_{*R}} = \dfrac{1}{T(S_R - S_*)} \displaystyle\int_{TS_*}^{TS_R} U(x,T)dx \end{cases} \tag{4.14}$$

And the consistency condition becomes:

$$\left(\frac{S_* - S_L}{S_R - S_L}\right) U_{*L} + \left(\frac{S_R - S_*}{S_R - S_L}\right) U_{*R} = U^{hll} \tag{4.15}$$

And a corresponding HLLC numerical flux is defined as

$$F_{i+\frac{1}{2}}^{hll} = \begin{cases} F_L & \text{if} \quad 0 \le S_L \\ F_L + S_L(U_{*L} - U_L) & \text{if} \quad S_L \le \dfrac{x}{t} \le S_* \\ F_R + S_R(U_{*R} - U_R) & \text{if} \quad S_* \le \dfrac{x}{t} \le S_R \\ F_R & \text{if} \quad \dfrac{x}{t} \ge S_R \end{cases} \tag{4.16}$$

with the intermediate fluxes F_{*L} and F_{*R} still to be determined.

According to Toro (2009), by integrating over appropriate control volumes, or more directly, by applying Rankine−Hugoniot Conditions across each of the waves of speeds S_L, S_*, S_R, one obtain

$$\begin{aligned} F_{*L} &= F_L + S_L\left(U_{*L} - U_L\right) \\ F_{*R} &= F_R + S_R\left(U_{*R} - U_R\right) \end{aligned} \tag{4.17}$$

The * states are defined by Toro (2009) as follow:

$$U_{*K} = \rho_K \left(\frac{S_K - u_K}{S_K - S_*} \right) \begin{bmatrix} 1 \\ S_* \\ v_K \\ w_K \\ \dfrac{E_K}{\rho_K} + \left(S_* - u_K\right)\left[S_* + \dfrac{p_K}{\rho_K\left(S_K - u_K\right)} \right] \end{bmatrix} \tag{4.18}$$

where K=L and K=R.

In order to determine completely the numerical fluxes in the HLLC Riemann solver,

we need to provide an algorithm for computing the wave speeds S_L and S_R. According to Toro (2009), the first step is to compute estimate for the pressure p∗ in the Star Region as

$$\begin{aligned} P_* &= \max\left(0, p_{pvrs}\right) \\ p_{pvrs} &= \frac{1}{2}(p_L + p_R) - \frac{1}{2}(u_R - u_L)\bar{\rho}\bar{a} \\ \bar{\rho} &= \frac{1}{2}(\rho_L + \rho_R), \bar{a} = \frac{1}{2}(a_L + a_R) \end{aligned} \tag{4.19}$$

Then compute the wave speed estimates for S_L and S_R as

$$\begin{aligned} S_L &= u_L - a_L q_L \\ S_R &= u_R + a_R q_R \end{aligned} \tag{4.20}$$

with

$$q_K = \begin{cases} 1 & \text{if } p_* \le p_K \\ \left[1 + \frac{\gamma+1}{2\gamma}\left(p_* / p_K - 1\right)\right]^{1/2} & \text{if } p_* > p_K \end{cases} \tag{4.21}$$

Then compute the intermediate speed S_* in terms of S_L and S_R as

$$S_* = \frac{p_R - p_L + \rho_L u_L (S_L - u_L) - \rho_R u_R (S_R - u_R)}{\rho_L (S_L - u_L) - \rho_R (S_R - u_R)} \tag{4.22}$$

The HLLC scheme was implemented by the Fluid Mechanics and Computational Sciences Group (FMaCS) [Zhong (2007)] into the FLOWer code which will be used as a solver in this project.

4.3.3 High Order Methods

High order methods could often get high accuracy and also perform sensitivity to the state of flow. In this project, two types of high order methods are presented: the Monotonic Upwind Scheme for Scalar Conservation Laws (MUSCL) introduced by van Leer (1974) and the Weighted Essentially Non-Oscillatory (WENO) scheme introduced by Liu (1994).

The idea of MUSCL scheme is to modify the piecewise constant data in the first order method. The simplest way is to replace the constant states u_i^n with linear functions $S_i(x)$. As shown in Figure 10, a piecewise reconstruction of u_i^n is

$$u_i(x) = u_i^n + \frac{(x - x_i)}{\Delta x}\Delta_i, \qquad x \in [0, \Delta x] \tag{4.23}$$

Where Δ_i is called a slope. The boundary extrapolated values can be then determined by:

$$u_i^L = u_i(0) = u_i^n - \frac{1}{2}\Delta_i; \quad u_i^R = u_i(\Delta_i) = u_i^n + \frac{1}{2}\Delta_i \tag{4.24}$$

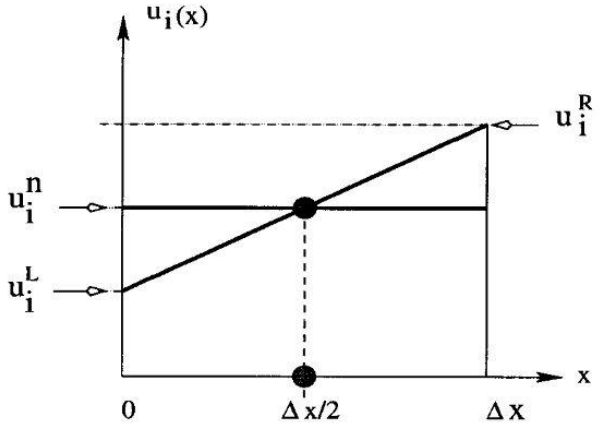

Figure 10: Piecewise linear MUSCL reconstruction of data [Source: Toro (2009)]

So far, the MUSCL scheme can provide highly accurate numerical solutions for a given system, even in cases where the solutions exhibit shocks, discontinuities, or large gradients. In addition, the intercell flux can also be used as the input for the other Riemann solvers; for instance, for the HLLC scheme.

The WENO scheme is constructed by Liu et al. (1994) as a third order scheme, which is an extension of the Essentially Non-Oscillatory (ENO) concept. For producing a high order accurate global approximation, ENO scheme assigns each cell to collect its own adaptive stencil for the purpose of reconstruction to avoid the growth of spurious oscillations. The idea of WENO scheme is, by using a convex combination approach, to combine all the interpolating polynomials on the stencils to be the approximating polynomial. This in another way helps WENO scheme to achieve high order accuracy and to eliminate the oscillatory on the convergence.

According to Liu et al. (1994), for the reconstruction within a cell *i*, the third order WENO is using two stencils (x_{i-1}, x_i) and (x_i, x_{i+1}). The polynomial interpolations are set by

$$P_0(x) = U_i + \frac{U_i - U_{i-1}}{\Delta x}(x - x_i)$$
$$P_1(x) = U_i + \frac{U_{i+1} - U_i}{\Delta x}(x - x_i) \tag{4.25}$$

Where the right interface value at i-1/2 and the left interface value at i+1/2 are $x = x_{i-1/2}$ and $x = x_{i+1/2}$.

The convex combination is then given by

$$P(x) = \frac{a_0}{a_0 + a_1} P_0(x) + \frac{a_1}{a_0 + a_1} P_1(x) \tag{4.26}$$

With

$$a_0 = \frac{C_0}{(\varepsilon + IS_0)^2}$$
$$a_1 = \frac{C_1}{(\varepsilon + IS_1)^2} \tag{4.18}$$

ε is a small positive number which avoids a division by zero in perfectly smooth flow. C_0 and C_1 are optimal weight factors. Finally, the smoothness indicators are

$$IS_0 = (U_i - U_{i-1})^2$$
$$IS_1 = (U_{i+1} - U_i)^2 \tag{4.27}$$

We shall specify C_0 and C_1 in the following two cases.

Case 1: At $x = x_{i-1/2}$, $C_0 = 1/2$ and $C_1 = 1$. Thus

$$a_0 = \frac{1}{2(\varepsilon + IS_0)^2}$$
$$a_1 = \frac{1}{(\varepsilon + IS_1)^2} \tag{4.28}$$

Case 2: At $x = x_{i+1/2}$, $C_0 = 1$ and $C_1 = 1/2$. Thus

$$a_0 = \frac{1}{(\varepsilon + IS_0)^2}$$
$$a_1 = \frac{1}{2(\varepsilon + IS_1)^2} \tag{4.29}$$

Compared to the CDS, these two high order schemes can provide more accurate numerical solutions. However, this means more computational cost will be needed. Meanwhile, with increasing the order of accuracy, the main problem is to avoid spurious oscillations in non smooth parts of the flow. So these non physical

oscillations which would introduce errors have to be aware. Otherwise, it will generate instability in the calculation and then lead to divergence.

According to Drikakis (2005), the high order schemes have several advantages. Firstly, the desired accuracy requires less memory and storage. Secondly, by using a coarser grid, high order schemes can also attain accurate results as classical methods. Thirdly, in the turbulence where the physical phenomenon is not yet fully understood, the high order schemes can provide higher accuracy in fundamental studies.

The WENO approach, which introduced above, is an extension of the ENO scheme. The purpose of the ENO method was to build a high-order scheme which keeps the order of accuracy without generated spurious oscillations. According to Liu (1994), a convex combination approach which is computed all the corresponding interpolating polynomials on the stencils is used in the WENO scheme to improve the order of accuracy. Regarding the smoothness of each candidate, a weighted average is produced. This leads to a reduction of the sensitivity to small changes as well as reducing the effect of the truncation error. Another advantage comes from WENO is that it can even prevent more oscillations. Due to these reasons, the WENO scheme would be expected to perform best.

4.4 Time Integration

As the flow employed in this project is steady flow, the time integration is essential to improve the efficiency. For this purpose, the dual-time stepping and the Runge Kutta method are used for the simulations.

As mentioned in FLOWer user handbook (2003), they are several reasons for using the explicit multistage schemes of Runge Kutta method: “They are simple to program, in particular at boundaries and for multiblock partitioned computational domains. Moreover, the number of stages and their coefficients can be varied in order to optimize both damping and convection of transient disturbances. Finally, the explicit

schemes usually do not require start-up procedures."

The simple form of the p stage Runge Kutta method can be written as

$$\begin{aligned} U_i^{(0)} &= U_i^{(n)} \\ U_i^{(s)} &= U_i^{(0)} - \alpha_s \Delta t H_i^{(s-1)} \qquad s = 1, 2, \ldots p \\ U_i^{(n+1)} &= U_i^{(p)} \end{aligned} \tag{4.30}$$

Where α_s are the stage coefficients of the *p* stage scheme, and *W* and *L* represent the solution and residual operator respectively.

For a fifth order Runge Kutta method which is employed in this project, the coefficients are

$$\alpha_1 = \frac{1}{4}, \alpha_2 = \frac{1}{6}, \alpha_3 = \frac{3}{8}, \alpha_4 = \frac{1}{2}, \alpha_5 = 1$$

Since the Runge Kutta method is an explicit scheme, the time step must be restricted by the CFL condition for stability. As mentioned in the FLOWer hand book (2003), the limitation of the maximum CFL number is 4 for 5 stage Runge Kutta method.

Chapter 5

Grid Generation and Case Set-Up

To achieve the main objective of this project, two typical front wings are chosen for all kinds of simulations by using the FLOWer code. The numerical investigation begins with the grid generation which is done by using the commercial software GRIDGEN. As in the current FLOWer code, the HLLC solver with MUSCL scheme (HLLC + MUSCL) and the WENO 3rd order scheme (HLLC + WENO3) are only implemented and available in 3D, 3D grid is generated by extending 2D plan with 10% length of chord for all the simulations. Although the simulations will be done in 3D fashion, only the centre plan which plumbs the span is used for analysis. Some data is calculated by using FORTRAN, while the graphical output is achieved by Tecplot.

5.1 Collection of Wing Models

As the main purpose for an F1 racing engineer who designs a front wing is to gain the maximum downforce under the strict regulation limitation, the wing profiles used in an aeronautical flow would cause some problems when applied to the racing car. In modern F1 racing, every team designs their own specific applications for the cars. Since the objective of this project is to investigate the ground effect of the front wing of a racing car, it was decided to use a wing profile of an F1 car developed by industry.

The basic single element wing was designed as the main element of the 1998 Tyrrell 026 F1 car front wing. Zerihan (2001) had done a series of relevant experiments in the wind tunnel of University of Southampton to study this wing. The data they got from the wind tunnel will be used as the reference experimental results for the purpose of comparison with the CFD simulations. The follow up double element wing was developed by using the single element wing as the main element wing (as mentioned above). The flap was designed for high lift applications for the racing car. A numerical

study will be carried out on this double element wing in this project.

5.2 Grid Generation

For the FLOWer code, the problem can only be solved by using structured grids. The ideal grid design should be make all the features structured in rectangles. The general strategy for generating the grids around an airfoil is to use a C-type grid with a semicircle farfield boundary in order to get high quality structured grids. However, in the two cases employed in this thesis, there is a limitation of the ground boundary which is very close to the suction surface of the front wing. So it is decided to use a hybrid C-H mesh topology for both cases. Although not all the features of the grid are ideal, this is probably the best topology we can have.

The grid for the single element wing is divided into 13 blocks, as shown in Figure 11. In order to match the ground height between the suction surface and the ground boundary, a C-type grid is generated around the aerofoil (Figure 12). The grid cells at the corners of the grid are not ideal, but this grid approach was the best compromised. Effort was made to force a perpendicular grid near to the trailing edge region due to the aerofoil has a thickness of 0.007c at the trailing edge. Outside the C grid to the entire farfield boundary, a H-type grid is employed to achieve high quality grids. The farfield boundary is located at a distance of 8c. While the flow around the nose of the airfoil has a large contribution on the overall behaviour of the airfoil, a higher density grid is required to capture the flow phenomenon accurately. Clustering on the grid is also made at the trailing edge to investigate the velocity profile inside the wake (Figure 13). As the flow between the suction surface and the ground accelerates, the grid nodes distributed at the suction surface would be 10% more than the pressure surface.

The grid topology used in this thesis is considered as the best for this type of the flows. However, the grid might not be perfect, as curves could be introduced for the block interfaces inside the domain which could reduce the skewness of the grid.

Improvement can be made in the future work.

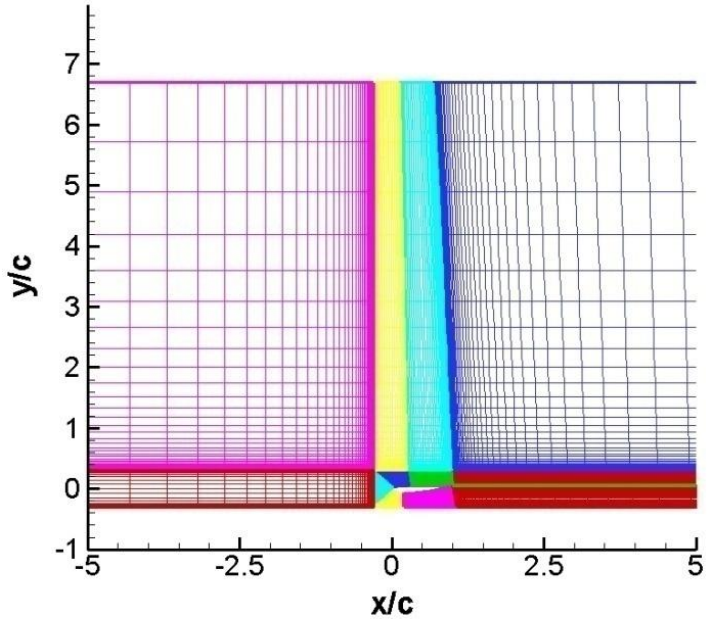

Figure 11: Multi-block mesh of the whole flow field for single element wing

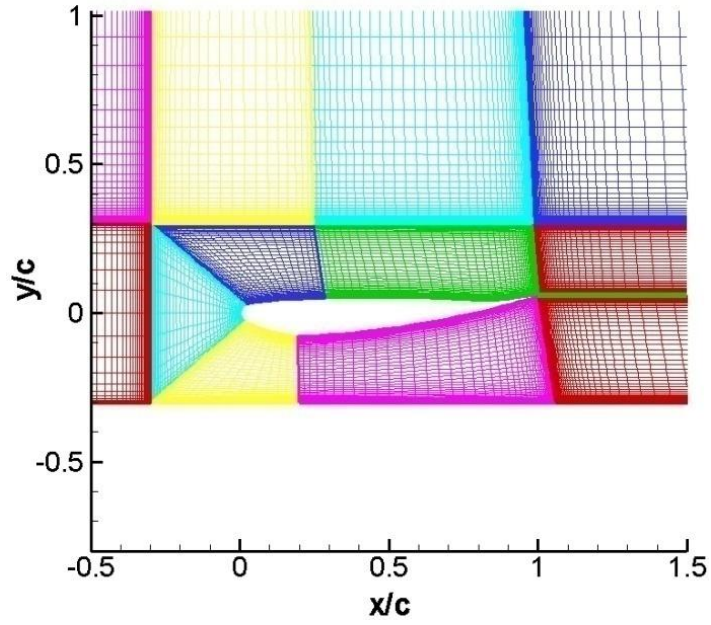

Figure 12: C-type blocks around the single element airfoil

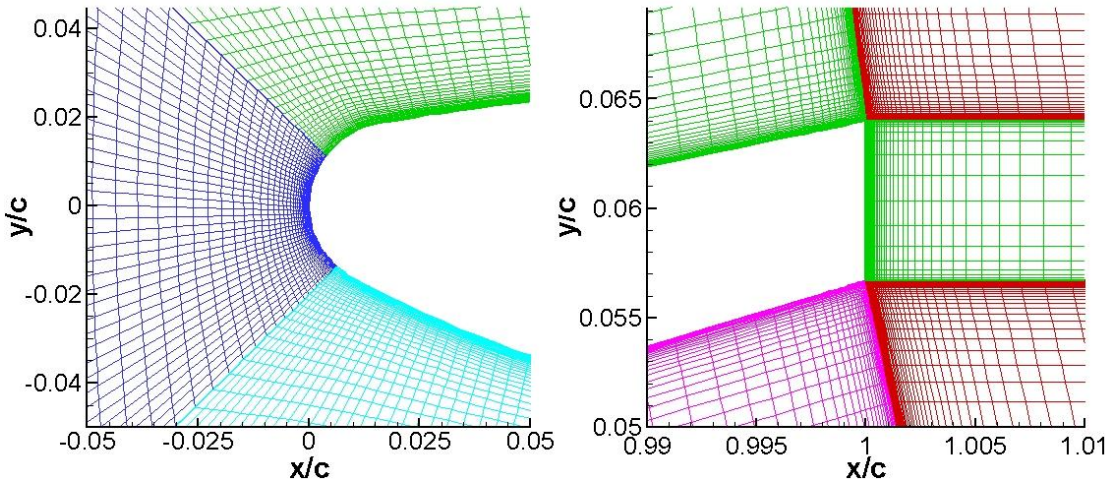

Figure 13: Clustered mesh at both the leading edge and the trailing edge of single element wing

The strategy for meshing the double element wing is nearly the same by just adding a flap into the grid. A C-type grid is decided to be generated around the flap as same as the main element wing. The whole block will be separated into 27 blocks for the double element wing (Figures 14 and 15) as the flap made the grid at the trailing edge of the main element wing more complicated. However, the meshing strategy for the flap is similar to the main element wing, where a great concentration would appear at both the leading edge and the trailing edge of the flap (Figure 16).

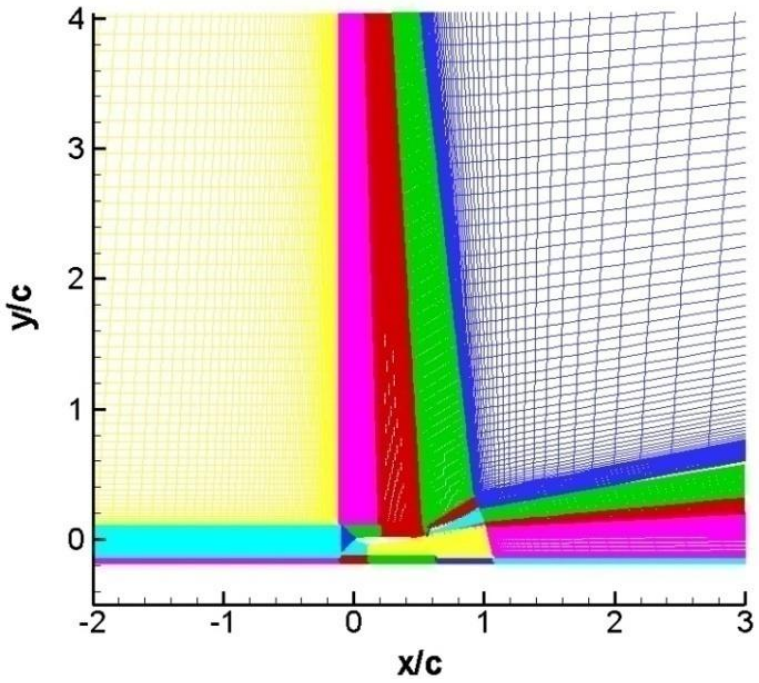

Figure 14: Multi-block mesh of the whole flow field for double element wing

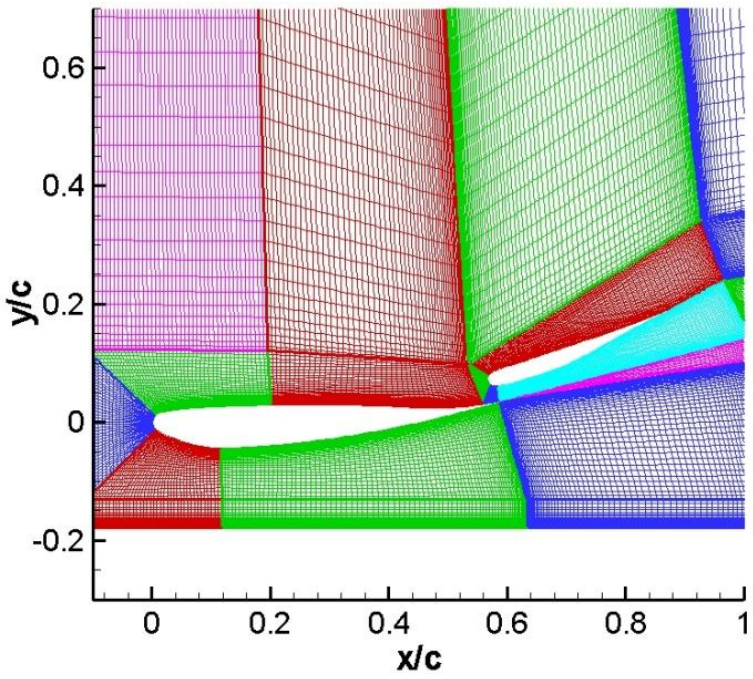

Figure 15: Blocks around the double element wing

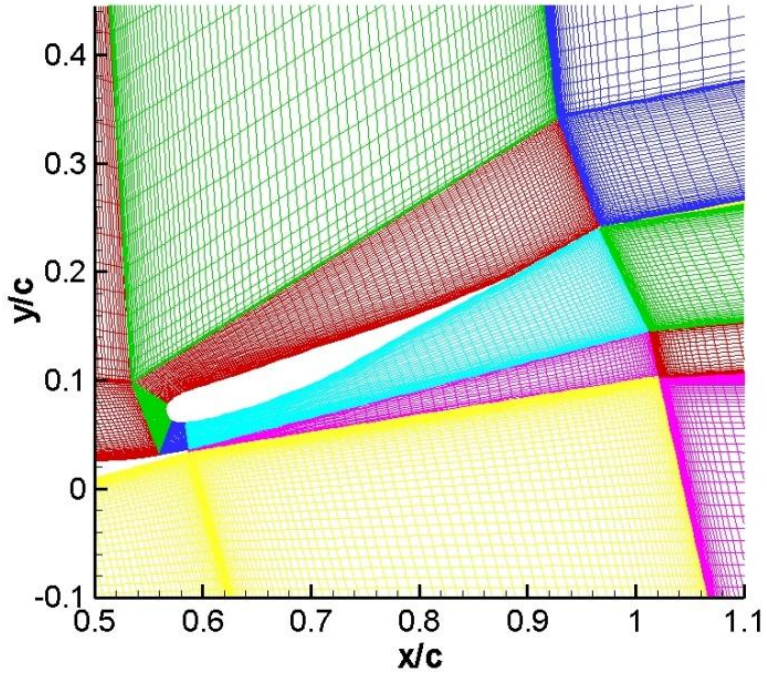

Figure 16: Blocks close-up for the flap

For the input in the FLOWer code, each block face requires a distinct specification of the boundary condition. Farfield boundary conditions are employed for the outer domain boundaries. The wing surface is defined as no-slip wall, while the ground boundary is defined as no-slip moving wall. Periodic boundary conditions are used for the z-plane. At the interface between blocks, the cut-to-another-block boundary condition is given.

For the computational purpose, structured grids are generated for both the single element wing and the double element wing. When considering a lift device such as airfoil, the boundary layer is always an important part during the calculation. As a result, the grid points needed to be concentrated near the wing body surface and extended by using sophisticated elliptic equations. Meanwhile, in order to capture the flow phenomena near the ground, a clustered of the grids points should be considered near the ground plane. The resolution of the boundary layer plays a vital role in the simulation. The parameter influencing the resolution is mainly depended on y^+, which

is a non-dimensional wall distance that can be defined as:

$$y^+ = \frac{uy_1}{\nu} \tag{5.1}$$

where u is the friction velocity which defined as $u = \left(\frac{\tau_\omega}{\rho}\right)^{1/2}$, y_1 is the distance from the nearest grid node to the wall, ν is local kinematic viscosity of the fluid.

So if the y^+ is small enough, the boundary layer is directly resolved, whereas wall functions are employed if cell size is too large. y^+ less than 1 is also a requirement for all low Reynolds number turbulence models. Otherwise, wall function may have to be used when grid is too coarse near the wall.

In order to achieve the requirement of the y^+, some estimation of y_1 should be done. A NASA Viscous Grid Spacing Calculator (http://geolab.larc.nasa.gov/APPS/YPlus/) is available online. The estimates are done for a turbulent flat plate in free air and are based on the Sutherland formula for viscosity. As we know that for a flat plate, $\tau_\omega = \left(\frac{\partial u}{\partial y}\right)_{y=0}$, so the estimation of y_1 could be done by using Reynolds number.

Combining the above equation and the calculation results from the NASA calculator, the chosen distances from the first grid point to the wall are that $y_1 = 4.2\times10^{-5}$ for the single element and $y_1 = 2.2\times10^{-5}$ for the double element case. As the flow conditions are not the same as in our current problem, some adjustments in the distances have to be made. In order to achieve y^+ less than 1 for our current problems, the length of the first cell from the airfoil and the ground is defined at 10^{-5} of chord length for the single element wing, and 3×10^{-6} of chord length for the double element wing. As a result, the y^+ for both around the wing surface and on the ground is less than 1. This can be seen from Figure 17 which shows the calculated y^+ in the single element and

the double elements cases (the WENO 3rd order scheme with the SST k-ω model).

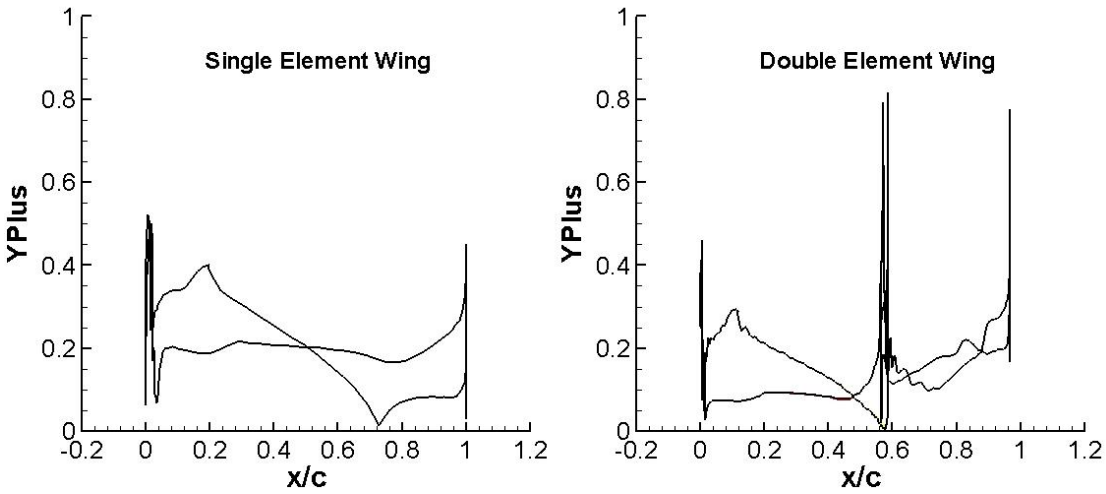

Figure 17: y^+ for single and double element wing

5.3 FLOWer Code and Initial Conditions

The FLOWer code which has been developed by the German Aerospace Center (DLR) solves the compressible, three-dimensional unsteady Euler and Reynolds-averaged Navier-Stokes equations. This code is applicable to simulate flows around complex aerodynamic configurations even with moving body. It is based on block-structured mesh with finite volume formulation and can be run in MPI parallel mode to accelerate simulations.

For the single element wing case, the freestream velocity is fixed to 30 m/s with the temperature at 20 ℃ and the Reynolds number fixed to 462000 for all the simulations. The objective to investigate the single element wing can be divided into two parts. The first part is to compare the simulation results with the experimental results with ground effect. In order to achieve this objective, three different numerical methods in conjunction with three different turbulence models are employed at various ground heights at a reference angle of attack (α =1 °). The second part is to investigate a numerical study of ground effect at various angles of attack.

For the double element wing case, the freestream velocity is also fixed to 30 m/s with the temperature at 20 ℃, but the Reynolds number is increased to 786000 due to the addition of the flap. Only numerical studies will be carried out during the investigation. In all simulations, the main element wing is fixed to the same reference angles of attack as in the single element wing case. Several changed flap angles are used for investigating the double element wing with ground effect.

The upstream boundary condition is considered as farfield boundary condition. It is defined using free stream data in both cases, where the Mach number is 0.0874, the Reynolds numbers are 462000 and 786000, respectively, based on the different chord lengths. The temperature for the flow is T = 293.15 K. As the ground boundary is defined as a moving ground with the same velocity of the freestream, there is no ground boundary layer at the inlet ground boundary. The streamwise component of turbulence intensity is 0.2%, as the same as in experiment.

Chapter 6

Simulations around a Single Element Wing in Ground Effect

In this chapter, various simulations are carried out to compare the influence of different numerical methods and different turbulence modelling. The main emphasis is on the comparison of CFD simulation results and experimental results. A set of comparisons would primarily be on aerodynamics performance and flow field over a single element wing at different heights and at one reference angle of attack (α =1 °). All the simulations use RANS as mentioned in chapter 3. A further numerical study with various angles of attack will also be presented in this chapter.

6.1 Influence of Numerical Method

In this section, three numerical schemes are applied to check the influence of the numerical method. These are: 1) the Jameson's central differencing scheme (CDS), 2) the HLLC solver with MUSCL scheme (HLLC + MUSCL) and 3) the WENO 3rd order scheme (HLLC + WENO3). The SST k-ω turbulence model is used in combination with these schemes. For the purpose of investigating the ground effect, different heights from h/c = 0.090 to h/c = 0.671 are employed.

6.1.1 Convergence Performance

Figures 18 to 35 give the convergence history for the comparison of three different numerical schemes at six different heights. Both the aerodynamical forces as well as the density residuals in computational cycles are shown.

These histories demonstrate that all numerical schemes at different heights can converge well after certain computational cycles. However, different schemes present different performance. From these figures, in the lower height between the wing and ground such as h/c = 0.090 and h/c = 0.134, the CDS can nearly achieve the

convergence of 10^{-5} in 30000 cycles. On the other hand, the high order HLLC + MUSCL scheme can only achieve nearly a convergence of 10^{-4} after more cycles (i.e. 60000). Although the high order HLLC + WENO3 scheme can reach the same as the CDS to the convergence of 10^{-5}, it needs another one time cycles to get to this level, compared to the HLLC + MUSCL scheme. At higher heights from h/c = 0.224 to h/c = 0.671, the situation is similar. CDS always gives a good convergence of nearly 10^{-5} after only 10000 cycles. The HLLC + MUSCL scheme would spend 30000 cycles to achieve a worse convergence which is 10^{-4}, while the high order HLLC + WENO3 scheme needs more than 60000 cycles to reach the convergence of 10^{-5}. The reason is that the CDS uses an implicit residual smooth technique which allows larger CFL number whilst for MUSCL + HLLC or WENO3 + HLLC uses only an explicit time integration in the FLOWer code (The CFL number used in CDS is 3.5, the CFL number used in MUSCL + HLLC and WENO3 + HLLC are both 1.0).

The forces history of *Cl* and *Cd* indicate that it is faster for the forces to get to a steady level than the residual density. At higher heights from h/c = 0.224 to h/c = 0.671, the result of CDS shows a faster speed to let the *Cl* and *Cd* achieve to constant, only after about 3000 cycles. The high order HLLC schemes including MUSCL and WENO 3rd complete their achievement to the same stable condition by using almost 30000 cycles. Compared to higher heights, lower heights where h/c = 0.090 and h/c =0.134 are more complex on the forces history. The fluctuating phenomenon here is more obvious than at higher heights due to the small distance between the wing surface and the ground. Pressure in this region between the wing surface and the ground at lower heights is smaller than at higher heights. On CDS, this fluctuation appears from the beginning, it decreases and after nearly 15000 cycles, it reaches stability. As in the rest of the analyses, the high order schemes, HLLC + MUSCL and HLLC + WENO3, would cost more computational cycles. The simulation would last nearly 60000 cycles to reach the steady state.

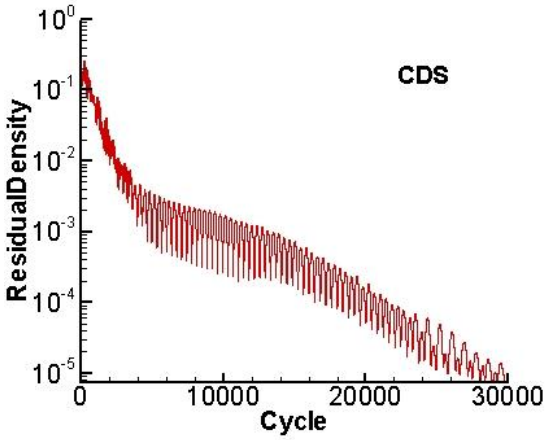

Figure 18: Histroy of density residual at h/c = 0.090

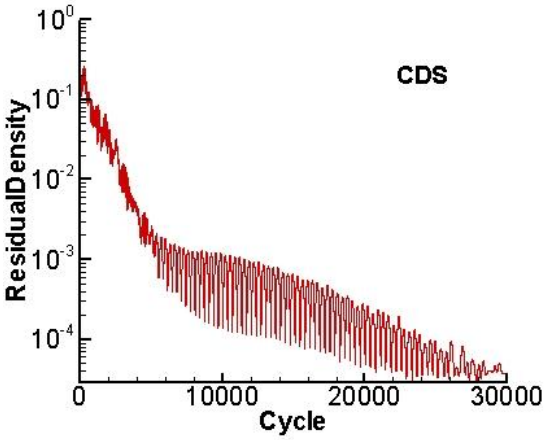

Figure 19: Histroy of density residual at h/c = 0.134

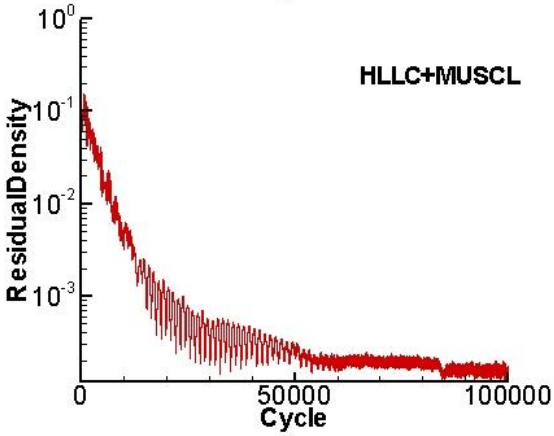

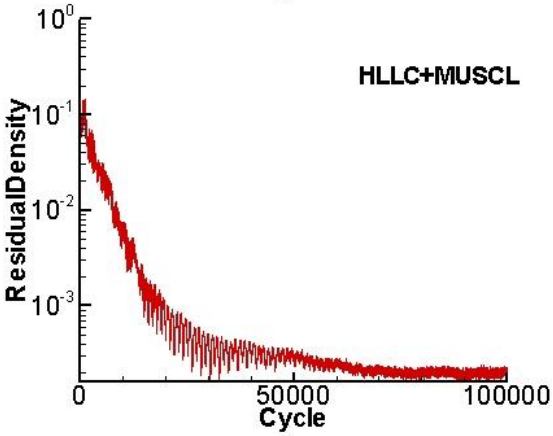

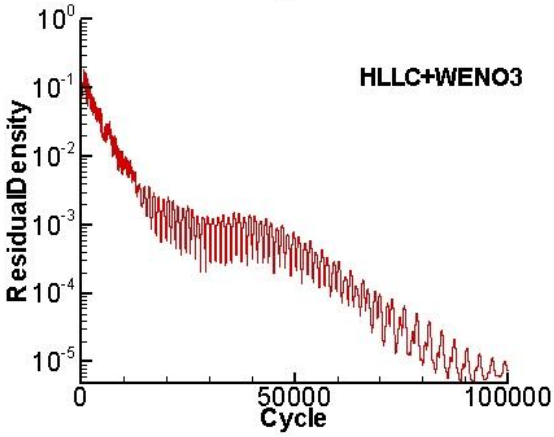

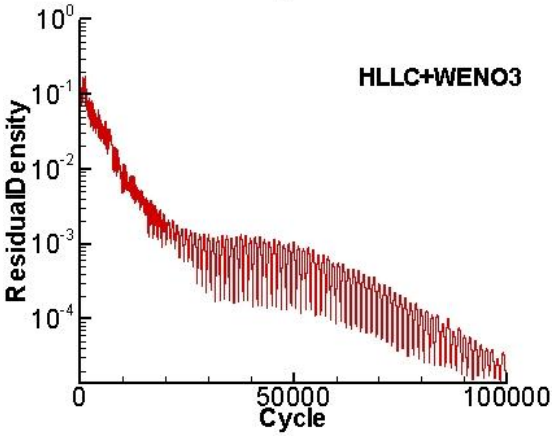

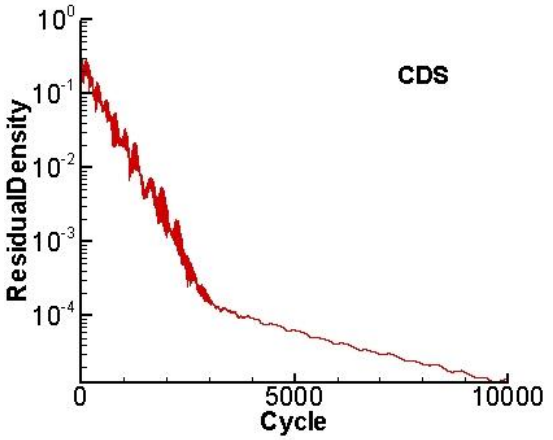

Figure 20: Histroy of density residual at h/c = 0.224

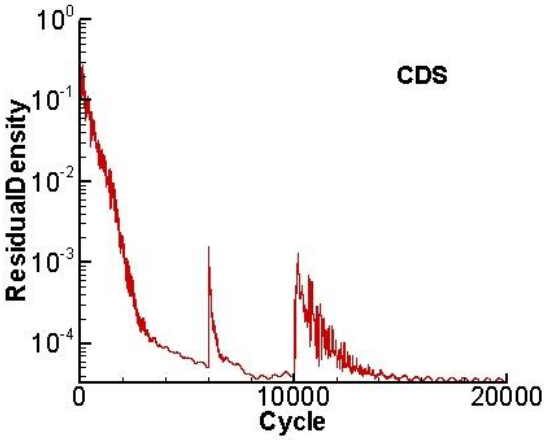

Figure 21: Histroy of density residual at h/c = 0.313

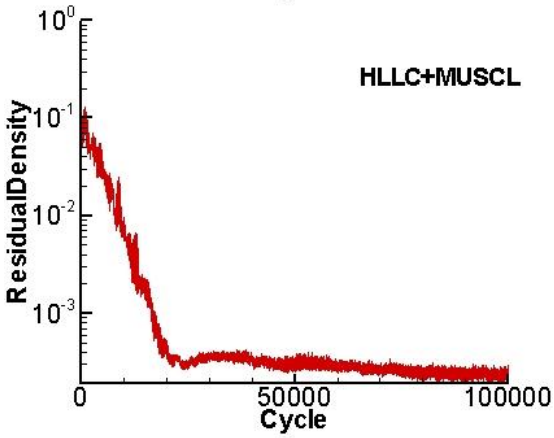

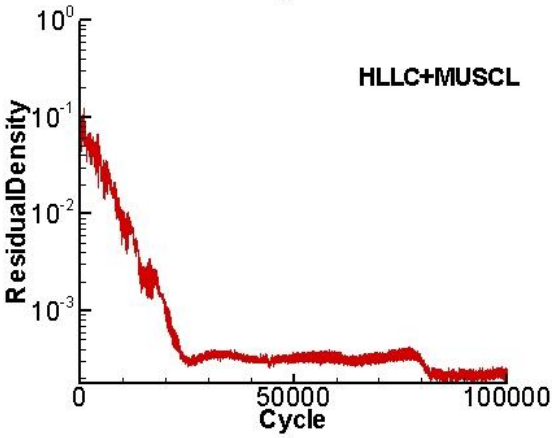

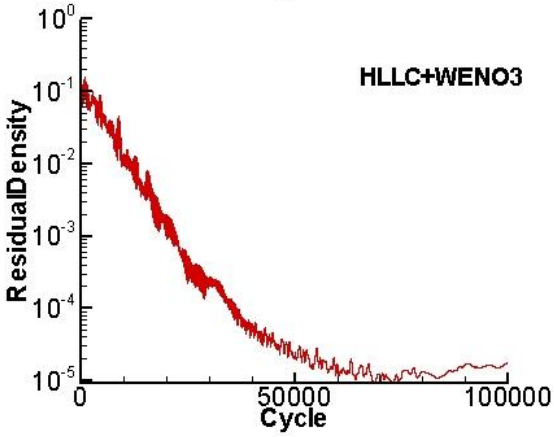

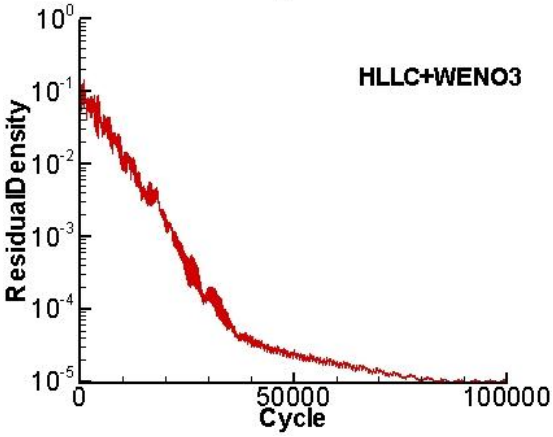

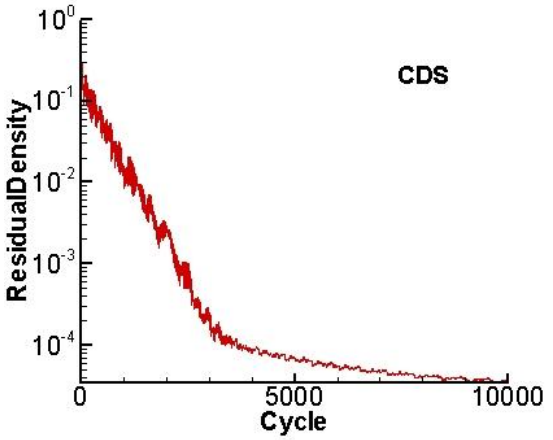

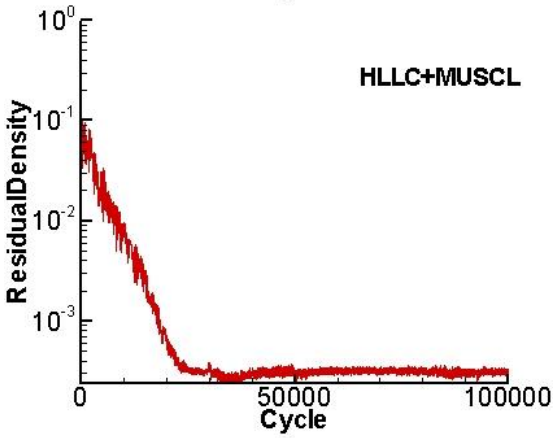

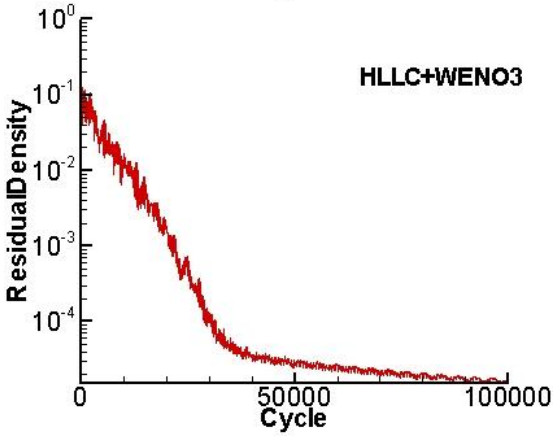

Figure 22: Histroy of density residual at h/c = 0.448

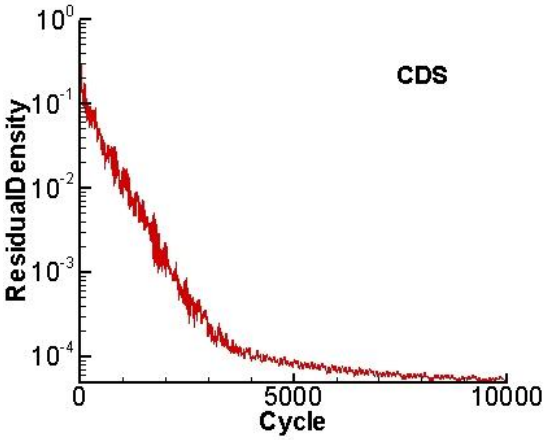

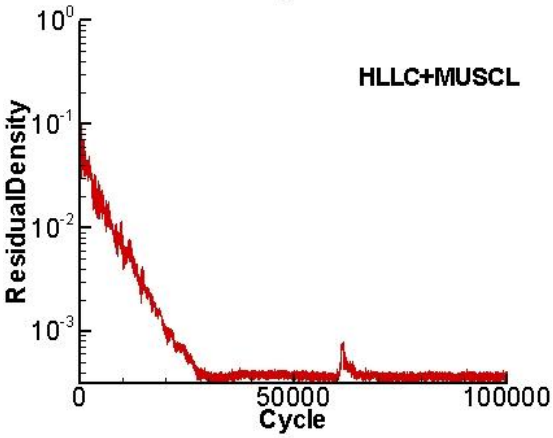

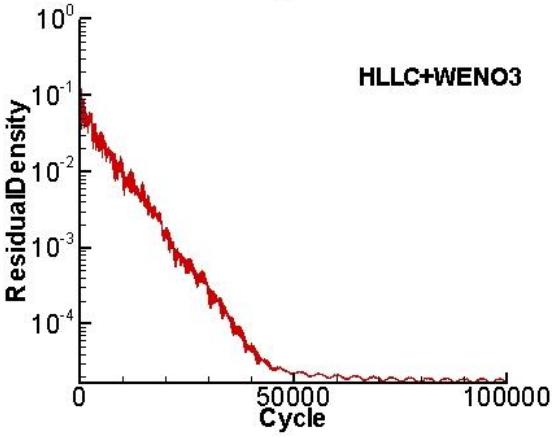

Figure 23: Histroy of density residual at h/c = 0.671

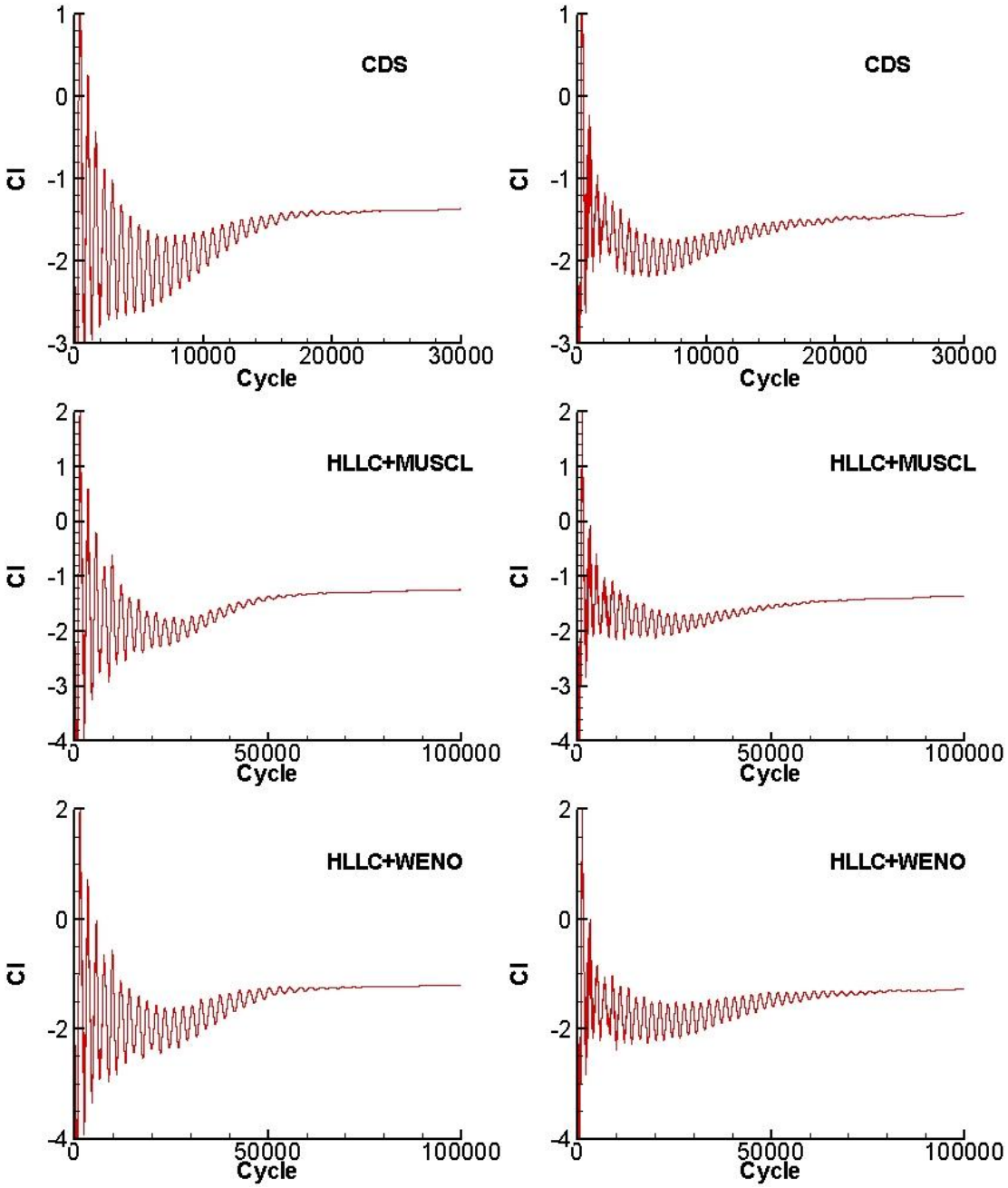

Figure 24: Lift coefficient at h/c = 0.090

Figure 25: Lift coefficient at h/c = 0.134

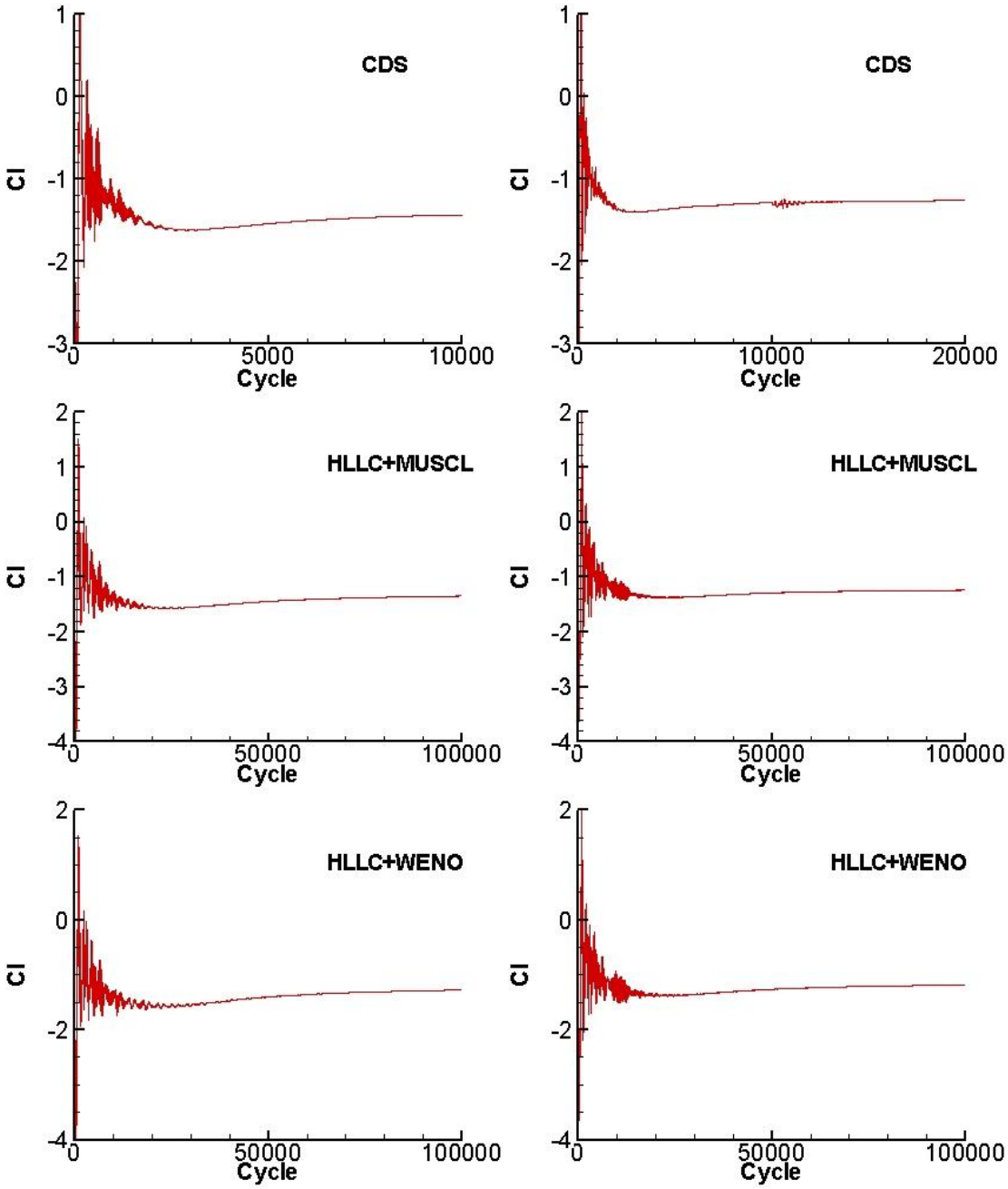

Figure 26: Lift coefficient at h/c = 0.224

Figure 27: Lift coefficient at h/c = 0.313

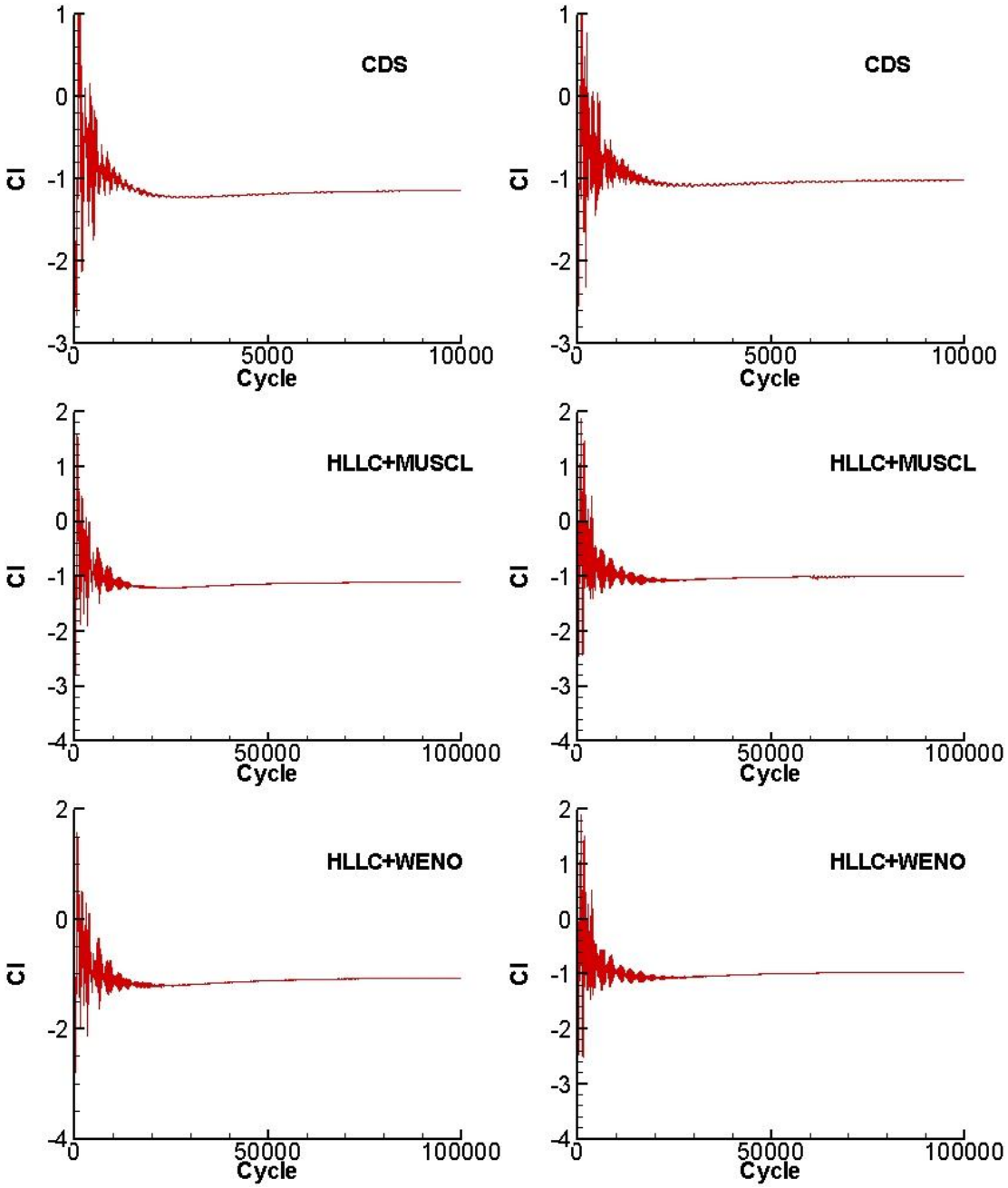

Figure 28: Lift coefficient at h/c = 0.448

Figure 29: Lift coefficient at h/c = 0.671

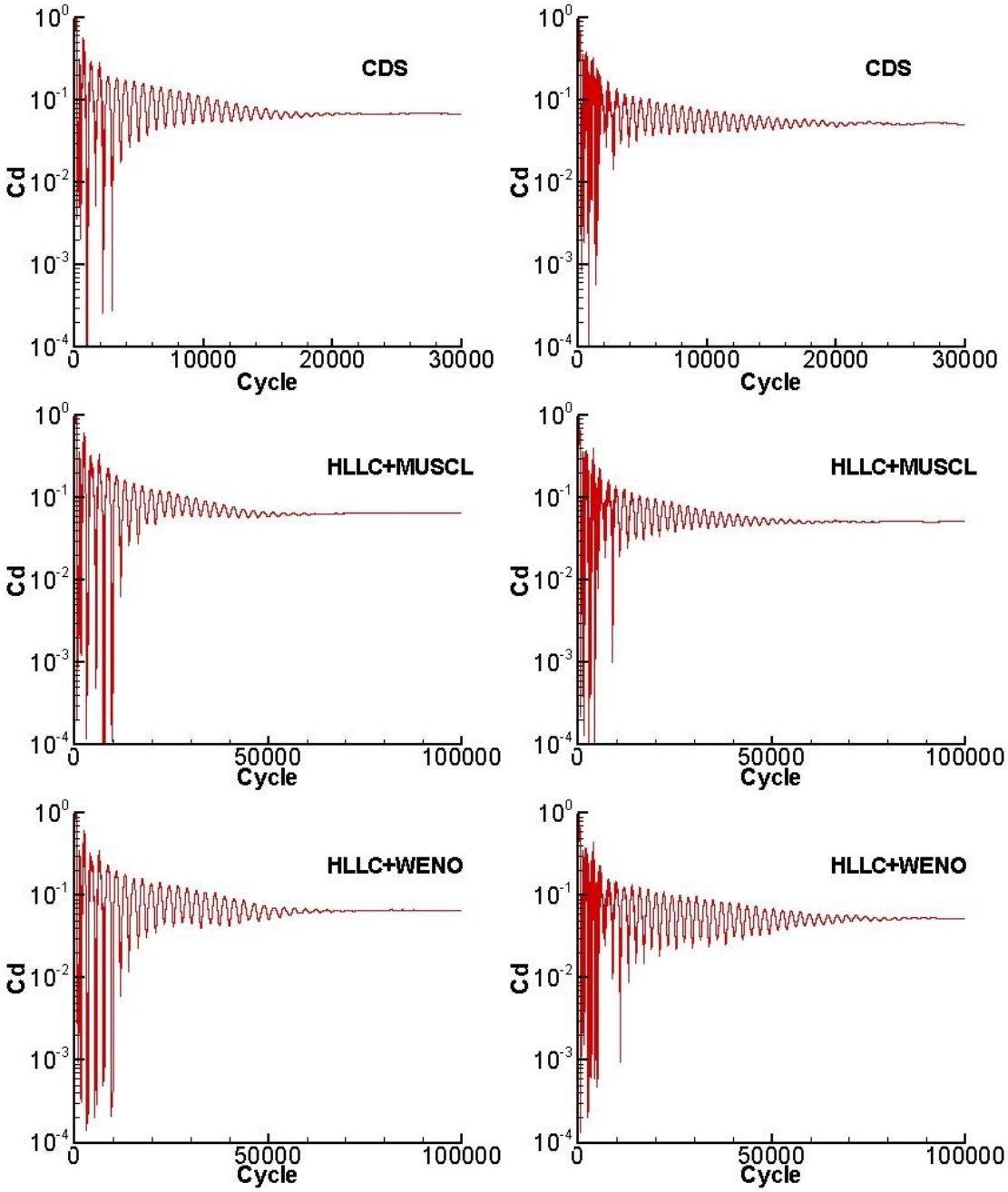

Figure 30: Drag coefficient at h/c = 0.090 Figure 31: Drag coefficient at h/c = 0.134

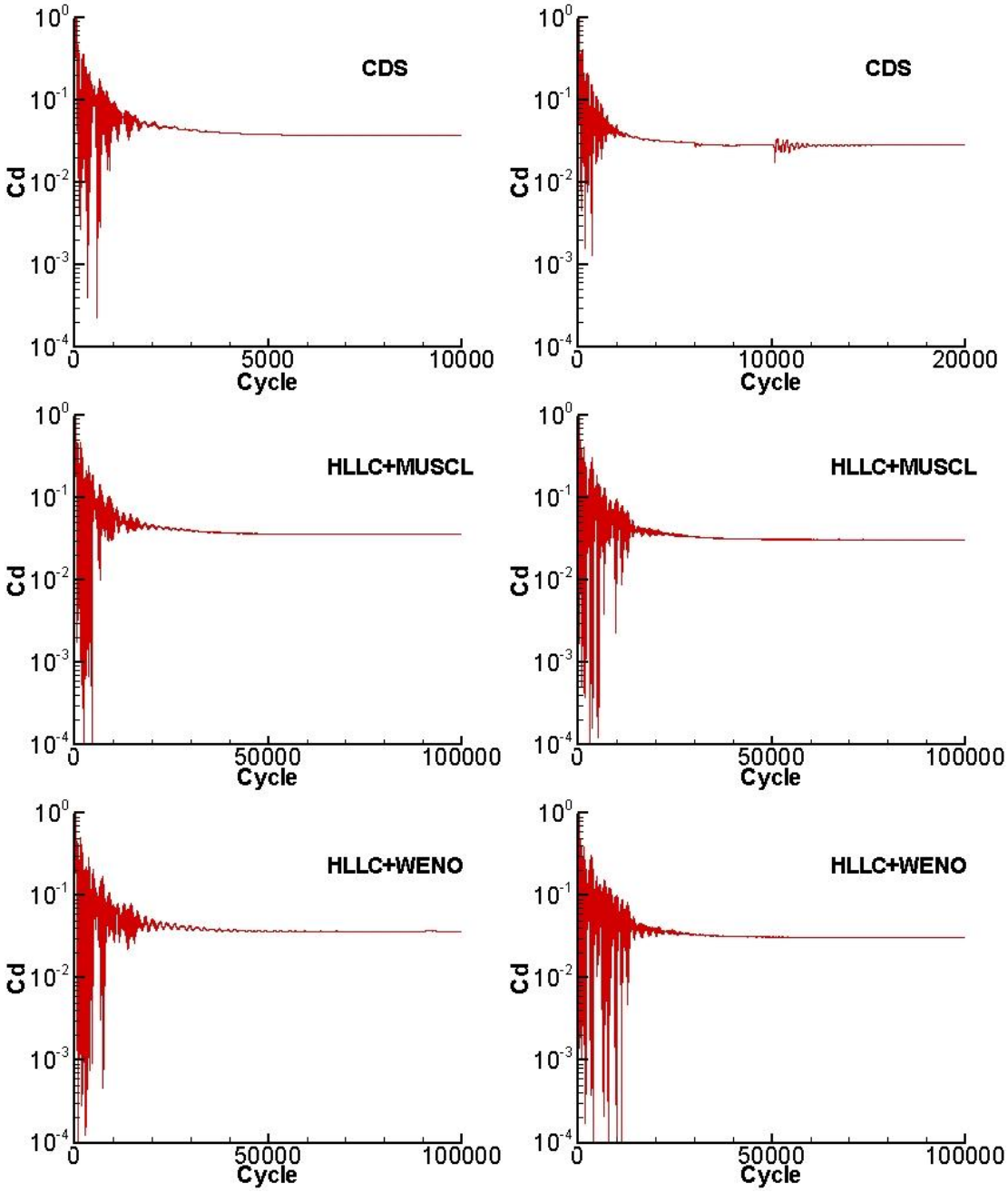

Figure 32: Drag coefficient at h/c = 0.224 Figure 33: Drag coefficient at h/c = 0.313

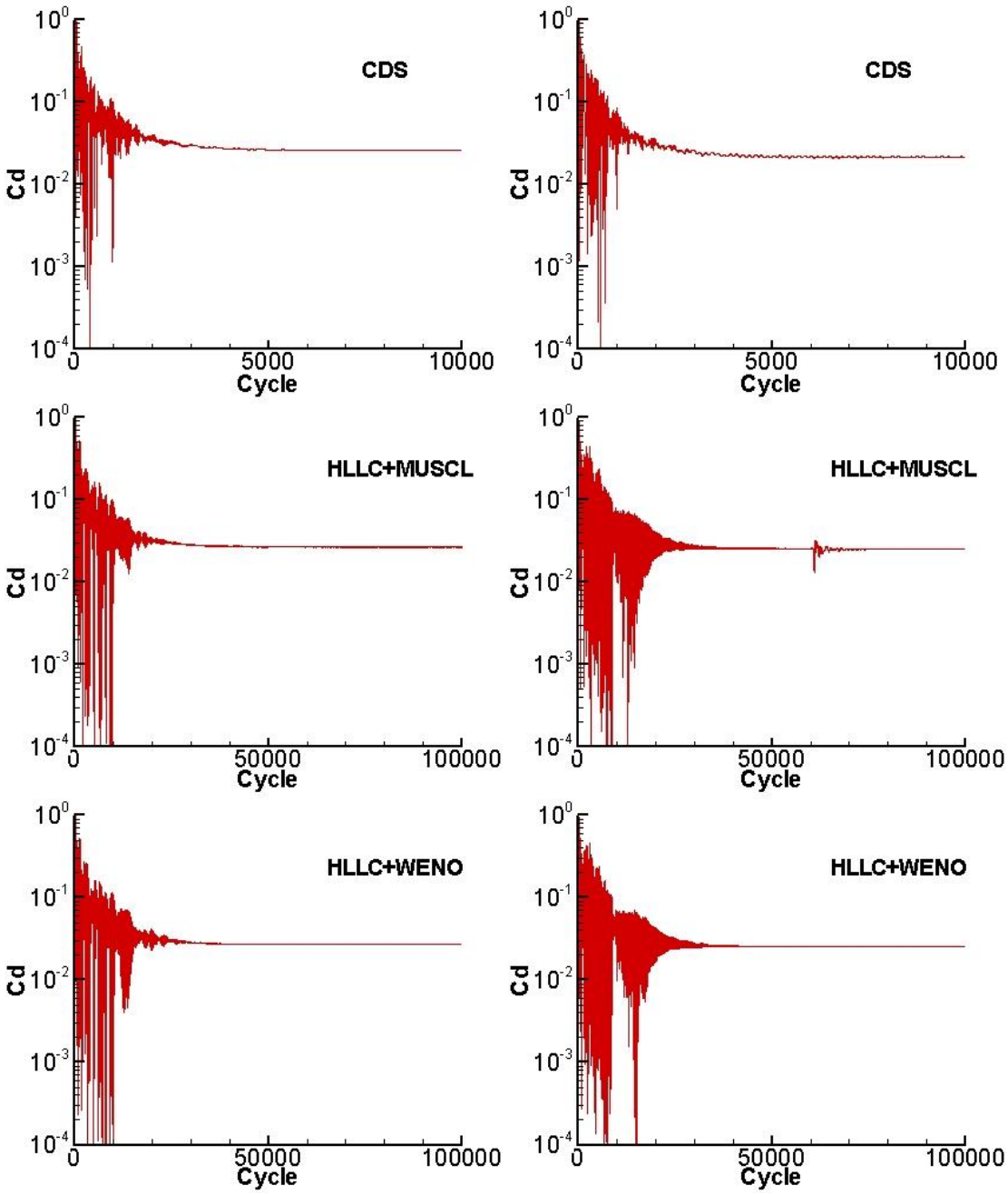

Figure 34: Drag coefficient at h/c = 0.448 Figure 35: Drag coefficient at h/c = 0.671

In brief, with the purpose to make every simulation converge, while taking into consideration that the density residual must be small enough and the forces should stay at a stable level in the mean time, the CDS spend less computational cycles than

the other two high order schemes. A comparison between the two high order schemes showed that the, HLLC + WENO3 could calculate better on the residual density history than the HLLC + MUSCL scheme.

6.1.2 Pressure Coefficient (Cp)

The Cp comparison of different schemes at various heights with experimental results is given in Figure 36.

At h/c = 0.671, the results from the three schemes are nearly identical, see Figure 36(a). Compared to the experimental points, the greastest difference appears on the suction surface, from the leading edge to x/c = 0.3, where the suction spike point and the suction peak region are included. All three schemes over predict the suction peak, especially the CDS. It can be more obviously seen at the peak point, at approximately x/c = 0.2. After the peak region and coming to the pressure recovery from x/c = 0.3 to the trailing edge, all three schemes agree well but still the pressure coefficient is slightly over predicted throughout this area. On the pressure surface, all the simulation results show a good agreement with the experimental points over the chord. The only exception appears at x/c =0.05 where the experiment presents a concave trend while the simulations give convex results. The same general trend over the surface can be found at h/c = 0.448, see Figure 36(b).

From h/c =0.313, the results from the high order schemes begin approaching the experimental points on the suction surface. The predicted pressure is still greater than in the experiment, but the difference becomes smaller. However, the CDS still over predicts throughout the whole suction surface compared to the other two schemes. On the pressure surface, the three schemes provide nearly identical results. The disparity trend at x/c = 0.05 is slightly smaller than at a higher height. But the magnitude of the pressure from x/c = 0.5 to the trailing edge is a little smaller than in the experiment.

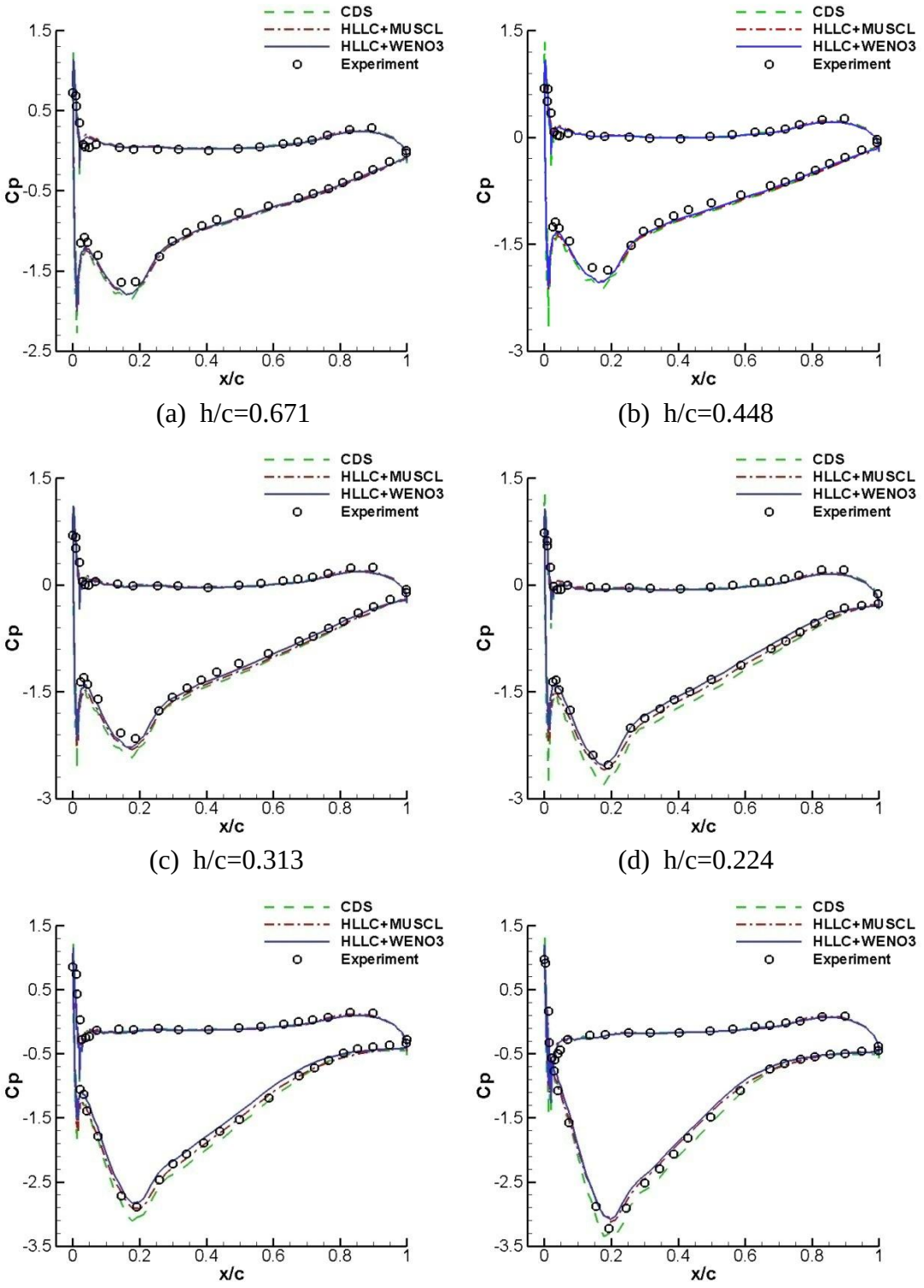

(a) h/c=0.671 (b) h/c=0.448

(c) h/c=0.313 (d) h/c=0.224

(e) h/c=0.134 (f) h/c=0.090

Figure 36: Coefficient of pressure by different numerical scheme

At lower heights, h/c = 0.224 and h/c = 0.134, the high order schemes further approach the experimental points on the suction surface. The two schemes, HLLC + MUSCL and HLLC + WENO3 agree well with the experimental results. CDS still highly over predicts throughout the whole suction surface. On the pressure surface, the three schemes agree well with others as well as the experimental points, and the disparity trend at x/c = 0.05 is going to disappear.

At the lowest height of all the simulations, h/c = 0.090, a small difference appears on the suction surface. The two high order schemes surprisingly under predict throughout most of the region of the chord. This difference can be observed clearly at the suction peak at x/c = 0.2. CDS keeps the over prediction but not as much as at lower heights. On the pressure surface, as well as at lower heights, all three simulations present results which are very well compared with the experimental data.

For all the ground heights, there is a significant difference between the simulative results and the experimental results. The predicted pressure that given by all the three schemes is greater than one at the stagnation point, whereas it should be no more than one in incompressible flow. This may due to two reasons: one is that this phenomenon could appear in compressible flow. According to Anderson (2007), in the flow of compressible fluids such as air, and particularly the high-speed flow of compressible fluids, $\rho v^2/2$ (the dynamic pressure) is no longer an accurate measure of the difference between stagnation pressure and static pressure, which is switched as $\rho v^2 \sin^2\theta$, where θ is the angle between the surface and the freestream. As a result, pressure coefficients can be greater than one in compressible flow. As the FLOWer code is a solver based on compressible flow, it could happen that Cp greater than one when using it to resolve the problem of incompressible flow. Another reason is that during the RANS prediction for turbulent flows, we employed eddy-viscosity models. In which the behavior are represented by calculating a local turbulent viscosity and adding it onto the molecular viscosity to give an effective viscosity at each cell [Wilcox (2006)]. This will lead to an over prediction of the kinetic viscosity, hence

result in the turbulence kinetic energy. So near the stagnation point, the stagnation pressure would raise well above 1. Although all three numerical methods overpredict the pressure near the stagnation point in this case, still the two high order schemes give better results which are less overpredicted than the CDS.

6.1.3 Lift and Drag Forces

In this section, the discussion is focused on the comparison among three different schemes with the experimental results. A further numerical analysis of the forces at different heights which is concentrated on the physical phenomena of ground effect will be presented in the sections later on.

The lift and drag coefficients which are obtained from using the three different schemes at different heights are shown in Table 1 and Table 2. The experimental results are also given in these tables in order to calculate the relative errors (ERR) which was defined as (Simulation result – Experimental result)/Experimental result. Two figures are drawn regarding *Cl* and *Cd* versus heights (see Figures 37 and 38) to further illustrate the results.

From Table 1 and Figure 37, the *Cl* data further prove the conclusion made in the previous section that with the height changing from high to low, the difference between simulations and experiment gets smaller. At the lowest height $x/c = 0.090$, the results with high order schemes, such as HLLC + MUSCL and HLLC + WENO3 present a negative difference with the experimental results. Again, it is clearly shown that the high order schemes are more accurate than the CDS on the simulation with ground effect. Additionally, between the two high order schemes, the HLLC + WENO3 scheme predicts a better result than the HLLC + MUSCL scheme. The biggest relative error of the HLLC + WENO3 scheme found in Table 1 is less than 7%, while the others are more than 10%.

h/c	0.671	0.448	0.313	0.224	0.134	0.090
Experiment	0.902	1.009	1.145	1.286	1.385	1.371
CDS	1.019	1.144	1.263	1.437	1.434	1.407
HLLC + MUSCL	0.994	1.102	1.242	1.348	1.398	1.337
HLLC + WENO3	0.961	1.066	1.182	1.290	1.365	1.314
ERR(CDS)	12.97%	13.38%	10.31%	11.74%	3.54%	2.63%
ERR(HLLC + MUSCL)	10.20%	9.22%	8.47%	4.82%	0.94%	-2.48%
ERR(HLLC + WENO3)	6.54%	5.65%	3.23%	0.31%	-1.44%	-4.16%

Table 1: Lift coefficients for numerical methods

It can be observed that all the predictions from the three numerical schemes gives negative results of *Cd* at all different heights in Table 2 and Figure 38. The trend of difference of *Cd* between the simulations and the experiment is quite the same with the trend of difference of *Cl* which decreases from the high to low height. It can be discovered that the two high order schemes are nearly unanimous in predicting drags (see Figure 38). And still, the high order schemes give better drag simulation results than the CDS.

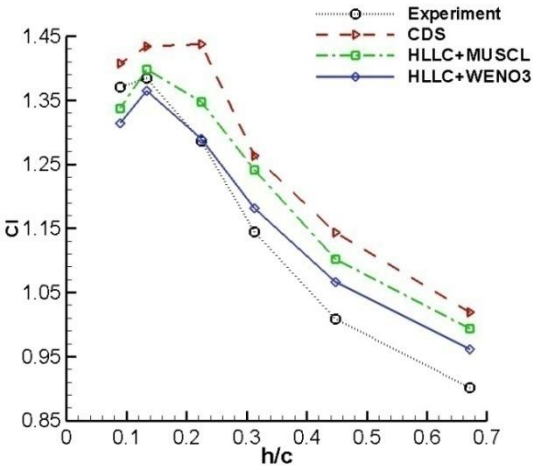

Figure 37: Lift coefficients at different heights for numerical methods

h/c	0.671	0.448	0.313	0.224	0.134	0.09
Experiment	0.0277	0.0317	0.0348	0.0425	0.0558	0.0689
CDS	0.0215	0.0258	0.0282	0.0369	0.0501	0.0678
HLLC + MUSCL	0.0253	0.0267	0.0311	0.0362	0.0526	0.0658
HLLC + WENO3	0.0256	0.0270	0.0316	0.0369	0.0526	0.0667
ERR(CDS)	-22.38%	-18.61%	-18.97%	-13.18%	-10.22%	-1.60%
ERR(HLLC + MUSCL)	-8.66%	-15.77%	-10.63%	-14.82%	-5.73%	-4.50%
ERR(HLLC + WENO3)	-7.58%	-14.83%	-9.20%	-13.18%	-5.73%	-3.19%

Table 2: Drag coefficients for different numerical methods

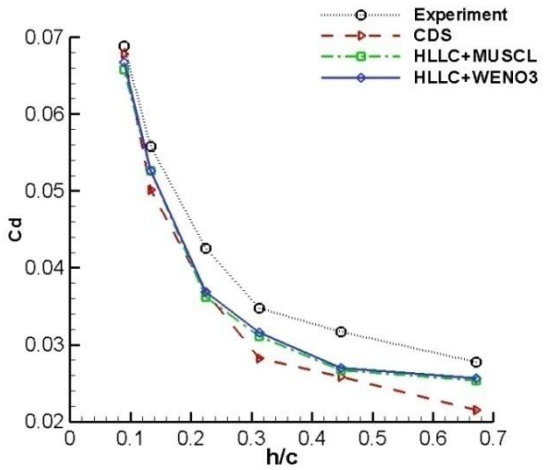

Figure 38: Drag coefficients at different heights for numerical methods

6.1.4 Velocity Profile at the Trailing Edge

Velocity profiles inside the boundary layer are taken at the trailing edge where *x/c* = 1.0 on the suction surface. The observation line is perpendicular to the suction surface. However, it is noted that for some reasons, presented by Zerihan et al. (2001), the experimental data very close to the surface was impossible to acquire. Computational velocity profiles at three different heights are compared, namely *h/c* = 0.067, *h/c* = 0.224 and *h/c* = 0.448.

Figure 39(a) shows the computational results of the three different numerical schemes

with the experimental results, for u/U_∞ at h/c = 0.067. The HLLC + MUSCL and the HLLC + WENO3 scheme give nearly the same result, whilst the CDS gives a much different prediction. All three schemes show a negative velocity region close to the surface (the same as the experimental results), which is regarded as a separation flow at the trailing edge. Through the boundary layer, the results from the two high order schemes appear more close to the shape of the experimental results. However, the velocity predicted by the two schemes is consistently bigger, approximately 0.1 higher for the u/U_∞ than the experimental results. Due to this, the computational simulations of the two high order schemes show a smaller separation region than the experiment. With the CDS, a thinner but stronger recirculation region is predicted.

At h/c = 0.134 (Figure 39(b)), all of the computational schemes present clearly a separated boundary layer. The results from the HLLC + WENO3 scheme lie clearly closer to the experimental data. However, a slight deviation appears from η/c = 0.045 to η/c = 0.075. It is found that the CDS has a similar manner to the experimental data but the difference between the computational and the experimental data are much bigger.

For the results at h/c = 0.224, which is illustrated in Figure 39(c), the velocity deficit near to the wing surface is much smaller. However, as the distance grows, all the schemes present quite different results in the whole boundary layer. The HLLC + WENO3 scheme still gives the best prediction compared with the experiments at h/c = 0.134. The simulation result is almost in very good agreement with the experimental data at the region very close to the surface, although when moving away from the surface, a small difference on u/U_∞ profile can be identified. Overall, amongst the three numerical schemes, the HLLC + WENO3 scheme provides the best prediction on the velocity profile at the boundary layer of trailing edge.

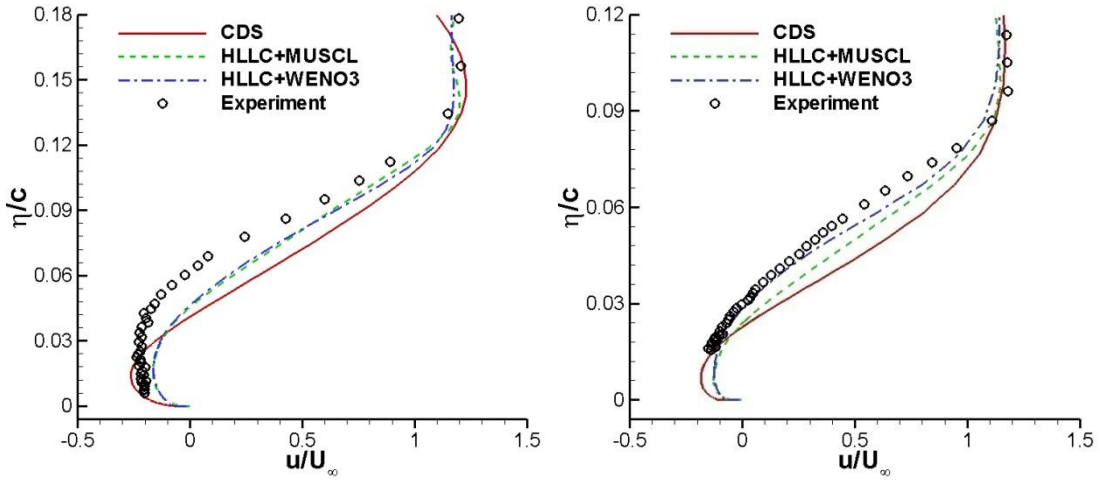

(a) h/c = 0.067 (b) h/c = 0.134

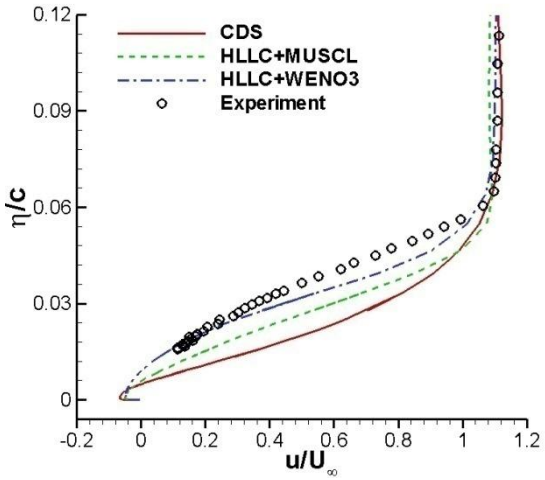

(c) h/c = 0.224

Figure 39: Boundary layer on suction surface at the trailing edge

6.1.5 Wake Analysis

To study the results in the wake, the comparisons are split into two regions which are named the nearfield wake and the farfield wake. The nearfield wake is defined as the region which is one chord length away from the trailing edge. The farfield wake is

defined as the region after the nearfield wake.

The nearfield wake

In the nearfield wake, the investigation is focused on two streamwise locations: x/c = 1.2 and x/c = 1.5. Three different heights are considered in the comparison, which are h/c = 0.134, h/c = 0.224 and h/c = 0.448. The simulation results compared with the experimental velocity results for both locations are plotted at different heights. Information on the wake thickness from the computations and the experiment is given in Table 3, where the Wake thickness δ_{99} is measured by 99% displacement thickness while the δ_{top} and δ_{bottom} are the top and the bottom of the wake thickness.

At the height of h/c = 0.134, the wake comparisons at x/c = 1.2 and x/c = 1.5 are shown in Figure 40(a) and Figure 40(b). The two high order schemes show similar results at x/c = 1.2. The main wake is a little thicker for both the HLLC + MUSCL and the HLLC + WENO3 schemes and the velocity u/U_∞ at the wake centre according to these two schemes is 0.1 smaller than the experimental results. The thickness of the main wake and the velocity at the wake centre predicted by the CDS are quite close to the experimental data, but they show an incorrect upward shift in the wake. At x/c = 1.5, from the Figure 40(b) that the velocity in the wake centre is severely under predicted. The wake thickness at this location is slightly smaller than the experiment for all the schemes. For the ground boundary layer, the CDS gives an increased thickness than the other schemes at both streamwise locations. At x/c =1.5, the two high order schemes over predict the velocity deficit of the ground boundary layer.

For the results at h/c = 0.224, the wake comparison at x/c = 1.2 and x/c = 1.5 are shown in Figures 40(c) and 40(d). The CDS and the HLLC + MUSCL scheme predict well on the thickness of the main wake, while the HLLC + WENO3 scheme presents slightly thicker wave. Meanwhile, the HLLC + WENO3 scheme has 0.1 smaller prediction for the velocity u/U_∞ at the wake centre, the same situation as at h/c = 0.134, compared to the experimental data. The HLLC + MUSCL scheme also under predicts the wake centre velocity u/U_∞, which is about 0.05. The CDS gives an

opposing prediction that the wake centre velocity u/U_∞ is about 0.03 bigger than the experiment. At x/c = 1.5, compared to the high order schemes which give exactly the same thickness of the main wake as the experimental results, the CDS models a little thicker (see Table 3). However, all three schemes still under predict the velocity of the wake centre, same as at h/c = 0.134. But the difference is much smaller, only $u/U_\infty \approx$ 0.05 lower than the experimental results, compared to $u/U_\infty \approx 0.2$ at h/c = 0.134. For the ground boundary layer, the CDS still gives an increased thickness compared to the other schemes at both streamwise locations. However, this time at x/c =1.5, the two high order schemes under predict the velocity deficits of the ground boundary layer.

Coming to a higher height at h/c = 0.448 (Figure 40(e) and Figure 40(f)), the results obtain from using the three schemes agree well at both streamwise locations. The high order schemes again model well with the thickness of the main wake while the CDS gives a slightly thicker results. The velocity of the wake centre is still under predicted according to the computations. The results for the CDS present the thickness of ground boundary layer to have decreased compared to previous heights. However, the thickness of this from the high order schemes is significantly closer to the experimental points.

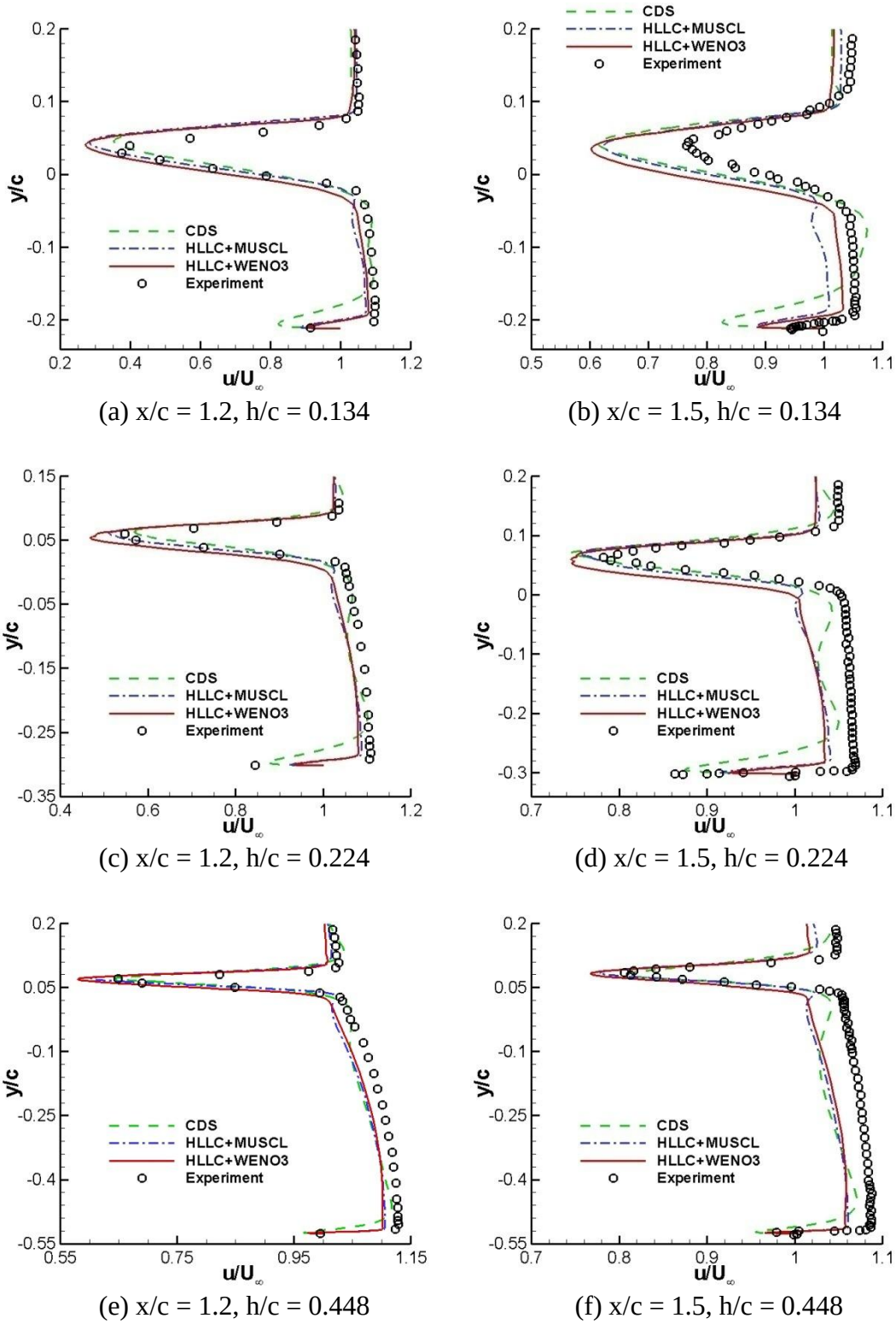

(a) x/c = 1.2, h/c = 0.134

(b) x/c = 1.5, h/c = 0.134

(c) x/c = 1.2, h/c = 0.224

(d) x/c = 1.5, h/c = 0.224

(e) x/c = 1.2, h/c = 0.448

(f) x/c = 1.5, h/c = 0.448

Figure 40: Wake profiles at x/c = 1.2 and x/c = 1.5

h/c	schemes	$u_{min}/U\infty$	y/c at u_{min}	y at δ_{top}	y at δ_{bottom}	δ_{99}/c
0.090	experiment	0.72	0.02	0.12	-0.10	0.22
	CDS	0.52	0.03	0.09	-0.09	0.18
	HLLC + MUSCL	0.52	0.02	0.08	-0.08	0.16
	HLLC + WENO3	0.52	0.02	0.08	-0.08	0.16
0.134	experiment	0.77	0.04	0.12	-0.05	0.17
	CDS	0.61	0.04	0.10	-0.05	0.15
	HLLC + MUSCL	0.62	0.04	0.09	-0.05	0.14
	HLLC + WENO3	0.60	0.03	0.09	-0.05	0.14
0.224	experiment	0.79	0.07	0.13	0.01	0.12
	CDS	0.74	0.07	0.14	-0.01	0.15
	HLLC + MUSCL	0.75	0.07	0.12	0.01	0.11
	HLLC + WENO3	0.75	0.06	0.11	-0.01	0.12
0.313	experiment	0.81	0.08	0.13	0.04	0.09
	CDS	0.75	0.07	0.14	0.02	0.12
	HLLC + MUSCL	0.77	0.08	0.12	0.03	0.09
	HLLC + WENO3	0.76	0.07	0.11	0.02	0.09
0.448	experiment	0.81	0.08	0.13	0.04	0.09
	CDS	0.81	0.08	0.16	0.02	0.14
	HLLC + MUSCL	0.78	0.08	0.14	0.04	0.10
	HLLC + WENO3	0.77	0.08	0.13	0.03	0.10

Table 3: Information for the experimental and the computational results at x/c = 1.5

The farfield Wake

In the farfield wake, the investigation is focused on two streamwise locations: *x/c* = 2.0 and *x/c* = 3.0. Results at three different heights, *h/c* = 0.067, *h/c* = 0.224 and *h/c* = 0.448 are compared. The simulation results are compared with the experimental velocity results for both locations at different heights. The information on wake thickness from the computations and the experiment is presented in Table 4 and Table 5.

At the lowest height, h/c = 0.067, the wake comparison at x/c = 2.0 and x/c = 3.0 are shown in Figures 41(a) and 41(b) for all simulations. It can be seen from the figures that, the wake has been combined with the ground boundary layer, especially at x/c = 0.3. The thickness of the wake does not appear in the table because it is not strictly valid. All three numerical schemes show similar results, but they all are all considerable different from the experimental profile. The velocity at the wake centre at both locations according to the three schemes is lower than the experimental results. For the ground boundary layer, due to the mergence between the wake and the ground boundary layer, all the schemes again under predict the velocity deficits of the ground boundary layer.

For the results at h/c = 0.224, the wake comparison at x/c = 2.0 and x/c = 3.0 are shown in Figures 41(c) and 41(d). The HLLC + MUSCL and HLLC + WENO3 schemes predict slightly thinner on the thickness of the main wake, while the CDS presents slightly thicker wake. Meanwhile, at x/c = 2.0, all results predict 0.06 lower for the velocity u/U_∞ at the wake centre, as well as outside the wake, compared to the experimental data. At x/c = 1.5, an obvious apophysis has been emerged inside the wake according to computations. This leads 0.05 lower modelling in the velocity u/U_∞ at the bottom side of the wake. For the ground boundary layer, the CDS still gives an increased thickness than the other schemes at both streamwise locations. At x/c =1.5, all three schemes over predict the velocity deficits of the ground boundary layer.

For a higher height at h/c = 0.448, (Figure 41(e) and Figure 41(f)), results from the three schemes agree well with each other at both streamwise locations. The high order schemes again provide a better prediction of the thickness of the main wake while the CDS gives slightly thicker results. The velocity of the wake centre is still under predicted according to the computations. The results for the CDS present a reduced thickness of the ground boundary layer compared to previous heights. However, the thickness in this case from the high order schemes is much closer to the experimental data.

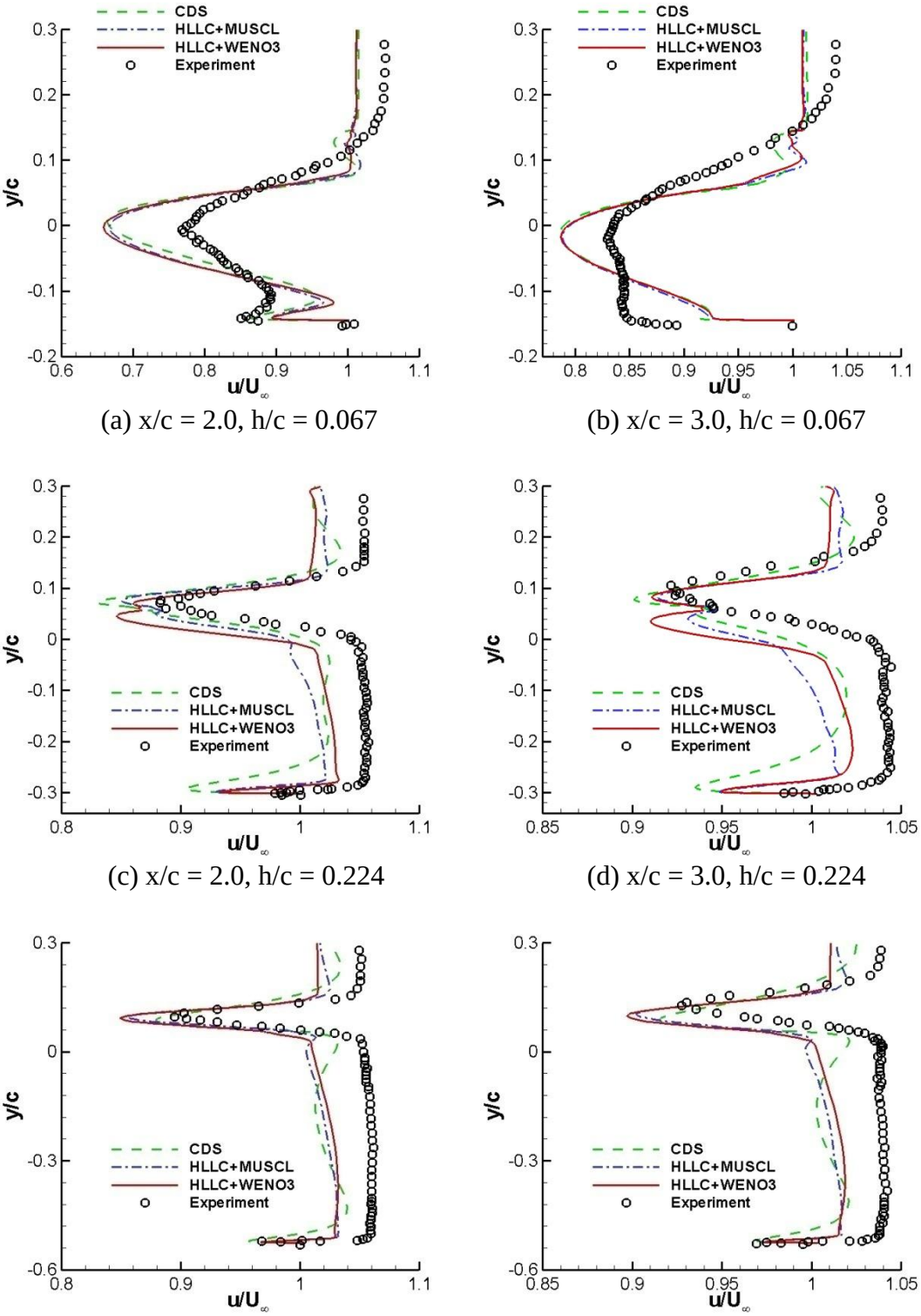

(a) x/c = 2.0, h/c = 0.067

(b) x/c = 3.0, h/c = 0.067

(c) x/c = 2.0, h/c = 0.224

(d) x/c = 3.0, h/c = 0.224

(e) x/c = 2.0, h/c = 0.448

(f) x/c = 3.0, h/c = 0.448

Figure 41: Wake profiles at x/c = 2.0 and x/c = 3.0

h/c	schemes	$u_{min}/U\infty$	y/c at u_{min}	y at δ_{top}	y at δ_{bottom}	δ_{99}/c
0.09	experiment	0.84	0.02	0.16	-0.11	0.27
	CDS	0.69	0.02	0.10	-0.09	0.19
	HLLC + MUSCL	0.70	0.01	0.09	-0.11	0.20
	HLLC + WENO3	0.70	0.01	0.09	-0.11	0.20
0.134	experiment	0.85	0.04	0.14	-0.07	0.21
	CDS	0.76	0.03	0.12	-0.09	0.21
	HLLC + MUSCL	0.77	0.03	0.10	-0.05	0.15
	HLLC + WENO3	0.75	0.03	0.10	-0.08	0.18
0.224	experiment	0.88	0.08	0.16	0.01	0.15
	CDS	0.83	0.07	0.16	0.00	0.16
	HLLC + MUSCL	0.85	0.07	0.13	0.00	0.13
	HLLC + WENO3	0.85	0.05	0.12	-0.01	0.13
0.313	experiment	0.89	0.09	0.16	0.04	0.12
	CDS	0.84	0.08	0.18	0.02	0.16
	HLLC + MUSCL	0.85	0.09	0.14	0.03	0.11
	HLLC + WENO3	0.84	0.08	0.14	0.01	0.13
0.448	experiment	0.90	0.10	0.16	0.04	0.12
	CDS	0.88	0.09	0.23	0.04	0.19
	HLLC + MUSCL	0.86	0.10	0.17	0.04	0.13
	HLLC + WENO3	0.85	0.09	0.17	0.03	0.14

Table 4: Wake information for experimental and computational results at x/c = 2.0

h/c	schemes	$u_{min}/U\infty$	y/c at u_{min}	y at δ_{top}	y at δ_{bottom}	δ_{99}/c
0.09	experiment	0.9	0.01	0.19	-0.12	0.31
	CDS	0.82	0.01	0.11	-0.12	0.23
	HLLC + MUSCL	0.82	-0.01	0.1	-0.13	0.23
	HLLC + WENO3	0.81	-0.01	0.1	-0.13	0.23
0.134	experiment	0.91	0.05	0.19	-0.08	0.27
	CDS	0.86	0.03	0.14	-0.08	0.22
	HLLC + MUSCL	0.86	0.01	0.12	-0.1	0.22
	HLLC + WENO3	0.85	0.01	0.12	-0.1	0.22
0.224	experiment	0.93	0.12	0.2	0.01	0.19
	CDS	0.9	0.08	0.19	-0.07	0.26
	HLLC + MUSCL	0.91	0.08	0.15	-0.04	0.19
	HLLC + WENO3	0.91	0.08	0.15	-0.03	0.18
0.313	experiment	0.93	0.14	0.22	0.04	0.18
	CDS	0.9	0.09	0.23	0.01	0.22
	HLLC + MUSCL	0.9	0.09	0.17	0.02	0.15
	HLLC + WENO3	0.9	0.09	0.17	0.01	0.16
0.448	experiment	0.93	0.13	0.22	0.06	0.16
	CDS	0.92	0.09	0.27	0.04	0.23
	HLLC + MUSCL	0.9	0.1	0.19	0.03	0.16
	HLLC + WENO3	0.9	0.1	0.19	0.03	0.16

Table 5: information for experimental and computational results at x/c = 3.0

6.1.6 Flow Visualization

In this section, some of the contours for flow visualisation are shown. However, due to the lack of experimental data, only the simulation results are presented for the analysis.

The mach contours and a close–up view of a part of the trailing edge, together with restricted streamlines for the three numerical methods are shown in Figure 42 to Figure 45 for the cases with different heights, respectively. All three numerical methods show that for lower height cases, flow on the suction surface near the trailing edge is separated as the height rises, the Mach number reduces on the suction surface while the streamlines at the trailing edge are better attached. At the lowest part of the suction surface, with regard to the high Mach region, the CDS gives a bigger Mach number compared to the other high order schemes.

The vorticity magnitudes at different heights are shown in Figure 46 to Figure 49. Both the wing boundary layer and the ground boundary layer can be clearly seen. Again, the results from the three numerical schemes show an attached flow at a higher height, h/c = 0.448. As the front wing approaches the ground, the vorticity magnitude increases; evidently due to the occurrence of flow separation at the trailing edge. The two high order schemes appear similar in simulation, while they are both more accurate than CDS on the vorticity modelling.

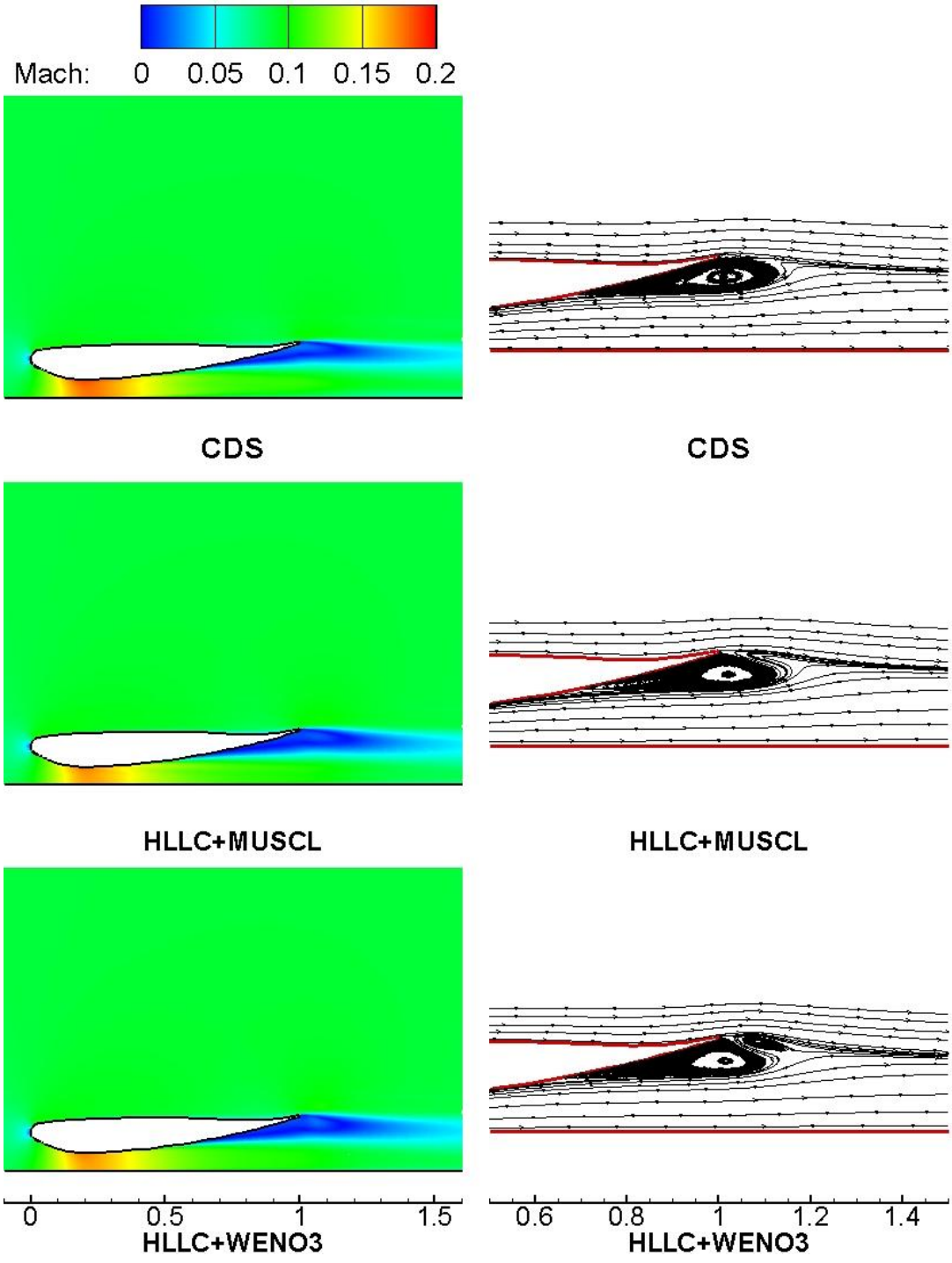

Figure 42: Mach contours and the trailing edge streamlines at h/c=0.067

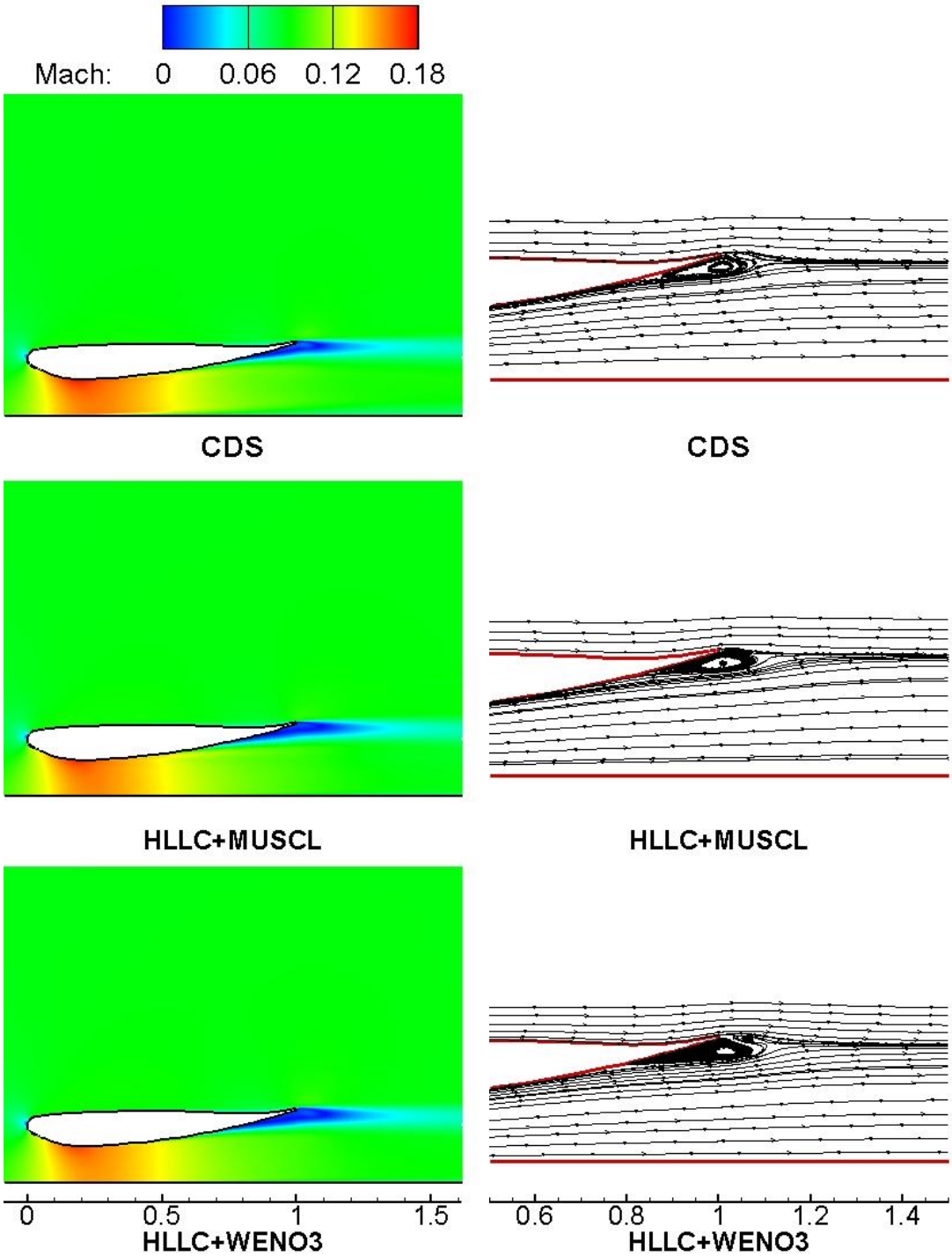

Figure 43: Mach contours and trailing edge streamlines at h/c=0.134

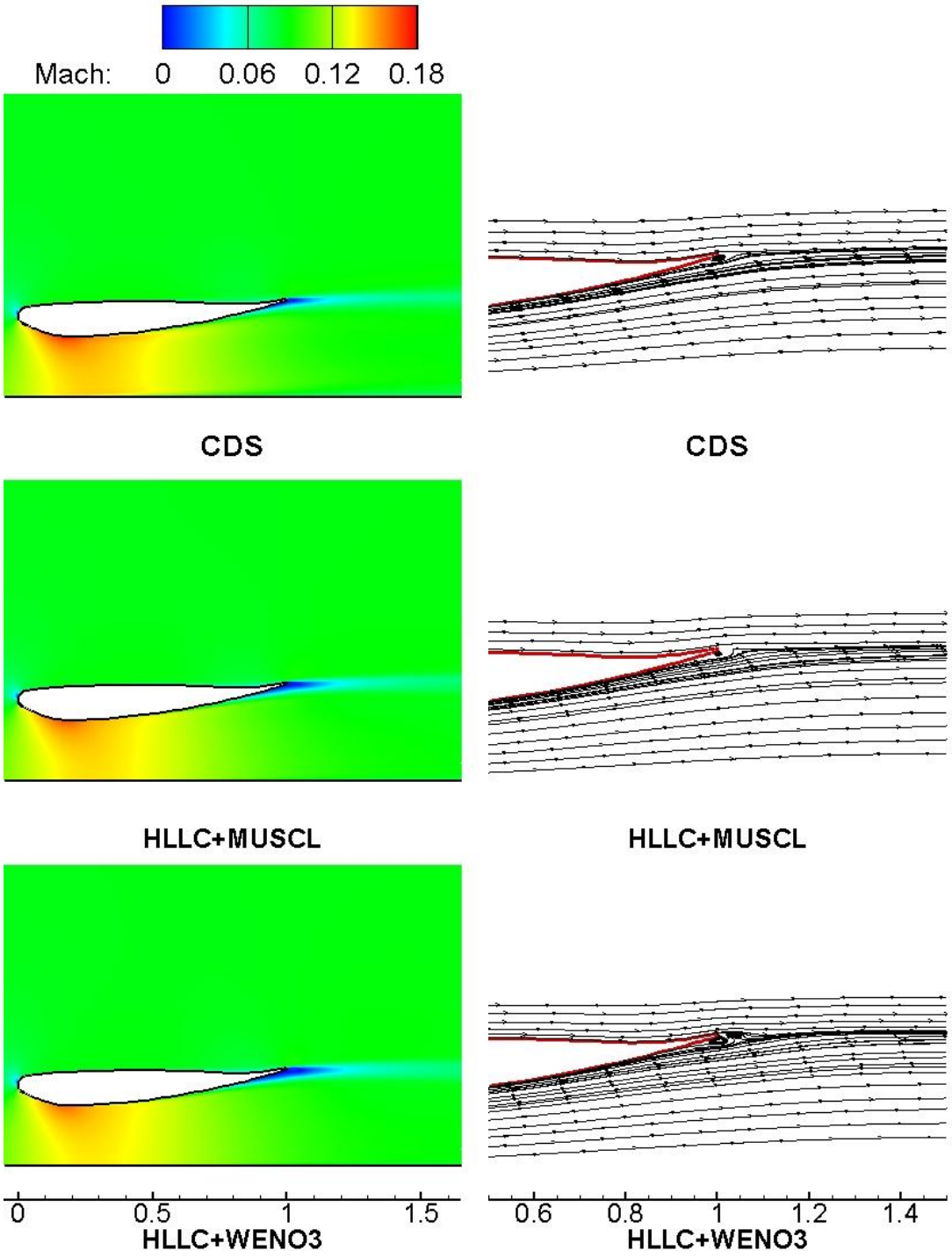

Figure 44: Mach contours and trailing edge streamlines at h/c=0.224

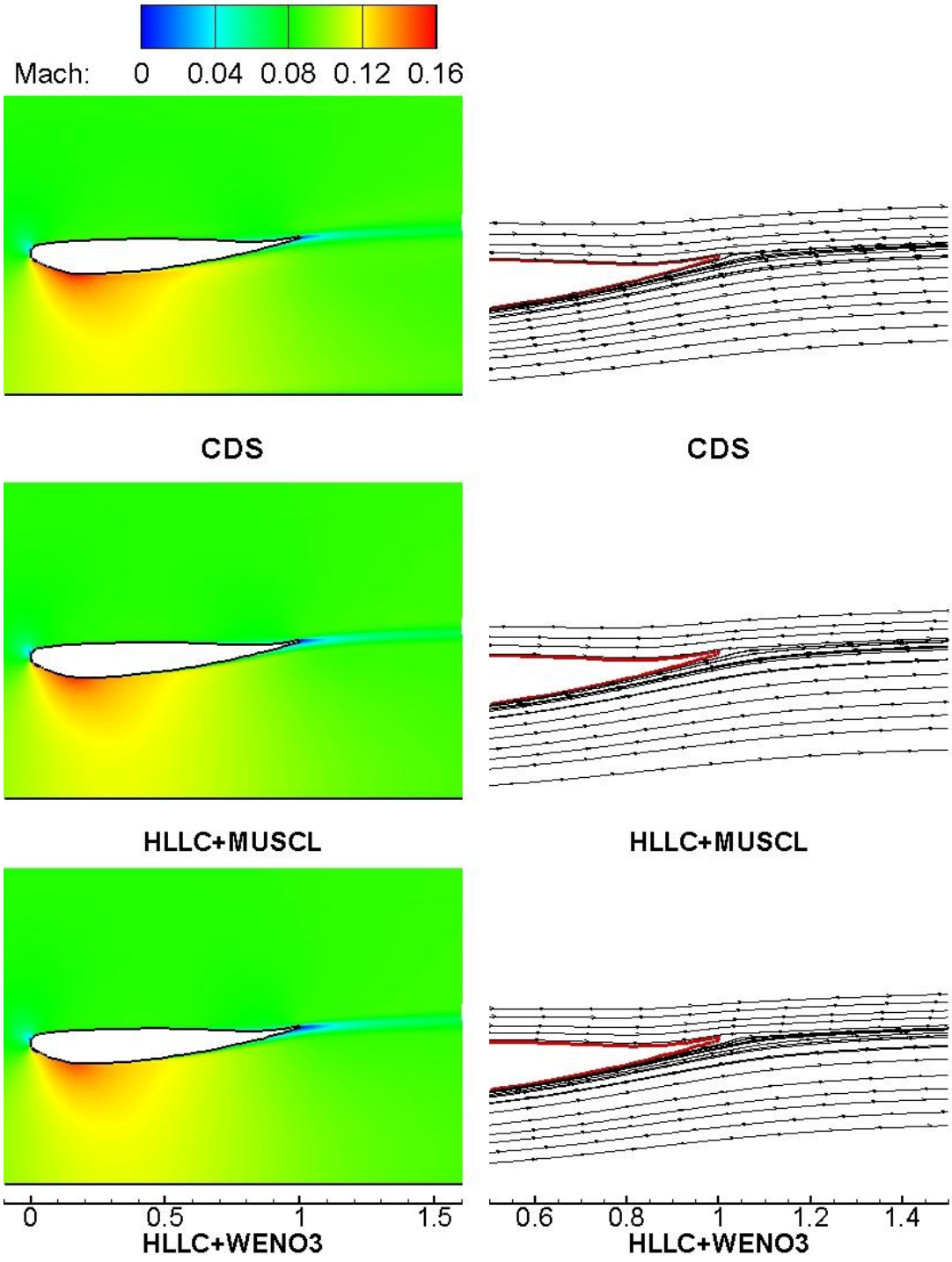

Figure 45: Mach contours and trailing edge streamlines at h/c=0.448

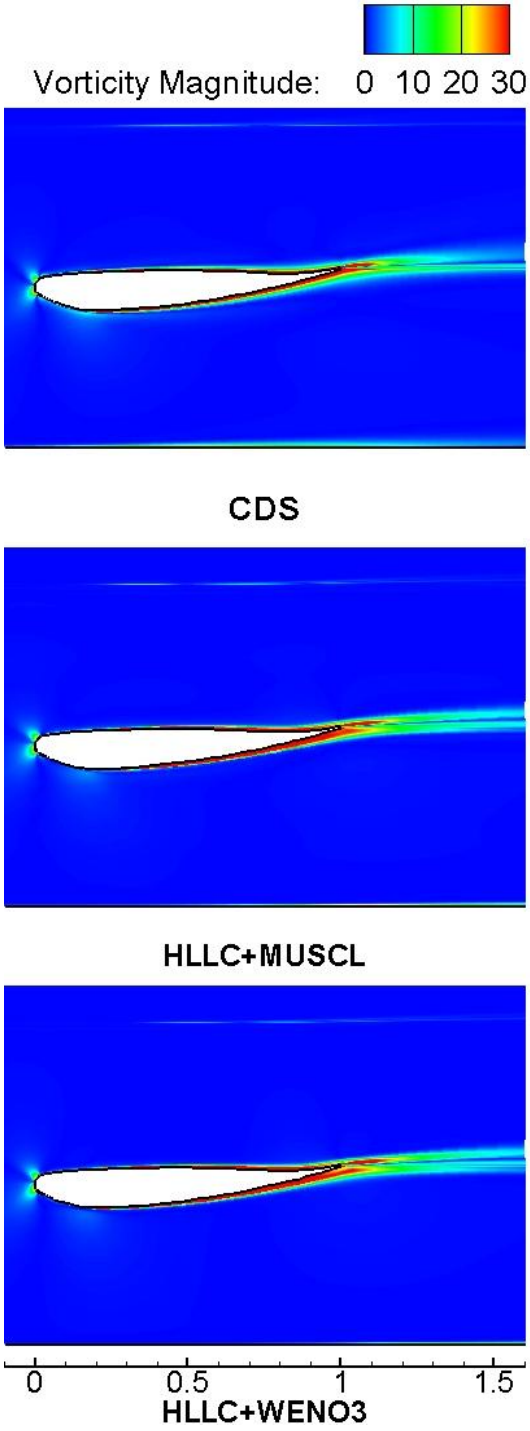

Figure 46: Vorticity magnitude at h/c=0.448

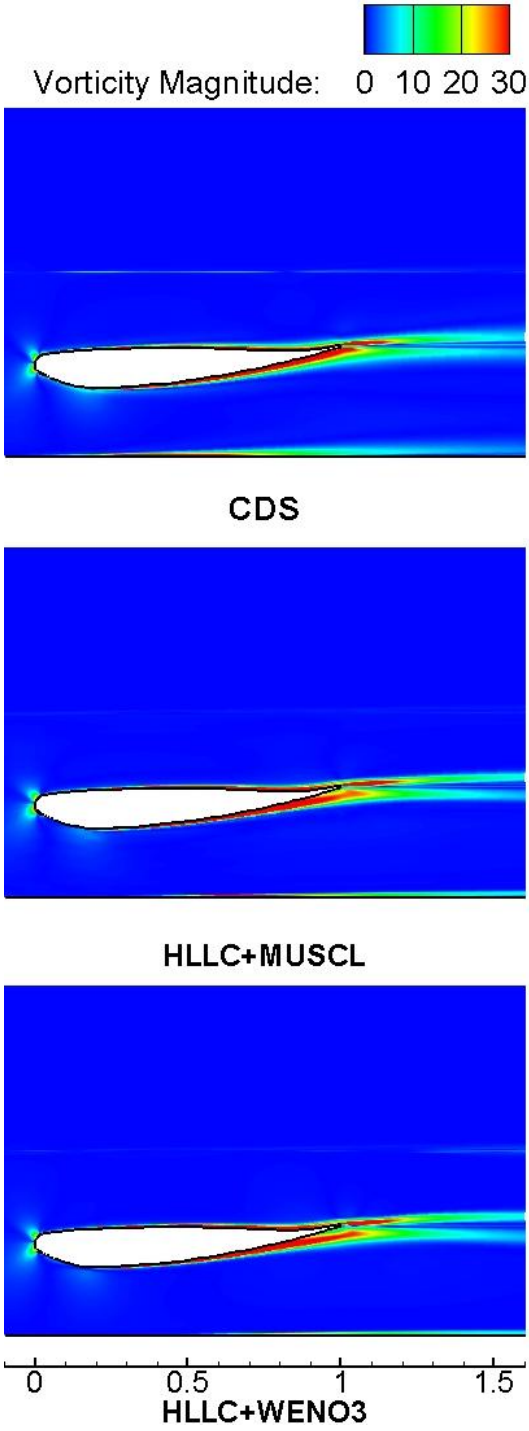

Figure 47: Vorticity magnitude at h/c=0.224

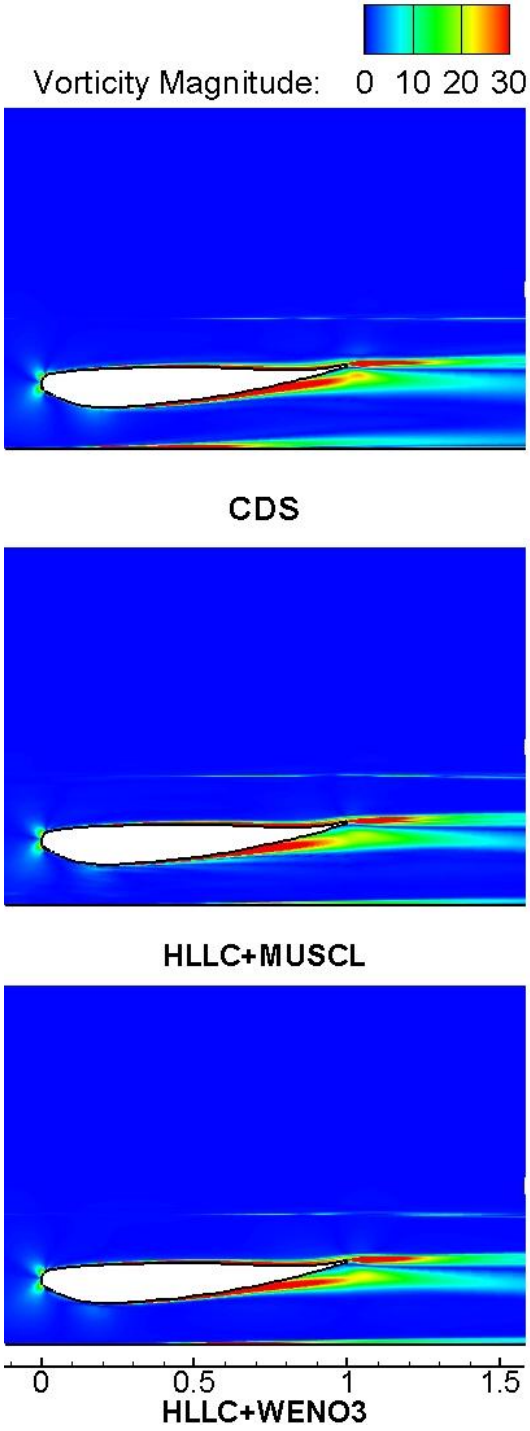

Figure 48: Vorticity magnitude at h/c=0.134

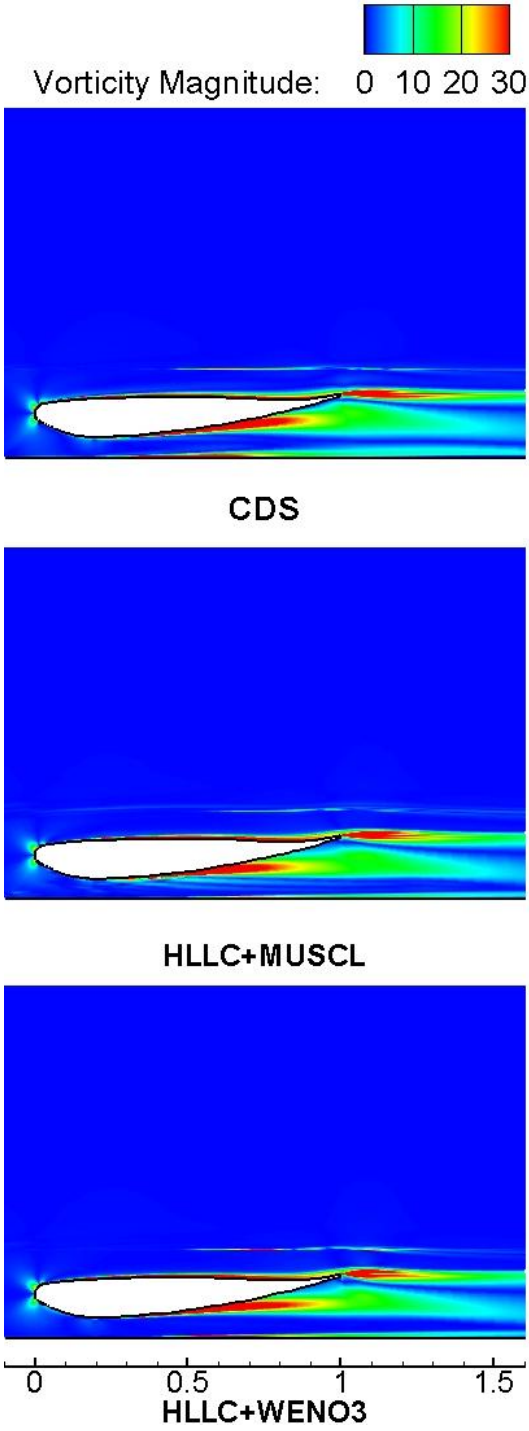

Figure 49: Vorticity magnitude at h/c=0.090

6.1.7 Summary

In this section 6.1, results obtained from using three numerical methods, which are the Jameson's central differencing scheme (CDS), the HLLC solver in conjunction with MUSCL scheme (HLLC + MUSCL) and the WENO 3rd order scheme (HLLC + WENO3), are compared at different heights respectively. The CDS predicts poorer results in the parameters that were discussed above, while its only advantage is the fastest convergence compared to the other schemes. The two high order schemes, HLLC + MUSCL and HLLC + WENO3, present similar but more accurate simulations for all the cases studied. However, they are more expensive computationally. On the other hand, for the most important parameters of the front wing, which are the lift and drag coefficient, the HLLC + WENO3 scheme gives a better result than the HLLC+MUCSL scheme. Moreover, the HLLC + WENO3 scheme shows satisfactory modelling on turbulent flow and vortices capture at low heights. For these reasons, the HLLC + WENO3 scheme is used as a preferred numerical method in the rest investigation.

6.2 Influence of Turbulence Modelling

In this section, three turbulence models are selected to check the influence of turbulence modelling. These are the Spalart-Allmaras (S-A) model, the SST *k-ω* model and the Wilcox *k-ω* model. As it was concluded in the previous section, the favourable HLLC + WENO3 numerical method is used in combination with these turbulence models. Various heights, from *h/c* = 0.090 to *h/c* = 0.671, which will be the same as in the previous section, are employed to investigate with the ground effect.

6.2.1 Convergence Performance

Figures 50 to 67 give the convergence history for comparing the three different turbulence models at six different heights. Both the density residuals and the aerodynamic forces in the computational cycles are shown.

These histories give information that all turbulence models at different heights can be converged after certain computational cycles. However, different schemes present different performances. From these figures, at a lower height between the wing and the ground, such as *h/c* = 0.090 and *h/c* = 0.134, for the same numerical method, all of the turbulence models need a certain computational cycle which is as high as 100000 to reach the convergence level. The simulation using the S-A model and the SST *k-ω* model can achieve nearly a convergence of 10^{-5} in the end, while using the Wilcox *k-ω* model it can only achieve nearly a convergence of 10^{-4}. At higher heights from *h/c* = 0.224 to *h/c* = 0.671, the situation changes. The simulation using the S-A model always attains a good convergence of more than 10^{-5} even nearly 10^{-6} at the two highest heights after 100000 cycles. For the other two equation turbulence models, the density residual would stay at as steady level after certain cycles. At the heights of *h/c* = 0.224 and *h/c* = 0.313, the simulation using the SST *k-ω* model achieves a convergence of 10^{-5} and becomes stable after 70000 cycles. Meanwhile, when using the Wilcox k-ω model only achieves a convergence of 10^{-4} but becomes stable with at 50000 cycles. For higher heights, which are *h/c* = 0.448 and *h/c* = 0.671, the two

equation turbulence models show exactly the same performance on the convergence history of the density residual. Both simulations could achieve a convergence of nearly 10^{-5} and become steady after 50000 computational cycles.

The forces histories of *Cl* and *Cd* indicate that the forces reach a steady level much faster than the density residuals. At higher heights from *h/c* = 0.224 to *h/c* = 0.671, all simulations using the three turbulence models show the fast speed in convergence in the history of *Cl* and *Cd*. They become constant only after about 30000 cycles, which is much faster than the residual density convergence history. When compared to higher heights, lower heights where *h/c* = 0.090 and *h/c* =0.134 are more complex on the forces history. The fluctuate phenomena here are more obvious than that at higher heights due to the smaller distance between the wing surface and the ground. The pressure in this region at lower heights is smaller than at higher heights. Again for all three turbulence models, this fluctuation appears from the beginning, and decreases over the time. Finally simulations using all these models reach the steady condition within about 30000 cycles.

In brief, with the purpose to make every simulation converged, taking also into account that the density residual must be small enough and the forces should stay at a steady level in the mean time, the simulations using the two two-equation turbulence models cost less computational cycles than the other one-equation turbulence model, namely the S-A model. However, the S-A model could achieve better convergence than the other two-equation models on the density residual history.

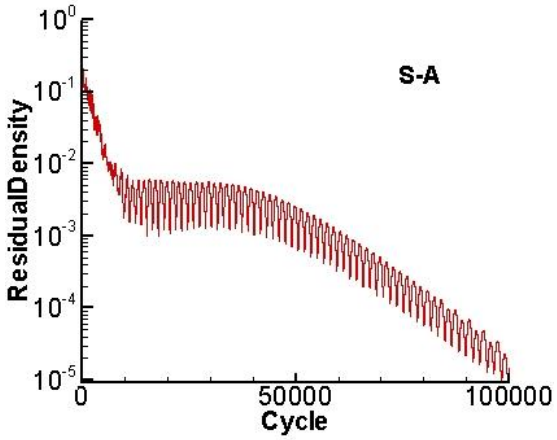

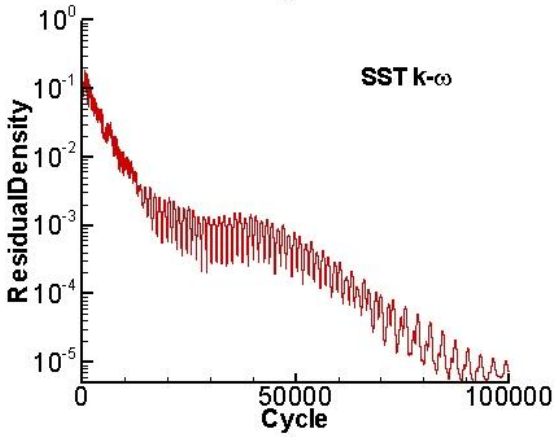

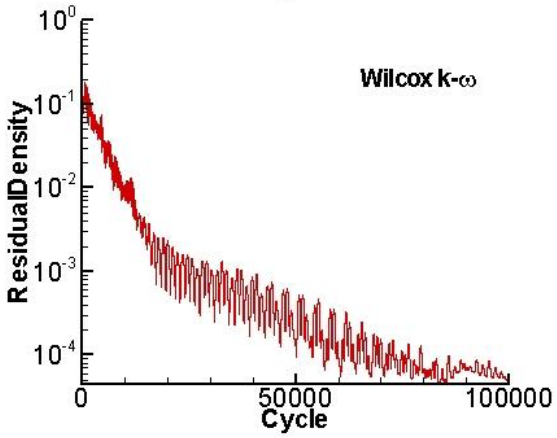

Figure 50: Histroy of density residual at h/c = 0.090

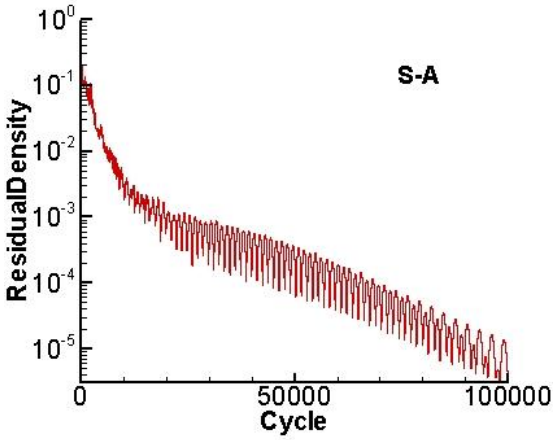

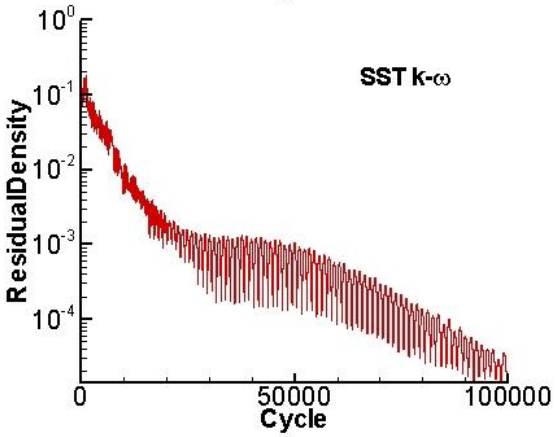

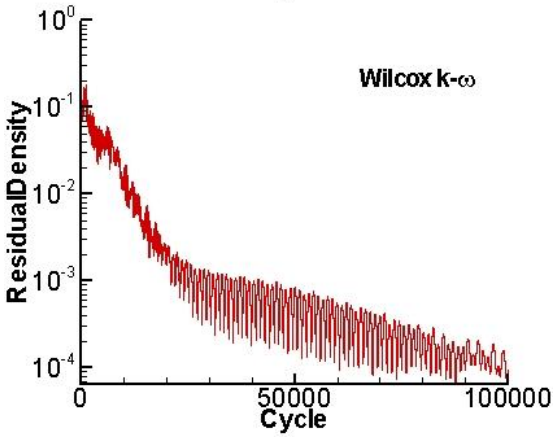

Figure 51: Histroy of density residual at h/c = 0.134

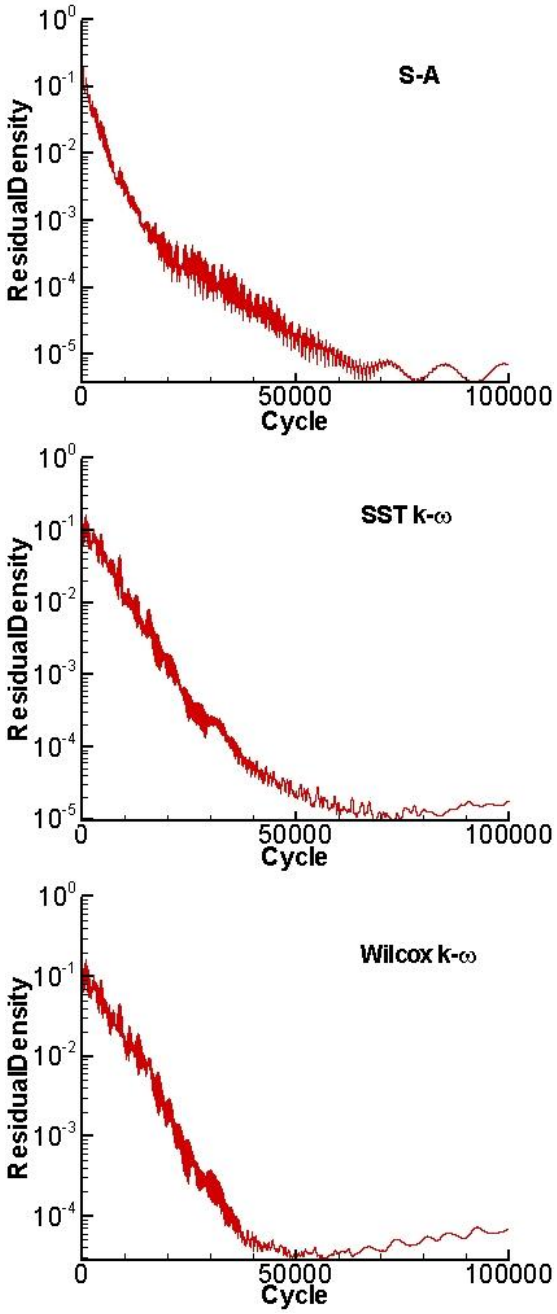

Figure 52: Histroy of density residual at h/c = 0.224

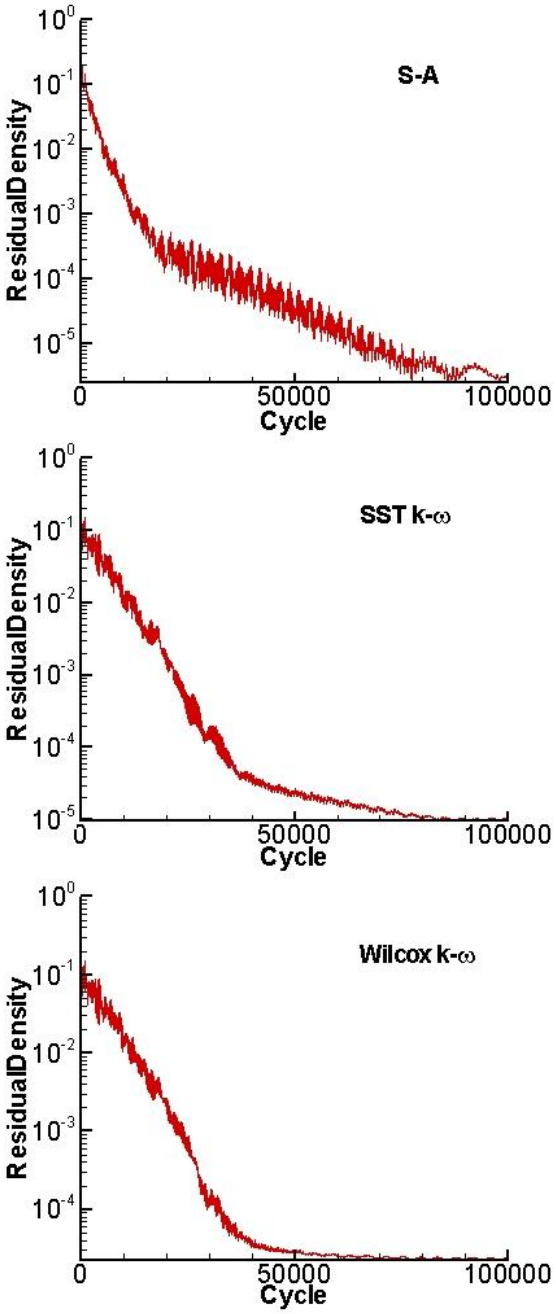

Figure 53: Histroy of density residual at h/c = 0.313

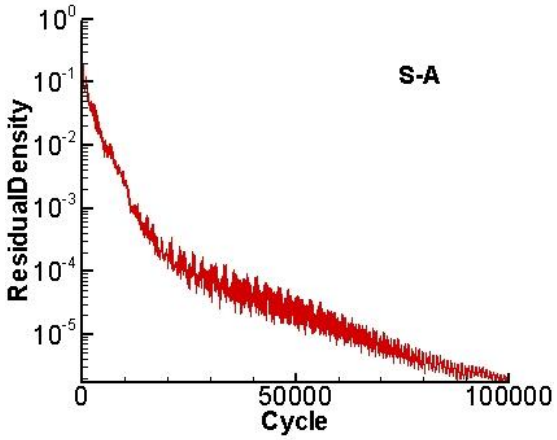

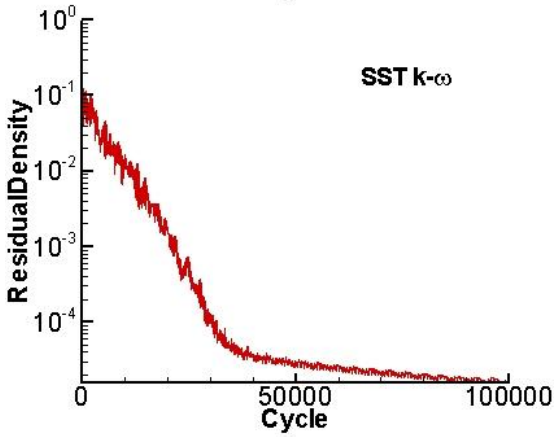

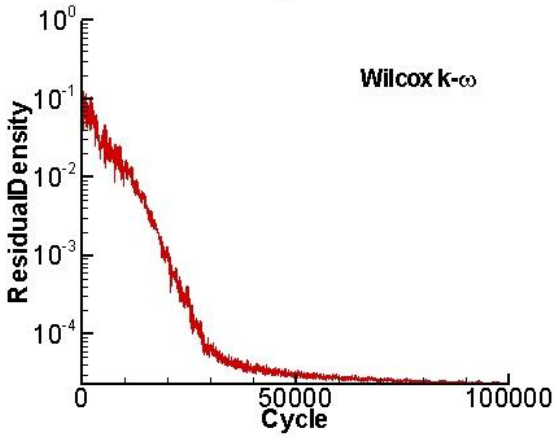

Figure 54: Histroy of density residual at h/c = 0.448

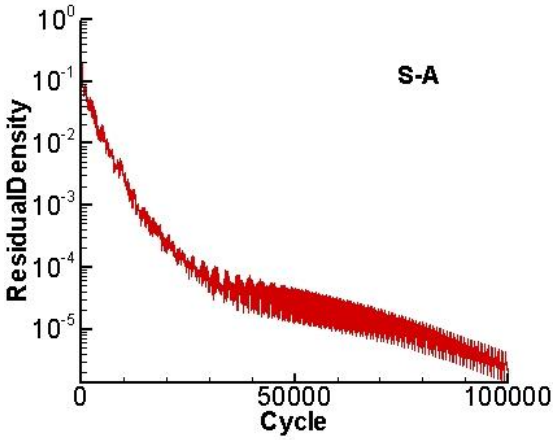

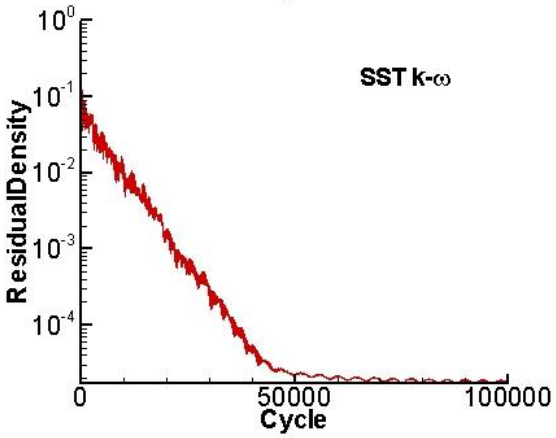

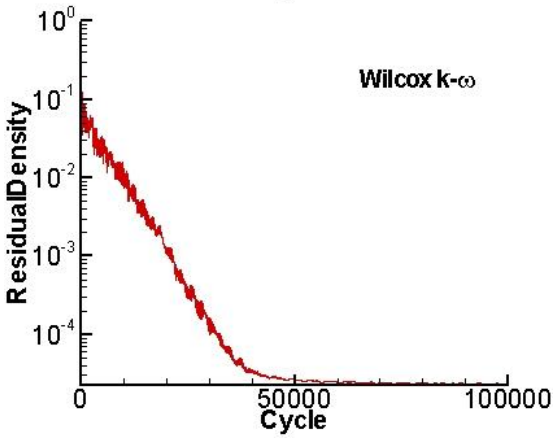

Figure 55: Histroy of density residual at h/c = 0.671

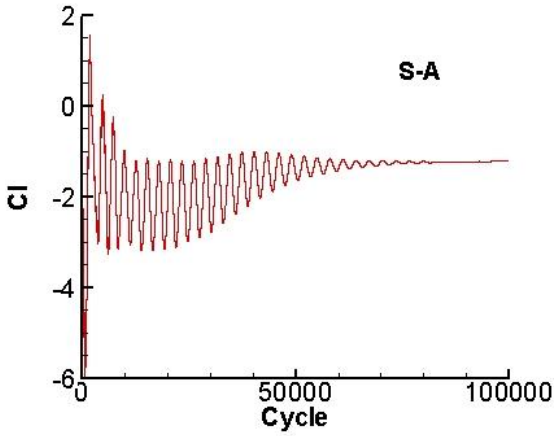

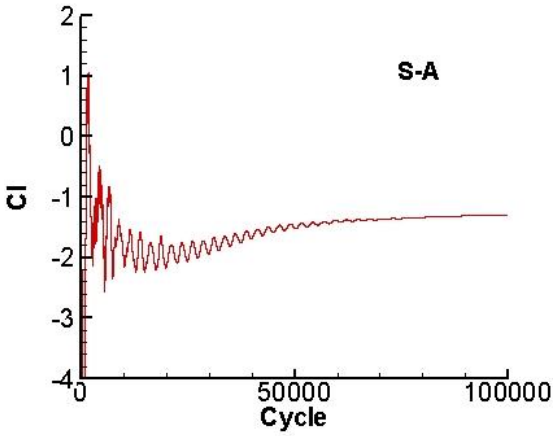

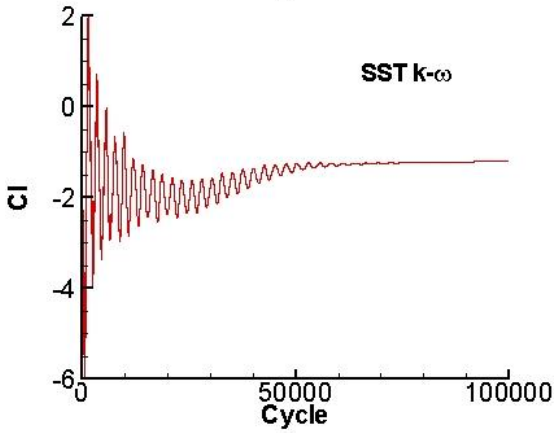

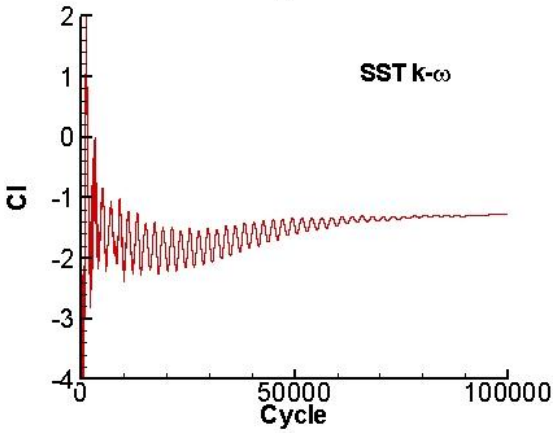

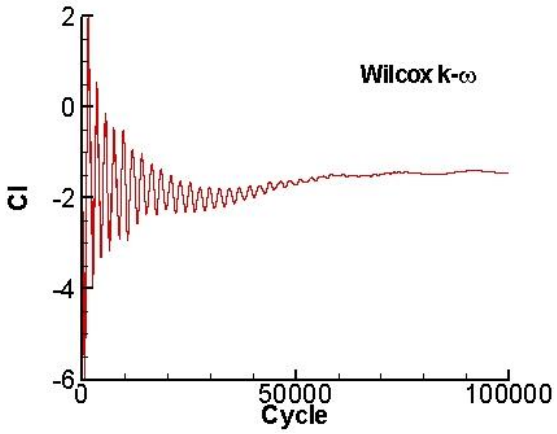

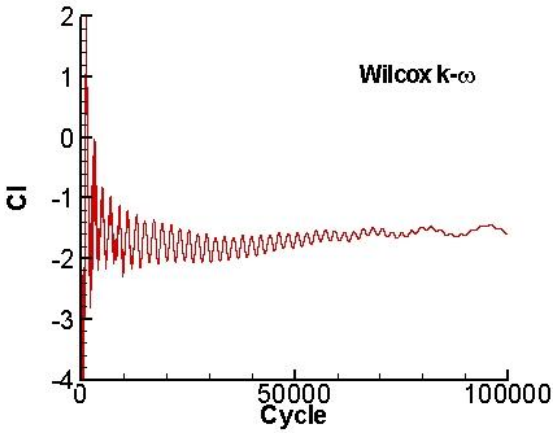

Figure 56: Lift coefficient at h/c = 0.090 Figure 57: Lift coefficient at h/c = 0.134

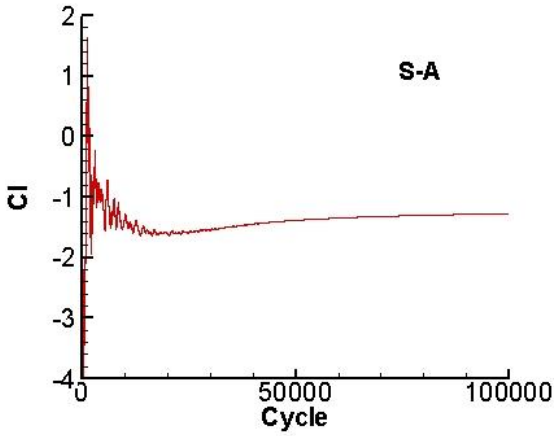

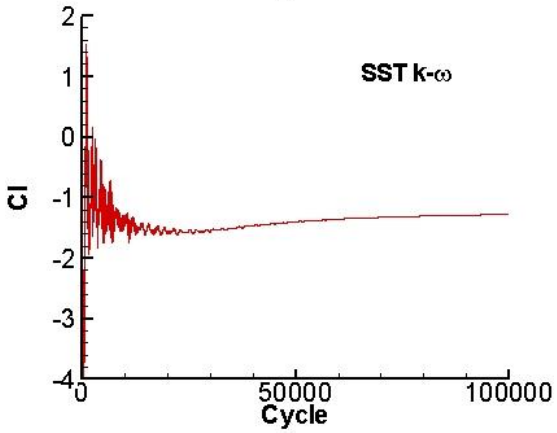

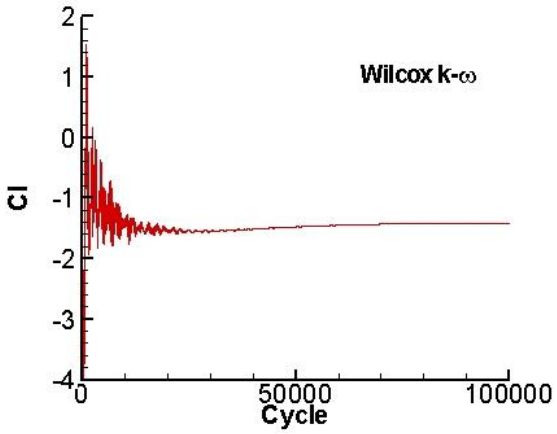

Figure 58: Lift coefficient at h/c = 0.224

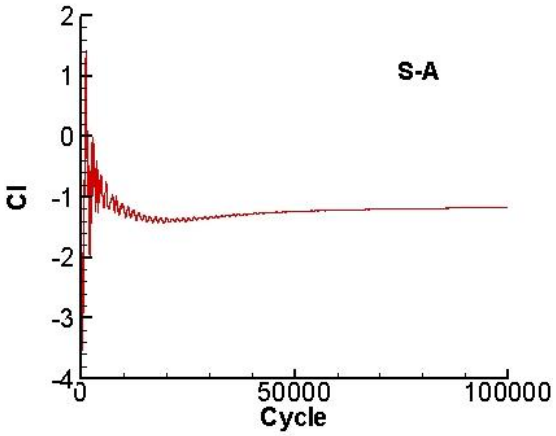

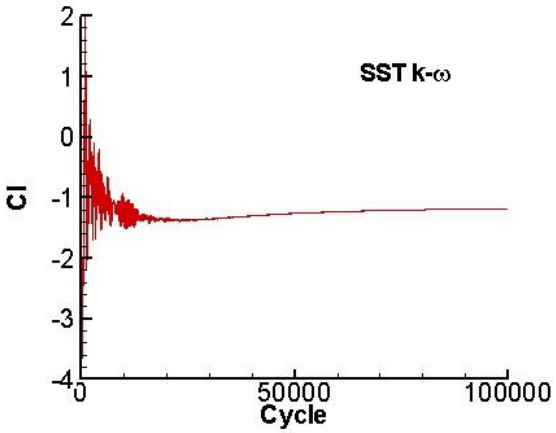

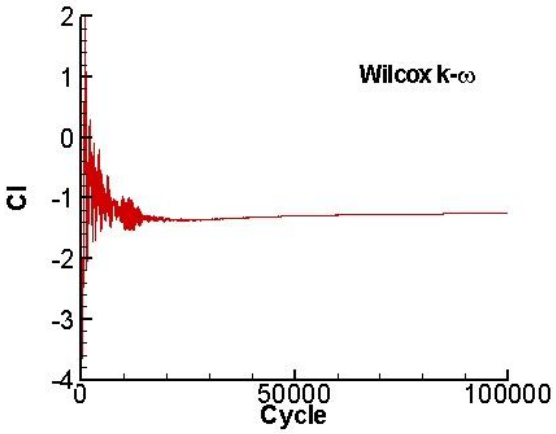

Figure 59: Lift coefficient at h/c = 0.313

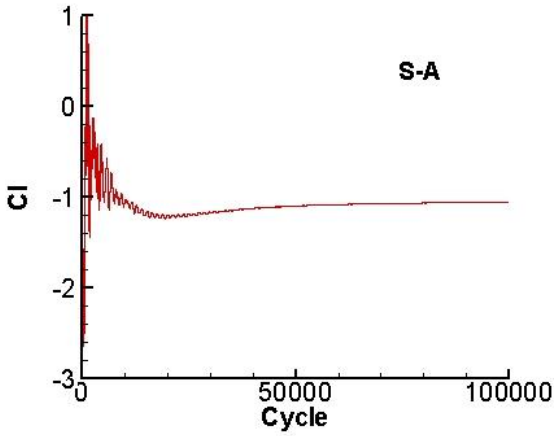

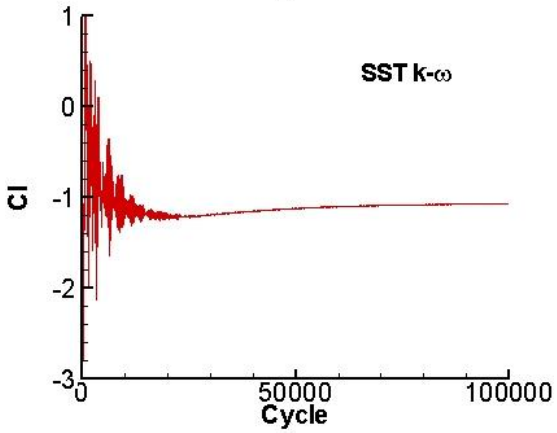

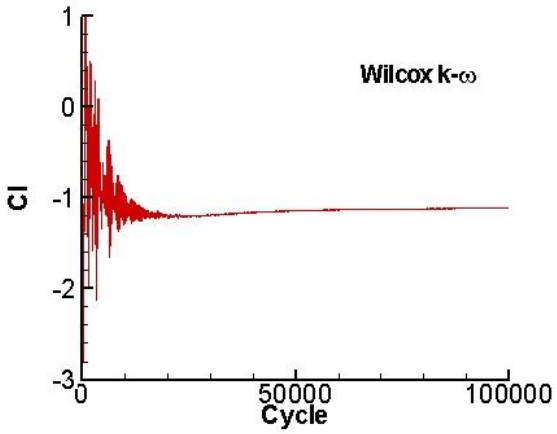

Figure 60: Lift coefficient at h/c = 0.448

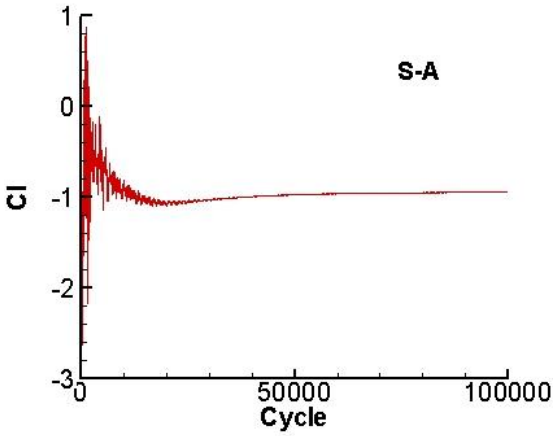

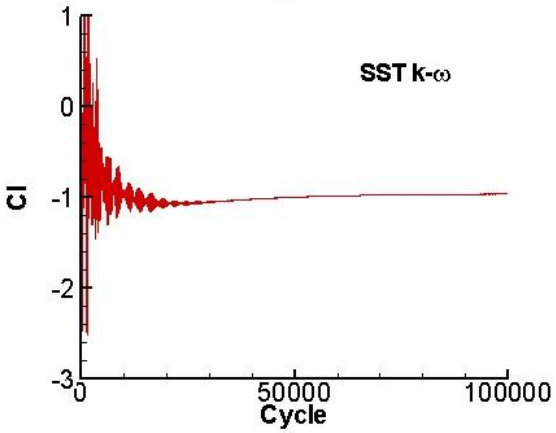

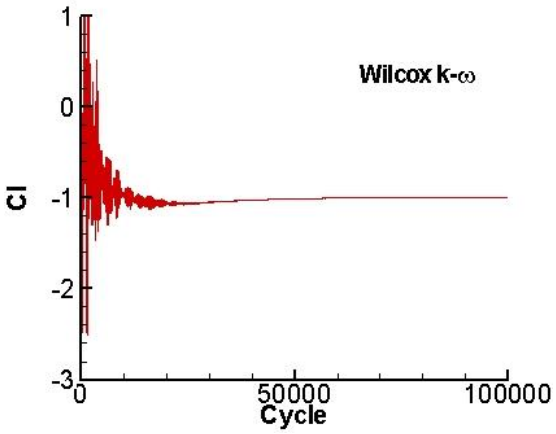

Figure 61: Lift coefficient at h/c = 0.671

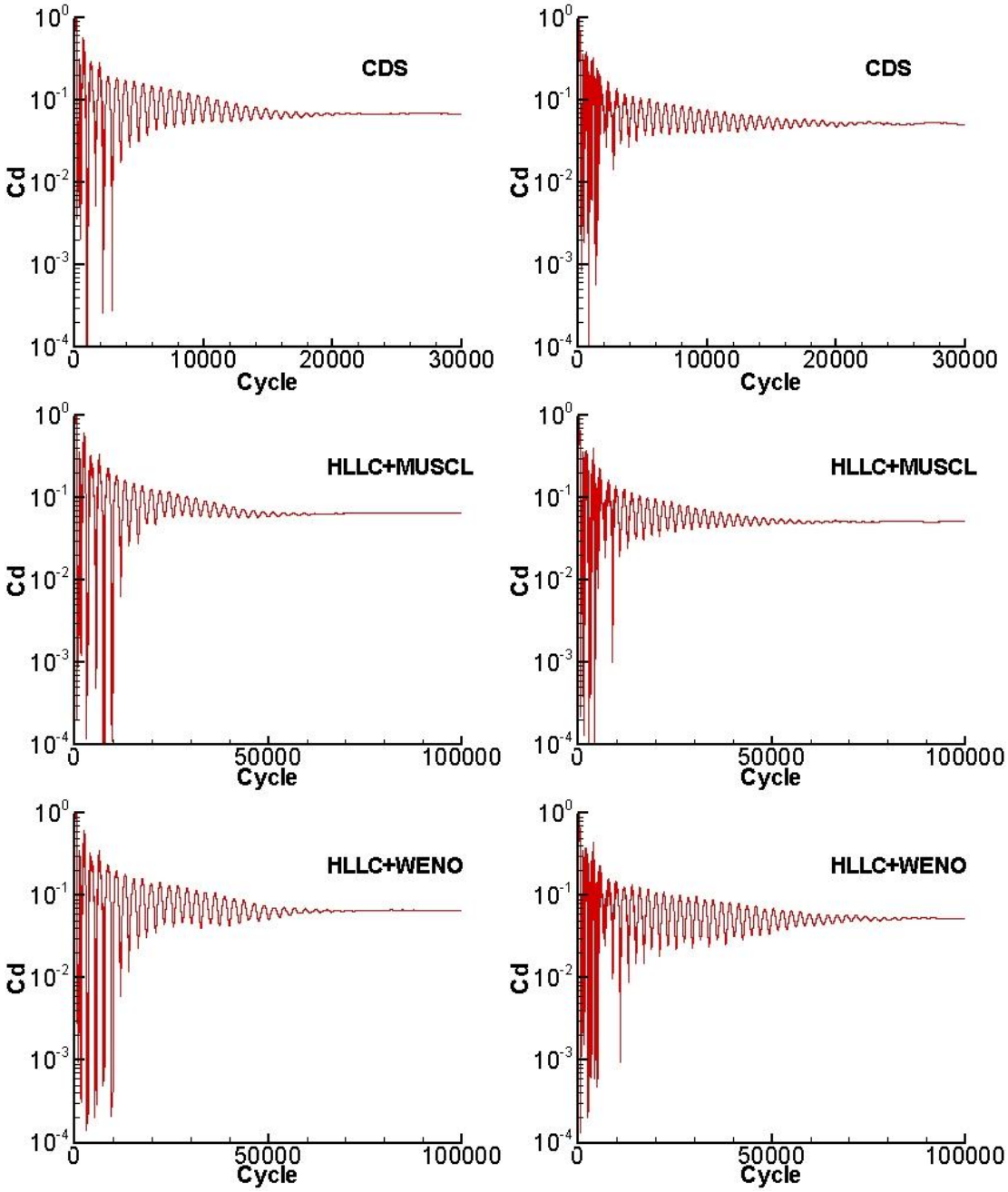

Figure 62: Drag coefficient at h/c = 0.090 Figure 63: Drag coefficient at h/c = 0.134

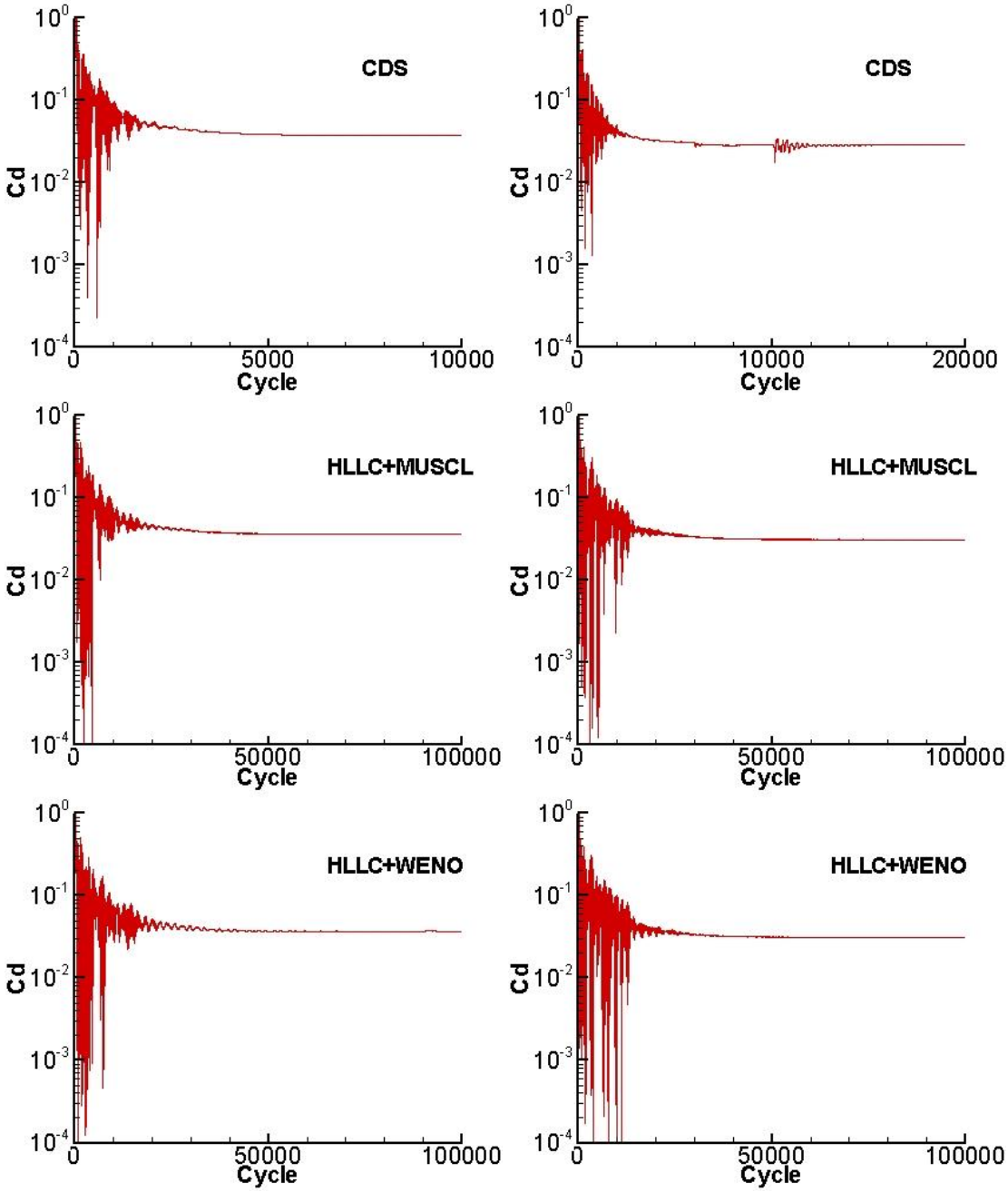

Figure 64: Drag coefficient at h/c = 0.224 Figure 65: Drag coefficient at h/c = 0.313

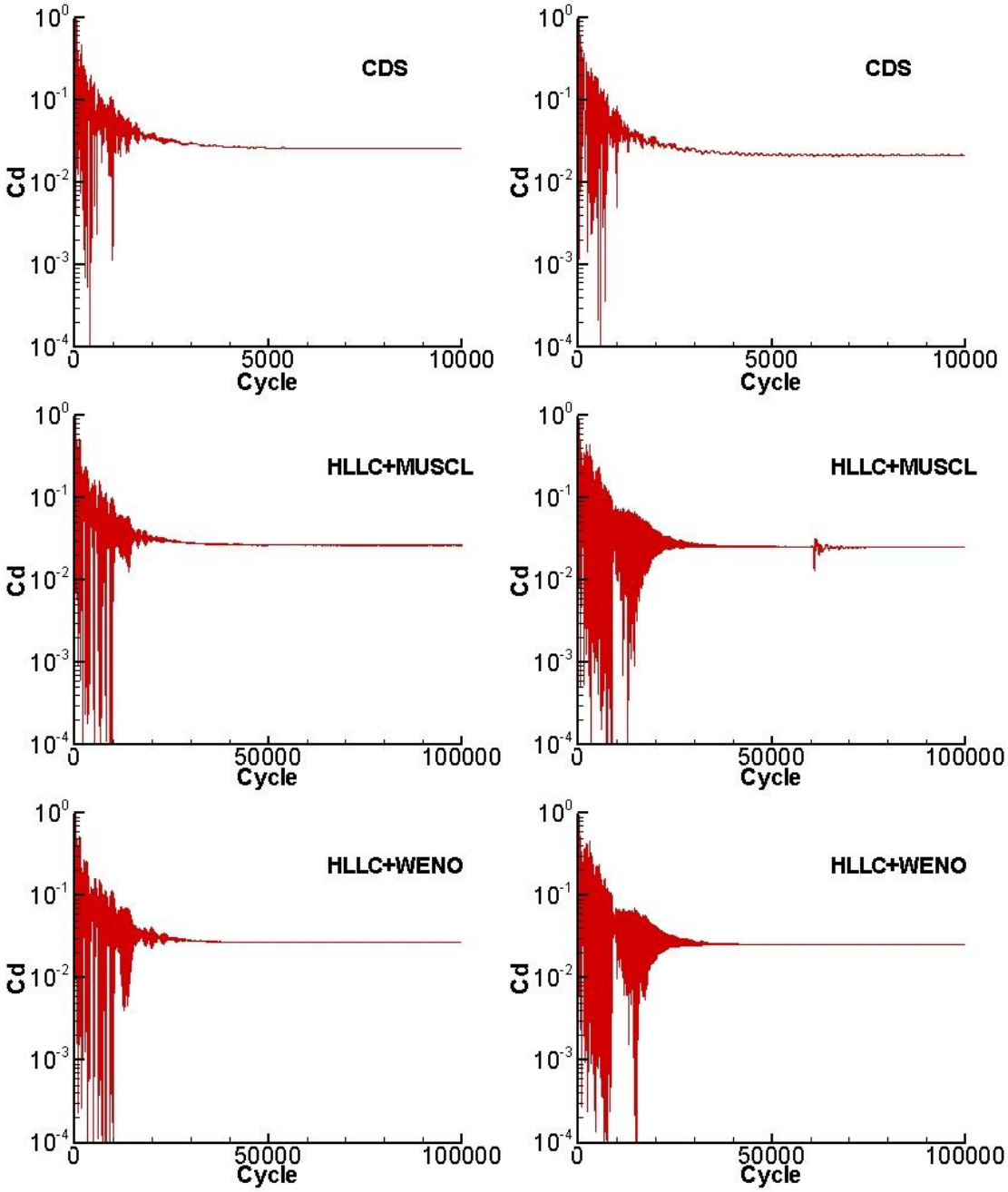

Figure 66: Drag coefficient at h/c = 0.448

Figure 67: Drag coefficient at h/c = 0.671

6.2.2 Coefficient of Pressure (Cp)

The Cp comparison for different turbulence models at various heights with the experimental results is given in Figure 68.

At h/c = 0.671, the three turbulence models resulted in nearly identical Cp on the wing surface. The biggest difference between the computational results and the experimental results appear on the suction surface, from the leading edge to x/c = 0.3, where the suction spike point and the suction peak region are included. All three schemes over predict the Cp there. This can be clearly seen at the peak point at approximately x/c = 0.2. After the peak region and coming to the pressure recovery, from x/c = 0.3 to the trailing edge, all Cp distributions are in very good agreement with the experimental data. The only exception appears at x/c =0.05, where the experiment presents a concave trend while the simulations give convex results. Almost the same general trend over the surface can be found at h/c = 0.448 and h/c = 0.313, see Figure 68(b) and Figure 68(c). However, on the suction surface, the prediction made by using the Wilcox k-ω model is gradually more and more over, compared with the other turbulence models when the front wing approaches the ground.

From h/c =0.224, the S-A and the SST k-ω models still present identical results at all heights. Meanwhile, the difference predicted by the Wilcox k-ω model becomes obvious compared to the other turbulence models. At h/c = 0.224, the S-A and the SST k-ω models give a slight under prediction on the suction surface, though the deficit is very small. However, the Wilcox k-ω model over predicts throughout the whole suction surface compared to the other two schemes. On the pressure surface, the three schemes provide almost the same results. The disparity trend at x/c = 0.05 is slightly smaller than that at a higher height. But the Cp magnitude of simulations from x/c = 0.5 to the trailing edge is a little smaller than in the experiment.

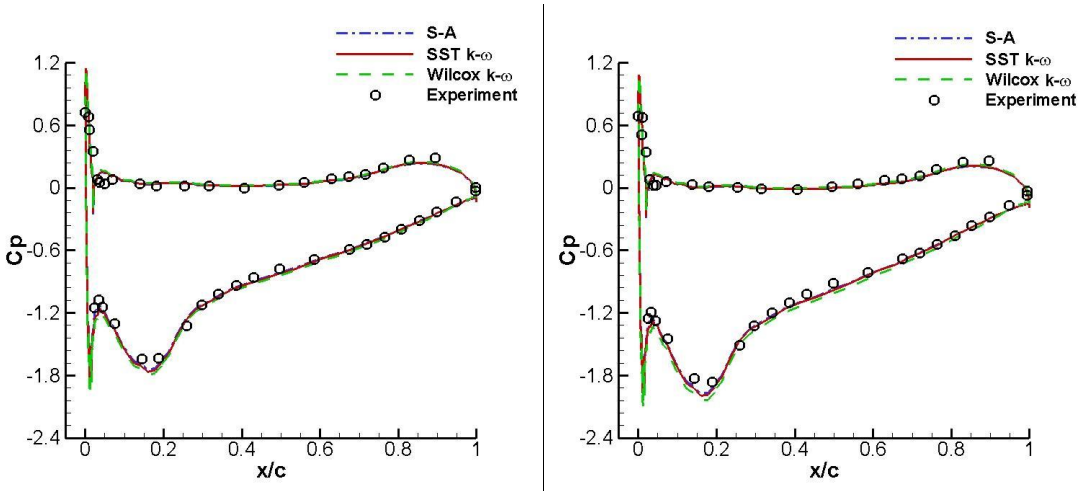

(a) h/c = 0.671 (b) h/c = 0.448

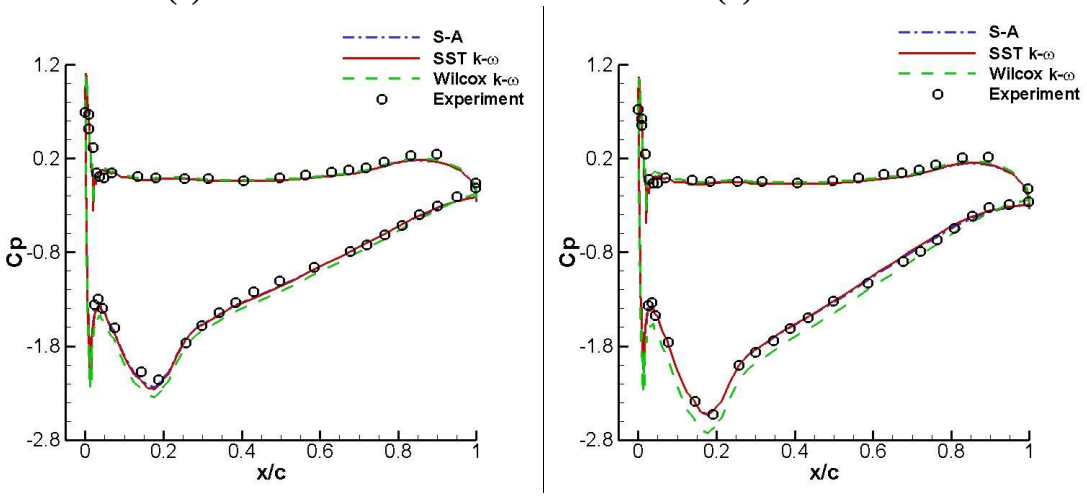

(c) h/c = 0.313 (d) h/c = 0.224

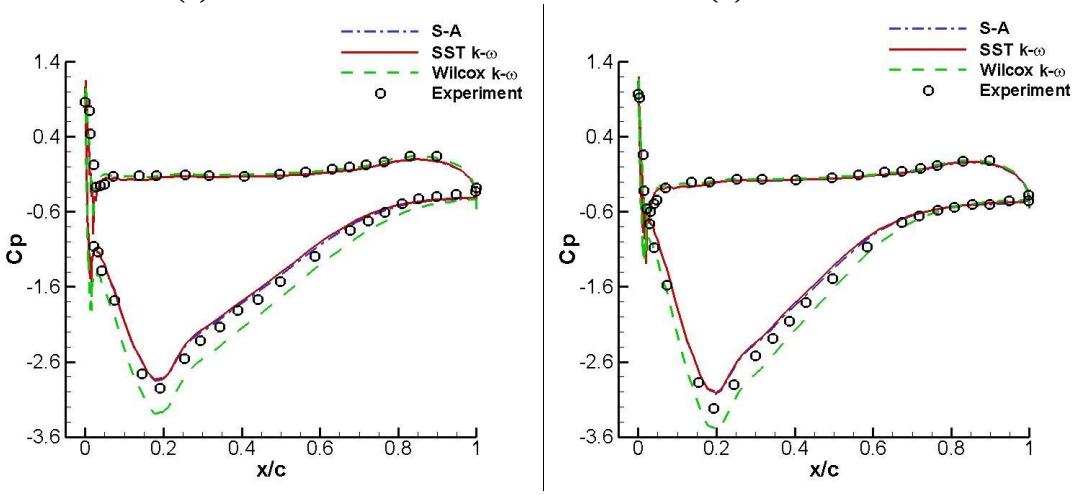

(e) h/c = 0.134 (f) h/c = 0.090

Figure 68: Coefficient of pressure by different turbulence models

At lower height, h/c = 0.134, the S-A and the SST k-ω models further under predict the Cp throughout the suction surface. This under prediction can be observed clearly this time. The Wilcox k-ω model still highly over predicts the Cp throughout the whole suction surface. On the pressure surface, the three schemes agree well with others, as well as the experimental points, and the disparity trend at x/c = 0.05 is going to disappear.

At the lowest height of all the simulations, h/c = 0.090, the disagreement between the computational results and the experimental result is more severe than that at all other heights. The S-A and the SST k-ω models further under predict throughout most of the region on the suction surface. This difference can be clearly observed at the suction peak at x/c = 0.2. The Wilcox k-ω model keeps over predicting the Cp, especially on the suction surface. On the pressure surface, as well as at lower heights, the Cp distributions obtained by all three simulations are all very well predicted compared to the experimental data.

Similar to the problem in section 6.1.2, the pressure at stagnation point is overpredicted by all three turbulence models. However, the S-A model shows a better prediction than the other two-equation models. This from another way proved that the turbulent kinetic energy which is modeled in the eddy viscosity models would probably lead to a result that the maximum pressure coefficient at the stagnation point becomes greater than one.

6.2.3 Lift and Drag Forces

As in section 6.1.3, in this section, the discussion is focused on the comparison among the three turbulence models with the experimental result.

The lift and drag coefficients, which are obtained from using the three different turbulence models at different heights are shown in Table 6 and Table 7. The experimental results are also given in these tables in order to calculate the relative

errors (ERR). Looking more directly, two figures are drawn regarding *Cl* and *Cd* versus heights in Figure 69 and Figure 70, respectively.

From Table 6 and Figure 69, the *Cl* data further proves the conclusion made in the previous section that with the height changing from high to low, the difference between the simulations and the experiment gets smaller. From Figure 69, it can easily be discovered that the S-A and the SST *k-ω* models are nearly unanimous in predicting lifts. At the two lowest heights, *x/c* = 0.134 and *x/c* = 0.090, the results with the S-A and the SST *k-ω* models present a negative difference from the experimental results. Again, these two models show clearly more accurate results than the Wilcox *k-ω* on the simulation with ground effect. Also, in spite of the greatest relative error of the S-A and the SST *k-ω* models found in Table 6, which is less than 7%, the relative error of the SST k-ω model is slightly smaller than the S-A model.

It can be observed that almost all the predictions from the three turbulence models give negative results at all different heights in Table 7 and Figure 70. From Figure 70, it can be found that the S-A model is nearly the same as the experimental points in predicting drags. The SST *k-ω* model gives under predictions throughout all heights. The Wilcox *k-ω* model models well at the two lowest height which are *h/c* = 0.090 and *h/c* = 0.134, but after the height *h/c* = 0.224, it joins the SST *k-ω* model to give nearly the same under prediction as the latter.

h/c	0.671	0.448	0.313	0.224	0.134	0.090
Experiment	0.902	1.009	1.145	1.286	1.385	1.371
S-A	0.967	1.066	1.184	1.296	1.361	1.308
SST *k-ω*	0.961	1.066	1.182	1.29	1.365	1.314
Wilcox *k-ω*	0.987	1.109	1.251	1.407	1.506	1.452
ERR(S-A)	7.21%	5.65%	3.41%	0.78%	-1.73%	-4.60%
ERR(SST *k-ω*)	6.54%	5.65%	3.23%	0.31%	-1.44%	-4.16%
ERR(Wilcox *k-ω*)	9.42%	9.91%	9.26%	9.41%	8.74%	5.91%

Table 6: Lift coefficients for turbulence models

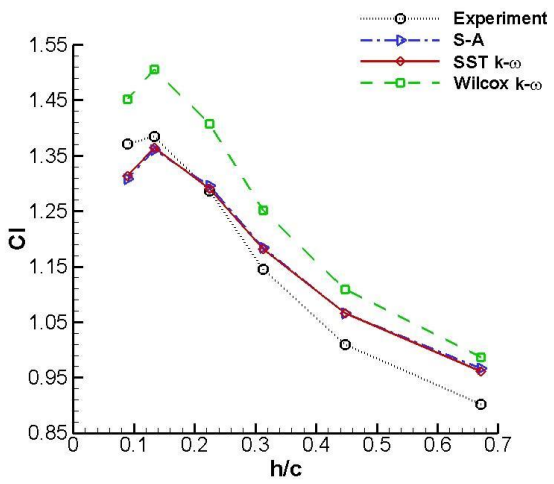

Figure 69: Lift coefficients at different heights for turbulence models

h/c	0.671	0.448	0.313	0.224	0.134	0.090
Experiment	0.0277	0.0317	0.0348	0.0425	0.0558	0.0689
S-A	0.0289	0.0307	0.0357	0.0417	0.0581	0.0720
SST *k-ω*	0.0256	0.0270	0.0316	0.0369	0.0526	0.0667
Wilcox *k-ω*	0.0258	0.0272	0.0316	0.0359	0.0589	0.0666
ERR(S-A)	4.33%	-3.15%	2.59%	-1.88%	4.12%	4.50%
ERR(SST *k-ω*)	-7.58%	-14.83%	-9.20%	-13.18%	-5.73%	-3.19%
ERR(Wilcox *k-ω*)	-6.86%	-14.20%	-9.20%	-15.53%	5.56%	-3.34%

Table 7: Drag coefficients for different turbulence models

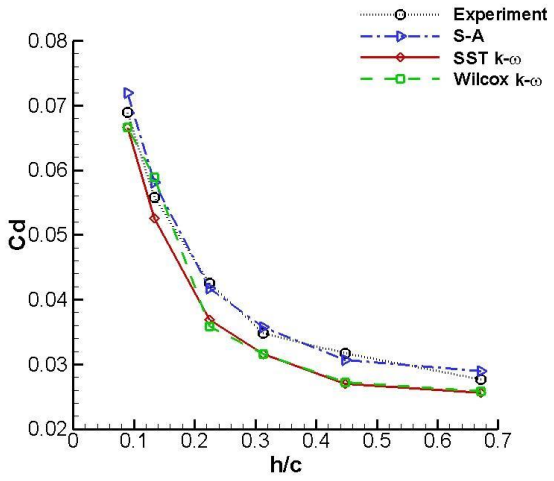

Figure 70: Drag coefficients at different heights for turbulence models

6.2.4 Velocity Profile at the Trailing Edge

Velocity profiles inside the boundary layer are taken at the trailing edge where x/c = 1.0 on the suction surface, the same condition as in section 6.1.4. Again, three different heights are brought into comparison, namely h/c = 0.067, h/c = 0.224 and h/c = 0.448.

Figure 71(a) shows the computational results of three different turbulence models with the experimental result, for u/U_∞ at h/c = 0.067. The S-A and the SST k-ω models give nearly the same result, while the Wilcox k-ω model has a very different prediction. All three models show a negative velocity region (the same as the experimental results). This will lead to a separation flow at the trailing edge. Through the boundary layer, the S-A and the SST k-ω models appear more close to the shape of the experimental results. However, the velocity predicted by the two models is consistently smaller, approximately 0.3 lower for the u/U_∞ than the experimental results. Due to this reason, the computational simulations of the S-A and the SST k-ω models show a smaller separation region than the experiment. With regards to the Wilcox k-ω model, this even gives under prediction on the velocity close to the surface. As the distance grows, the velocity of u/U_∞ becomes significantly lower than the experiment, even 0.2 smaller than the other two models throughout the whole boundary layer. So the boundary layer is the thinnest among the three models.

At h/c = 0.134 (Figure 71(b)), the results from the S-A and the SST k-ω models present clearly a separated boundary layer, while the results from the Wilcox k-ω model does not. The SST k-ω model agrees well with the experimental data from the surface where η/c = 0.015 to η/c = 0.045 while a slight deviation appears from η/c = 0.045 to η/c = 0.074. The S-A model shows an under prediction on u/U_∞ near the surface by 0.1 and keeps it throughout the whole boundary. It is disappointing to find that the Wilcox k-ω model has a similar manner to the result at h/c = 0.067. The velocity magnitude of u/U_∞ reaching almost 0.2, is lower through the boundary layer compared with the experiment.

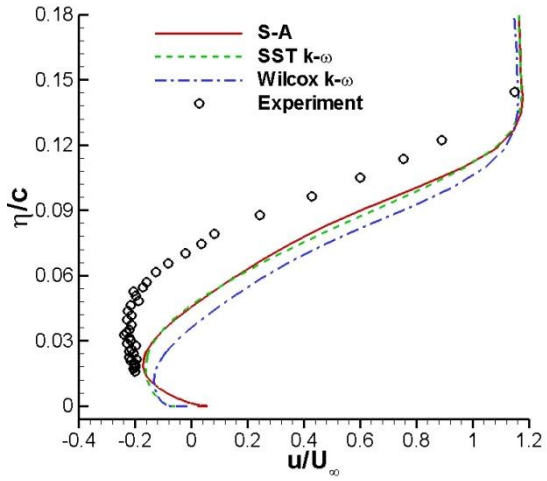

(a) h/c=0.067

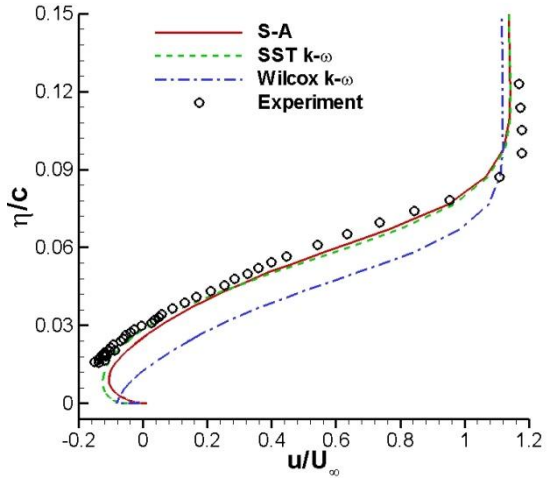

(b) h/c=0.134

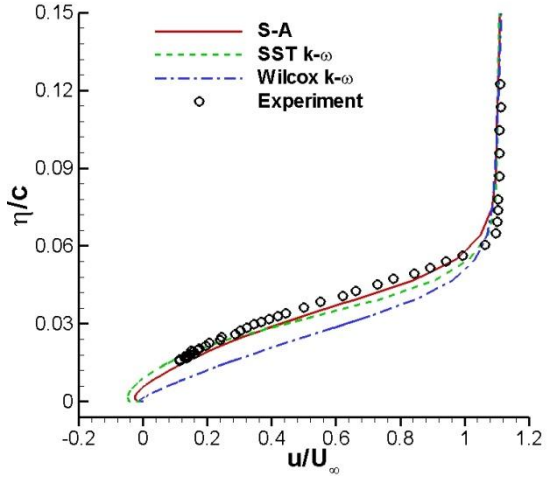

(c) h/c=0.224

Figure 71: Boundary layer on suction surface at the trailing edge

For the results at h/c = 0.224, which is illustrated in Figure 71(c), the greatest difference compared to the two other lower heights is found very close to the suction surface where η/c = 0.015. All the results from three models have a positive velocity, as the flow attached. Besides this difference, at this height, all the models present the same trend as at h/c = 0.134.

6.2.5 Wake Analysis

To study the results in the wake of different turbulence models, the comparisons are still split into the nearfield and the farfield wake.

Nearfield wake

In the nearfield wake, the investigation is focused on two streamwise locations: x/c = 1.2 and x/c = 1.5. Three different heights are compared; these are: x/c = 0.134, x/c = 0.224 and x/c = 0.448. The simulation results which are compared with the experimental velocity results for both locations are plotted at different heights. Information on the wake thickness and the ground boundary layer from the computations and the experiment is given in Table 8.

At the height of h/c = 0.134, the wake comparison at x/c = 1.2 and x/c = 1.5 are shown in Figure 72(a) and Figure 72(b). The S-A and the SST k-ω models show similar results at x/c = 1.2. The main wake is a little thicker for all models and the velocity u/U_∞ at the wake centre according to these three models are about 0.1 lower than the experimental results. At x/c = 1.5, it can be easily seen from the figure that the velocity in the wake centre is severely under predicted for all models. The wake thickness at this location is slightly smaller than the experiment for all models. For the ground boundary layer, the CDS gives an increased thickness than the other schemes at both streamwise locations. At x/c =1.5, the S-A and the SST k-ω models over predict the velocity deficits of the ground boundary layer. Between the main wake and the ground boundary layer, the Wilcox k-ω model fails to predict velocity compared to

the other two models at both locations.

For the results at h/c = 0.224, the wake comparisons at x/c = 1.2 and x/c = 1.5 are shown in Figure 72(c) and Figure 72(d). At x/c = 1.2, all three models are well modelled on the thickness of the main wake, while the Wilcox k-ω model presents slightly thicker wake. Meanwhile, all three models have a nearly 0.1 lower prediction for the velocity u/U_∞ at the wake centre, (the same situation as at h/c = 0.134), compared to the experimental data. At x/c = 1.5, the SST k-ω model gives exactly the same thickness of the main wake with the experimental results, while the other models present a little thicker. However, all three schemes still under predict the velocity u/U_∞ of the wake centre, as same as at h/c = 0.134. But the difference is much smaller, only about 0.05 lower than the experimental results for the SST k-ω model, compared to $u/U_\infty \approx 0.2$ at h/c = 0.134. For the ground boundary layer, all three models give good results at both streamwise locations. However, this time at x/c =1.5, the S-A and the SST k-ω models under predict the velocity deficits of the ground boundary layer.

Coming to a higher height at h/c = 0.448 (Figure 72(e) and Figure 72(f)), the results from using the three models agree with each other well at both streamwise locations; the only difference is in the wake centre at x/c = 1.5. All three modles model well the thickness of the main wake. The velocity of the wake centre is still under predicted according to the computations. At x/c = 1.5, the SST k-ω model shows a better prediction on the velocity of the wake centre. All the thickness of the ground boundary layer from these models is significantly closer to the experimental points.

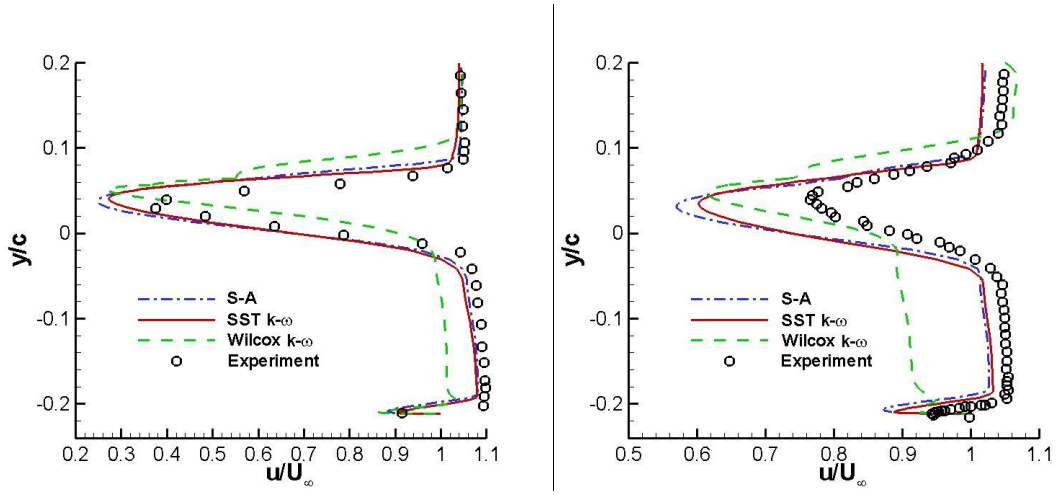

(a) x/c=1.2, h/c=0.134

(b) x/c=1.5, h/c=0.134

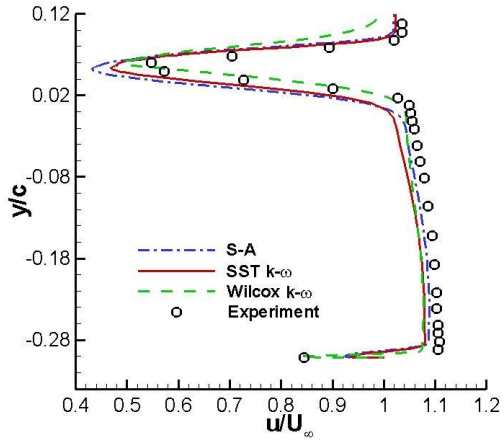

(c) x/c=1.2, h/c=0.224

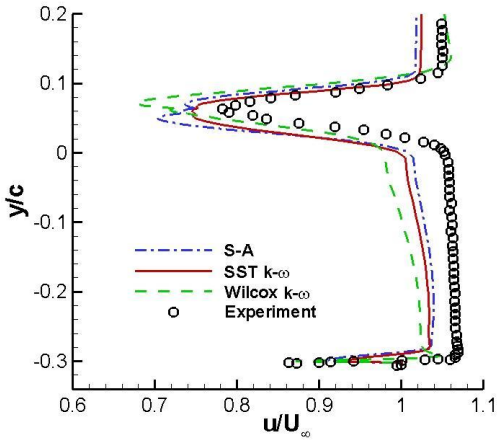

(d) x/c=1.5, h/c=0.224

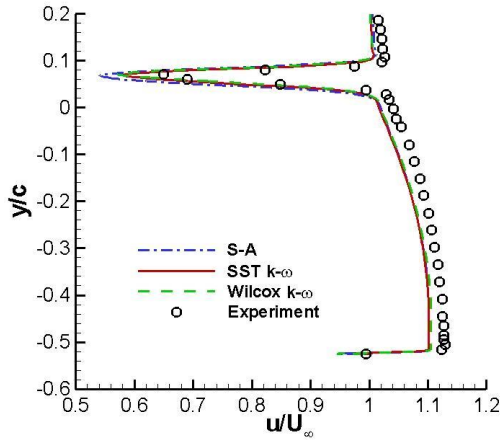

(e) x/c=1.2, h/c=0.448

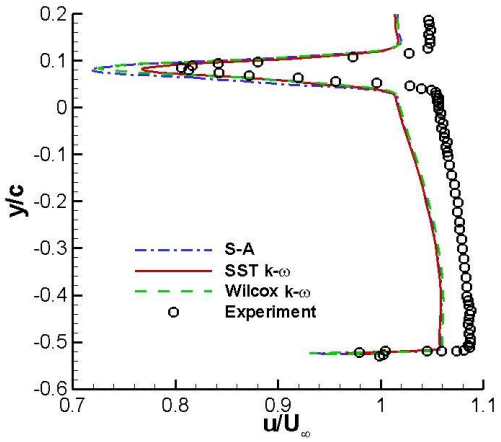

(f) x/c=1.5, h/c=0.448

Figure 72: Wake profiles at x/c = 1.2 and x/c = 1.5

h/c	Schemes	$u_{min}/U\infty$	y/c at u_{min}	y at δ_{top}	y at δ_{bottom}	δ_{99}/c
0.090	Experiment	0.72	0.02	0.12	-0.10	0.22
	CDS	0.52	0.03	0.09	-0.09	0.18
	HLLC + MUSCL	0.52	0.02	0.08	-0.08	0.16
	HLLC + WENO3	0.52	0.02	0.08	-0.08	0.16
0.134	Experiment	0.77	0.04	0.12	-0.05	0.17
	CDS	0.61	0.04	0.10	-0.05	0.15
	HLLC + MUSCL	0.62	0.04	0.09	-0.05	0.14
	HLLC + WENO3	0.60	0.03	0.09	-0.05	0.14
0.224	Experiment	0.79	0.07	0.13	0.01	0.12
	CDS	0.74	0.07	0.14	-0.01	0.15
	HLLC + MUSCL	0.75	0.07	0.12	0.01	0.11
	HLLC + WENO3	0.75	0.06	0.11	-0.01	0.12
0.313	Experiment	0.81	0.08	0.13	0.04	0.09
	CDS	0.75	0.07	0.14	0.02	0.12
	HLLC + MUSCL	0.77	0.08	0.12	0.03	0.09
	HLLC + WENO3	0.76	0.07	0.11	0.02	0.09
0.448	Experiment	0.81	0.08	0.13	0.04	0.09
	CDS	0.81	0.08	0.16	0.02	0.14
	HLLC + MUSCL	0.78	0.08	0.14	0.04	0.10
	HLLC + WENO3	0.77	0.08	0.13	0.03	0.10

Table 8: Wake information for experimental and computational results at x/c = 1.5

The Farfield Wake

In the farfield wake, the investigation is focused on two streamwise locations: *x/c* = 2.0 and *x/c* = 3.0. Results at three different heights are brought into comparison, which are *x/c* = 0.067, *x/c* = 0.224 and *x/c* = 0.448. The simulation results which are compared with the experimental velocity results for both locations are figured at different heights. The information on the wake thickness from the computations and the experiment is presented in Tables 9 and 10.

At the lowest height at h/c = 0.067, the wake comparison at x/c = 2.0 and x/c = 3.0 are shown in Figure 73(a) and Figure 73(b). From the figures, the wake has been combined with the ground boundary layer, especially at x/c = 0.3. The thickness of the wake does not appear in the table because it is not strictly valid. All three turbulence models show similar results, but they all considerably different from the experimental profile, especially for the Wilcox k-ω model. The velocity at the wake centre at both locations according to the three schemes is lower than the experimental results. For the ground boundary layer, due to the mergence between the wake and the ground boundary layer, all the models again under predict the velocity deficits of the ground boundary layer.

For the results at h/c = 0.224, the wake comparson at x/c = 2.0 and x/c = 3.0 are shown in Figure 73(c) and Figure 73(d). All three models give an agreement to model slightly thinner on the thickness of the main wake. Meanwhile, at x/c = 2.0, all three models have about 0.06 lower prediction for the velocity u/U_∞ at the wake centre, even extending to the outside of the wake, compared to the experimental data. At x/c = 1.5, an obvious apophysis has emerged inside the wake according to the computations. This leads to about 0.05 lower in modelling the velocity u/U_∞ at the bottom side of the wake. For the ground boundary layer, all these models show an increased thickness than the experiment and over predict the velocity deficits of the ground boundary layer.

For a higher height at h/c = 0.448 (Figure 73(e) and Figure 73(f)), the situation is the same as in the locations x/c = 1.2 and x/c = 1.5 at this height. All three models agree well with each other at both streamwise locations. And again, they model well the thickness of the main wake (Table 9 and Table 10). The velocity of the wake centre is still under predicted according to the computations but the difference modelled by the SST k-ω model is smaller than the other two models. The results for the Wilcox k-ω model present an over prediction on the velocity deficits of the ground boundary layer, while the others highly agree with the experimental points.

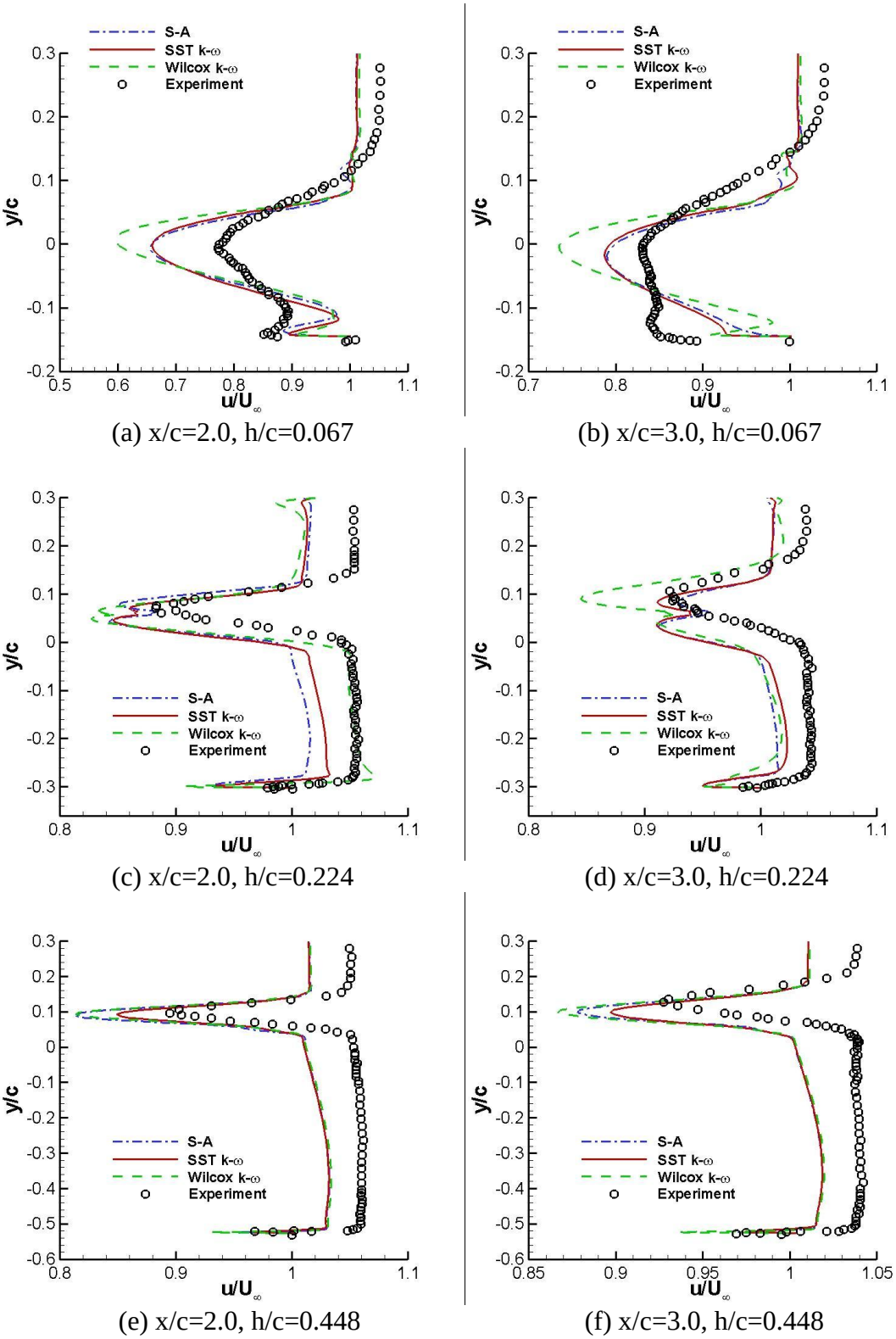

(a) x/c=2.0, h/c=0.067

(b) x/c=3.0, h/c=0.067

(c) x/c=2.0, h/c=0.224

(d) x/c=3.0, h/c=0.224

(e) x/c=2.0, h/c=0.448

(f) x/c=3.0, h/c=0.448

Figure 73: Wake profiles at x/c = 2.0 and x/c = 3.0

From the figures above, for all heights, in the region of main wake, the velocity deficit can be seen due to the flow separation after the trailing edge. And the velocity deficit is reducing due to small scale turbulence when the flow moving to downstream. In the region between the wing trailing edge and the ground, the flow velocity can be seen to grow greater than the freestream velocity due to the lower pressure under the suction surface. Although the ground moves with a velocity equal to freestream, the accelerated flow near to the ground gives rise to the effective boundary layer above the ground. However, a velocity deficit inside the ground boundary layer can be seen for most cases. It is believed that this is due to the flow is retarding due to the adverse pressure gradient in the streamwise direction from peak suction which is shown in previous section.

h/c	Schemes	$u_{min}/U\infty$	y/c at u_{min}	y at δ_{top}	y at δ_{bottom}	δ_{99}/c
0.09	Experiment	0.84	0.02	0.16	-0.11	0.27
	CDS	0.69	0.02	0.10	-0.09	0.19
	HLLC + MUSCL	0.70	0.01	0.09	-0.11	0.20
	HLLC + WENO3	0.70	0.01	0.09	-0.11	0.20
0.134	Experiment	0.85	0.04	0.14	-0.07	0.21
	CDS	0.76	0.03	0.12	-0.09	0.21
	HLLC + MUSCL	0.77	0.03	0.10	-0.05	0.15
	HLLC + WENO3	0.75	0.03	0.10	-0.08	0.18
0.224	Experiment	0.88	0.08	0.16	0.01	0.15
	CDS	0.83	0.07	0.16	0.00	0.16
	HLLC + MUSCL	0.85	0.07	0.13	0.00	0.13
	HLLC + WENO3	0.85	0.05	0.12	-0.01	0.13
0.313	Experiment	0.89	0.09	0.16	0.04	0.12
	CDS	0.84	0.08	0.18	0.02	0.16
	HLLC + MUSCL	0.85	0.09	0.14	0.03	0.11
	HLLC + WENO3	0.84	0.08	0.14	0.01	0.13
0.448	Experiment	0.90	0.10	0.16	0.04	0.12
	CDS	0.88	0.09	0.23	0.04	0.19
	HLLC + MUSCL	0.86	0.10	0.17	0.04	0.13
	HLLC + WENO3	0.85	0.09	0.17	0.03	0.14

Table 9: Wake information for experimental and computational results at x/c = 2.0

h/c	Schemes	$u_{min}/U\infty$	y/c at u_{min}	y at δ_{top}	y at δ_{bottom}	δ_{99}/c
0.09	Experiment	0.9	0.01	0.19	-0.12	0.31
	CDS	0.82	0.01	0.11	-0.12	0.23
	HLLC + MUSCL	0.82	-0.01	0.1	-0.13	0.23
	HLLC + WENO3	0.81	-0.01	0.1	-0.13	0.23
0.134	Experiment	0.91	0.05	0.19	-0.08	0.27
	CDS	0.86	0.03	0.14	-0.08	0.22
	HLLC + MUSCL	0.86	0.01	0.12	-0.1	0.22
	HLLC + WENO3	0.85	0.01	0.12	-0.1	0.22
0.224	Experiment	0.93	0.12	0.2	0.01	0.19
	CDS	0.9	0.08	0.19	-0.07	0.26
	HLLC + MUSCL	0.91	0.08	0.15	-0.04	0.19
	HLLC + WENO3	0.91	0.08	0.15	-0.03	0.18
0.313	Experiment	0.93	0.14	0.22	0.04	0.18
	CDS	0.9	0.09	0.23	0.01	0.22
	HLLC + MUSCL	0.9	0.09	0.17	0.02	0.15
	HLLC + WENO3	0.9	0.09	0.17	0.01	0.16
0.448	Experiment	0.93	0.13	0.22	0.06	0.16
	CDS	0.92	0.09	0.27	0.04	0.23
	HLLC + MUSCL	0.9	0.1	0.19	0.03	0.16
	HLLC + WENO3	0.9	0.1	0.19	0.03	0.16

Table 10: Wake information for experimental and computational results at x/c = 3.0

6.2.6 Flow Visualization

In this section, some of the contours for flow visualisation are shown. However, due to the lack of experimental data, only the simulative results are presented to support the analysis.

The mach contours and a close-up view of a part of the trailing edge together with restricted streamlines for the three numerical methods are shown together in Figure 74 to Figure 77 for the cases with different heights, respectively. All three turbulence models present an agreement that as the height rises, the Mach number is reduced on the suction surface while the streamlines at the trailing edge are better attached. At the lowest part of the suction surface, with regard to the high Mach region, the Wilcox k-ω model gives a bigger Mach number compared to the other models. By carefully observing the streamlines at the trailing edge, it can be found that the SST k-ω model is more sensitive in capturing vortices.

The vorticity magnitudes at different heights are shown in Figure 78 to Figure 81. Still the results from the three turbulence models show an attached flow at the higher height at h/c = 0.448. As the front wing approaches the ground, the vorticity magnitude increases, due to the occurrence of flow separation at the trailing edge. The S-A and the SST k-ω models appear a similar simulation while they are both more accurate than the Wilcox k-ω model on the vorticity modelling.

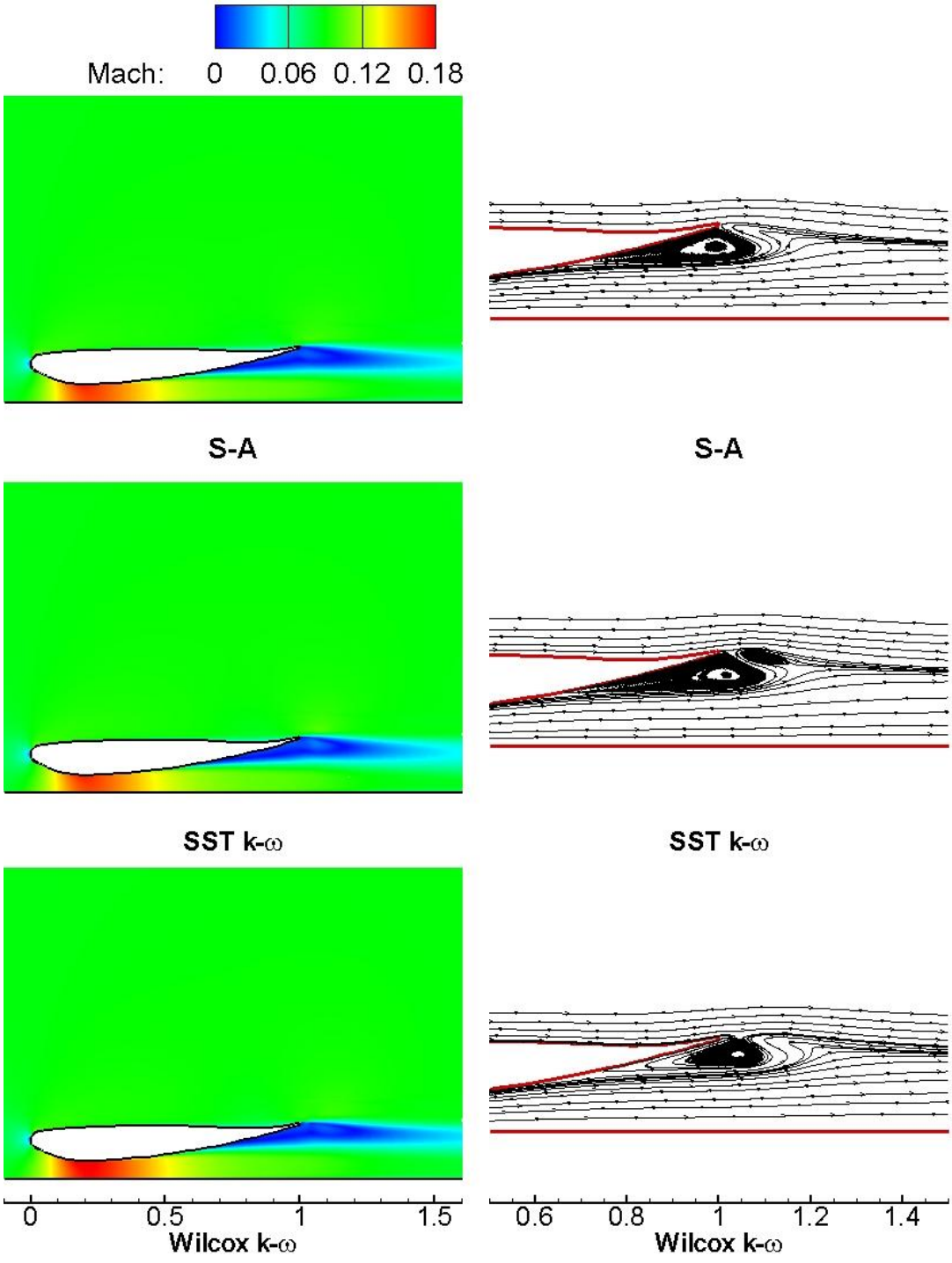

Figure 74: Mach contours and trailing edge streamlines at h/c=0.067

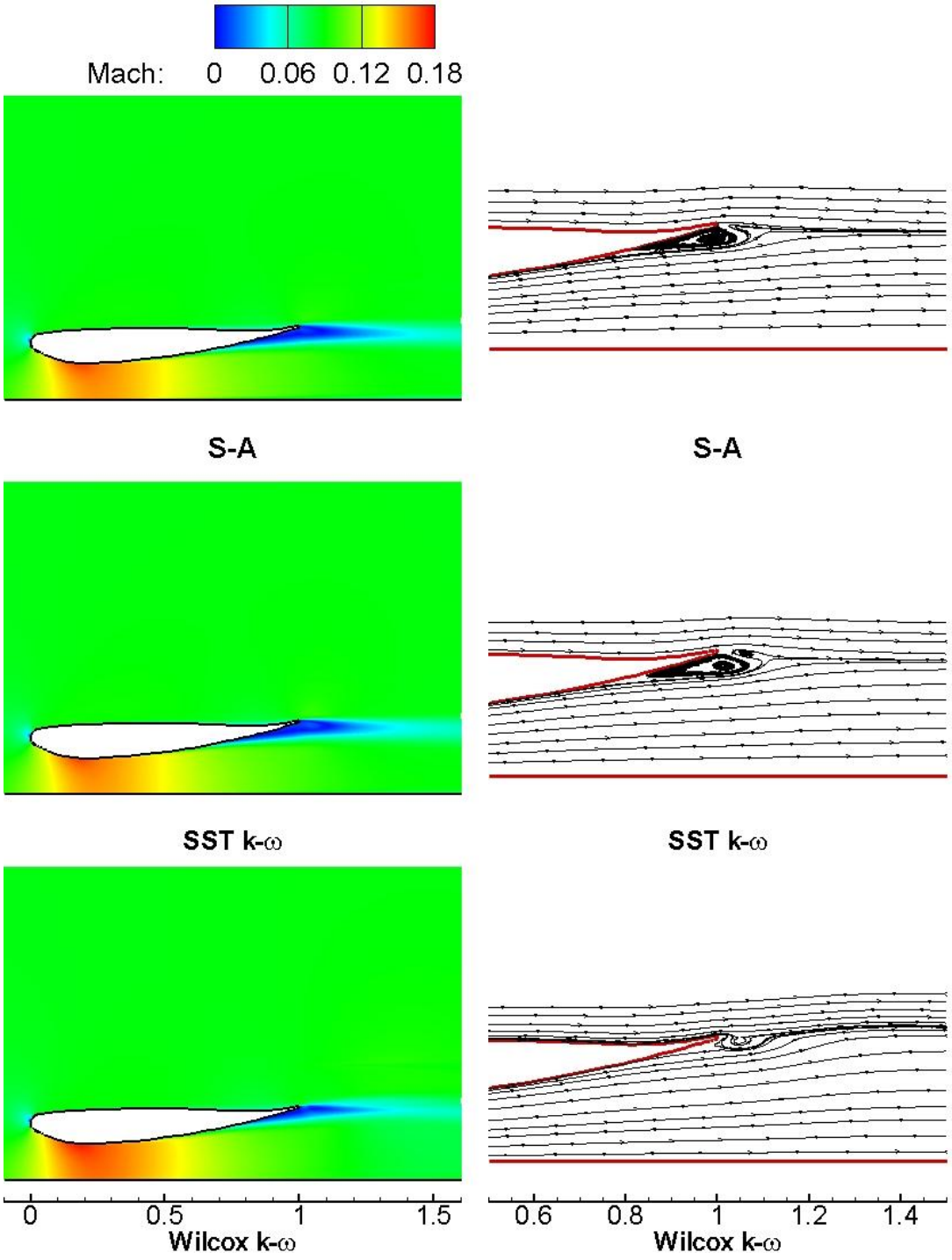

Figure 75: Mach contours and trailing edge streamlines at h/c=0.134

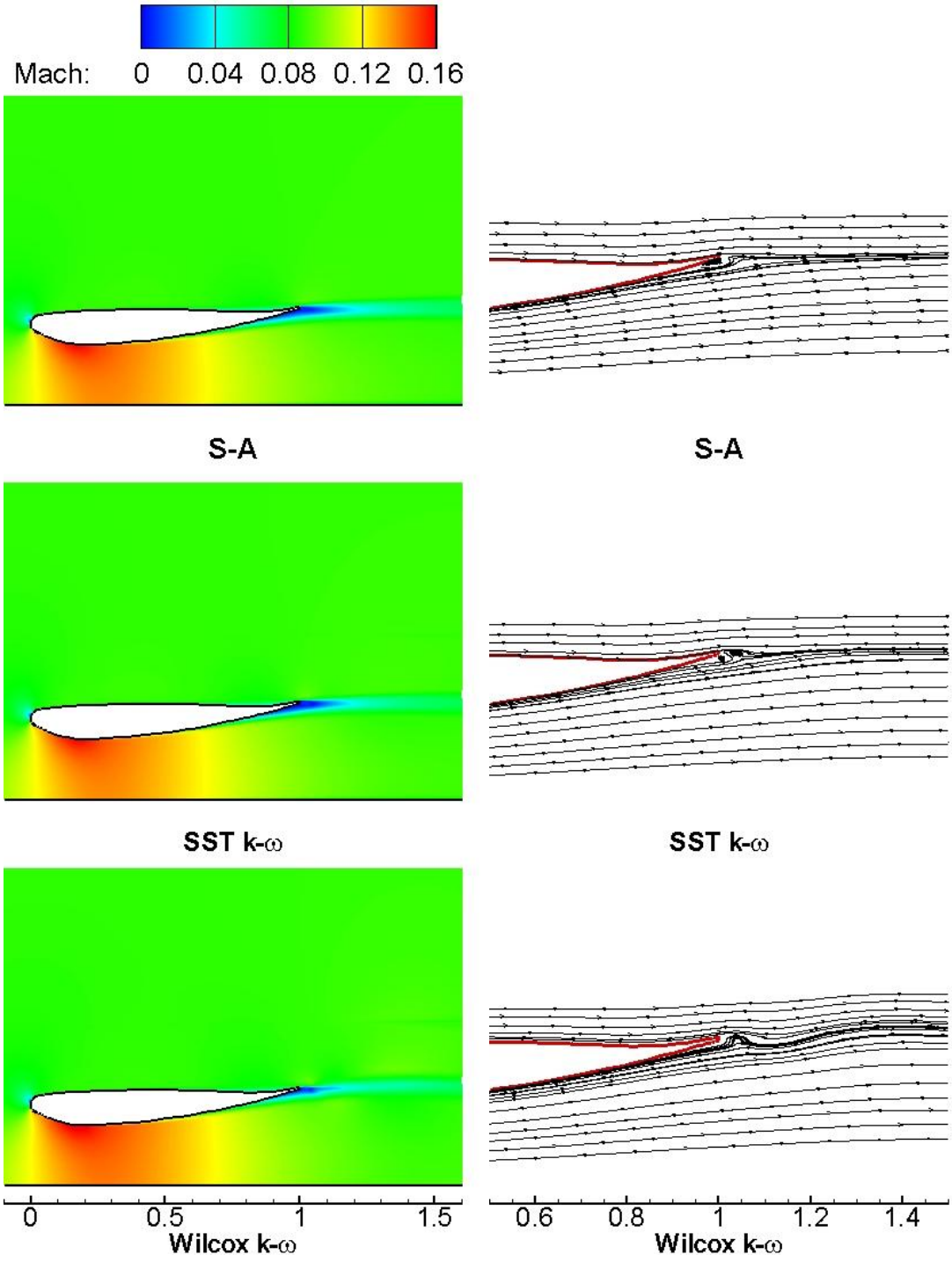

Figure 76: Mach contours and trailing edge streamlines at h/c=0.224

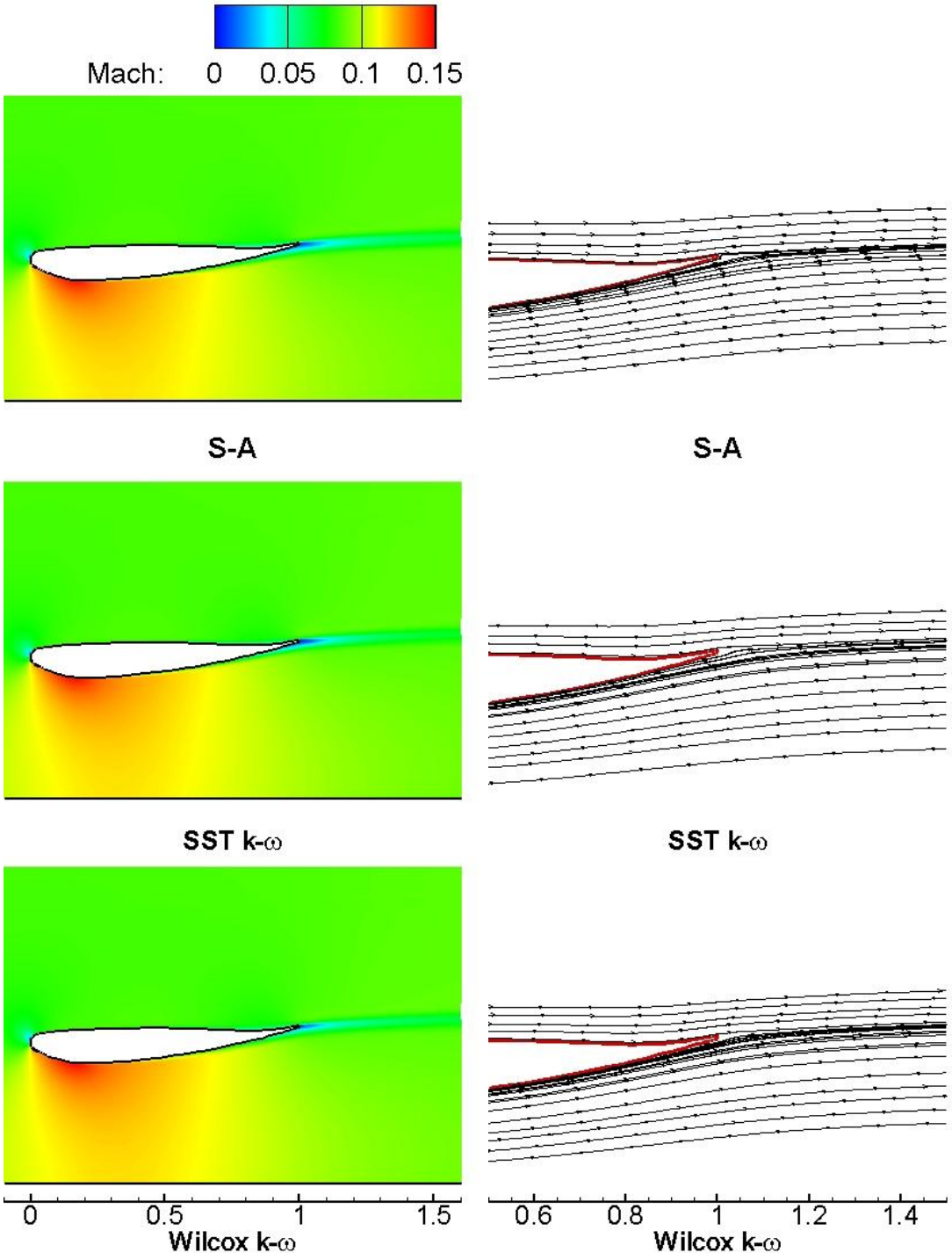

Figure 77: Mach contours and trailing edge streamlines at h/c=0.448

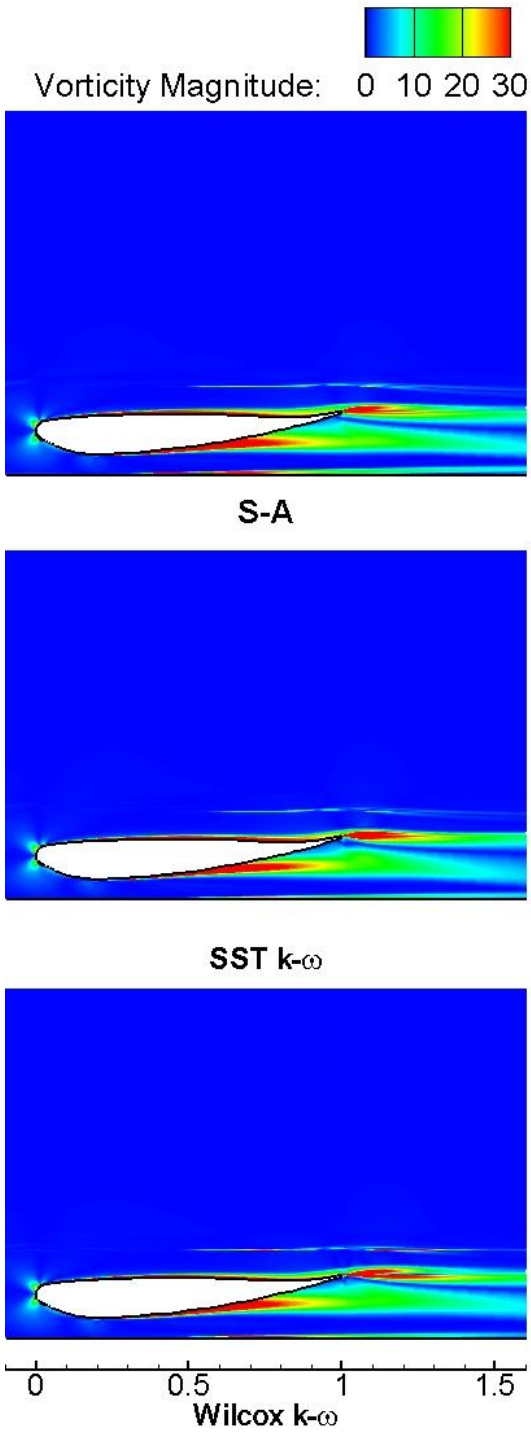

Figure 78: Vorticity magnitude at h/c=0.067

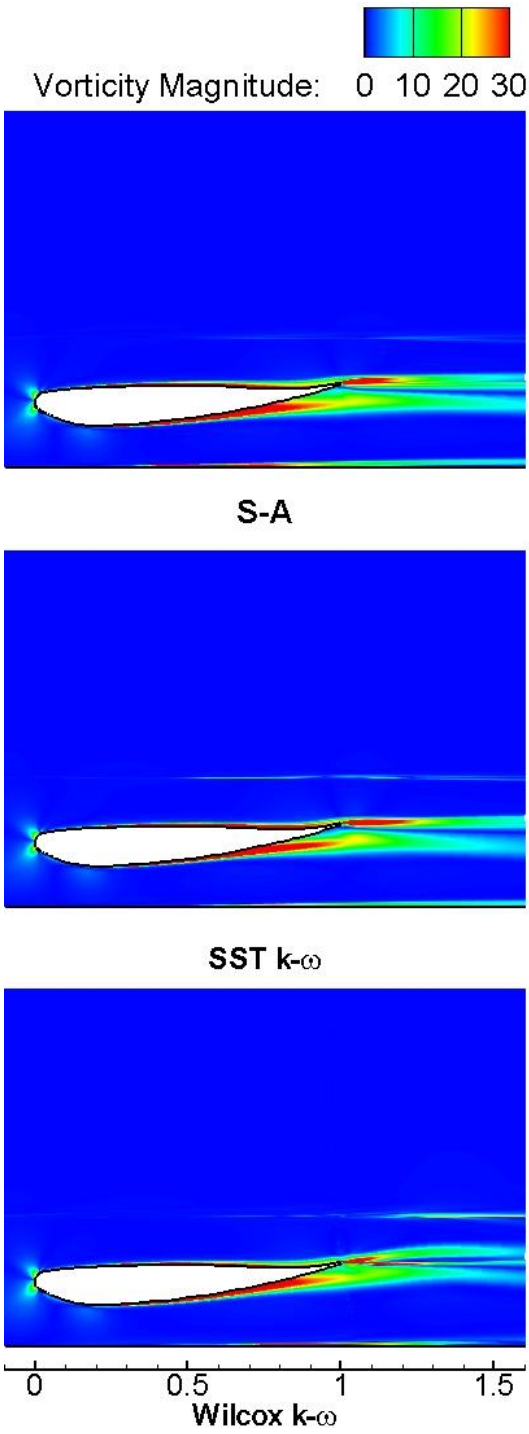

Figure 79: Vorticity magnitude at h/c=0.134

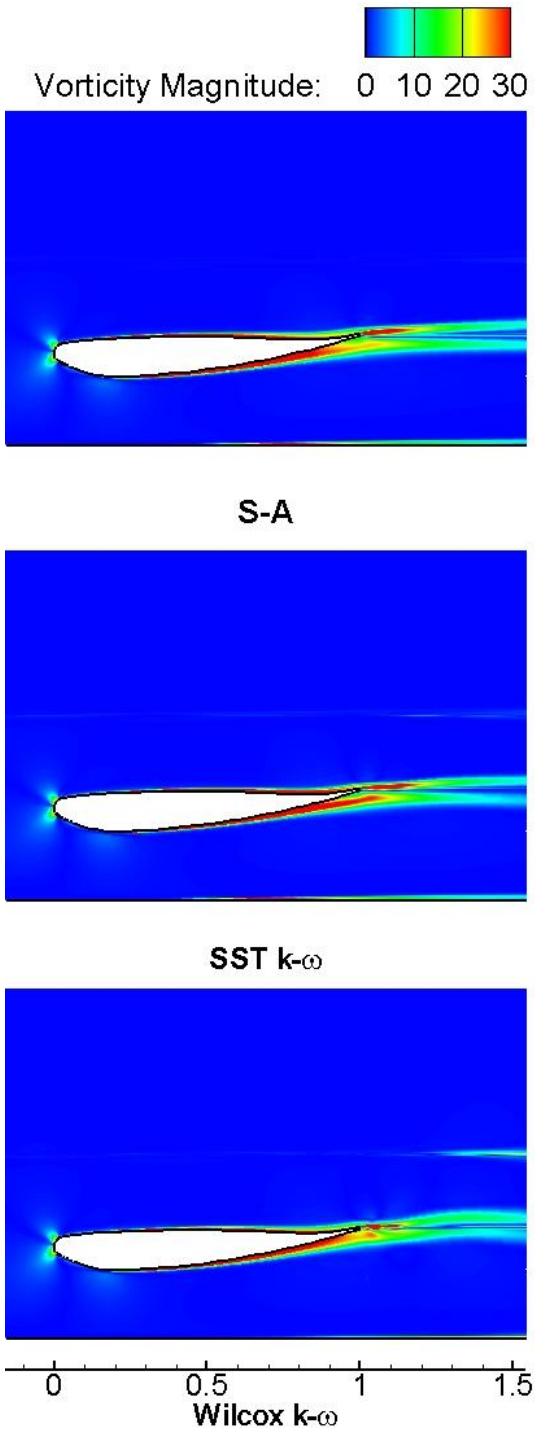

Figure 80: Vorticity magnitude at h/c=0.224

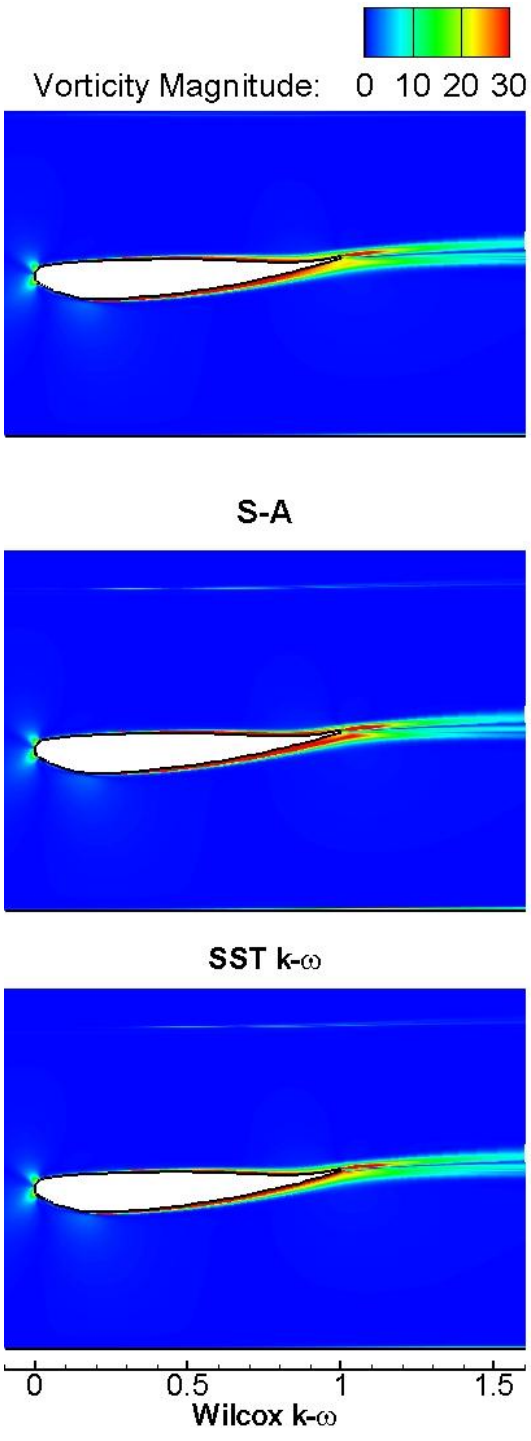

Figure 81: Vorticity magnitude at h/c=0.448

The streamlines in Figure 75 to Figure 78 show that the trailing edge vortices are very well captured even for the small vortices at the ground height h/c = 0.224. As we all known that the flow physics is highly related to the grid quality used in the simulation, an extra grid block has been generated to encounter the flow behind the trailing edge which is of a finite thickness. The grid topology and generation have been discussed in Chapter 5. Figure 82 is a close-up view of the grid and the streamlines around the trailing edge typically for the case of h/c = 0.224. It shows that with this special designed grid topology and grid structure, the vortices and the flow behind the trailing edge have been very well resolved. This shows that the designed grid is adequate for resolving the flow phenomena around and after the trailing edge in this project.

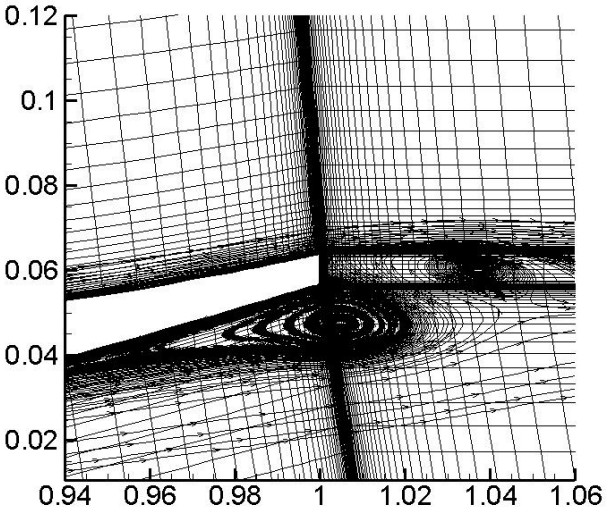

Figure 82: The streamline together with the grid at the trailing edge for the case *h/c* = 0.224

6.2.7 Summary

In section 6.2, results obtained from using three turbulence models, which are the Spalart-Allmaras (S-A) model, the SST *k-ω* model and the Wilcox *k-ω* model, are compared at different heights respectively. The Wilcox *k-ω* model predicts poor

results in all the parameters that were discussed above. The S-A and the SST *k-ω* models present similar but more accurate simulations during the whole processing. However, for the most important parameters of the front wing, which are the lift and drag coefficient, the SST *k-ω* model gives a better result than the S-A model; the same happens in the wake analysis. Moreover, the SST *k-ω* model also shows satisfactory modelling on turbulent flow and vortices capturing at low heights. For these reasons, the SST *k-ω* model is used as a preferred turbulence model in the following investigation.

Chapter 7

Numerical Studies of the Aerodynamic Performance for a Single Element Wing in Ground Effect

In this chapter, various numerical simulations based on a single element wing at different height and different angles of attack are carried out to investigate the aerodynamic performance and the flow field around the single element wing. The discussion is firstly focused on the ground effect of the single element wing at a reference angle of attack which is $\alpha = 1^{o}$, then moved onto various angles. From the comparative study which was carried out in chapter 6, the WENO 3rd order scheme is chosen as the numerical method, and the SST k-ω model as the turbulence model for the simulation and investigation.

7.1 Ground Effect at a Reference Angle of Attack

In this section, a range of heights, from h/c = 0.067 to h/c = 1.007, will be selected for this research. The main concern for the discussion is about the aerodynamic performance. In addition, some wake profiles are used to demanstrate the ground effect at different heights from the ground.

7.1.1 Lift and Drag Forces

Figure 83 shows the coefficient of downforce versus ground heights. A peak in the Cl curve can be found at $h/c \approx 0.2$. After this peak, as the height is rises, the downforce (Cl) continues to drop from a peak value of Cl = 1.37 to Cl = 0.92 at the biggest height h/c = 1.007. Before the height where the maximum downforce is located. The downforce (Cl) is also decreasing when the wing is approaching the ground. The results of the drag with heights are presented in Figure 84. The drag increases with the wing approaching the ground. However, the drag does not keep the same manner as

the downforce, which decreases after reaching the maximum magnitude. The drag will continues to grow as the wing gets closer to the ground. Also, it becomes apparent from Figure 84 that, the slope of the drag curve increases when the wing gets closer to the ground.

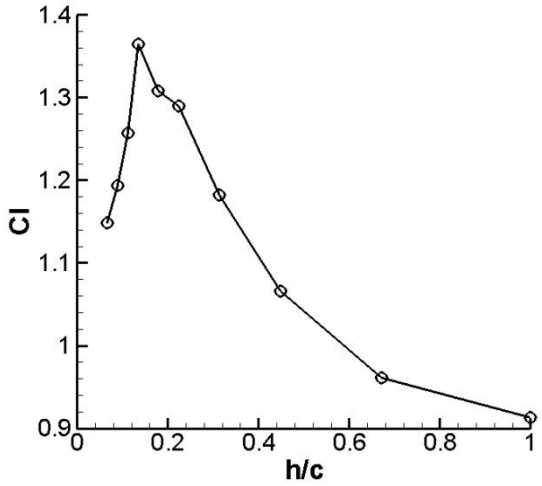

Figure 83: Coefficient of lift with different heights

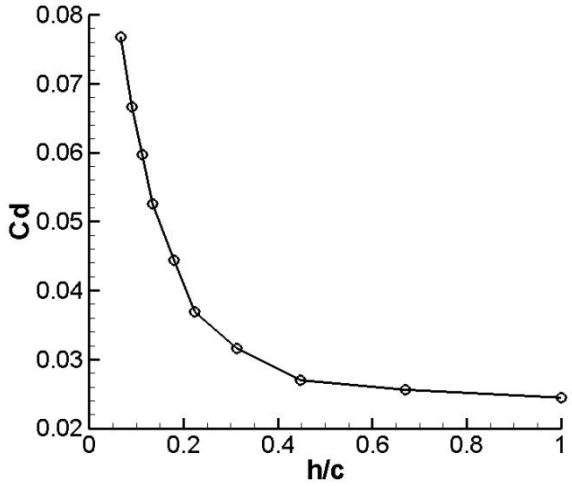

Figure 84: Coefficient of drag with different heights

7.1.2 Surface Pressure

The surface pressure on the wing centre plan at various ground heights is drawn in Figure 85. Figure 85(a) shows the Cp distribution at moderate and large heights from *h/c* = 0.224 to *h/c* = 1.007 while Figure 85(b) gives the Cp comparison for smaller heights from *h/c* = 0.067 to *h/c* = 0.179. For the moderate and large heights in Figure 85, the flow is accelerated between the wing and the ground when the wing approaches the ground, the suction pressure increases during the whole suction surface, including the suction peak and the pressure gradient for recovery. For the small ground heights shown in Figure 85(b), the situation is similar for the suction peak which still increases as the wing gets closer to the ground, even for the heights which are smaller than the height of the maximum downforce. But compared to the larger heights, the pressure at the leading edge on the pressure surface and the suction surface gets closer, even reverse at the extreme low height *h/c* = 0.067. Again, in Figure 85, a constant pressure part can be found close to the trailing edge in the suction surface. This constant pressure region increases when the wing approaches the ground. This profile indicates a separated flow occurred in this region and leads to a separated boundary layer from the trailing edge. Meanwhile, the pressure at the pressure surface is similar for all heights, with a trend of small decrease as the ground height reduces.

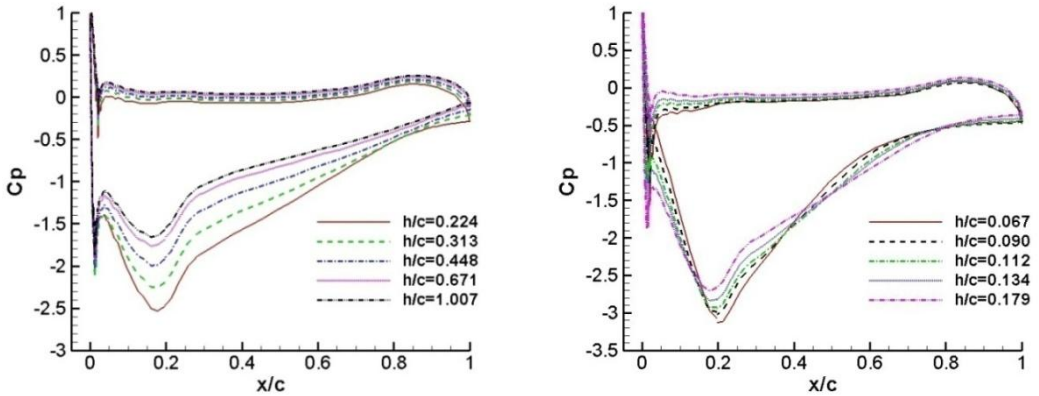

(a) Surface pressure at big heights (b) Surface pressure at small heights

Figure 85: Surface pressure at different heights

7.1.3 Wake and Ground Boundary Layer

To investigate the wake of the wing at various heights, two near-field locations are taken at x/c = 1.2 and x/c = 1.5 (Figure 86). The wake profiles are from a little above the trailing edge to the moving ground.

From these two figures, it can be obviously found that the thickness of the main wake increases as the wing approaches the ground. This is because the increased suction peak causes a similar increasing recovery pressure gradient which was discussed in the previous section. The greater pressure will lead to a thicker boundary layer of the wing, and then a thicker wake, as the wing gets closer to the ground. At the same time, along with the reduction of the height, the flow begins to separate and hence, a severe deficit is generated on the main wake. Also because of the separation, the wake has not passed along the angle of the trailing edge, but along a small angle lower. This action is reflected in the figures with the profile of lower magnitude of the wake centre velocity, especially at the downstream location x/c = 1.5. The velocity accelerates between the wing and the ground due to the increased suction pressure in this region. But for all heights, this high speed flow reaches approximately the same value.

The ground boundary layer can be seen in both streamwise locations. Although the ground moves at the same speed as the free stream, the accelerated flow above the ground results the ground boundary layer. Meanwhile, a velocity deficit appears in the ground boundary and develops slightly more while the wing moves close to the ground. It is because the fluid originally runs at freestream speed. But after the suction peak, it begins to retard due to the pressure gradient recovery.

A series of wake surveys at different ground heights from h/c = 0.448 to h/c = 0.067 are presented respectively in Figure 86. From these figures, it can be clearly seen that the wake thickness grows while the flow moves towards streamwise and the velocity at the centre of the wake is reduced. However, as discussed above, after the separation

emerging at lower height such as h/c = 0.134 and h/c =0.067, the wake passes a small angle lower than the wing trailing edge angle, whilst at a higher height it passes towards the wing trailing edge angle.

For the ground boundary layer, the thickness grows as the flow moves downstream. This growth becomes evident when the wing is closer to the ground. The deficit of velocity inside the ground boundary layer is very similar at all streamwise locations at greater heights. However, as the wing approaches the ground, this deficit slightly increases in the locations closer to the trailing edge. Again, at the lowest height h/c = 0.067, the wake merges with the ground boundary layer from x/c = 2.0.

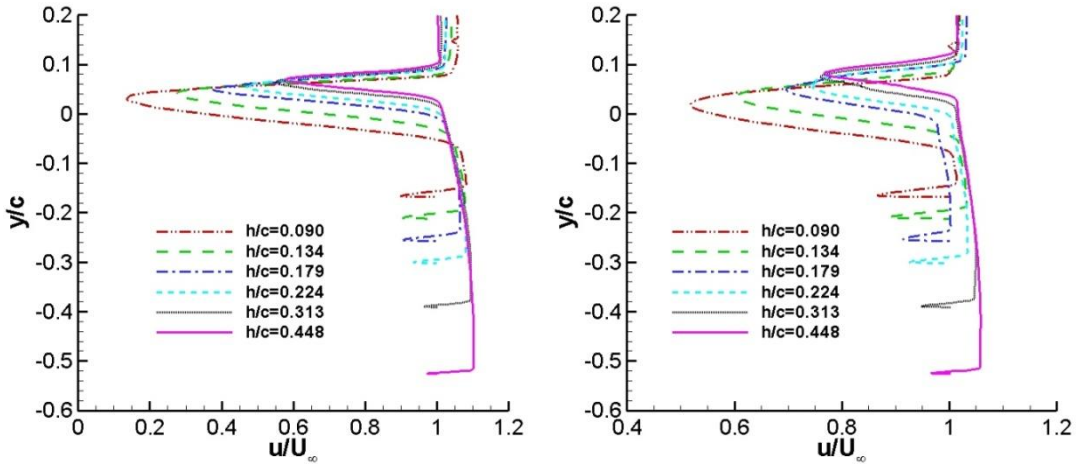

(a) x/c = 1.2 (b) x/c = 1.5

Figure 86: Wake profile for different heights

From Figure 87, we can see that as the flow moves downstream from x/c = 1.2 to x/c = 3.0, the velocity deficit in the wake centre is reducing and approaching u/U_∞ = 1, in particular for the cases h/c=0.448 and h/c=0.224. Although the velocity has not been fully recovered at the x/c = 3.0, following this trend, the velocity would be expected to recover to freestream when the flow moves downstream to farfield.

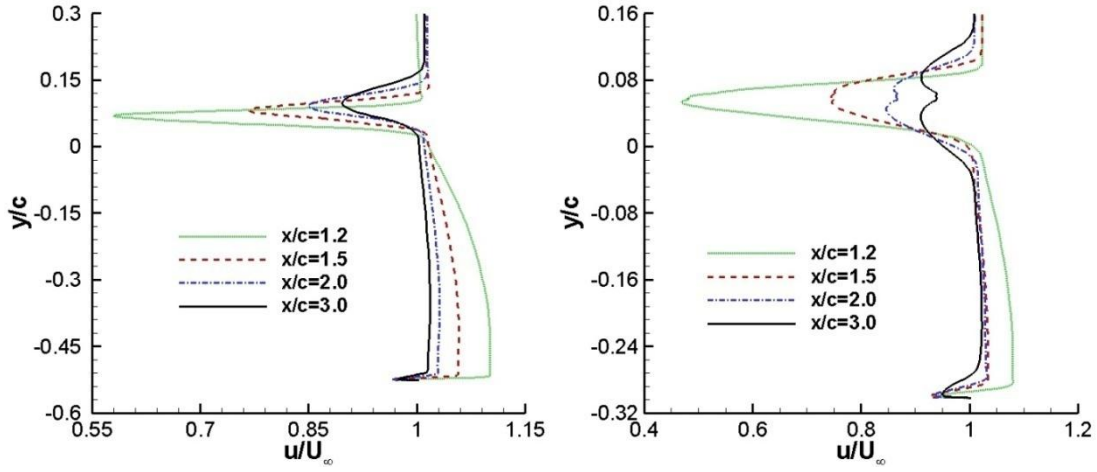

(a) h/c = 0.448 (b) h/c = 0.224

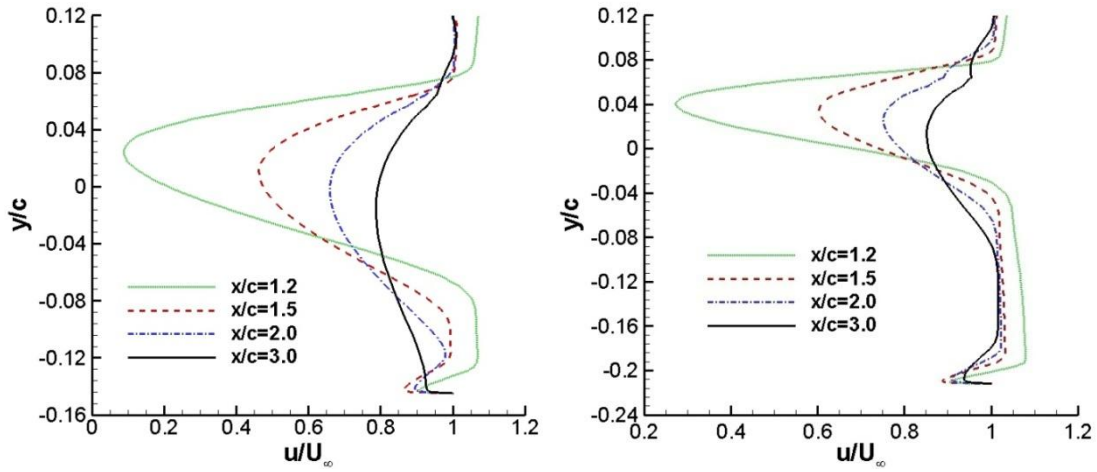

(c) h/c = 0.134 (d) h/c = 0.067

Figure 87: Wake profile for different heights

7.2 Ground Effect at Various Angle of Attack

In this section, some simulations of the single element wing at various angles of attack at different ground heights will be carried out for the investigation. The focus is on the aerodynamic performance along with surface pressure results. For some reasons on

mesh quality, the simulations could only successfully run at angles of attack under 10 degrees. Even so, at very low ground heights, simulations failed to run by using the WENO 3rd numerical scheme.

7.2.1 Lift and Drag Forces

Two different curves are generated from the results, due to the different purpose. Figure 88 shows forces with ground heights for various angles of attack and Figure 88 shows the lift and drag curves at various heights.

From Figure 88, as the wing approaches the ground, the downforce increases at the beginning. This increment turns to decrement when the wing approaches the ground to a certain height, where h/c = 0.313 for α = 5 ºand h/c = 0.134 for α = 1 º. Also, the ground height sensitivity for gaining downforce at the maximum downforce height is reduced when the angle of attack increases, where the curve is almost flat at α = 10 º. The slope of the drag continues to increase as the wing gets closer to the ground for all the angles. Also larger angle of attack will result in larger drag for a certain ground height.

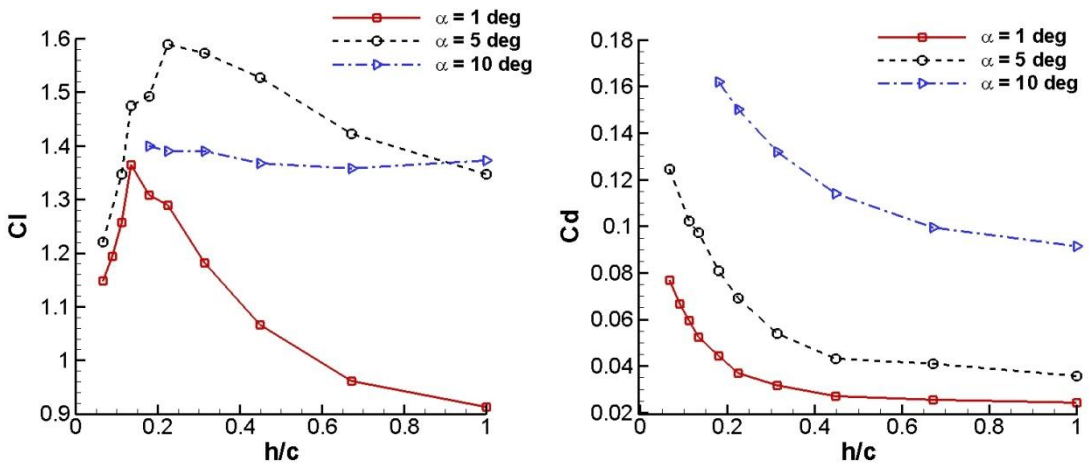

Figure 88: Lift and drag coefficients with different height for the same angles of attack

The lift curves and drag curves for *h/c* = 0.134 and *h/c* = 0.224 are shown in Figure 89. For both heights, the stall angle of attack happens at α = 5 °where the downforce will reduce if the angle continues increasing. At the stall angle, the maximum downforce for *h/c* = 0.224 is larger than *h/c* = 0.134 and will still be larger in the reducing region after the stall angle. But before the stall angle, the situation is opposite and the downforce for *h/c* = 0.134 is slightly bigger than that for *h/c* = 0.224.

The drags for both ground heights grow as the angle of attack increases and the tendency is similar. After the stall angle, the dragcurves are presented as a straight line; while before the stall angle, the slope slightly enlarges as the angles increase. The drags at all ground heights for *h/c* = 0.134 are a little larger than *h/c* = 0.224.

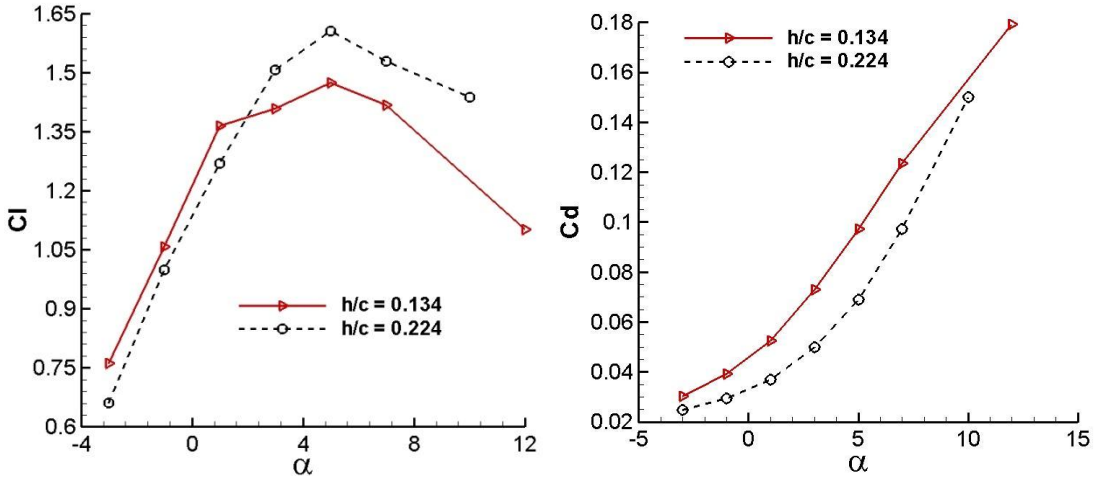

Figure 89: Lift and drag coefficients at different heights

7.2.2 Surface Pressure

The surface pressure in the centre plan of the wing with various ground heights at α = 5 °and α = 10 °is drawn in Figure 90 and Figure 91 respectively. The Cp distributions for the two angles are similar to the reference angle of attack. The pressure on the suction surface increases as the wing approaches the ground until the recovery pressure presents a flow separation result, as seen by the constant pressure regions.

But the ground height is smaller when the flow separation appears compared to the reference angle of attack. For α = 5º, it can be seen that the flow starts separating at the trailing edge when the ground height is lower than *h/c* = 0.448. And for α = 10º, the constant pressure regions for all heights are much larger than smaller angles. This leads to an earlier separation with a greater boundary layer separation in the trailing edge region. Also, the separation would make the downforce reduce compared to the lower angle of attack.

Meanwhile, the surface pressure with various angles of attack at *h/c* = 0.134 and *h/c* = 0.224 are presented in Figure 92 and Figure 93 respectively. For both heights, as the angle of attack rises, the suction pressure increases during the whole suction surface, including the suction peak and the pressure gradient for recovery. Again, as the angle rises, a constant pressure part can be found close to the trailing edge in the suction surface and the region increases at the same time. The large constant pressure part leads to a decreasing downforce which is shown in previous section. At the pressure surface, the profile is different due to the various angles at the front half part of the wing, but joining together at the back half part.

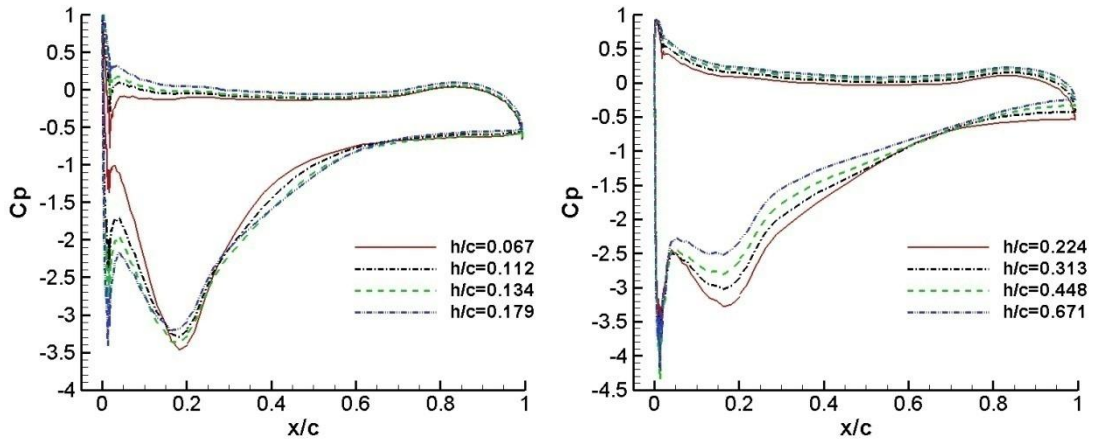

Figure 90: Surface pressure at α = 5º

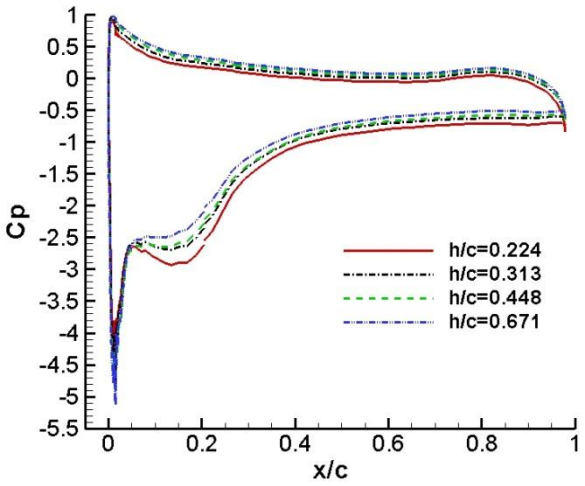

Figure 91: Surface pressure at α = 10º

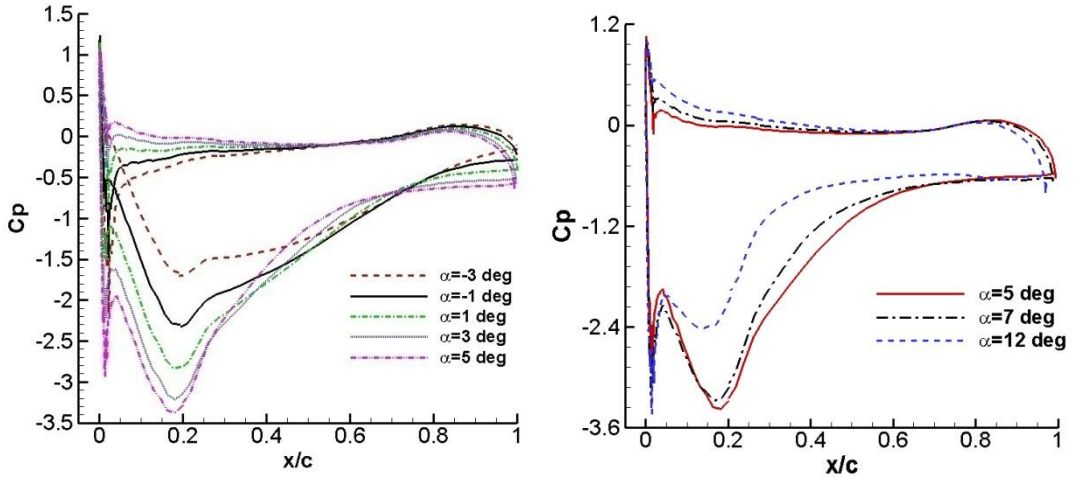

Figure 92: Surface pressure at h/c = 0.134

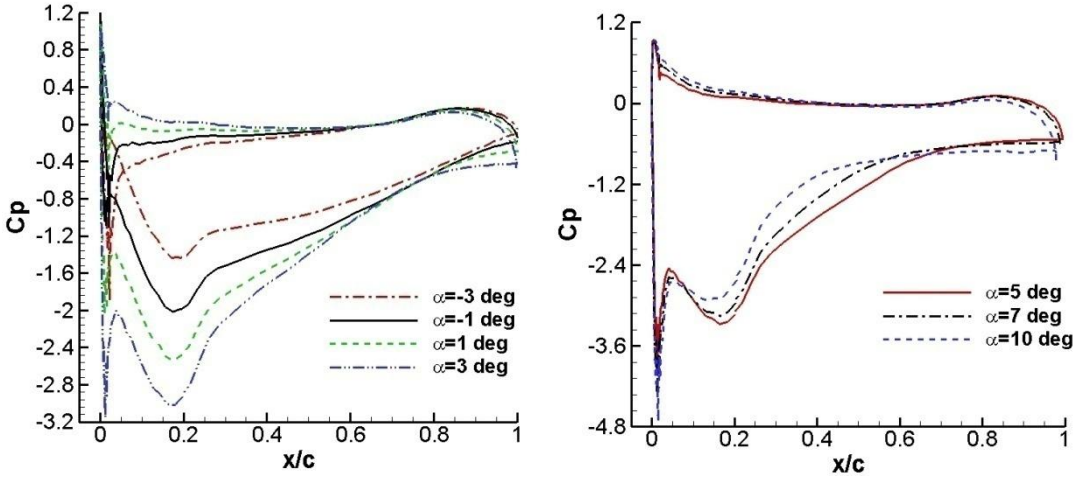

Figure 93: Surface pressure at h/c = 0.224

7.3 Flow Visualization of Ground Effect at Various Angles of Attack

In order to get a more direct viewing to support the analysis, some flow parameters contours plus the streamlines at the trailing edge are drawn in the following figures for studying the ground effect at different angles of attack.

For all angles of attack with all the ground heights, a high Mach number region can be apparently found under the suction surface where the wing is at the closest distance to the ground (Figure 94 to Figure 96). This means the flow itself accelerates when it passes the narrow channel. It is another way of proving why the suction peak pressure emerges there. As the Mach number increases with the wing approaching to the ground, the pressure at the suction surface rises negatively along with that. Meanwhile, a low Mach number region comes out near the trailing edge making the flow separate. The details of the separation flow near the trailing edge are presented by using streamlines from Figure 97 to Figure 100.

It can be clearly seen that the flow separation becomes severe as the angle of attack grows. Especially at a higher height, where h/c = 0.448 and h/c =1.007, the flow is well attached through the whole wing at α = 1 º and α = 5 º, but large vortices can be seen near the trailing edge at α = 10 º. Again, a comparison could be made in the condition of each angle of attack. At reference angle α = 1 º, the flow attached well at moderate and large heights. The separation appears only when the wing is very close to the ground (h/c = 0.134). At α = 5 º, the flow separation is bigger, but still at h/c = 0.448 and h/c = 1.007. However, when the angle is increased to α = 10 º, the flow separation appears at all heights that chaotic vortices is generated with it near the trailing edge. As the wing approaches to the ground, the separation becomes clearer, that the separation point moves forward and the vortices grow bigger.

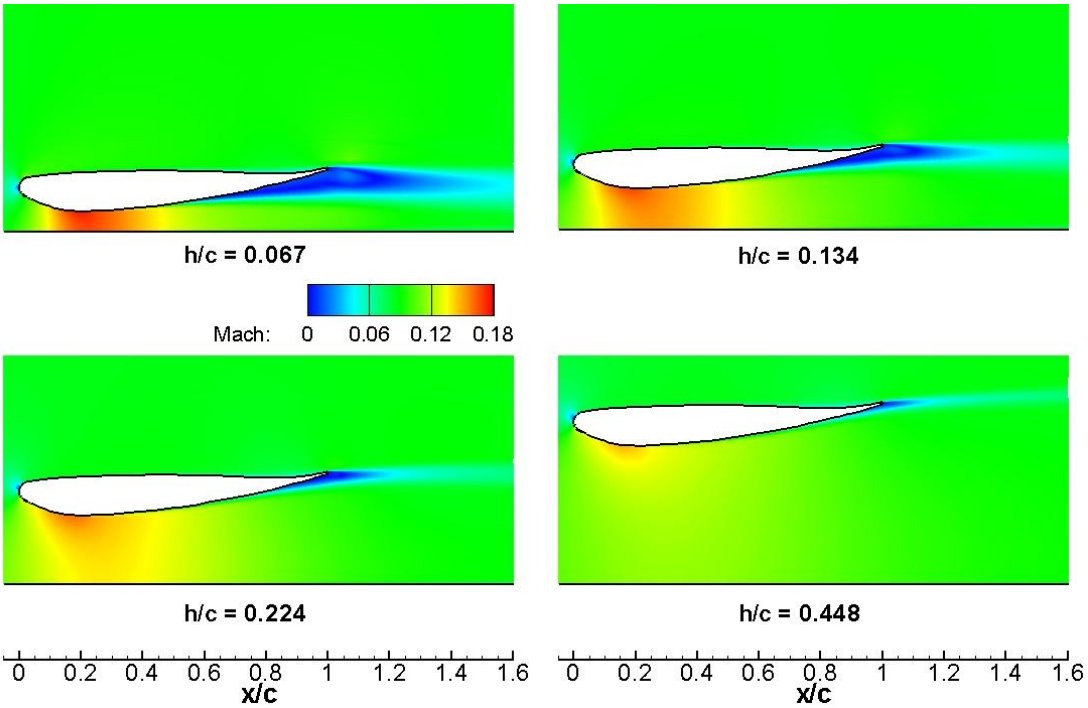

Figure 94: Mach contours at reference angle of attack α = 1º

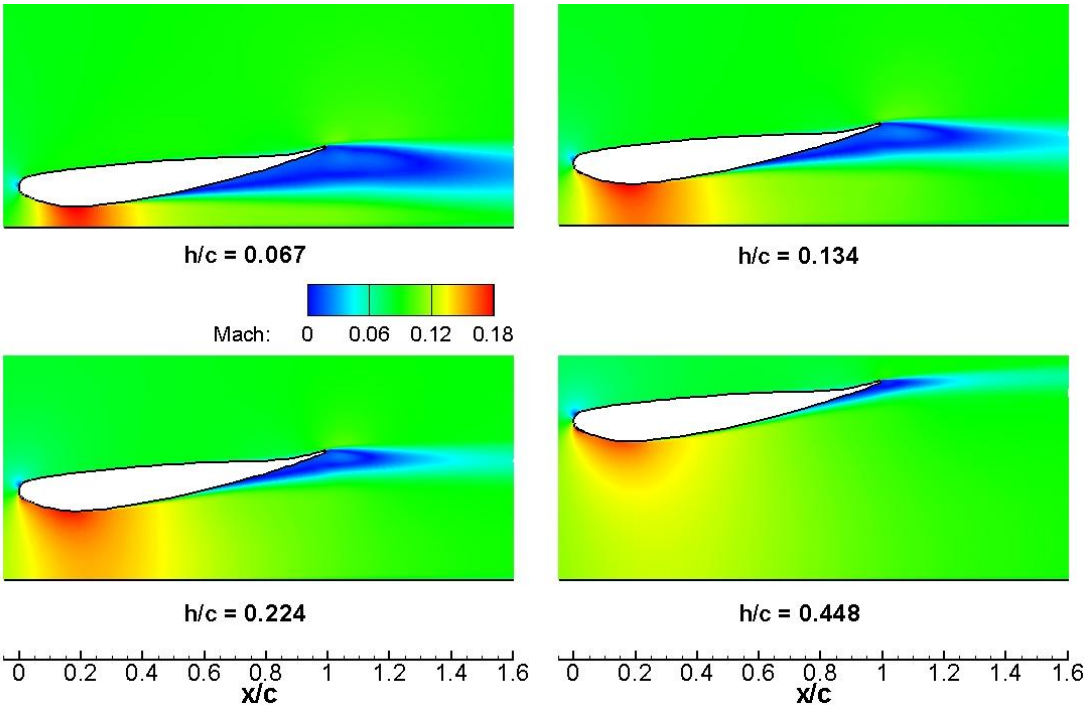

Figure 95: Mach contours at α = 5º

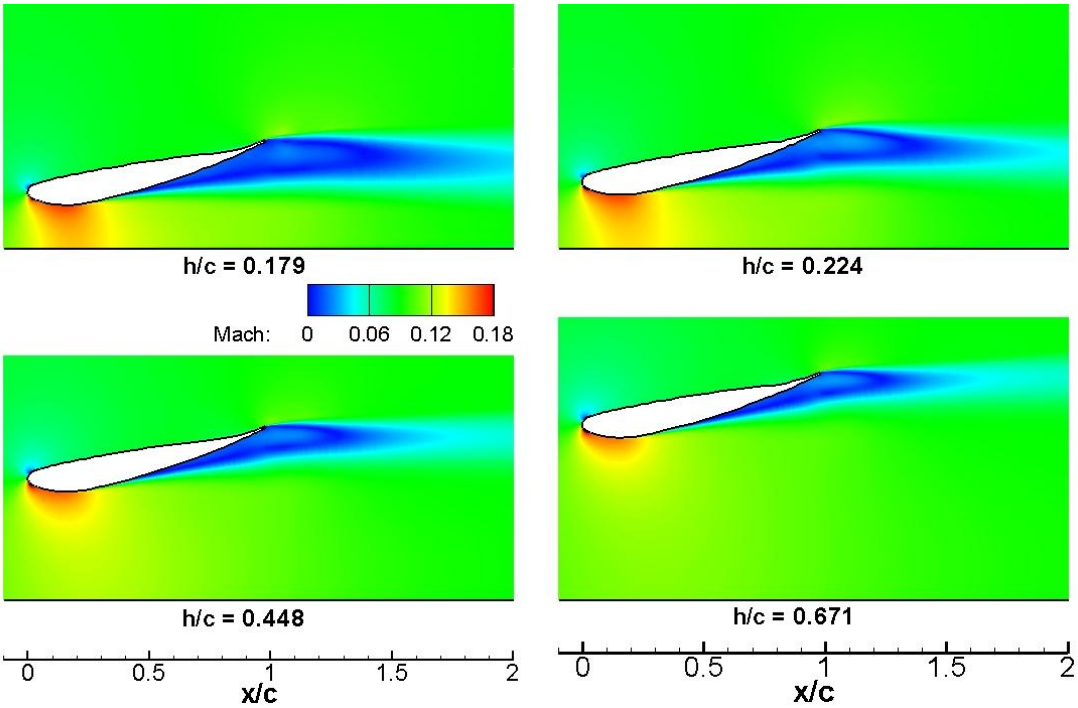

Figure 96: Mach contours at α = 10º

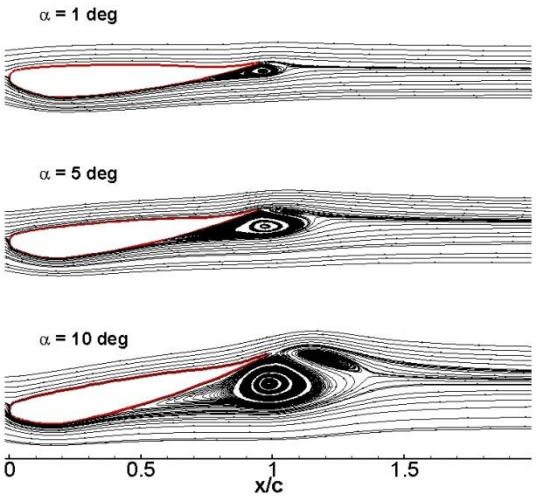

Figure 97: Streamlines at h/c = 0.134

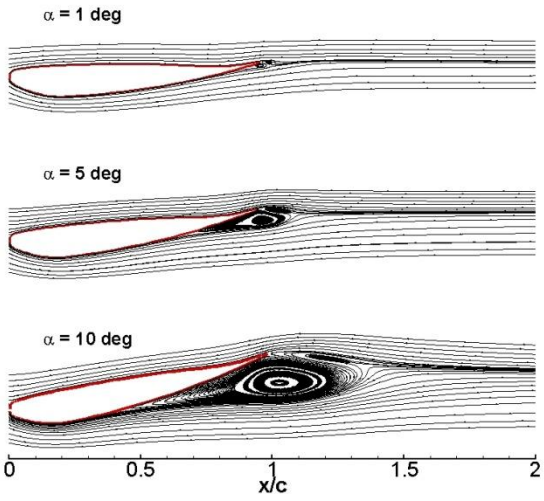

Figure 98: Streamlines at h/c = 0.224

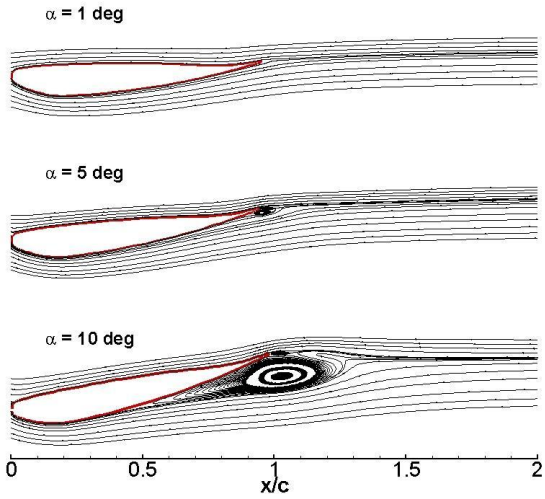

Figure 99: Streamlines at h/c = 0.448

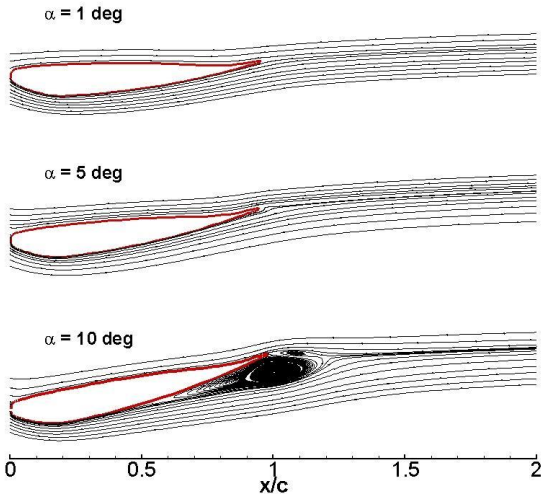

Figure 100: Streamlines at h/c = 1.007

The captured vortices are also revealed by the vorticity magnitude in Figure 101 to Figure 103. A clear separation boundary layer can be seen at large angles of attack and as the wing gets closer to the ground, the separation becomes stronger.

Also in the vorticity magnitude, the wake is clear and a tiny ground boundary layer can be found at low ground heights.

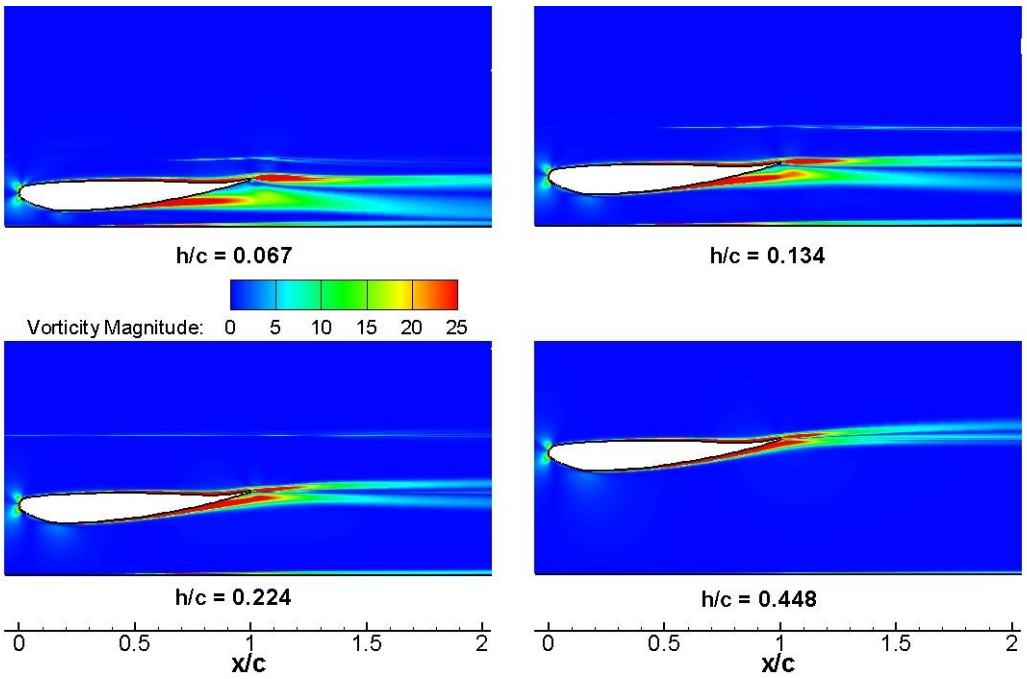

Figure 101: Vorticity magnitude contours at α = 1°

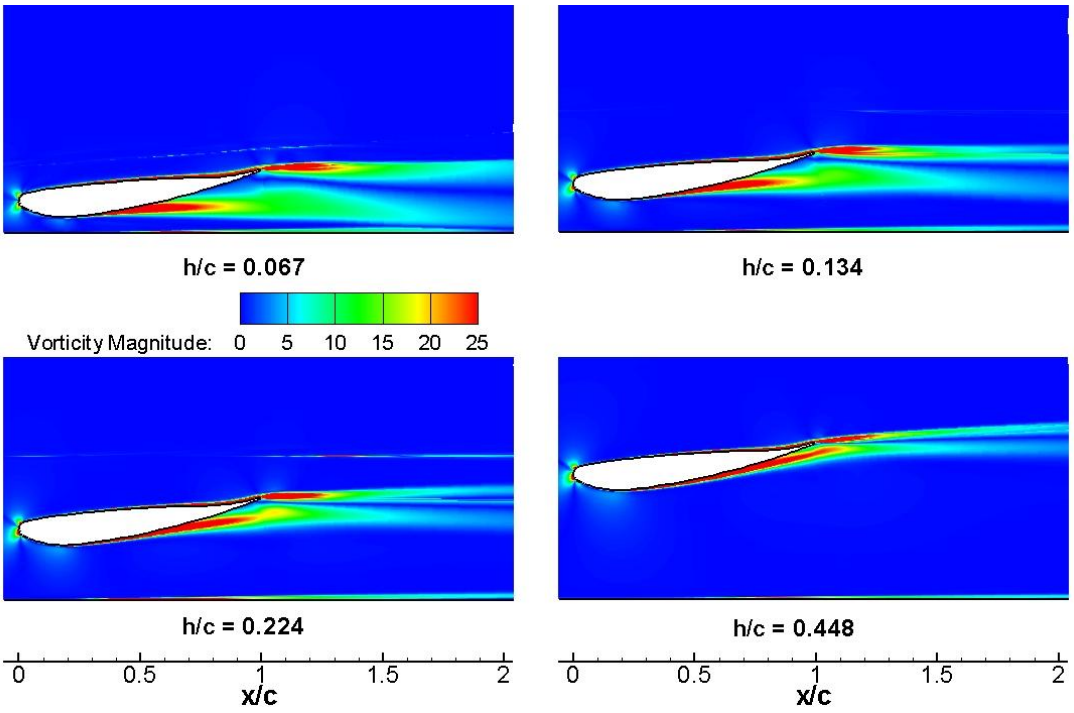

Figure 102: Vorticity magnitude contours at α = 5º

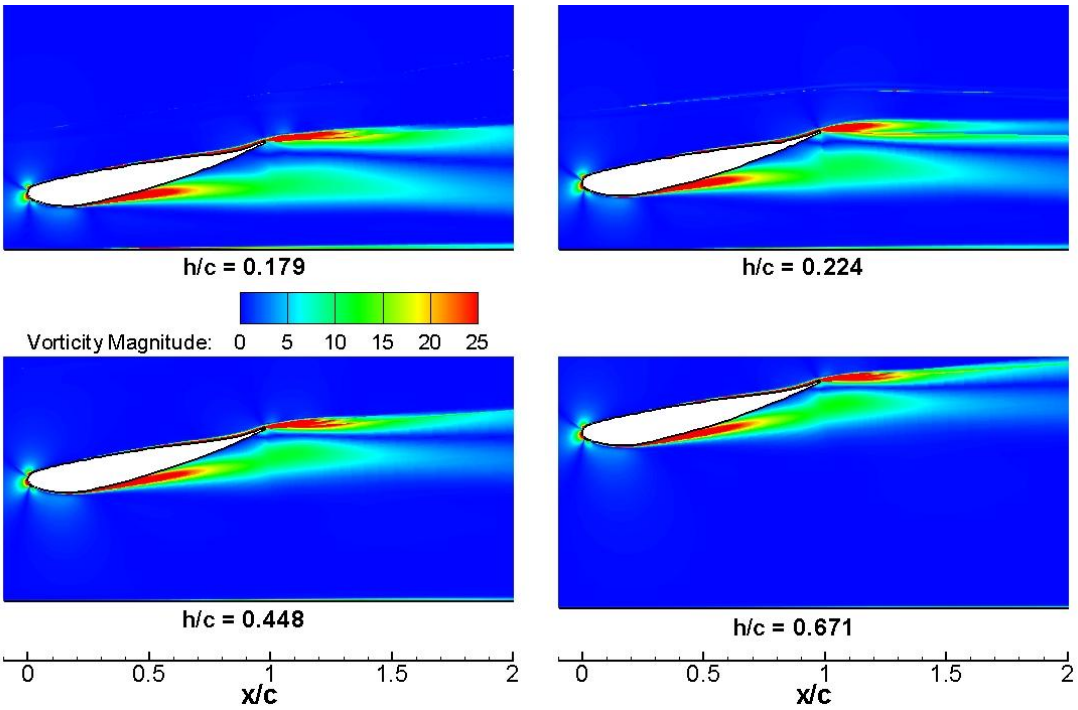

Figure 103: Vorticity magnitude contours at α = 10º

7.4 Summary

In this chapter, a series of pure simulations which were focused on aerodynamic performance were accomplished with a variety of configurations for the single element wing by using the HLLC solver with the WENO 3rd order scheme in conjunction with the SST k-ω model.

For the single element wing, the downforce continues increasing as the height is reduced, until it reaches the height of the maximum downforce. Then, the downforce will turn to fall rapidly below this height. The situation keeps similar when the angle of attack grows larger. At the same time, the downforce itself is increased with the growing angle of attack. However, after it reaches the stall angle, the downforce drops fast and no longer changes with the reduced height. The drag does not follow the same manner as the downforce. It keeps increasing as the ground height reduces for all heights. Moreover, the slope of the drag even also increases as the wing is close to the ground. The effect of reducing the height on the pressure distribution is generally the same as the angle of attack is increased. The pressure increases over the whole suction surface while it slightly decreases on the pressure surface. Meanwhile, a constant pressure part near the trailing edge is growing as the angle of attack increased. This leads to a flow separation and then causes the downforce decreasing. From the wake analysis, as the ground height is reduced, the thickness of the wake increases. And it also leads to an increased velocity deficit in the wake centre. An existence of vortex shedding from the trailing edge, which is caused by the constant pressure part near the trailing edge, can be found visually from the simulations. The shedding itself becomes larger not only as the angle of attack grows bigger, but also as the wing approaches the ground.

Chapter 8

Numerical Studies on Double Element Wing in Ground Effect

In this chapter, various numerical simulations based on a double element wing will be carried out to analyse the aerodynamic performance with ground effect. The main element wing is fixed at the same reference angle of attack as the single element wing in *section 7.1*, while the flap changes its angle relative to the main element. The rotating point is located at x/c = 0.567, y/c =0.067, which is the leading edge of the flap. Five different flap angles are set up and various ground heights will be employed at each flap angle respectively. The investigation aspects for the double element wing are similar to that with the single element, on which both the aerodynamic performance and the flow field results will be focused. Again, as in *chapter 7*, the 3rd WENO order scheme is chosen as the numerical method in conjunction with the SST k-ω model as the turbulence model for the simulation.

8.1 Lift and Drag Forces

The total downforce generated by the double element wing versus ground heights is shown in Figure 104. It can be seen that the basic tendency of the downforce curve for all the flap angles is generally similar to the single element wing. The downforce increases as the ground height is reduced until it reaches a peak point where $h/c \approx 0.13$. Again, from this figure, it is clearly shown that along with the increasing in the flap angle, the total downforce will get also gradually bigger for all ground heights. However, this phenomenon only appeared before the flap reaches a certain stall angle of the double element wing. After that, at α_{flap} = 32 º, although the downforce keeps the same level at high ground heights, when the height is reduced to a low distance, it still drops quickly from the maximum Cl = 4.78 to Cl = 3.89 at h/c = 0.105.

From this figure, we can see with a double element wing, the lift coefficients are much higher than that in a single element wing, which was discussed in the previous chapters.

In order to see the contribution in generating downforce of each wing respectively, the total downforce is divided into downforce of the main element and downforce of the flap (Figure 105). It is surprising to find that at each flap angle, the downforce of the flap has remained fundamentally unchanged for all heights. It leads to the curve profile of the downforce of the main element similar in shape to the total downforce curve. It is noted that, as the flap angle increases, both the downforce of the main element and the downforce of the flap become slightly bigger until they reach the stall angle.

The results of the drag with heights are presented in Figure 106. The tendency is also similar to that in the single element wing, the drag increases when the wing approaches the ground same as the downforce until it reaches the maximum. However, the drag does not keep a similar manner as in the downforce which decreases fast after reaching the maximum magnitude. The drag continues to grow bigger when the wing gets closer to the ground. Also apparently from Figure 106, the slope of the drag curve increases while the wing approaches the ground and the larger flap angle will apparently bring a bigger drag for all ground heights.

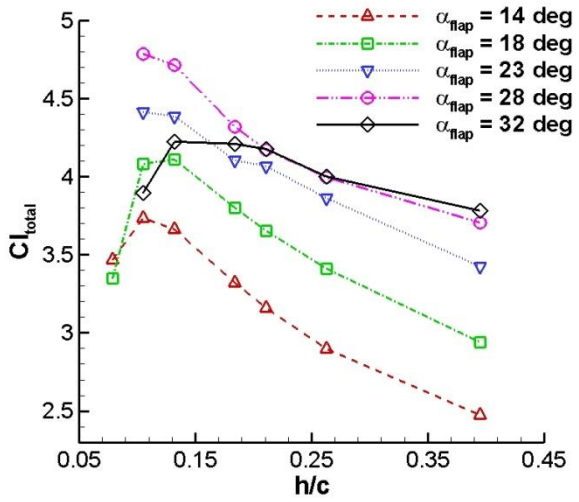

Figure 104: Total downforce at different flap angles with different heights

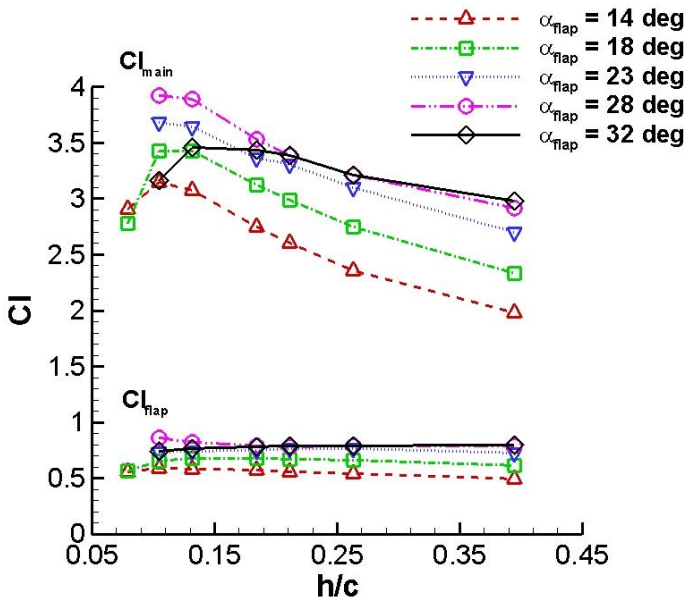

Figure 105: Separation downforce for main element and flap at different flap angles with different heights

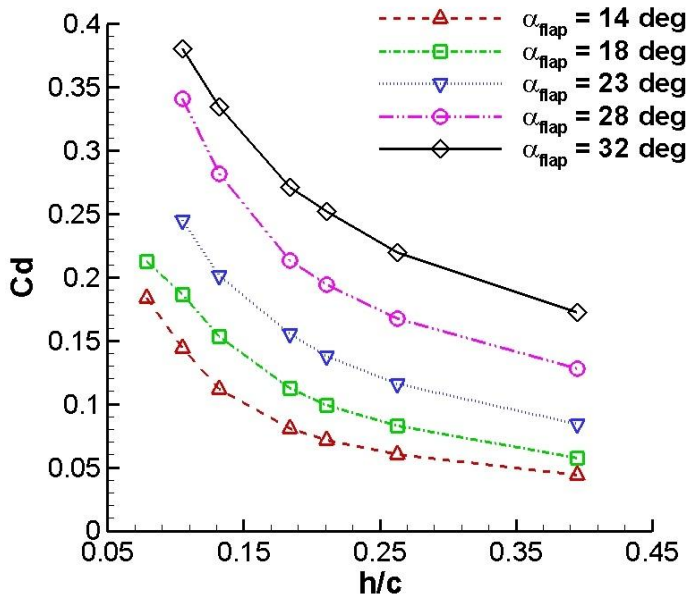

Figure 106: Drag coefficients at different flap angles with different heights

8.2 Surface Pressure

The surface pressures in the wing central plan at various ground heights for each flap angle are drawn in Figure 107 to Figure 111 respectively. At α_{flap} = 14 º, as the ground height is reduced from large heights, the suction pressure increases both on the lower surface of the main element and the flap, in the same manner as at the single element wing. But the increment on the main element is much greater than on the flap. However, if the height continues reducing, the increase in pressure will not be as much as at large heights. The main suction peak at *h/c* = 0.184, *h/c* =0.132 and *h/c* =0.079 are almost the same. Meanwhile, a clear suction pressure peak can be found at *x/c* ≈ 0.05 at *h/c* = 0.079. Also at the same height, a separation flow occurs near the trailing edge of the main element, while it does not appear at other heights. This phenomenon may explain why the downforce decreases at this height. The pressure on the lower surface for the flap is similar for all the lower heights. Again, for all ground heights, the suction spike pressure at the leading edge is much larger than the suction peak pressure, which leads to a considerable downforce generated in this

region. The pressure at the pressure surface is similar for all heights, with a trend of a slight decrease as the ground heights are reduced.

The general trend of the surface pressure for α_{flap} = 18 ºis similar to the previous flap angle, but the situation at the lowest height, *h/c* = 0.079, is significantly different. The suction pressure for both the main element and the flap is not increasing but decreasing. Due to the wing being too close to the ground, the flow in this small gap becomes complicated and unexpected.

For others larger flap angles, the basic tendency is similar: the pressures on the pressure surface remain almost the same and the suction pressure for both the main element and the flap will be increased when the wing approaches to the ground. However, the increment becomes gradually smaller as the flap angle rises.

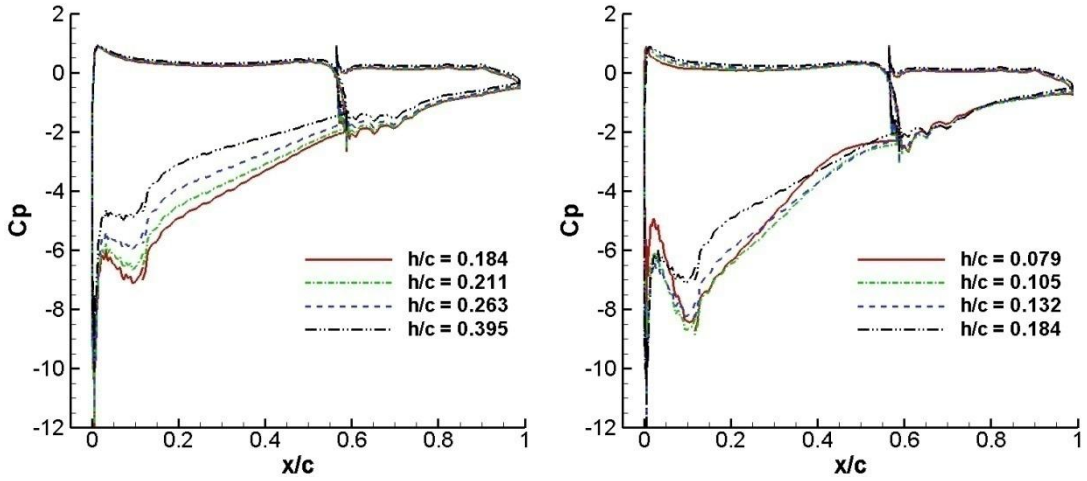

Figure 107: Surface pressure for various heights at α_{flap} = 14 º

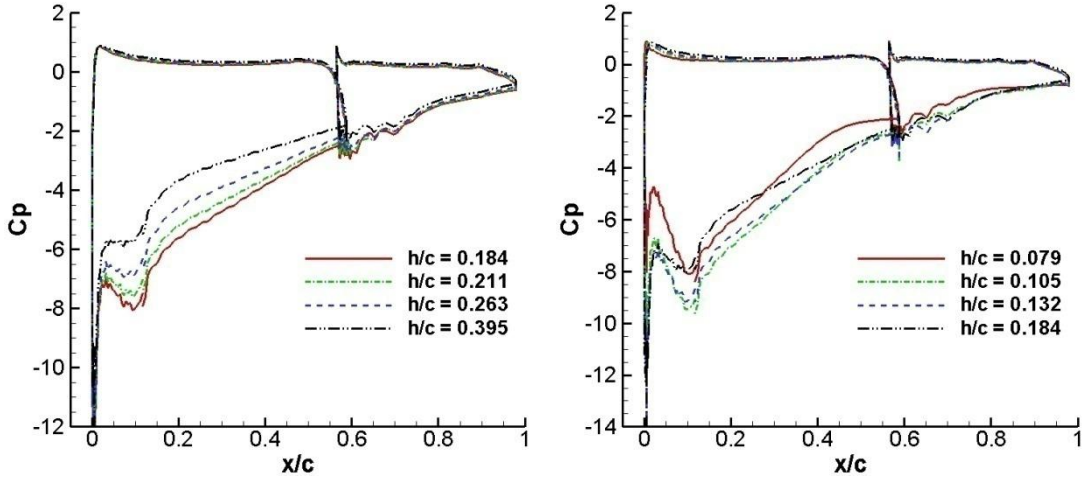

Figure 108: Surface pressure for various heights at α_{flap} = 18 º

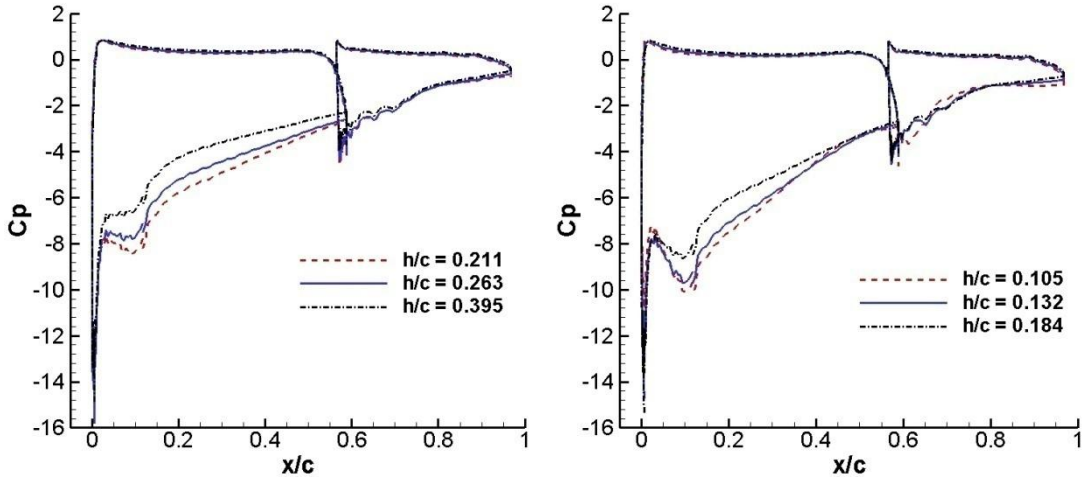

Figure 109: Surface pressure for various heights at α_{flap} = 23 º

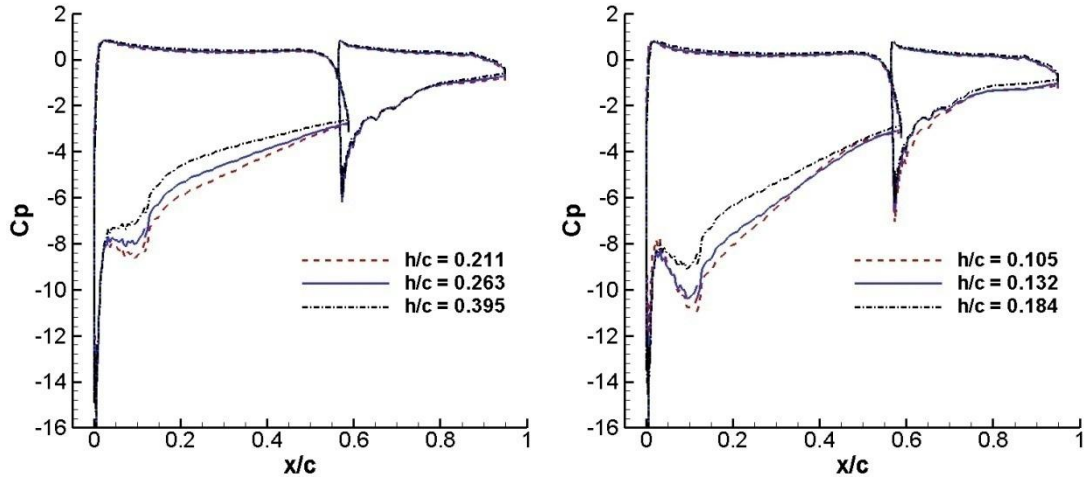

Figure 110: Surface pressure for various heights at α_{flap} = 28 º

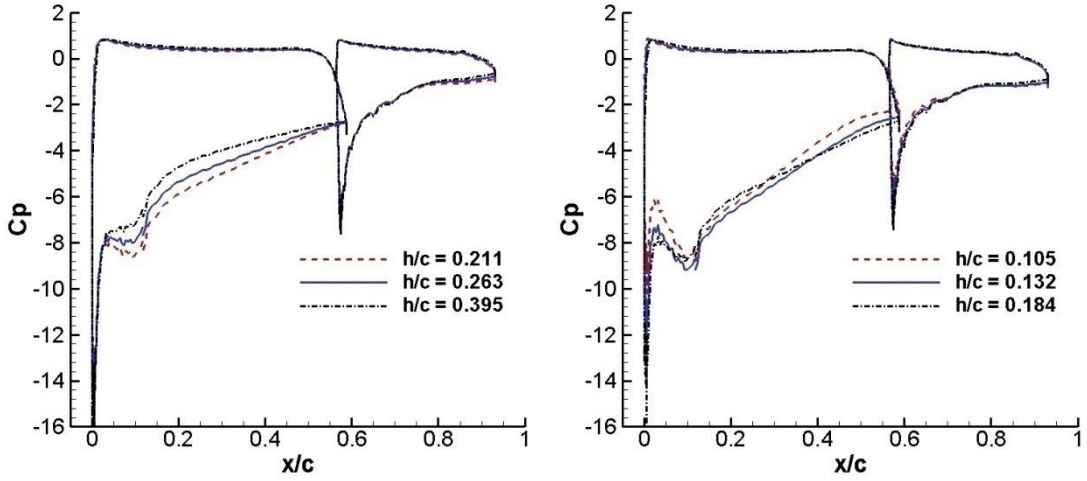

Figure 111: Surface pressure for various heights at α_{flap} = 32 °

The comparison of the surface pressure for the single element wing and the double element wing with different flap angles is shown in Figure 112. The chord coordinate for the single element wing has been non-dimensionalised by using the chord of the main element of the double element wing. It can be apparently seen that the pressure on the suction surface has increased significantly by adding the flap for all the angles. The suction peak for both the single and the double element wing is occurred at the same location. However, the suction spike near the leading edge grows greater than the suction peak for the double element wing. On the pressure surface, the added flap leads to a slightly larger pressure and is also smoother in the region from the leading edge to $x/c \approx 0.1$.

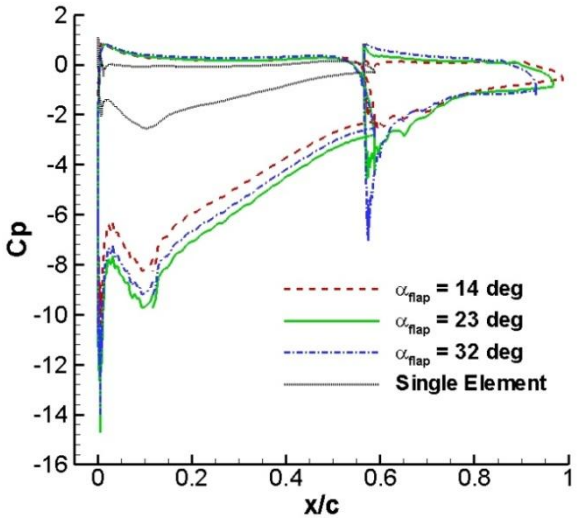

Figure 112: Comparison of surface pressure for the single element wing and the double element wing

The influence of the flap angle at the same ground heights are presented in Figure 113 and Figure 114. For both the main element and the flap, the shape of the suction surface pressure keeps to be similar but increases while the flap angle rises. However, this increment stops after the flap angle reaches a certain level. For the lower height h/c = 0.132, the suction pressure reduced when the flap angle grows to α_{flap} = 32 º. For the higher height h/c = 0.211, the suction pressure keeps a similar profile at α_{flap} = 23 º, α_{flap} = 28 ºand α_{flap} = 32 º. A flow separation can be found at a large flap angle near the trailing edge of the flap, due to the constant pressure in this region. On the pressure surface, the pressure remains almost the same on the main element, while increases slightly on the flap as the flap angle rises.

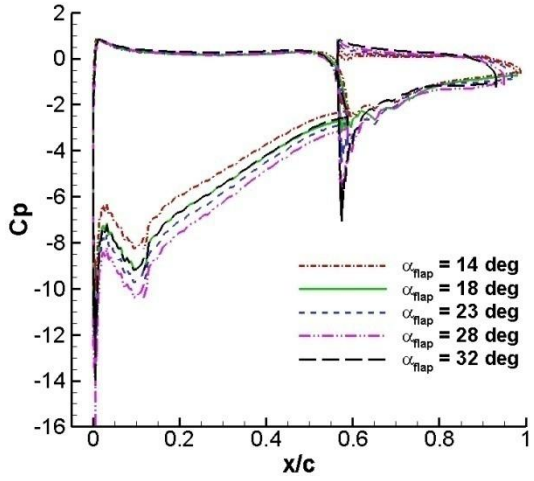

Figure 113: Surface pressure at *h/c* = 0.132

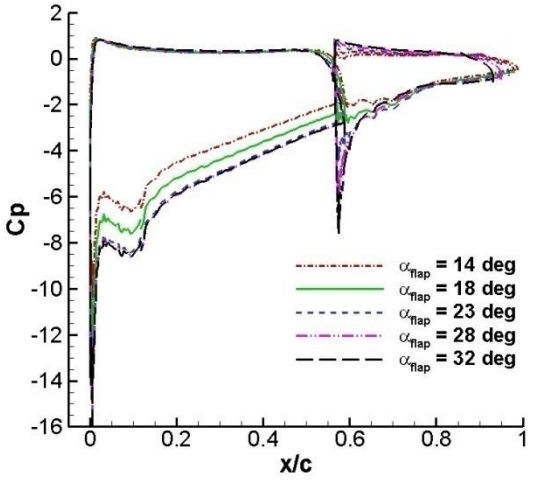

Figure 114: Surface pressure at *h/c* = 0.211

8.3 Wake and Ground Boundary Layer

To investigate the wake of the double element wing at various heights and at different flap angles, two near-field locations are taken at *x/c* = 1.2 and *x/c* = 1.5 which are the same as the single element wing. The wake profiles are from a little above the trailing edge of the flap to the moving ground, shown from Figure 115 to Figure 119.

From these figures, it can be obviously found that the thickness of the main wake increases as the wing approaches to the ground for all flap angles. The reason is the same as in single element wing that was caused by the increased suction peak hence a similar increasing recovery pressure gradient. It will lead to a thicker boundary layer of the wing, and then thicker wake, as the wing gets closer to the ground. At the same time, the top side of the wake does not change significantly, while the main contribution of the wake thickness is largely due to the bottom side from the suction surface of the wing.

Compared to the single element wing at *x/c* = 1.2, another small deficit of velocity can be seen on the top side of the main wake. It is considered generated by the flap, while

the main deficit appears to be due to the main element. As moving downstream, this small deficit disappears and mixes with the main wake. Also, the thickness of the wake increases while the velocity deficit reduces, for the turbulence mixing, as found in the single element wing. The mergence between the wake of the flap and the main element is fully developed, because no discontinuity can be found in the location x/c = 1.5. Another similar aspect with the single element wing is that the velocity accelerates between the wing and the ground due to the increased suction pressure in this region. And for all heights, this high speed flow reaches approximately the same value. In the same manner as the single element wing, the ground boundary layer can be seen in both streamwise locations. Meanwhile, a velocity deficit appears in the ground boundary and develops slightly bigger while the wing moves close to the ground. However, when the flap angle is large enough to reach the stall angle like α_{flap} = 32 º, the ground boundary layer becomes similar for all the ground heights.

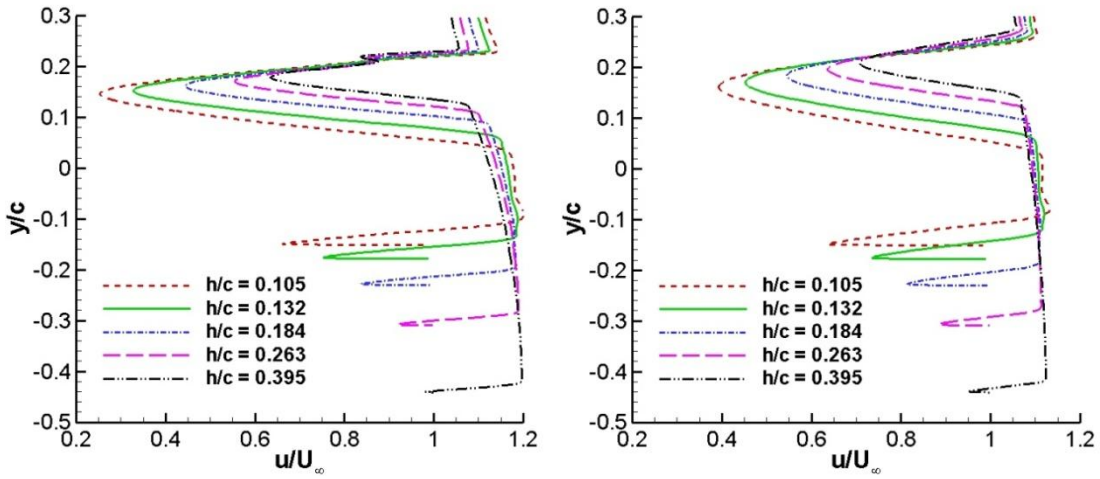

(a) x/c = 1.2 (b) x/c = 1.5

Figure 115: Wake profile for α_{flap} = 14 º

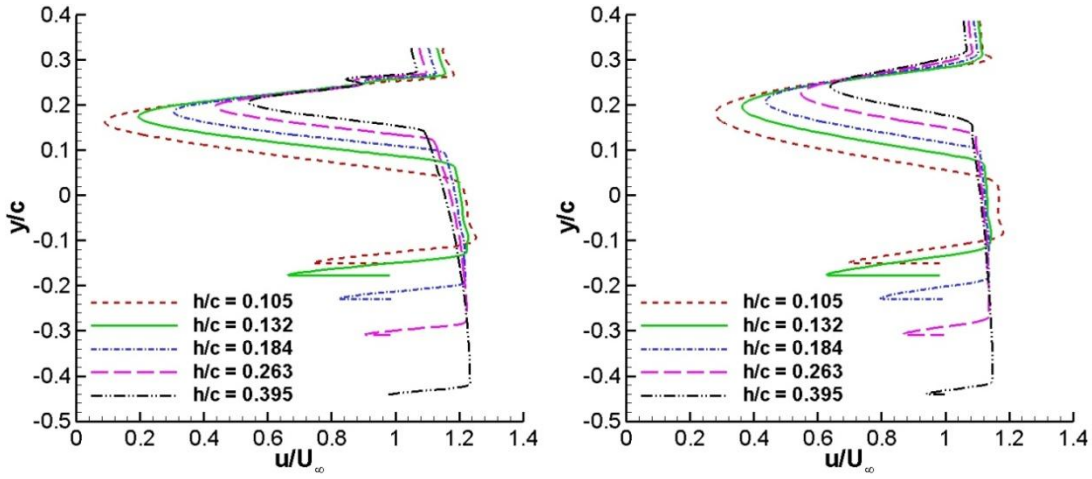

(a) x/c = 1.2 (b) x/c = 1.5

Figure 116: Wake profile for α_{flap} = 18 º

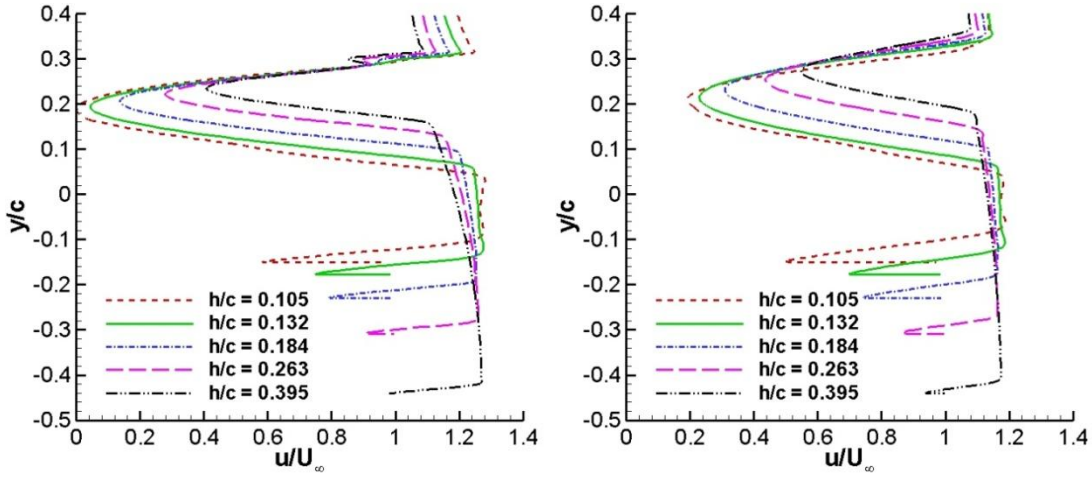

(a) x/c = 1.2 (b) x/c = 1.5

Figure 117: Wake profile for α_{flap} = 23 º

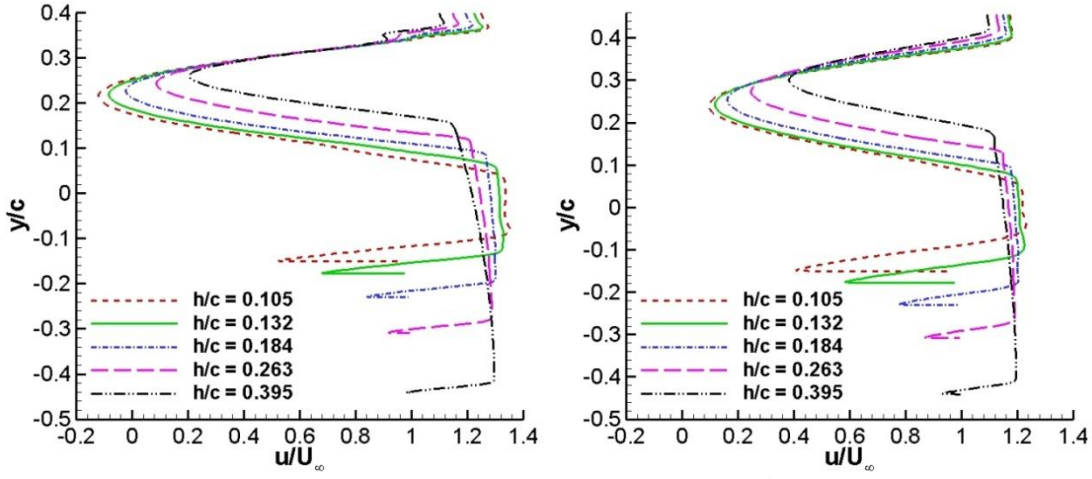

(a) x/c = 1.2 (b) x/c = 1.5

Figure 118: Wake profile for α_{flap} = 28 º

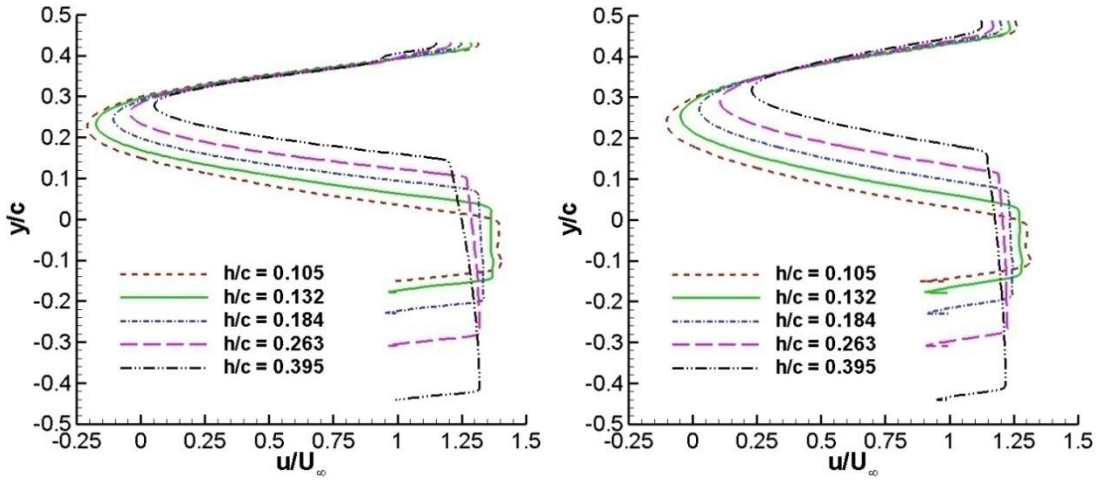

(a) x/c = 1.2 (b) x/c = 1.5

Figure 119: Wake profile for α_{flap} = 32 º

A set of comparisons of that wake profile at various flap angles are presented in Figure 120 to Figure 122. It can be clearly understood that both the wake thickness and the velocity deficit are greater as the flap angle rises, because the flow passes along with the upper surface of the flap that the larger flap angle would lead to a larger angle of flow direction. Again, the flow is accelerated between the ground and the wing surface. And the larger flap angles have a greater extend velocity in this region.

The ground boundary layer is similar for all flap angles at higher heights, such as h/c = 0.211 and h/c = 0.395. However, at the lower height h/c = 0.105, both the thickness and the velocity deficit inside the boundary layer are reduced when the flap angle becomes smaller besides the stall angle which shows nearly no velocity deficit inside the boundary layer.

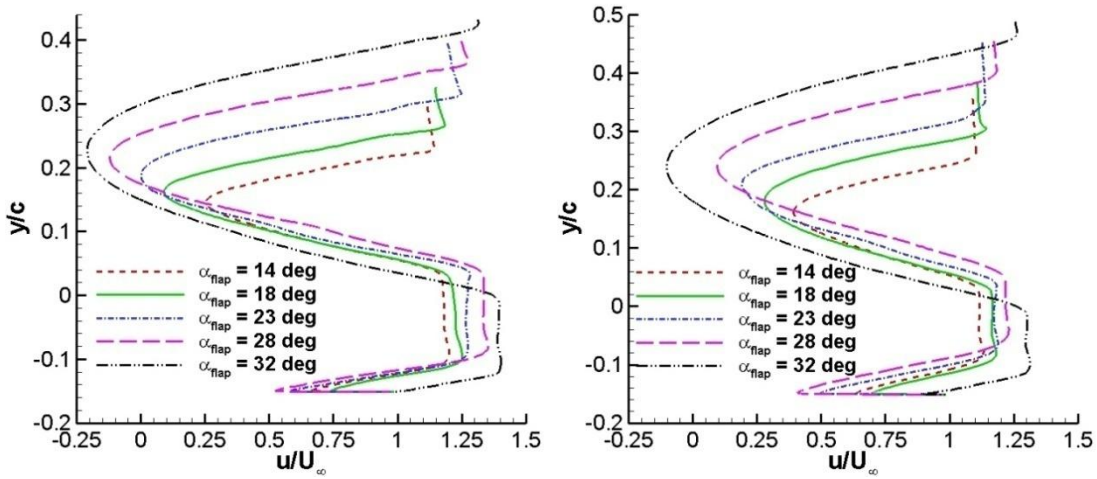

(a) *x/c* = 1.2 (b) *x/c* = 1.5

Figure 120: Wake profile for *h/c* = 0.105

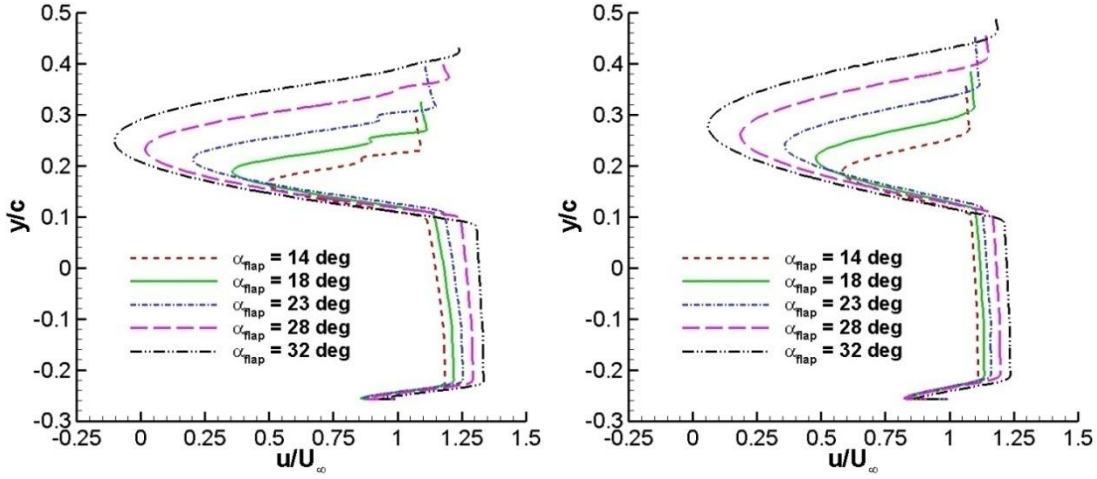

(a) *x/c* = 1.2 (b) *x/c* = 1.5

Figure 121: Wake profile for *h/c* = 0.211

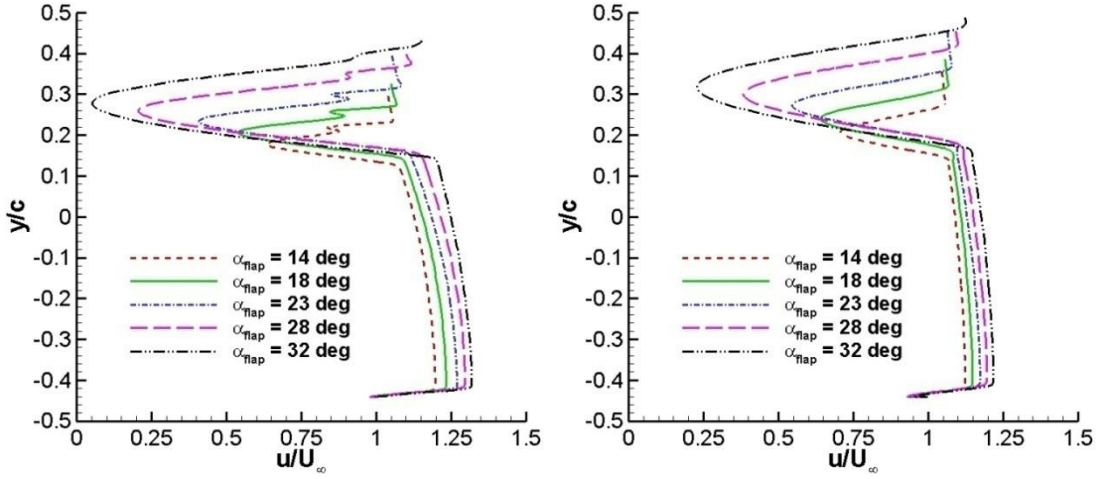

(a) *x/c* = 1.2 (b) *x/c* = 1.5

Figure 122: Wake profile for *h/c* = 0.395

8.4 Flow Visualisation

In order to get more intuitive viewing to support the analysis, some flow contours and the streamlines are drawn in the following figures for studying the ground effect of the double element wing.

In the same situations as the single element wing that for all flap angles with all the ground heights, a high Mach number region can be apparently found under the main element suction surface where the wing is within the closest distance to the ground (Figure 123 to Figure 127). This means that the flow accelerates hence the dense streamline shown at this part. Also under the suction surface of the main element, the Mach number increases while the wing approaches the ground. The flap angle dimension affects slightly the Mach number at higher heights. However, when the wing is closer to the ground, the larger flap angle will bring a bigger Mach number on the suction surface, hence will generate more downforce. Meanwhile, a low Mach number region comes out along the wake of the main element and is fully developed under the trailing edge of the flap. The Mach number here is reduced since either the wing is closer to the ground or the flap angle becomes larger, while the area of this low mach number region increases at the same time. Once the Mach number is low enough, vortices will appear, such as the larger flap angles α_{flap} = 28 ºand α_{flap} = 32 º.

The vorticity magnitude shown in Figure 128 to Figure 132 is another way to see the captured vortices. As the flap angle increases, a stronger shear layer can be found after the main element and leads to a great velocity gradient, which finally forms as vortices.

Although the added flap has increased the true angle of attack compared to the single element wing, the flow still attaches well at small flap angles. The use of the double element wing instead of the single one brings great advantages. Even at large flap angles, the big vortices only emerge when the wing is very close to the ground.

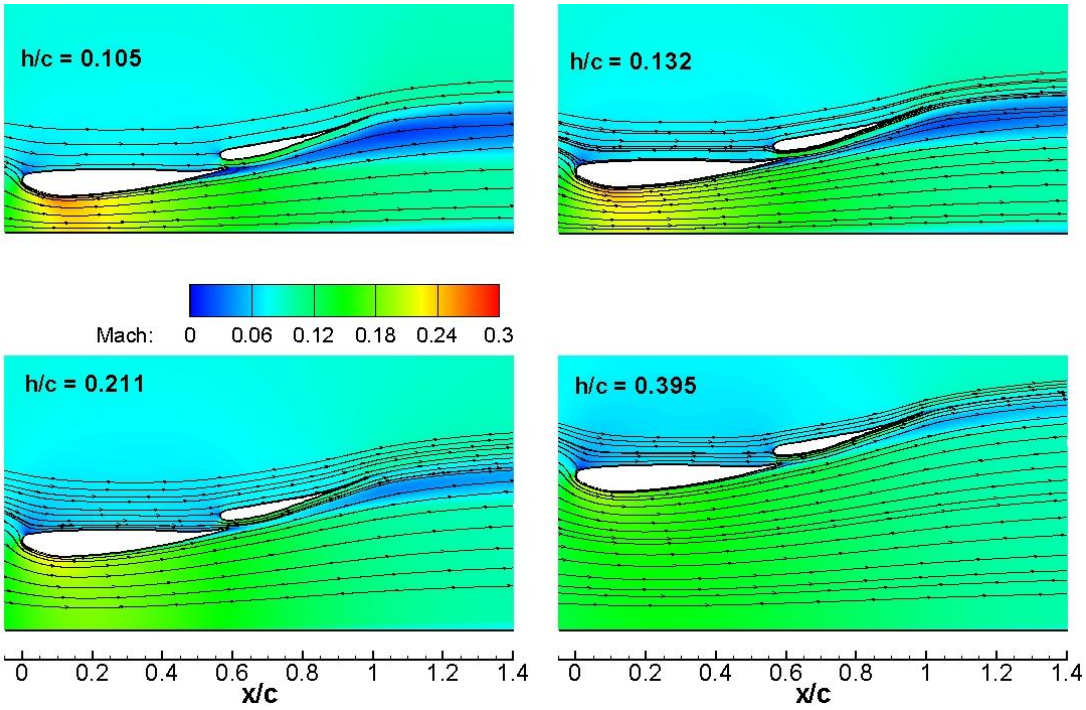

Figure 123: Mach contour with streamlines at α_{flap} = 14 º

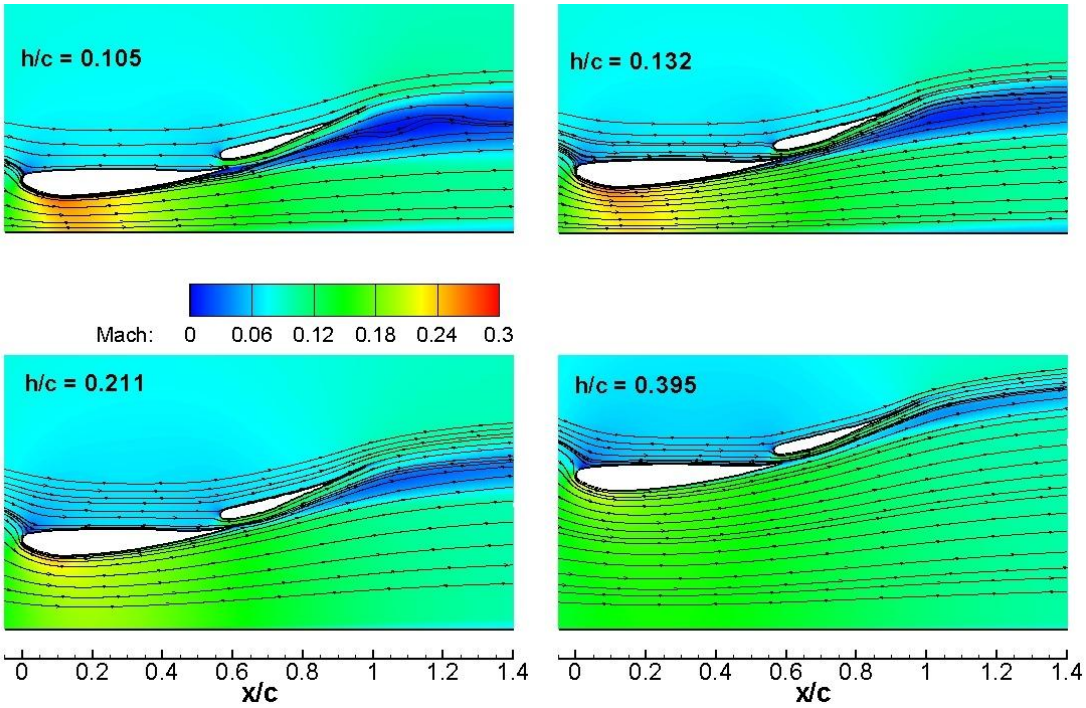

Figure 124: Mach contour with streamlines at α_{flap} = 18 º

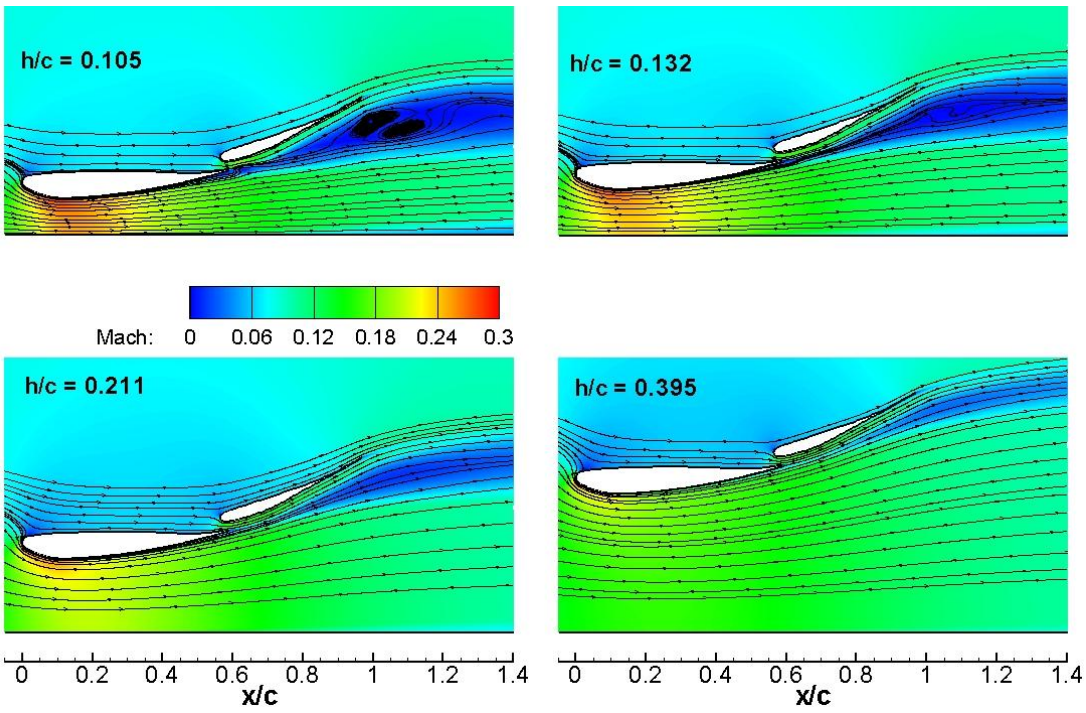

Figure 125: Mach contour with streamlines at α_{flap} = 23 º

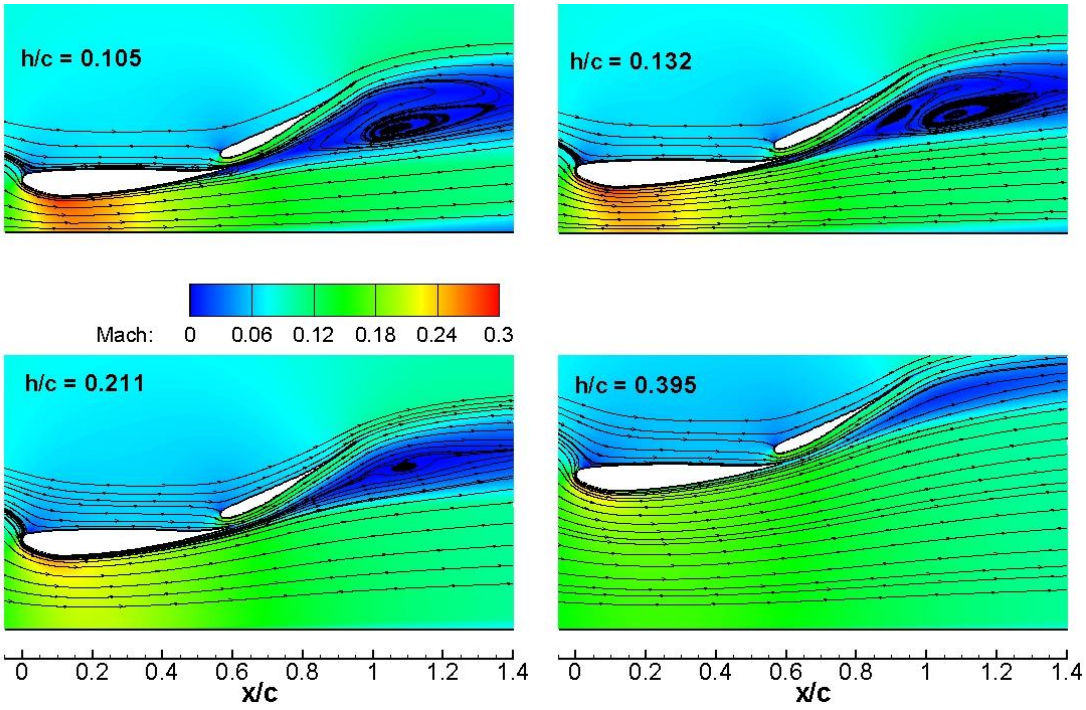

Figure 126: Mach contour with streamlines at α_{flap} = 28 º

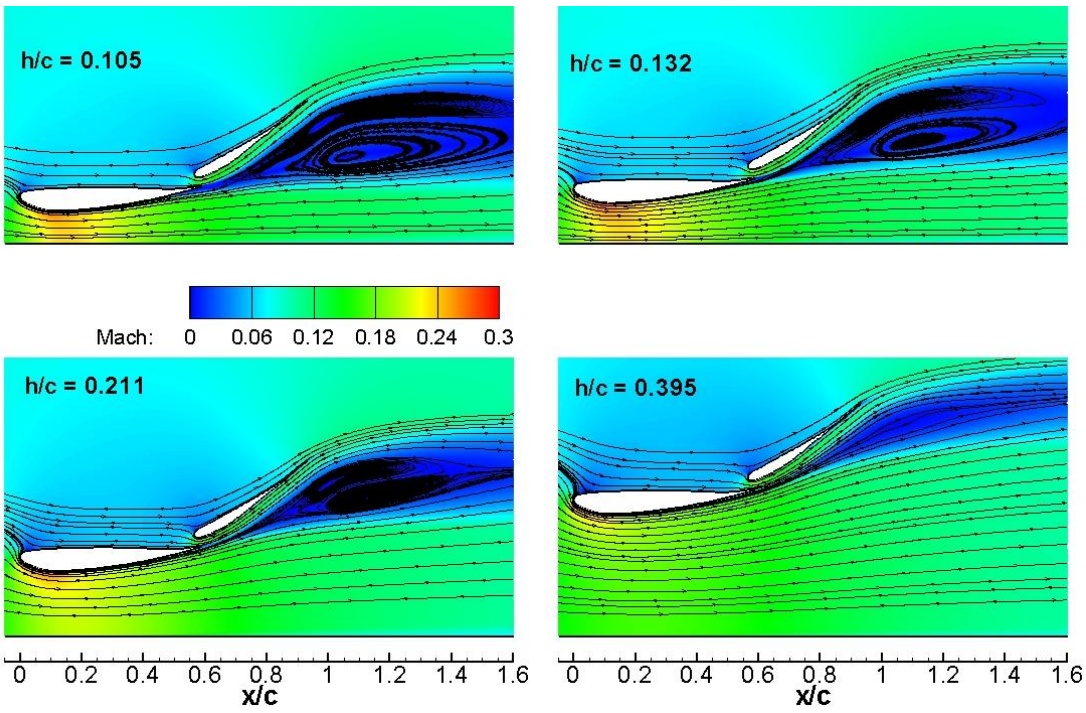

Figure 127: Mach contour with streamlines at α_{flap} = 32 º

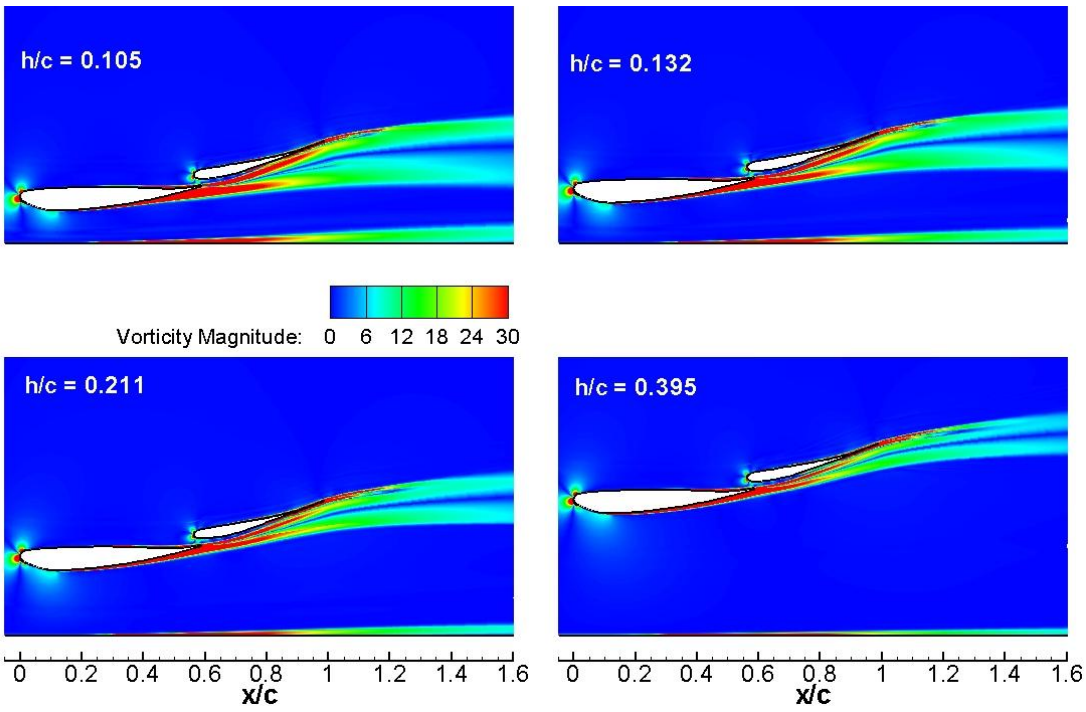

Figure 128: Vorticity magnitude at α_{flap} = 14 º

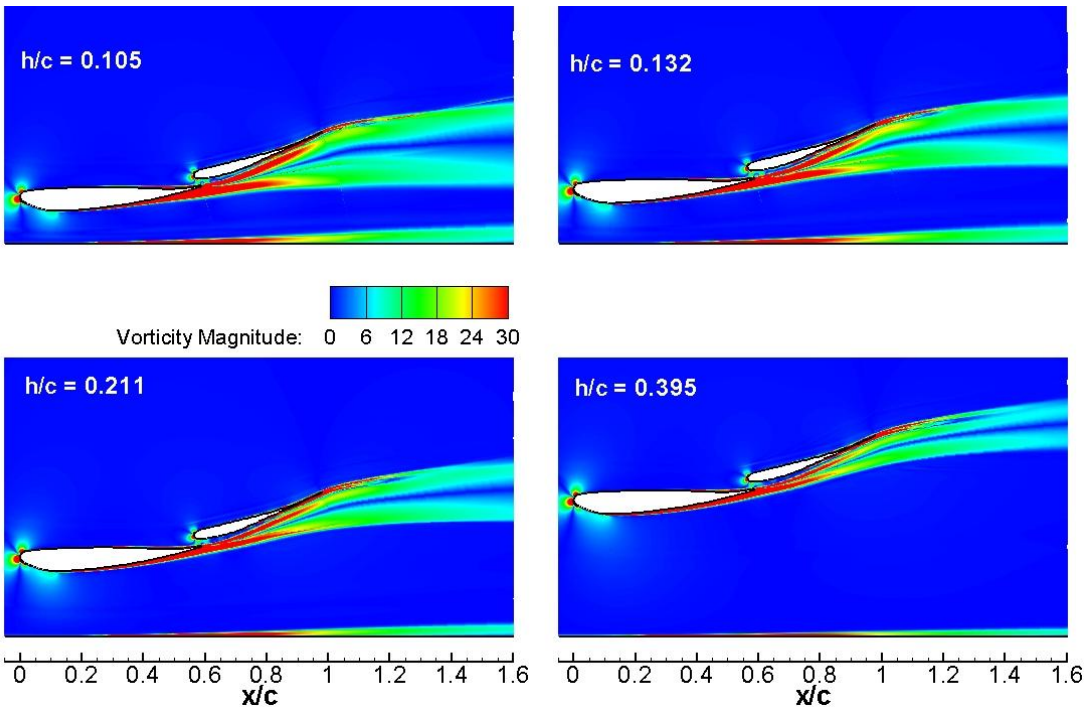

Figure 129: Vorticity magnitude at α_{flap} = 18 º

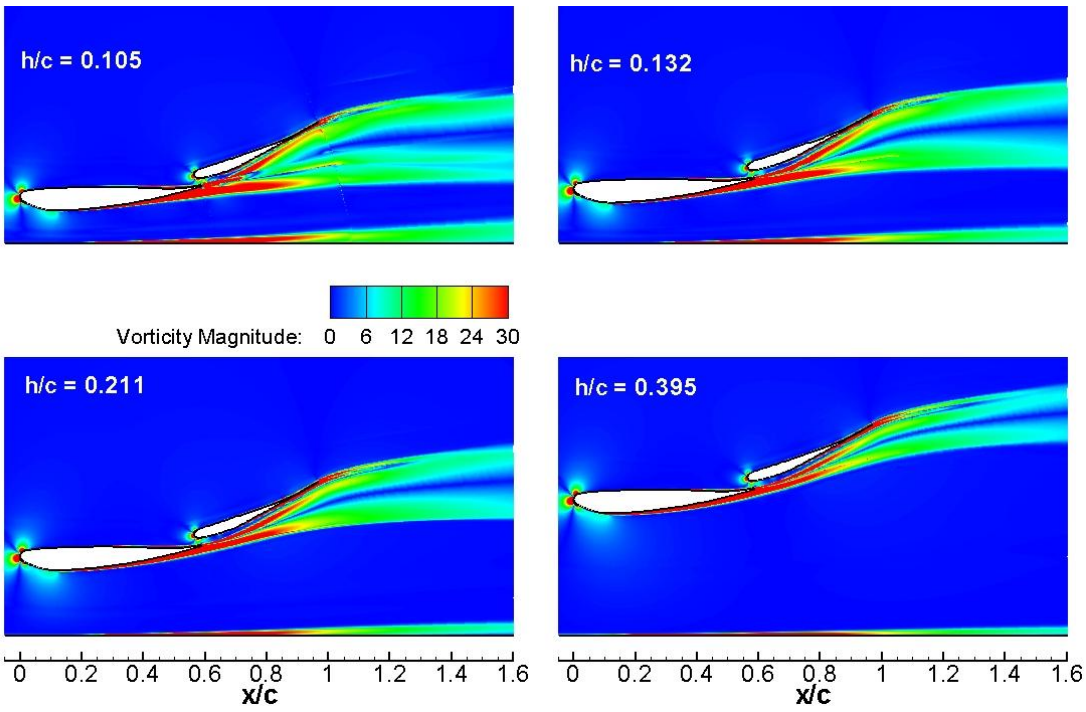

Figure 130: Vorticity magnitude at α_{flap} = 23 º

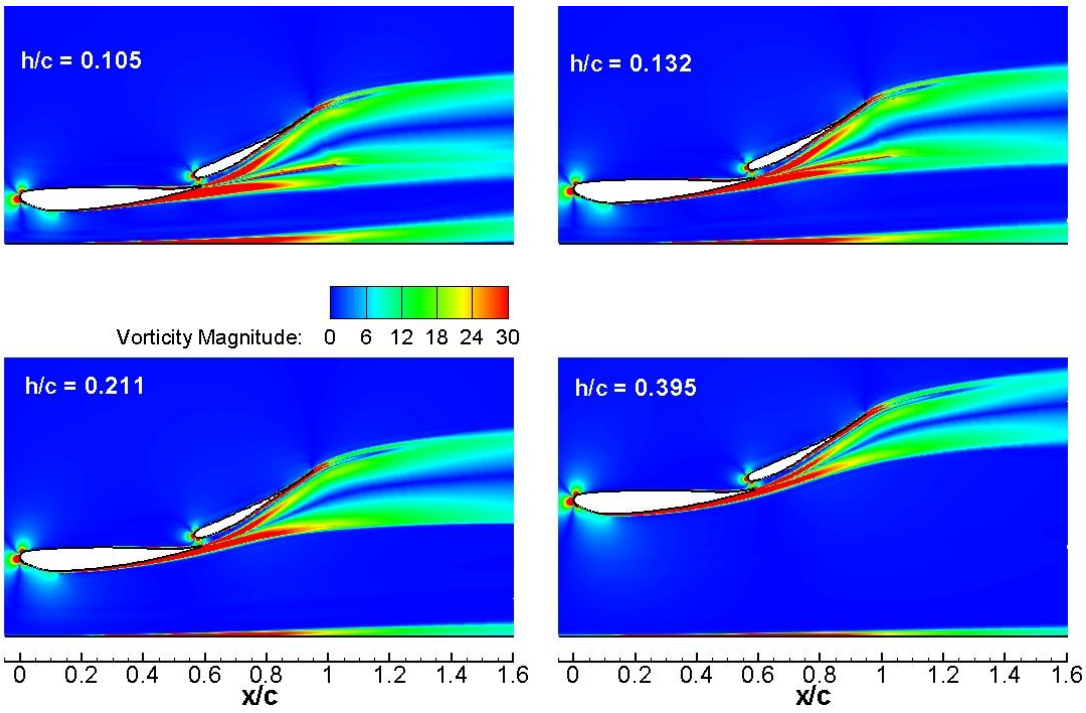

Figure 131: Vorticity magnitude at α_{flap} = 28 º

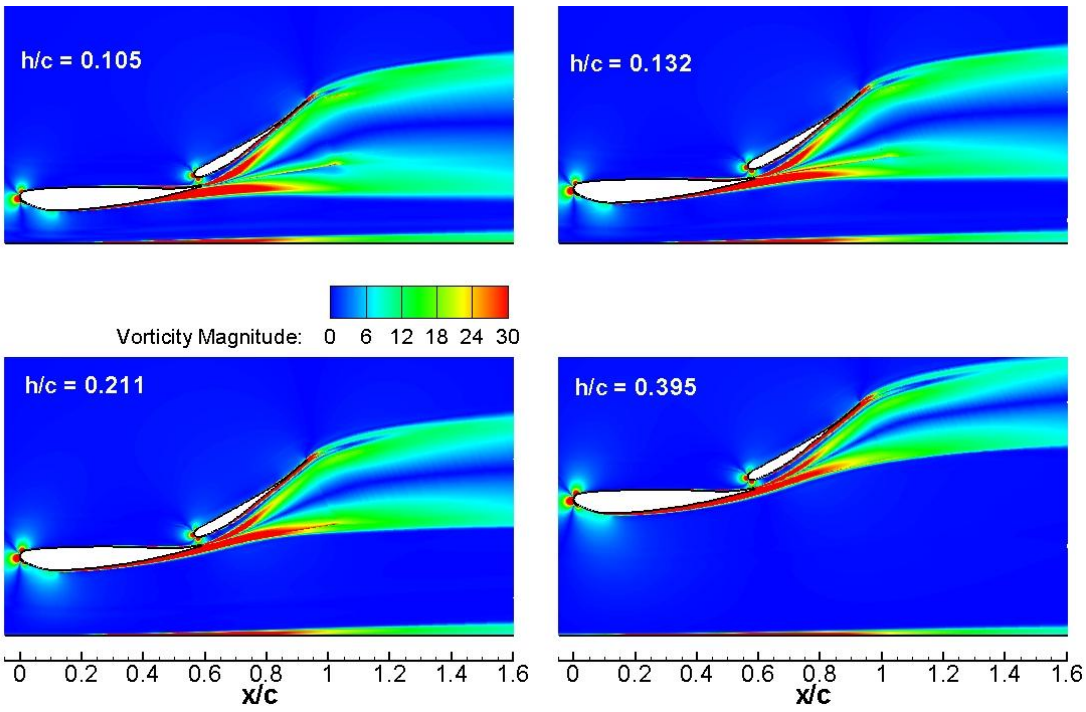

Figure 132: Vorticity magnitude at α_{flap} = 32 º

8.5 Summary

In this chapter, a series of pure simulations which were focused on aerodynamic performance were accomplished with a variety of configurations for the double element wing by using the HLLC solver with the WENO 3rd order scheme in conjunction with the SST k-ω model.

For the double element wing, various simulations were carried out under the configurations that the main element is fixed while the flap angle can be changed. The general tendency for both the downforce and the drag are similar with the single element wing, however the magnitude is much bigger. It can be otherwise stated that the added flap will bring extra downforce due to the increased camber of the whole double element wing. Surprisingly, it is found from the flow visualisation that the increased camber does not bring a significant vortex shedding after the trailing edge until the flap grows to a certain high angle. Again, the thickness of the wake increases as the wing gets closer to the ground.

Chapter 9

Conclusions and Recommendations for Future Work

In this MSc by research project, turbulent flows around both a single and a double element wing in ground effect were carried out by using the FLOWer code.

Firstly, three different numerical schemes in conjuction with three different turbulence models were employed in the single element wing simulations to discuss the computational accuracy by comparing the simulated and the experimental results.

For the investigation of numerical methods, three numerical schemes, which are the Jamson's central differencing scheme (CDS), the HLLC solver with MUSCL scheme (HLLC + MUSCL) and the 3rd order WENO scheme (HLLC + WENO3), are compared in the single element wing simulations at different ground heights respectively. The CDS predicts poor results in all the aerodynamic parameters which are concerned, while the only advantage is the fastest convergence compared to the others schemes as it uses the implicit residual smooth technique, which allows larger CFL number to be used. The two high order schemes, the HLLC + MUSCL and the HLLC + WENO3, present similar but more accurate simulations than the CDS during the whole processing. However, for the most important parameters of the front wing, which are the lift and the drag coefficients, the HLLC + WENO3 scheme gives a better result than the HLLC+MUCSL. Moreover, the HLLC + WENO3 scheme shows satisfactory modelling on turbulent flow and vortices capturing at low heights. For these reasons, the HLLC + WENO3 scheme is used as the numerical method during the further numerical investigation carried out in this project.

Like the numerical methods' investigation, three turbulence models, which are the Spalart-Allmaras (S-A) model, the SST k-ω model and the Wilcox k-ω model, are also carried out at different heights respectively. Compared to the Wilcox k-ω model, the

S-A and the SST *k-ω* models predict similar but more accurate simulations during the whole process. Again, regarding the most important aerodynamic parameters which are the lift and the drag coefficients, the SST *k-ω* model gives a better result than the S-A model and also in the wake analysis. For these reasons, the SST *k-ω* model is used as the turbulence model during the following numerical investigations in this project.

Further on, the ground effect was investigated computationally by using the HLLC solver with the 3rd order WENO scheme in conjunction with the SST *k-ω* model. A series of numerical simulations which were focused on aerodynamic performance were accomplished with a variety of configurations for both the single and the double element wing.

For the single element wing, the downforce continues increasing as the height is reduced, until it reaches the height of the maximum downforce. Then, the downforce will turn to fall rapidly below this height. The situation keeps similar when the angle of attack grows larger. At the same time, the downforce itself is increased with the growing angle of attack. However, after it reaches the stall angle, the downforce drops fast and no longer changes with the reduced height. The drag does not follow the same manner as the downforce. It keeps increasing as the ground height reduces for all heights. Moreover, the slope of the drag also increases as the wing is close to the ground. The effect of reducing the height on the pressure distribution is generally the same when the angle of attack is increased. The pressure increases over the whole suction surface while it slightly decreases on the pressure surface. From the wake analysis, as the ground height is reduced, the thickness of the wake increases. And it also leads to an increased velocity deficit in the wake centre. An existence of vortex shedding from the trailing edge can be found visually from the simulations. The shedding itself becomes larger not only as the angle of attack grows bigger, but also as

the wing approaches the ground.

For the double element wing, various simulations were carried out under the configurations that the main element is fixed at a certain angle while the flap angle can be changed. The general tendency for both the downforce and the drag are similar with the single element wing, however the magnitude is much bigger. It can be otherwise stated that the added flap will bring extra downforce due to the increased camber of the whole double element wing. Surprisingly, it is found from the flow visualisation that the increased camber does not bring a significant vortex shedding after the trailing edge until the flap grows to a certain high angle. Again, the thickness of the wake increases as the wing gets closer to the ground.

Based on the current investigation of this project, some suggestions for future works can be made as follows:

1. To refine the mesh by employing more grid points or reconstructing the strategy of the blocks, such as inducting the O-grid around the entire wing.
2. To validate the unsteady solution instead of steady with higher order resolutions, such as DES or LES approaches for the turbulent flow over the wing to achieve high accuracy, especially in capturing the flow separation and the vortex shedding.
3. To simulate 3-D wing cases for both the single and the double element wing to investigate the flow status in a spanwise direction. Also, the true front wing is designed with an endplate. So the flow around a wing with an endplate and the tip vortex investigation would be another important objective of studying the front wing.
4. To continue the optimization of the flap of the double element wing. Further research could be focused on the gap and overlap of the flap and also the chord proportion of the main element and the flap.

Reference

Agathangelou, 1998, B. and Gascoync, M. “Aerodynamic considerations of a Formula 1 racing car”. SAE Publication 980399.

Ahmed, M. R., Takasaki, T. and Kohama, Y., 2006, "Experiments on the Aerodynamics of a Cambered Airfoil in Ground Effect", 44th AIAA Aerospace Sciences Meeting and Exhibit; Reno, NV; USA; 9-12 Jan. 2006, Vol. AIAA Paper 2006-0258, American Institute of Aeronautics and Astronautics, 1801 Alexander Bell Drive, Suite 500, Reston, VA, 20191-4344, USA.

Anderson, J. D., 2007, “Fundamentals of aerodynamics,” McGraw-Hill Higher Education.

Blazek, J., 2001, “Computational fluid dynamics: principles and applications,” 1st edition, Elsevier, Amsterdam.

Coulliette, C. and Plotkin, A., 1996, “Aerofoil ground effect revisited”, Aeronautical Journal, pp 65-74, February.

Dominy, R.G., 1992, “Aerodynamics of Grand Prix cars”, Proceedings of the institution of Mechanical Engineers, Part D: Journal of Automobile Engineering, 206:267-274.

Drikakis, D. and Rider, W., 2005, “High-Resolution Methods for Incompressible and Low-Speed Flows”, Springer-Verlag.

E. F. Toro, 1999, “Riemann solvers and numerical methods for fluid dynamics”, 2nd edition. Springer-Verlag, Berlin.

F1 official website,

http://www.formula1.com/inside_f1/understanding_the_sport/5281.html

F. Menter, 1993, "Zonal Two Equation k-ω Turbulence Models for Aerodynamic flows," AIAA Paper 93-2906.

Ferziger, J. H., 1999 "Computational methods for fluid dynamics." Springer Verlag, March.

Garry, K.P. , 1996, "Some effects of ground clearance and ground plane boundary layer thickness on the mean base pressure of a bluff vehicle type body", Journal of Wind Engineering and Industrial Aerdynamics, 62: 1-10.

Godir, P., Zingg, D.W. and Nelson, T.E., 1997, "Highlift aerodynamic computations with one- and two-equation turbulence models", AIAA Journal, 35(2): 237-243, February.

Jasinski, W.J., and Selig, M.S., 1998, "Experimental Study of Open-Wheel Race Car Front Wings," SAE Paper 983042, Nov.

Jameson, A. and Baker, T. J., 1983, "Solution of the Euler equations for complex configurations," AIAA Paper 83-1929.

Jameson, A., Schmidt, W. and Turkel, E., 1981, "Numerical solutions of the Euler equations by finite volume methods using Runge-Kutta time-stepping schemes," AIAA Paper 81-1259.

Katz, J., 2006, "Aerodynamics of Race Cars", Annual Review of Fluid Mechanics, vol. 37, no. 38, pp. 27-63.

Katz, J., 1995, "Race car aerodynamics : designing for speed," Cambridge.

Knowles, K., Donahue, D.T., and Finnis, M. V., 1994, “A Study of Wings in Ground Effect,” RAeS Conference on Vehicle Aerodynamics, Royal Aeronautical Society, London, pp. 22.1-22.13.

Kroll, N. et al., 2000, “FLOWer installation and user handbook,” Version 116, MEGAFLOW-1001.

Liu, X. et al., 1994, “Weighted essentially non-oscillatory schemes,” Journal of Computational Physics, vol. 115, pp. 200-212.

Mahon, S. and Zhang, X., 2003, "Computational Analysis of an Inverted Double-Element Airfoil in Ground Effect", vol. 128, no. 6, pp. 1172-1180.

Mahon, S. and Zhang, X., 2003, "Computational Analysis of Pressure and Wake Characteristics of an Aerofoil in Ground Effect", Journal of Fluids Engineering (Transactions of the ASME), vol. 127, no. 2, pp. 290-298.

Melvin, A. and Martinelli, L., 2008, "Aerodynamic Shape Optimization of Multi-element Airfoils in Ground Effect", 46th AIAA Aerospace Sciences Meeting and Exhibit, vol. AIAA Paper 2008-327.

Menter, F. R., “Two-equation eddy-viscosity turbulence models for engineering applications”, AIAA Journal, vol. 32, pp. 268-289.

M. M. Karim, M. M. Rahman and M. A. Alim, 2009, “Computation of Axisymmetric Turbulent Viscous Flow Around Sphere”, Journal of Scientific Research, vol. 1(2), pp. 209-219.

NASA Viscous Grid Spacing Calculator,
http://geolab.larc.nasa.gov/APPS/YPlus/

Nye, Doug, 1985, Autocourse History of the Grand Prix car 1966 - 1985, Hazleton publishing, ISBN 0-905-138-37-6

Nuhait, A.O. and Mook, D.T., 1989, "Numerical Simulation of wings in steady and unsteady ground effects", Journal of Aircraft, 12(26):1081-1089, December 1989.

Ranzenbach, R. and Barlow, J. B., 1995, "Cambered airfoil in ground effect - Wind tunnel and road conditions", AIAA Applied Aerodynamics Conference, 13th, San Diego, CA, Technical Papers. Pt. 2; UNITED STATES; 19-22 June 1995, Vol. AIAA Paper 1995-1909, Washington, DC: American Institute of Aeronautics and Astronautics.

Ranzenbach, R., and Barlow, J.B., 1994, "Two Dimensional Airfoil in Ground Effect, an Experimental and Computational Study," SAE paper 94-2509.

Ranzenbach, R., and Barlow, J.B., 1995, "Cambered Aerofoil in Ground Effect: Wind Tunnel and Road Conditions," AIAA Paper 95-1909, June.

Ranzenbach, R., and Barlow, J.B., 1996, "Cambered Aerofoil in Ground Effect, an Experimental and Computational Study," SAE Paper 96-0909.

Ranzenbach, R., Barlow, J.B., and Diaz, R.H., 1997, "Multielement Aerofoil in Ground Effect, an Experimental and Computational Study," SAE Paper 97-2238, JUNE.

Raymond, A.E., 1921, "Ground influence on aerofoils", Technical Report, NACA-TN-67, NACA.

Screbrinsky, Y.M. and Biachuev, S.A., 1946, "Wing tunnel investigation of the horizontal motion of a wing near the ground", Technical Report NASA-TM-1095, NACA.

Shew, J. E. and Wyman, L. R., 2005, "Race Car Front Wing Design", 43rd AIAA Aerospace Sciences Meeting and Exhibit; Reno, NV; USA; 10-13 Ja. 2005, Vol. AIAA Paper 2005-0139, American Institute of Aeronautics and Astronautics, 1801 Alexander Bell Drive, Suite 500, Reston, VA, 20191-4344, USA.

Spalart, P. R., and Allmaras, S. R., 1992, "A One-Equation Turbulence Model for Aerodynamic Flows," AIAA Paper, 92–0439.

Soso, M. D. and Wilson, P. A., 2006, "Aerodynamics of a wing in ground effect in generic racing car wake flows", Proceedings of the Institution of Mechanical Engineers D, Journal of Automobile Engineering, vol. 220, no. D1, pp. 1-13.

Steinbach, D. and Jacob, K., 1991, "Aerodynamic aspects of wings near ground", Transactions of the Japan Society for Aeronautical and Space Sciences, 34(104): 56-70, August 1991.

Tsubokura, M., Kitoh, K., Oshima, N., Nakashima, T., Zhang, H. and Onishi, K. (2007), "Large Eddy Simulation of Unsteady Flow Around a Formula Car on Earth Simulator", Vol. SAE Document 2007-01-0106, Society of Automotive Engineers, 400 Commonwealth Dr , Warrendale, PA, 15096, USA.

V. Patrick, 2006, "CFD study of wing tip vortices for inverted airfoils in ground effect," MSc student, Cranfield University.

Versteeg, H. K. et al., 1995, "An introduction to Computational Fluid Dynamics – The Finite Volume Method," 1st Edition, Longman Scientific and Technical Harlow.

W. Kieffer, S. M., N.Armbya, "CFD study of section characteristics of Formula Mazda race car wings", Mathematical and Computer Modelling, Vol.43 pp. 1275–1287.

Wilcox, D. C., 2006, “Turbulence Modelling for CFD”. 3rd Edition. Birmingham Press, Inc., San Diego, California.

Y. Moryoseff and Y. Levy, 2001, “Computational Study of the Flow about an Oscillating Wing in Ground Effect,” AIAA Paper, 2001-0863.

Zahm, A.F. and Bear, R.M., 1921, “Ground plane influence on airplane wings”, Journal of the Franklin Institute, pages 687-693, May 1921.

Zerihan, J. and Zhang, X., 2003, "Aerodynamics of a Double-Element Wing in Ground Effect", AIAA Journal, 2003 0001-1452, vol.41 no.6 (1007-1016).

Zerihan, J. and Zhang, X., 2001, "A single element wing in ground effect - Comparisons of experiments and computation ", Aerospace Sciences Meeting and Exhibit, 39th, Reno, NV, Jan. 8-11.

Zerihan, J. and Zhang, X., 2000, "Aerodynamics of a single element wing in ground effect", Journal of Aircraft, vol. 37, no. 6, pp. 1058-1064.

Zhang, X., Zerihan, J., Ruhrmann, A. and Deviese, M., 2002, Tip vortices generated by a wing in ground effect. In Proceedings of the 11th International Symposium on Applications of Laser Techniques to Fluid Mechanics. 11th International Symposium on Applications of Laser Techniques to Fluid Mechanics Lison, Portugal, Instituto Superior Technico.